Jordan Journal of
PHYSICS
An International Peer-Reviewed Research Journal

Volume 18, No. 4, Oct. 2025

Jordan Journal of Physics (*JJP*): An International Peer-Reviewed Research Journal funded by the Scientific Research and Innovation Support Fund, Jordan, and published quarterly by the Deanship of Research and Graduate Studies, Yarmouk University, Irbid, Jordan.

Manuscripts should be submitted to:

Prof. Muhammad S. Bawa'aneh
Editor-in-Chief, Jordan Journal of Physics
Deanship of Research and Graduate Studies
Yarmouk University-Irbid-Jordan
Tel. 00 962 2 7211111 Ext. 2075
E-mail: *jjp@yu.edu.jo*
Website: *https://jjp.yu.edu.jo*

Jordan Journal of
PHYSICS
An International Peer-Reviewed Research Journal

Volume 18, No. 4, Oct. 2025

The Hashemite Kingdom of Jordan

Yarmouk University

Jordan Journal of PHYSICS

An International Peer-Reviewed Research Journal

Funded by the Scientific Research and Innovation Support Fund

Volume 18, No. 4, Oct. 2025

Instructions to Authors

Instructions to authors concerning manuscript organization and format apply to hardcopy submission by mail, and also to electronic online submission via the Journal homepage website (http://jjp.yu.edu.jo).

Manuscript Submission

Manuscripts are submitted electronically through the journal's website:

https://jjp.yu.edu.jo/

Original *Research Articles*, *Communications* and *Technical Notes* are subject to critical review by minimum of two competent referees. Authors are encouraged to suggest names of competent reviewers. *Feature Articles* in active Physics research fields, in which the author's own contribution and its relationship to other work in the field constitute the main body of the article, appear as a result of an invitation from the Editorial Board, and will be so designated. The author of a *Feature Article* will be asked to provide a clear, concise and critical status report of the field as an introduction to the article. *Review Articles* on active and rapidly changing Physics research fields will also be published. Authors of *Review Articles* are encouraged to submit two-page proposals to the Editor-in-Chief for approval. Manuscripts submitted in *Arabic* should be accompanied by an Abstract and Keywords in English.

Organization of the Manuscript

Manuscripts should be typed double spaced on one side of A4 sheets (21.6 x 27.9 cm) with 3.71 cm margins, using Microsoft Word 2000 or a later version thereof. The author should adhere to the following order of presentation: Article Title, Author(s), Full Address and E-mail, Abstract, PACS and Keywords, Main Text, Acknowledgment. Only the first letters of words in the Title, Headings and Subheadings are capitalized. Headings should be in **bold** while subheadings in *italic* fonts.

Title Page: Includes the title of the article, authors' first names, middle initials and surnames and affiliations. The affiliation should comprise the department, institution (university or company), city, zip code and state and should be typed as a footnote to the author's name. The name and complete mailing address, telephone and fax numbers, and e-mail address of the author responsible for correspondence (designated with an asterisk) should also be included for official use. The title should be carefully, concisely and clearly constructed to highlight the emphasis and content of the manuscript, which is very important for information retrieval.

Abstract: A one paragraph abstract not exceeding 200 words is required, which should be arranged to highlight the purpose, methods used, results and major findings**.**

Keywords: A list of 4-6 keywords, which expresses the precise content of the manuscript for indexing purposes, should follow the abstract.

PACS: Authors should supply one or more relevant PACS-2006 classification codes, (available at http://www.aip.org/pacs/pacs06/pacs06-toc.html)

Introduction: Should present the purpose of the submitted work and its relationship to earlier work in the field, but it should not be an extensive review of the literature (e.g., should not exceed 1 ½ typed pages).

Experimental Methods: Should be sufficiently informative to allow competent reproduction of the experimental procedures presented; yet concise enough not to be repetitive of earlier published procedures.

Results: should present the results clearly and concisely.

Discussion: Should be concise and focus on the interpretation of the results.

Conclusion: Should be a brief account of the major findings of the study not exceeding one typed page.

Acknowledgments: Including those for grant and financial support if any, should be typed in one paragraph directly preceding the References.

References: References should be typed double spaced and numbered sequentially in the order in which they are cited in the text. References should be cited in the text by the appropriate Arabic numerals, enclosed in square brackets. Titles of journals are abbreviated according to list of scientific periodicals. The style and punctuation should conform to the following examples:

1. Journal Article:

a) Heisenberg, W., Z. Phys. 49 (1928) 619.
b) Bednorz, J. G. and Müller, K. A., Z. Phys. B64 (1986) 189
c) Bardeen, J., Cooper, L.N. and Schrieffer, J. R., Phys. Rev. 106 (1957) 162.
d) Asad, J. H., Hijjawi, R. S., Sakaji, A. and Khalifeh, J. M., Int. J. Theor. Phys. 44(4) (2005), 3977.

2. Books with Authors, but no Editors:

a) Kittel, C., "Introduction to Solid State Physics", 8th Ed. (John Wiley and Sons, New York, 2005), chapter 16.
b) Chikazumi, S., C. D. Graham, JR, "Physics of Ferromagnetism", 2nd Ed. (Oxford University Press, Oxford, 1997).

3. Books with Authors and Editors:

a) Allen, P. B. "Dynamical Properties of Solids", Ed. (1), G. K. Horton and A. A. Maradudin (North-Holland, Amsterdam, 1980), p137.
b) Chantrell, R. W. and O'Grady, K., "Magnetic Properities of Fine Particles" Eds. J. L. Dormann and D. Fiorani (North-Holland, Amsterdam, 1992), p103.

4. Technical Report:

Purcell, J. "The Superconducting Magnet System for the 12-Foot Bubble Chamber", report ANL/HEP6813, Argonne Natt. Lab., Argonne, III, (1968).

5. Patent:

Bigham, C. B., Schneider, H. R., US patent 3 925 676 (1975).

6. Thesis:

Mahmood, S. H., Ph.D. Thesis, Michigan State University, (1986), USA (Unpublished).

7. Conference or Symposium Proceedings:

Blandin, A. and Lederer, P. Proc. Intern. Conf. on Magnetism, Nottingham (1964), P.71.

8. Internet Source:

Should include authors' names (if any), title, internet website, URL, and date of access.

9. Prepublication online articles (already accepted for publication):

Should include authors' names (if any), title of digital database, database website, URL, and date of access.

For other types of referenced works, provide sufficient information to enable readers to access them.

Tables: Tables should be numbered with Arabic numerals and referred to by number in the Text (e.g., Table 1). Each table should be typed on a separate page with the legend above the table, while explanatory footnotes, which are indicated by superscript lowercase letters, should be typed below the table.

Illustrations: Figures, drawings, diagrams, charts and photographs are to be numbered in a consecutive series of Arabic numerals in the order in which they are cited in the text. Computer-generated illustrations and good-quality digital photographic prints are accepted. They should be black and white originals (not photocopies) provided on separate pages and identified with their corresponding numbers. Actual size graphics should be provided, which need no further manipulation, with lettering (Arial or Helvetica) not smaller than 8 points, lines no thinner than 0.5 point, and each of uniform density. All colors should be removed from graphics except for those graphics to be considered for publication in color. If graphics are to be submitted digitally, they should conform to the following minimum resolution requirements: 1200 dpi for black and white line art, 600 dpi for grayscale art, and 300 dpi for color art. All graphic files must be saved as TIFF images, and all illustrations must be submitted in the actual size at which they should appear in the journal. Note that good quality hardcopy original illustrations are required for both online and mail submissions of manuscripts.

Text Footnotes: The use of text footnotes is to be avoided. When their use is absolutely necessary, they should be typed at the bottom of the page to which they refer, and should be cited in the text by a superscript asterisk or multiples thereof. Place a line above the footnote, so that it is set off from the text.

Supplementary Material: Authors are encouraged to provide all supplementary materials that may facilitate the review process, including any detailed mathematical derivations that may not appear in whole in the manuscript.

Revised Manuscript and Computer Disks

Following the acceptance of a manuscript for publication and the incorporation of all required revisions, authors should submit an original and one more copy of the final disk containing the complete manuscript typed double spaced in Microsoft Word for Windows 2000 or a later version thereof. All graphic files must be saved as PDF, JPG, or TIFF images.

Allen, P.B., "…….", in: Horton, G.K., and Muradudin, A. A., (eds.), "Dynamical…….", (North……..), pp….

Reprints

Twenty (20) reprints free of charge are provided to the corresponding author. For orders of more reprints, a reprint order form and prices will be sent with the article proofs, which should be returned directly to the Editor for processing.

Copyright

Disclaimer

Indexing

JJP is currently indexing in:

<table>
<tr><td> 
</td><td>Emerging Sources Citation Index (ESCI)

Journal Impact Factor 2022

0.7</td></tr>
<tr><td colspan="2"> 
</td></tr>
</table>

Jordan Journal of
PHYSICS
An International Peer-Reviewed Research Journal

Volume 18, No. 4, Oct. 2025

Table of Contents:

Volume 18, Number 4, 2025. pp. 423-433

Jordan Journal of Physics

ARTICLE

Enhanced Thermal and Dielectric Properties of Copper Oxide Nanoparticles Blended Polyisoprene Antibiofilm

M. Abila Jeba Queen[a] and **K. C. Brigh**[b]

[a] *Department of Physics, Holy Cross College (Autonomous), Nagercoil-629004, Tamil Nadu, India.*

[b] *Department of Physics, Mar Ivanio's College (Autonomous), Thiruvananthapuram, Kerala, India.*

Doi: **https://doi.org/10.47011/18.4.1**

Received on: 21/01/2024; *Accepted on: 08/09/2024*

Abstract: In order to improve the properties of polyisoprene (natural rubber), a small quantity of copper oxide (CuO) nanoparticles was incorporated using a mechanical method. Copper oxide nanoparticles were synthesized by the simple chemical reaction between copper acetate and oxalic acid. 0.4 g of the prepared copper oxide nanoparticles was impregnated into the isoprene. The structural properties of nanoparticles confirmed the monoclinic crystal system with a = 4.685Å, b = 3.423 Å, c = 5.132 Å, $\alpha = \beta = 90^{o}$, $\gamma = 99.52^{o}$, and V = 81.17 $Å^3$, whereas the copper blended rubber exhibited a lower ordered crystalline structure with an interplanar distance of 2.1567 Å along the (0 2 0) orientation. The dislocation densities of isoprene with varied copper oxide and copper oxide were found to be 2.5932 x 10^{22} m^{-2} and 1.12665 x 10^{15} m^{-2}, respectively. The polyisoprene matrix with a higher dislocation density confirms its hardest nature. The thermal stability increased by adding a lower quantity of copper oxide nanoparticles into the rubber matrix, reaching about 390 °C. The dielectric constant and loss of the materials were studied at various frequencies and temperatures. The dielectric properties were found to vary with the incorporation of copper oxide nanoparticles. The outstanding antibacterial actions against *Staphylococcus Aureus* bacteria were also identified.

Keywords: Natural rubber, Lattice strain, Thermal stability, Antibacterial activity.

Introduction

In the past decade, there has been a surge in research efforts focused on the development of polymer materials, which are highly organic and eco-friendly. The prospect of getting polymers from naturally occurring sources like polyisoprene, otherwise called natural rubber, has opened new possibilities for developing various everyday products, including containers, shoes, tires, rubber bands, tubes, and construction parts [1, 2]. Natural rubber polymer is essential in daily life due to its widespread use as a raw material in household, medical, and industrial products such as tubes, tires, coatings, and gloves. Recent developments in polyisoprene by metal oxide, rare earth complexes [3-5], and biomaterials have made it possible to tailor different properties of rubbers, especially their mechanical, thermal, and electrical properties in terms of strength, flexibility, and ease of processing for various engineering applications [6]. Natural rubber, with the chemical formula cis-1,4-polyisoprene, is an important organic ligand exhibiting unique coordination abilities of the double bond. Its flexibility limits its resistance to heat and ozone attack [7]. The demand for nanomaterial-metal complexes with natural rubber has attracted attention due to their thermal stability of bioinorganic models [8], such as elasticity, resilience, efficient heat dispersion, abrasion resistance, and heat resistance [9-10].

Corresponding Author: M. Abila Jeba Queen **Email**: jeba.abi@gmail.com

The remarkable characteristics of copper oxide (CuO) nanoparticles, low production cost, non-toxicity, and narrow band gap have drawn a lot of attention. These distinctive characteristics make them effective materials for a wide range of applications in solar energy conversion, adsorbents, gas sensors, superconductors, supercapacitors, lithium-ion batteries, and catalysts [11-13]. Numerous reports have proven CuO nanoparticles' antibacterial efficacy against the Gram-positive and Gram-negative pathogens. Bacteria-associated infections are the most serious cases. The literature has described a variety of surface-coated polymer-based medical implants with bactericidal properties. Polyisoprene-based polymers are noted for their special activity against pathogenic bacteria [14]. However, there are a few medical reports on medical products made using natural rubber, namely production of surgical gloves, condoms, urinary catheters, and other things [15]. The biomaterials have great promise because of their mechanical qualities, high elasticity, and capacity to form films [16].

To find a way to produce isoprene-incorporated copper oxide nanoparticles with unique physical and biological properties, this paper investigates the preparation and characterization of such composites. Natural rubber latex collected from the southern part of India was incorporated with the copper oxide nanoparticles and characterized. The structural parameters were analyzed by X-ray diffraction (XRD) and EDAX analysis. To evaluate the enhancement of natural rubber performance by copper oxide addition, thermal performance was tested using thermal analysis under a nitrogen atmosphere, and dielectric properties were studied using an LCR meter. Infections due to microorganisms play a significant role in mankind and industry. This paper also discussed the antibiofilm activity against *Escherichia coli, Staphylococcus aureus,* and *Pseudomonas aeruginosa.* Overall, the activity of copper oxide nanoparticles affects the physical and biological properties of isopropene.

Materials and Methods

Materials

Analytical-grade chemicals such as copper(II) acetate monohydrate [Cu $(CH_3COO)_2$. H_2O], oxalic acid ($C_2H_2O_4$), and formic acid (CH_2O_2) were used in the synthesis process. Natural rubber, chemically known as polyisoprene latex, was collected from the southern part of India and used directly without further purification. Double-distilled water was used as the solvent throughout the preparation process.

Preparation of Copper Oxide Nanoparticles

Copper oxide nanoparticles were prepared through a simple one-step chemical reaction between copper acetate monohydrate and oxalic acid. An aqueous solution was prepared by dissolving 0.4 mol of copper acetate monohydrate in 50 mL of distilled water. Similarly, 0.4 mol of oxalic acid was dissolved in 50 mL of distilled water to form a separate solution. A chemical reaction takes place during the mixing of copper acetate and oxalic acid solution at 40 °C under magnetic stirring for 3 hours, during which a precipitate formed. The resulting precipitate was centrifuged and washed twice with distilled water to remove any unreacted precursors. The obtained copper oxalate precipitate was then dried in a hot-air oven at 100 °C for 5 hours. Finally, the dried powder was calcined in a muffle furnace at 500 °C for 2 hours to obtain copper oxide nanoparticles.

Fabrication of Heterogeneous Copper Oxide Nanoparticle-Blended Polyisoprene

Natural rubber latex, consisting primarily of carbon and hydrogen, was collected from the southern part of India. Copper oxide (CuO) nanoparticles were incorporated into the natural rubber latex by a simple mechanical method and fabricated into layered sheets using a two-roll milling machine. Initially, 500 mL of viscous natural rubber latex was mixed with 250 mL of distilled water and stirred thoroughly for about 10 minutes. Subsequently, 5 mL of formic acid and 0.4 g of CuO nanoparticles were mechanically blended with the latex mixture. The prepared latex solution was allowed to stand at room temperature for approximately 5 hours to facilitate coagulation. The coagulated heterogeneous CuO–polyisoprene mixture was then processed using a two-roll milling machine to form sheets of the desired thickness. The resulting sheets were left at room temperature for about 15 days to ensure complete removal of residual moisture.

Result and Discussion

X-Ray Diffraction Analysis

Investigation on phase, crystalline nature, and structure of the synthesized copper oxide nanoparticles and copper oxide blended polyisoprene was done using an X-ray diffractometer with a wavelength of 1.54060Å and with the TOPS software package. The XRD pattern of copper oxide nanoparticles obtained from the chemical synthesis is shown in Fig. 1.

The development of CuO, an inorganic compound, was confirmed by the XRD analysis. CuO exhibited a sharp, intense peak at 2θ = 22.812°, indicating a highly ordered crystalline structure with an interplanar distance of 3.89520 Å along the (0 2 1) orientation. The peaks of CuO nanoparticles, with d-spacing values (Å) of 1.93735, 1.79541, 2.14025, 1.94659, 2.32205, 2.48627, 1.76953, 1.77606, and 3.89520, correspond to the planes (1 1 2), (1 5 1), (1 3 1), (1 1 3), (1 3 0), (0 4 2), (3 1 1), (-2 0 2), and (0 2 1), according to the International Centre for Diffraction Data (ICDD) Card No. 41-0254. The highly intense peaks indicate that the prepared nanoparticles belong to the category of monoclinic crystal structure with a CuO phase, without the formation of any additional peaks due to the probable Cu_2O and $Cu(OH)_2$ impurities. Therefore, it was confirmed that the synthesized nanoparticles are in CuO phase with the lattice parameters a = 4.685Å, b = 3.423 Å, c = 5.132 Å, α = β = 90°, γ = 99.52°, and V = 81.17 $Å^3$. These results are in close agreement with the findings reported by Nasihat *et al*. [17].

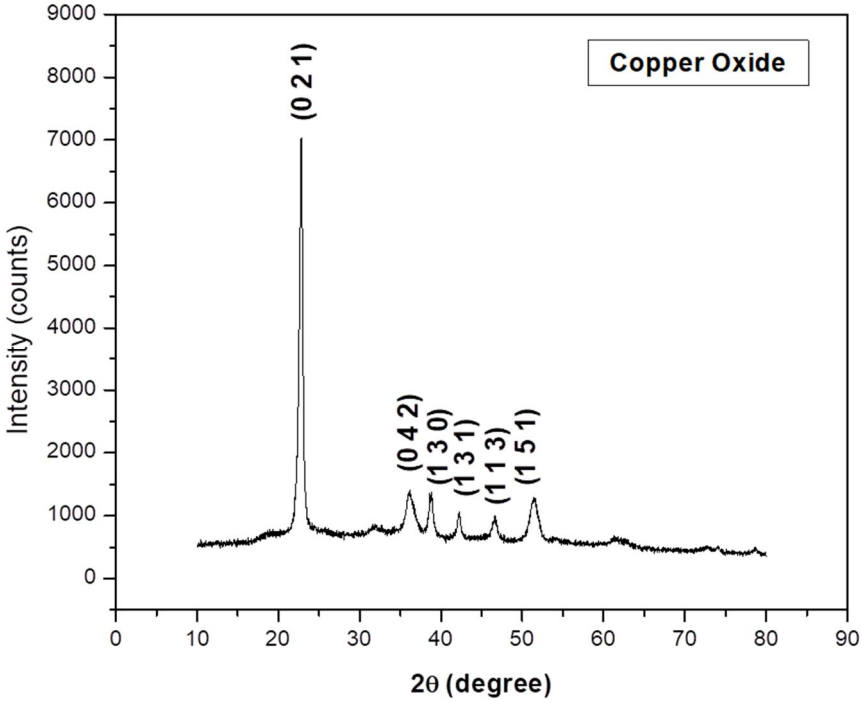

FIG. 1. XRD pattern of copper oxide nanoparticles.

The diffraction pattern of the mechanically prepared heterogeneous copper oxide nanoparticles blended with natural rubber polyisoprene is depicted in Fig. 2. Copper oxide nanoparticles blended with polyisoprene reveal that a broad peak at 2θ = 20.02109° experiences a lower ordered crystalline structure with an interplanar distance of 2.1567 Å along (0 2 0) orientation. Abraham *et al*. [18] found that the diffraction pattern of pure natural rubber displays an A-type amylose allomorph identified by a broad peak at 2θ= 17.9° and a strong peak at 25.07°. They also proved that adding nanocellulose to the natural rubber makes the shift towards a higher two theta value. This shift is due to the closely packed arrangement of copper oxide and natural rubber matrix. Therefore, the polymer matrix has no perfect crystal system, which in turn leads to the broadening of the peaks. This broadening also indicates a larger crystallite size of the polymer compared to the copper oxide nanoparticles.

Since polyisoprene is a cis-1,4 polymer, it is typically amorphous in nature. However, upon the addition of 0.4 g of copper oxide nanoparticles, a slight improvement in crystallinity was observed, as confirmed by the

diffraction peak at 2θ = 20°. This result is consistent with the findings of Pazhooh *et al.* [19], who analyzed natural rubber containing a low concentration of copper nanoparticles and found that the copper peaks were less intense than those of pure natural rubber. This reduction in peak intensity can be attributed to the overlap of copper and carbon peaks that occurs when trace amounts of CuO nanoparticles are mechanically incorporated into the natural rubber matrix [20].

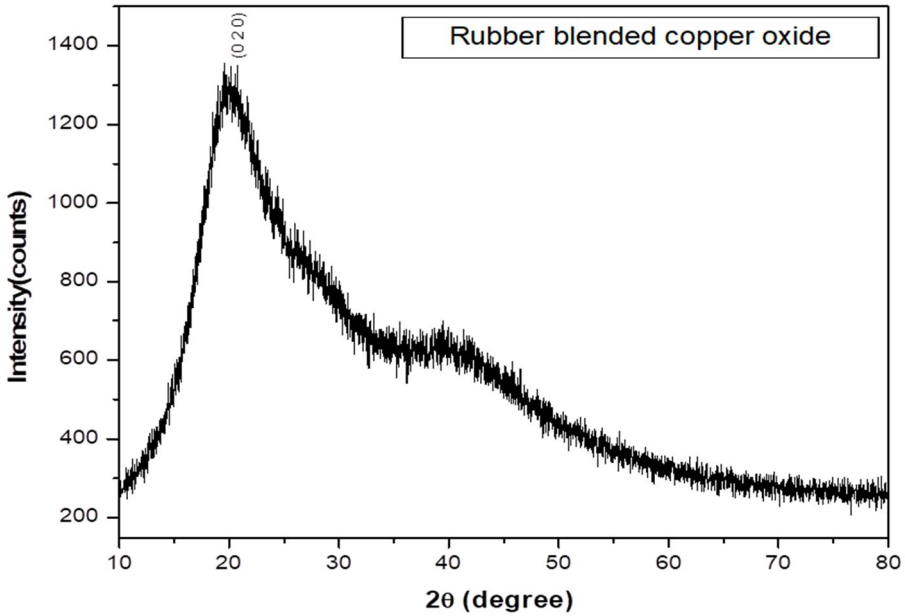

FIG. 2. XRD pattern of as-prepared rubber-blended copper oxide.

Additionally, the crystallite sizes of the chemically prepared CuO nanoparticles and the mechanically prepared rubber-blended CuO were calculated using Scherrer's equation [21] for the intense peaks:

$$D = \frac{0.9\lambda}{\beta \cos \theta} \quad (1)$$

where λ is the wavelength of the X-ray, θ is the angle of diffraction, and β is the full-width half-maximum.

The crystallite sizes obtained from the X-ray diffraction analysis of CuO and isoprene varied CuO were found to be 29.79 and 161.03 nm, respectively. Furthermore, the particle size of the CuO nanoparticles derived from diffraction analysis was correlated with the scanning electron microscopic image data shown in Fig. 3.

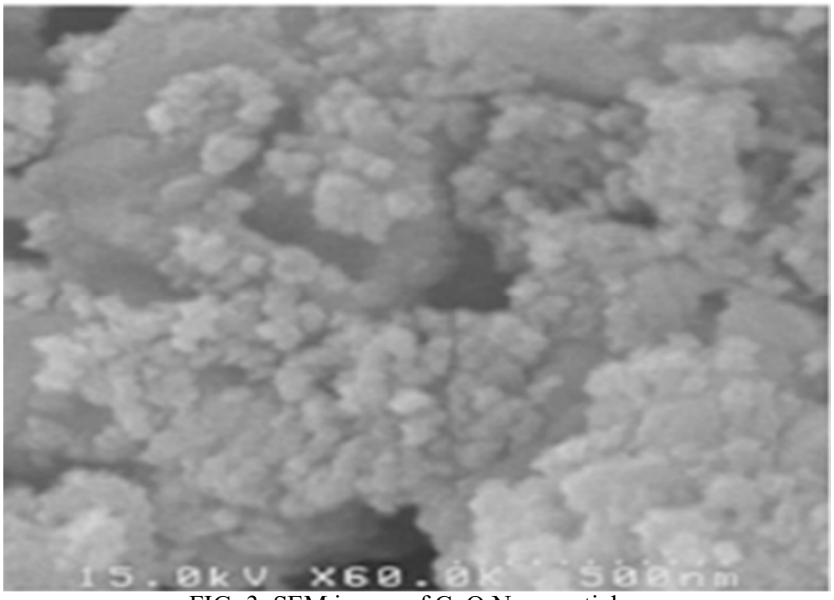

FIG. 3. SEM image of CuO Nanoparticles.

Dislocation density (δ), defined as the length of dislocation lines per unit volume of the prepared sample, was evaluated using the relation [22]:

$$\delta = \frac{1}{D^2} \quad (2)$$

The number of particles per unit surface area (N) in the prepared samples was determined as:

$$N = \frac{d}{D^3} \quad (3)$$

Lattice strain (ε), a measure of lattice dislocation, arises due to its crystal imperfections [23].

$$\varepsilon = \frac{\beta}{4 \tan \theta} \quad (4)$$

The dislocation density of the isoprene varied copper oxide was found to be higher (2.5932 x 10^{22} m^{-2}) compared to copper oxide (1.12665 x 10^{15} m^{-2}). The number of particles per surface area decreased for CuO nanoparticles (2.6443 x 10^{21} m^{-2}) compared to the isoprene-varied copper oxide (4.1760 x 10^{23} m^{-2}). Since dislocation is a crystallographic irregularity found inside the material, a higher dislocation density indicates greater hardness [24]; therefore, it was concluded that isoprene-varied copper oxide is harder than the copper oxide nanoparticles. Polymer mixed nanoparticles showed a higher lattice strain of 1.1318, while for the unmixed copper oxide, the lattice strain was 0.3519. Isoprene varied copper oxide with higher crystallographic irregularity and number of particles per unit surface area can be attributed to stronger covalent interactions between the carbon and hydrogen atoms in the polymer matrix. Elemental confirmation of the copper oxide nanoparticles was carried out with the EDAX analysis, as depicted in Fig. 4.

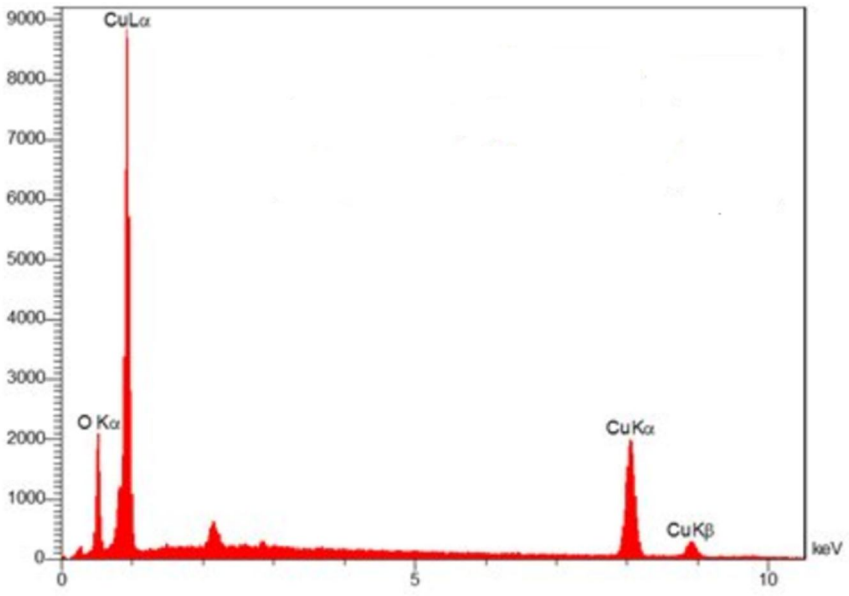

FIG. 4. EDAX spectrum of CuO nanoparticles.

From elemental analysis, it was identified that the elements copper and oxygen are present in the compound as the stoichiometric ratio of 1:1 with weight percentages of 53.55 and 46.45, respectively. The obtained atomic percentages of copper and oxygen were found to be 58.04 and 42.12, respectively.

Thermal Analysis

The thermal analysis of copper oxide nanoparticles and isoprene-varied copper oxide was performed at the temperature range of 0-1000 °C under a normal nitrogen atmosphere. The natural rubber matrix exhibits poor thermal conductivity compared to copper oxide nanoparticles. Thermogravimetric (TG) curves that determine mass loss over a temperature range for copper oxide nanoparticles and isoprene-varied copper oxide are shown in Figs. 5 and 6, respectively. It was noted that copper oxide experienced complete weight loss at 300 °C due to the liberation of oxygen molecules, whereas the rubber-blended copper oxide showed weight loss at about 392 °C. The thermal stability of isoprene molecules was reported in the temperature range of 200 –270 °C, during which both chain scission and cross-linking take place, by Bolland *et al*. [25]. In our case, due to the addition of copper oxide nanoparticles, the thermal stability of the polymer material

improved. Thus, from the thermogravimetric analysis, it was confirmed that the prepared copper oxide and the isoprene-varied copper oxide retained their texture up to 300 and 395 °C, without decomposition below these temperatures.

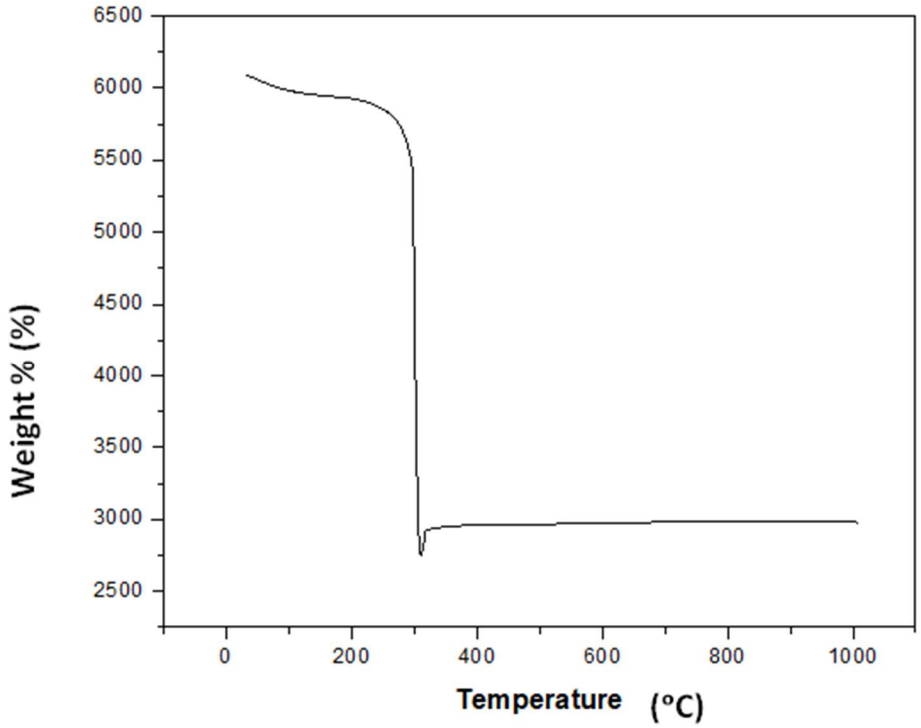

FIG. 5. TG curve for copper oxide nanoparticles.

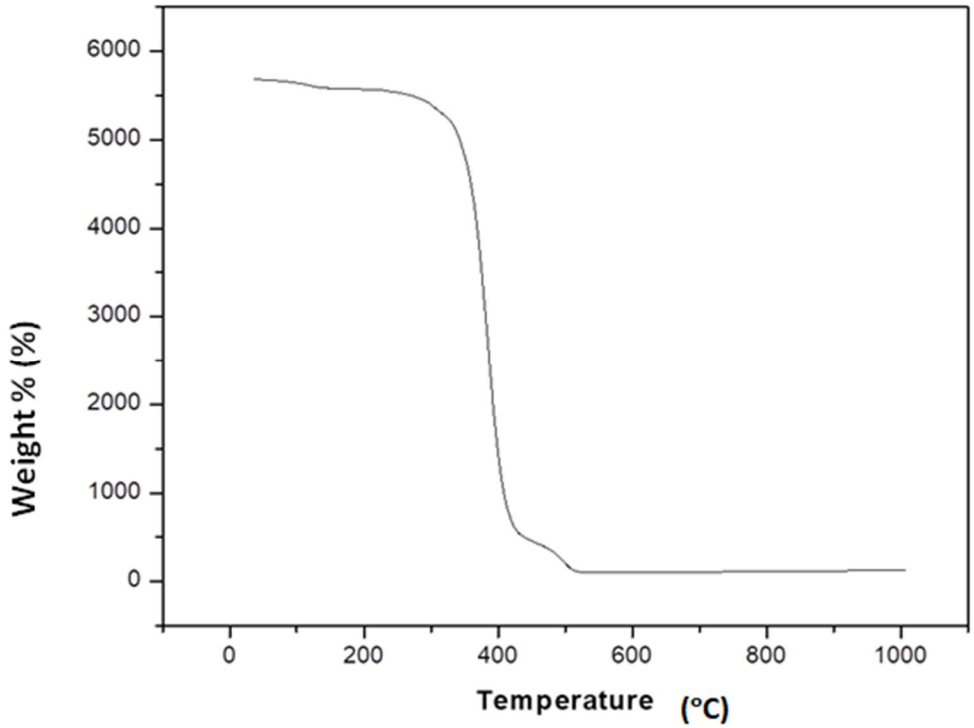

FIG. 6. TG curve of the rubber-blended copper oxide.

Differential thermal analysis (DTA) of copper oxide nanoparticles and isoprene-varied copper oxide was performed at the temperature range of 0-1000 °C under a normal nitrogen atmosphere. DTA determines the chemical degradation due to the exothermic and endothermic peaks over a temperature range. Phase transitions for copper oxide nanoparticles and isoprene-varied copper oxide are given in Figs. 7 and 8, respectively.

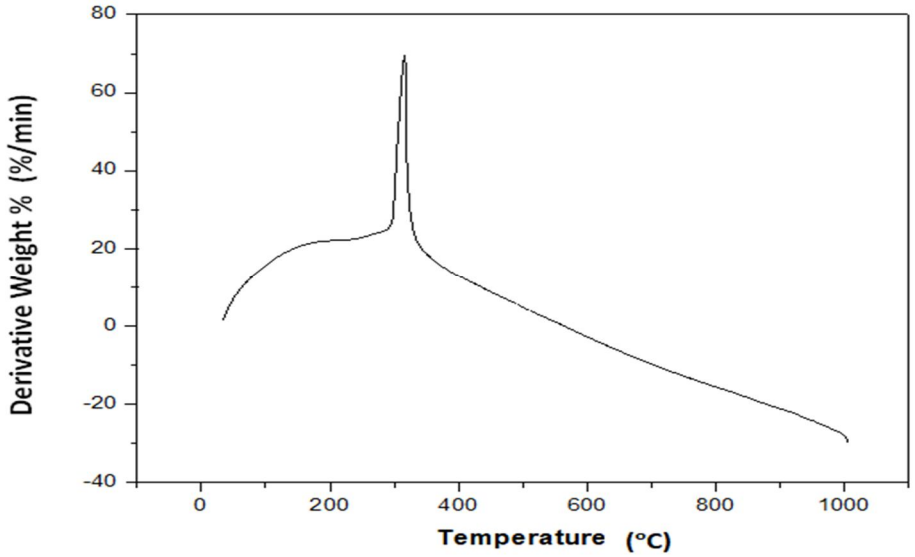

FIG. 7. DTA curve of copper oxide nanoparticles.

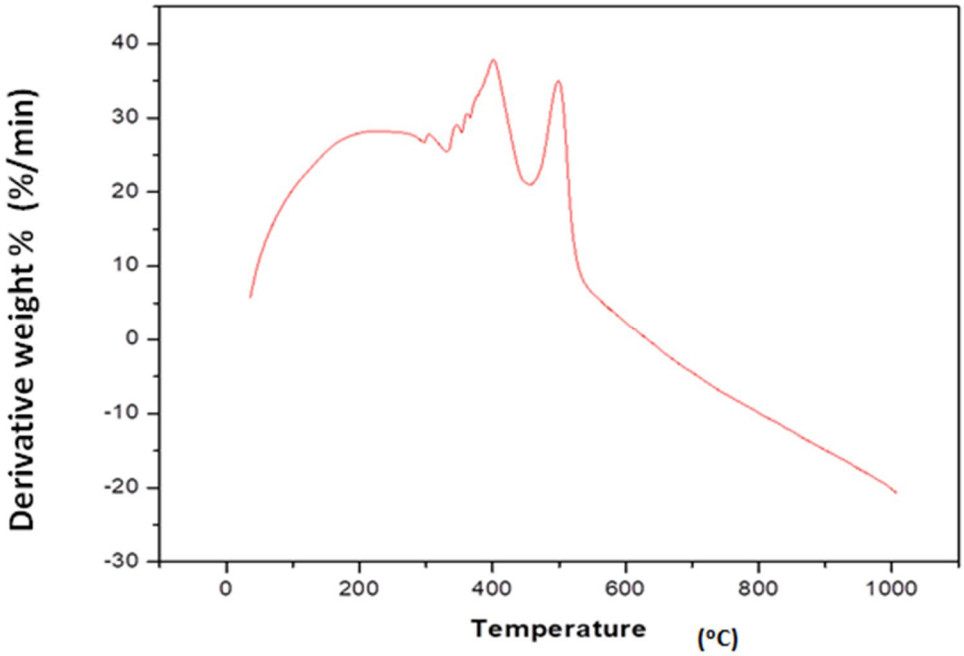

FIG. 8. DTA curve of rubber-blended copper oxide.

In the DTA curve, a sharp exothermic peak for copper oxide nanoparticles was identified at 300 °C, due to the absolute liberation of oxygen molecules. The final product left behind due to the increase in temperature is copper. From the DTA curve of rubber-blended copper oxide, it was known that the prepared material experienced two exothermic peaks: at 392 and 495 °C. These exothermic peaks are due to the liberation of H_2O and C_5H_6 molecules. There may be a phase transition from CuO to Cu at the transition temperature of 300 °C.

Dielectric Studies

The Dielectric constant of the rubber-blended copper oxide was recorded using a high-precision LCR meter at various frequencies. The dielectric constant of the prepared samples was calculated using the relation:

$$C = \frac{\varepsilon_0 A}{d} \quad (5)$$

To fetch the information about the material's ability to store energy due to the relaxation process, the dielectric constant of isoprene-varied copper oxide was measured as a function of frequency shown in Fig. 9. Various temperature values and dielectric constant of rubber-blended copper oxide are summarized in Table 1.

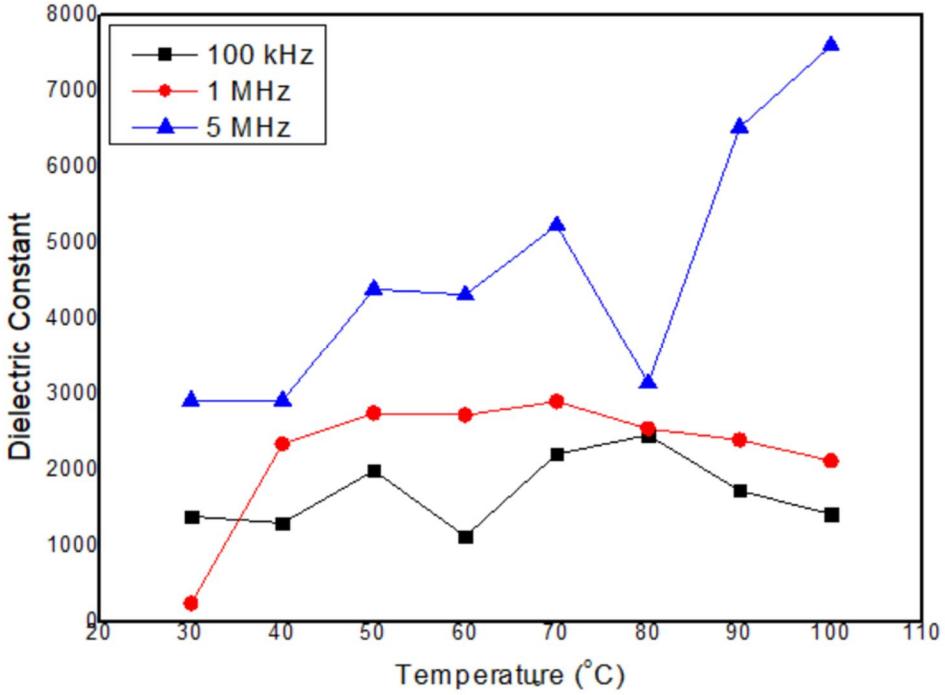

FIG. 9. Dielectric constant of rubber-blended copper oxide.

TABLE 1. Dielectric constant of rubber-blended copper oxide.

S.No.	Temperature °C	Dielectric Constant		
		100KHZ	1MHZ	5MHZ
1.	30	1384.8823	239.0045	2909.3859
2.	40	1296.1698	2338.7530	2909.9540
3.	50	1989.2723	2740.8252	4386.0697
4.	60	1120.1541	2717.8252	4311.2523
5.	70	2202.8671	2894.9051	52223.3162
6.	80	2453.6110	2539.7295	3138.5718
7.	90	1723.8111	2390.6545	6511.8203
8.	100	1412.4371	2115.3394	7586.6919

In rubber-blended copper oxide, the dielectric constant was measured at three different frequencies: 100 kHz, 1 MHz, and 5 MHz. From the dielectric studies, it was noticed that the maximum value of dielectric constant occurred at higher temperatures and 5MHz. The highest value of the dielectric constant was observed at a higher frequency of about 5 MHz. The variation in dielectric constant is attributed to the polarization mechanisms, including electronic, ionic, orientation, and space charge [26]. Ionic polarization in the copper oxide nanoparticles-varied polyisoprene arises mainly from the movement of copper, carbon, hydrogen, and oxygen ions present in the polymer matrix. Dielectric loss measured at 100 kHz and 1 MHz with varied temperature remained almost constant; therefore, the material at this particular frequency can be utilized as a filter. Orientation polarization results from the polar oxygen in the polyisoprene chain, which causes asymmetry in the cross-linked bonds. As the temperature and frequency simultaneously increase, the dipoles of Cu and O enhance the dielectric properties.

The dielectric loss curve and the corresponding dielectric parameters of the rubber-blended copper oxide are given in Fig. 10 and Table 2, respectively.

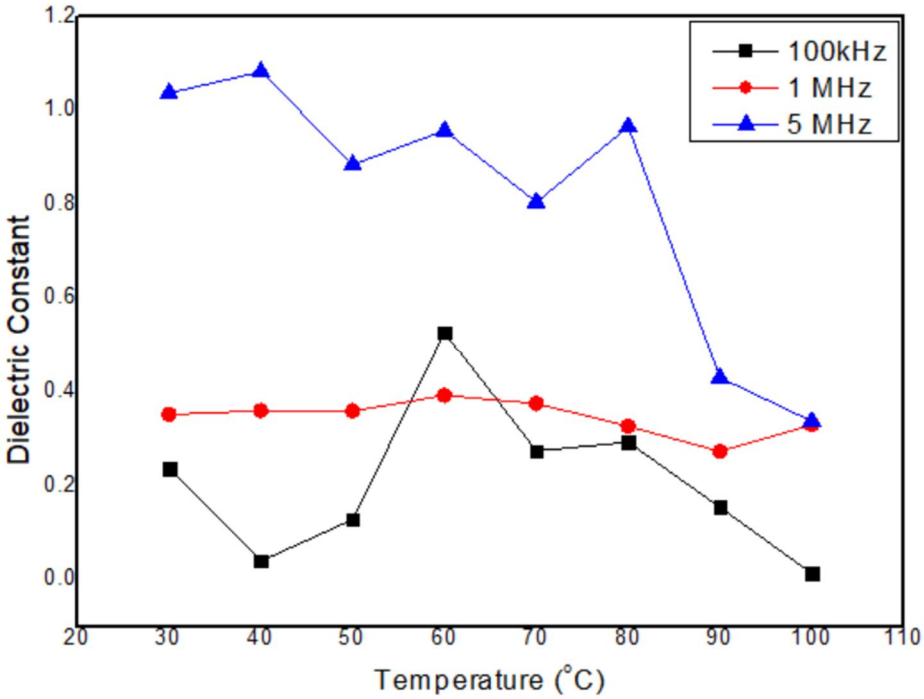

FIG. 10. Dielectric loss of rubber-blended copper oxide.

TABLE 2. Dielectric loss parameters of rubber-blended copper oxide.

S.No.	Temperature (°C)	Dielectric Loss		
		100HZ	1MHZ	5MHZ
1.	30	0.23605	0.35071	1.0359
2.	40	0.03901	0.35887	1.0814
3.	50	0.12775	0.35865	0.8837
4.	60	0.52638	0.3914	0.9562
5.	70	0.27347	0.37423	0.8044
6.	80	0.291946	0.32608	0.9641
7.	90	0.15365	0.27239	0.429
8.	100	0.01317	0.32924	0.3364

When an a.c. voltage is applied to the isoprene-varied copper oxide sheet, a fraction of the electrical energy is absorbed while the remainder is lost in the form of heat; this loss corresponds to the dielectric loss [27]. From the dielectric measurements, it was identified that at 100 kHz, fluctuations in dielectric loss occurred due to polarization effects. At 1 MHz, the dielectric loss remains nearly constant, suggesting that the material can function effectively as a filter. At 5 MHz, a decrease in dielectric loss was observed. From an application perspective, materials with a monoclinic crystal structure and higher dielectric constants at elevated temperatures and frequencies are suitable for use as frequency filters [28, 29].

Antibacterial Studies

The antibacterial activity of copper oxide nanoparticles and rubber-varied copper oxide films was evaluated against bacterial strains, including *Escherichia coli, Staphylococcus Aureus,* and *Pseudomonas aeruginosa*. The agar disc diffusion (Kirby-Bauer) method was employed, in which bacterial strains were swabbed onto the agar medium using sterile cotton. The test discs were placed on the surface of the medium, allowed to diffuse for 5 minutes, and then incubated at 37 °C for 24 hours. The antibacterial activity was assessed by measuring the diameter of the zone of inhibition (ZOI). The ZOI produced by the copper oxide nanoparticles against *Escherichia coli, Staphylococcus Aureus,* and *Pseudomonas aeruginosa* bacterial strains is shown in Fig. 11 and summarized in Table 3.

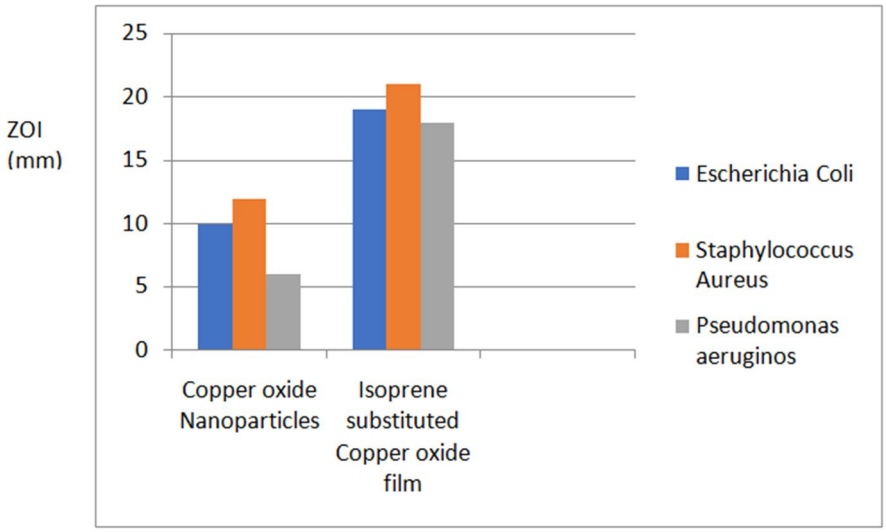

FIG. 11. Antibacterial activity chart.

TABLE 3. Diameters of the ZOI produced by the samples against the microbes.

S.No.	Microbes	Positive control levofloxacin	Zone size in diameter (mm)	
			Copper oxide nanoparticles	Isoprene-substituted copper oxide film
1.	Escherichia coli	27	10	19
2.	Staphylococcus aureus	22	12	21
3.	Pseudomonas aeruginosa	25	6	18

From the studies, it was confirmed that the copper oxide nanoparticles and isoprene-substituted copper oxide film exhibit high antibacterial activity against *Staphylococcus aureus* bacteria, with a ZOI diameter of 12 and 21 mm, respectively. In contrast, the antibacterial activity of copper oxide against *Escherichia coli* and *Pseudomonas* aeruginosa was relatively low, with ZOI values of 10 mm and 6 mm, respectively. For the isoprene-substituted copper oxide film, the antibacterial activities against *Escherichia coli* and *Pseudomonas aeruginosa* were 19 and 18 mm, respectively. According to the literature [30-32], natural rubber itself exhibits notable antibacterial properties. Therefore, the natural rubber-varied copper oxide nanoparticles film can be utilized as an anti-biofilm material to prevent infections caused by *Staphylococcus aureus* bacteria.

Conclusion

In summary, natural rubber-varied copper oxide nanoparticles with excellent thermal and dielectric properties were successfully prepared by incorporating a low content of copper oxide nanoparticles. A simple chemical method was employed to synthesize CuO nanoparticles and fabricate the natural rubber-varied copper oxide anti-biofilm. Structural variations arose due to the isoprene polymer. The crystallite sizes of copper oxide nanoparticles and isoprene-varied copper were found to be 29.7924 and 161.03515 nm, respectively, which was further confirmed by scanning electron microscopy. Compared to copper oxide nanoparticles, dislocation density, lattice strain, and the number of particles per unit surface of the polymer matrix increased widely. This is due to the higher cross-linkage between carbon and hydrogen molecules. Thermal analysis proved that the stability of copper oxide is about 300 °C, but the incorporation of copper oxide into natural rubber enhanced the thermal stability of the composite to around 395 °C. The dielectric properties were also improved, indicating potential applications of the composite film in energy storage devices. The nanoparticles and composite films were evaluated for antibacterial activity against *Escherichia coli, Staphylococcus Aureus,* and *Pseudomonas aeruginosa* bacterial strains. Copper oxide-varied natural rubber film is an excellent antibacterial agent and can be utilized as an anti-biofilm, which prevents infection against the *Staphylococcus aureus* bacteria. This study provides valuable insights for the design and fabrication of isoprene-varied copper oxide films for medical applications.

References

[1] Dick, J.S., "Compounding Materials for the Polymer Industries", (Noyes, Park Ridge, Ill, USA, 1987).

[2] Chuayjuljit, S., Imvittaya, A., Na-Ranong, N., and Potiyaraj, P., J. Metals Mater. Minerals, 12 (1) (2002) 51.

[3] Ricci, G., Sommazzi, A., Masi, F., Ricci, M., Boglia A., and Leone, G., Chem. Rev., 254 (2010) 661.

[4] Faisca Phillips, A.M., Suo, H.Y., Guedes da Silva, M.d.F.C., Pombeiro, A.J.L., and Sun, W.-H., Coord. Chem. Rev., 416 (2020) 213332.

[5] Friebe, L., Nuyken, O., and Obrecht, W., Adv. Polym. Sci., 204 (2006) 1.

[6] Masłowski, M., Miedzianowska, J., and Strzelec, K., Polymers, 11 (2019) 972.

[7] Krishnan, Y., Chandran, S., Usman, N., Smitha, T.R., Parameswaran, P.S., and Prema, K.H., Int. J. Chem. Stud., 3 (1) (2015) 15.

[8] Weyhermüller, T., Wagner, R., Khanra, S., and Chaudhuri, P., Dalton Trans., 15 (2005) 2539.

[9] Kuala Lumpur, "Natural Rubber Statistics 2015", (Malaysia Rubber Board, Malaysia, 2015).

[10] Ismail, H., Ahmad, Z., and Mohd Ishak, Z.A., Polym. Test., 20 (6) (2001) 607.

[11] Geng, W., Ma, Z., Zhao, Y., Yang, J., He, X., Duan, L., Li, F., Hou, H., and Zhang, Q., Sens. Actuators B, 325 (2020) 128775.

[12] Oosthuizen, D.N., Motaung, D.E., and Swart, H.C., Appl. Surf. Sci., 466 (2019) 545.

[13] Yin, M. and Liu, S., Sens. Actuators B, 227 (2016) 328.

[14] Pandiyarajan, T., Udayabhaskar, R., Vignesh, S., Arthur James, R., and Karthikeyan, B., Mater. Sci. Eng. C, 33 (4) (2013) 2020.

[15] Arakkal, A., Aazem, I., Honey, G., Vengellur, A., Bhat, S.G., and Sailaja, G.C.S., J. Appl. Polym. Sci., 138 (1) (2021) 49608.

[16] Peter, A., Bindiya, E.S., Honey, G., Jose, J., Bhat, S.G., John, H., and Abhitha, K., Nano-Struct. Nano-Objects, 32 (2022) 100920.

[17] Nasihat Sheno, N. and Morsali, A., Int. J. Nanosci. Nanotechnol., 8 (2) (2012) 99.

[18] Abraham, E., Elbi, P.A., Deepa, B., Jyotishkumar, P., Pothen, L.A., and Narine, S.S., Polym. Degrad. Stab., 97 (2012) 2378.

[19] Pazhooh, H.N., Bagheri, R., and Adlo, A., Polym., 108 (2017) 135.

[20] Athanassiou, E.K, Grass, R.N., and Stark, W.J., Nanotechnology, 17(6) (2006) 1668.

[21] Scherrer, P., Göttinger Nachrichten Gesell., 2 (1918) 98.

[22] Vinila, V.S. and Isac, J., Micro Nano Technol., 1 (2022) 319.

[23] Bindu, P. and Thomas, S., J. Theor. Appl. Phys., 8 (2014) 123.

[24] Mishra, S.K., Roy, H., Lohar, A.K., Samantha, S.K., Tiwari, S., and Dutta, K.,IOP Conf. Ser.: Mater. Sci. Eng., 75(2015) 012001.

[25] Bolland, J.L. and Orr,W.J.C., Trans. Inst. Rubber Ind., 21 (1945)133.

[26]Retna Kumar, T., Abila Jeba Queen, M., Bright, K.C.,Ilangovan, R., and Sankaranarayanan, K.,Chem.Africa,6 (2023)3229.

[27]RetnaKumar, T., Abila Jeba Queen, M., Bright, K.C.,Ilangovan, R., andSankaranarayanan, K., Eur. Chem. Bull., 12(3)(2023) 1633.

[28] AbilaJebaQueen, M., Bright, K.C., and Aji Udhaya, P., J. Mater. Sci.: Mater. Electron.,34 (2023)181.

[29] AbilaJebaQueen, M., Bright, K.C., and Aji Udhaya, P.,Trans. Electr. Electron. Mater.,25(2024) 458.

[30]Zhang,N.andCao,H.,Mater. (Basel), 13(5) (2020) 1039.

[31]Zancanela,D.C.,Funari,C.S.,Herculano,R.D., Mello,V.M.,Rodrigues,C.M.,Borges,F.A.,de Barros,N.R.,Marcos,C.M.,Almeida,A.M.F.,and Guastaldi,A.C.,Mater. Sci. Eng. C,97(2019) 576.

[32] Abila Jeba Queen, M., Rinu, S.K., and Aji Udhaya, P.,J. Adv. Sci. Res., 11 (1) (2020) 83.

Volume 18, Number 4, 2025. pp. 435-442

Jordan Journal of Physics

ARTICLE

Influence of Gas Flow Rate on the Plasma Temperature and Electron Density of an Atmospheric Argon Plasma Jet

Muna A. Issa[a,b] and **Kadhim A. Aadim**[a]

[a] *Department of Physics, College of Science, University of Baghdad, Iraq.*

[b] *Quality Assurance and Performance Evaluation Department, Mustansiriyah University, Baghdad, Iraq.*

Doi: **https://doi.org/10.47011/18.4.2**

Received on: 25/04/2024; *Accepted on: 16/10/2024*

Abstract: In this paper, an approach based on optical emission spectroscopy (OES) is used to experimentally determine the electron temperature (T_e) and electron number density (n_e) in an atmospheric argon (Ar) plasma jet. The Boltzmann plot method is applied to compute these parameters for gas flow rates ranging from 0.5 to 2.5 l/min. The results show the effect of gas flow rates on the plasma emission spectrum of argon (Ar I). Specifically, increasing the flow rate leads to an increase in the intensity of the spectral lines, particularly at 763.51 nm. Spectral lines of other molecules, such as N_2 and N_2^+, were also observed, showing the molecular interaction within the plasma. Strong OH and NO molecular emissions were detected, with OH emissions predominantly observed between 308 and 315 nm. Additionally, nitrogen molecular spectrum transitions were detected between 330 and 440 nm, including N_2^+ ions in the range of 391-436 nm. These results indicate that the gas flow rate is directly proportional to the emission intensity in the plasma, thus reflecting gas flow impacts on the plasma properties.

Keywords: Argon gas (Ar), Spectral characterization، Plasma temperature, Electron density, Plasma jet.

1. Introduction

Plasma is considered the fourth state of matter, alongside solid, liquid, and gas. It contains a collection of charged particles (ions and electrons) generated by heating a gas to an extremely high temperature or by exposing it to a very strong electromagnetic field, causing atomic ionization [1]. There are various production methods, including laser-induced plasma [2]. This method involves intense laser pulses focused on a material, causing it to ionize and form plasma. This technique is often used in fields like spectroscopy, material analysis, and fusion research. Unlike traditional plasma generation methods that require low-pressure environments, atmospheric pressure plasma operates at or near atmospheric pressure [3]. Dielectric barrier discharge plasma (DBD) [4] involves using an insulation material to generate plasma by applying an alternating electrical field across the material. This method is found in ozone generation, air purification, and thin-film deposition applications.

Cold atmospheric plasma (CAP) has been applied to modifying surfaces [5-7], producing nanoparticles from various materials. The combined effects of UV-radiation, moderate heat, and reactive types (such as oxygen-ROS and nitrogen-RNS) have often been recognized as the primary contributors to the antimicrobial activity of plasma. The impact of these distinct factors can fluctuate based on the parameters of the device [8]. Hydroxyl and oxygen groups are generated very efficiently in plasmas operating in atmospheric air and are identified regularly as

Corresponding Author: Muna A. Issa **Email**: muna.ahmed@sc.uobaghdad.edu.iq

crucial factors in the inactivation of germs. Therefore, this contributes greatly to the plasma's productivity. Devices operating in atmospheric air demonstrate notable efficiency in creating these agents. In recent times, cold atmospheric plasma (CAP) therapy has demonstrated considerable efficacy across a range of medical and biomedical applications [9-11], encompassing therapeutic, antimicrobial, and antineoplastic functions [12, 13]. This therapy is used due to its minimal cost, environmental friendliness, and lack of expensive equipment requirements.

Plasma diagnostics can be assessed by determining the electron temperature (T_e) and the electron density (n_e). Optical emission spectroscopy (OES) is the diagnostic method used for plasma analysis [14]. It takes a line devoid of self-absorption to determine n_e using the Stark broadening effect [15]. Self-absorption is a condition that can manifest itself in virtually any radiating system, including plasma. Furthermore, the plasma formation process in the air typically exhibits a significant temperature gradient due to the cooling effect of the ambient air [16]. In the outer regions of the cold plasma, elevated atom concentrations exist in lower energy states. Consequently, this situation could result in a noteworthy reabsorption of the emitted radiation lines [17]. A spectrograph and a detector are utilized to detect the plasma plume and achieve spectral resolution. The generated plasma spectrum can collect information regarding the elemental composition and various quantitative and qualitative data. The widths, variations, and shapes of the emission lines offer insights into the plasma's temperature and electron density. This research aims to understand how changes in the flow of argon gas affect the spectral emission intensity of argon and other molecular species present in the plasma. This contributes to a better understanding of plasma behavior and interactions within the atmospheric context.

2. Experimental Details

In the experimental setup, atmospheric cold plasma was generated utilizing a custom-built plasma jet system, as depicted in Fig. 1. A homemade DC power supply was employed, capable of generating high voltages up to a maximum of 13 kV at a frequency of 35 kHz. Within this setup, T_e and n_e were assessed across various gas flow-rate values.

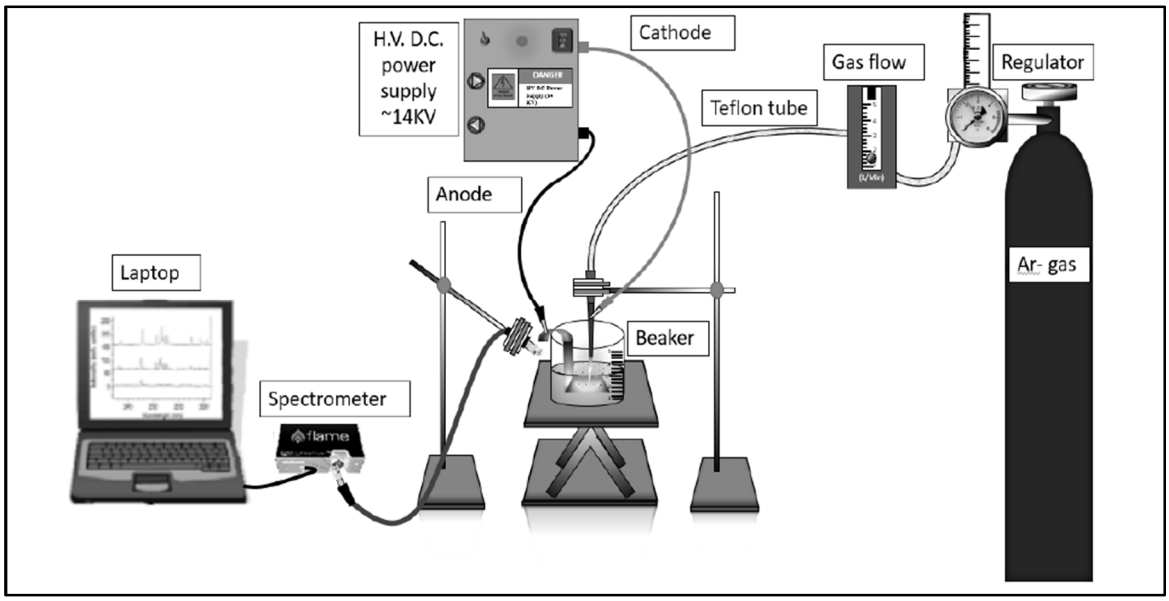

FIG. 1. DC plasma jet schematic with accompanying optical emission spectroscopic.

The configuration of the plasma jet was investigated in this work by detecting the excited species and their concentrations using the OES technique applied to discharges produced via an Ar plasma jet. Spectral data were recorded within the wavelength range of 160-1010 nm, directly from the jet of plasma in both radial and axial directions. To determine T_e (S3000-UV-NIR), as depicted in Fig. 2, a spectrometer was employed to collect and analyze the spectral data for this investigation.

FIG. 2. Spectrometer utilized in the experiment.

The spectrograph and detector are utilized to detect the plasma plume and achieve spectral resolution. Information regarding the elemental composition and various quantitative and qualitative data can be gleaned from the generated plasma spectrum. The emission lines' widths, variations, and shapes offer insights into plasma for n_e and temperature. Plasma temperature is a crucial thermodynamic property, as it characterizes and forecasts other plasma attributes, such as the distribution of energy level populations and particle speeds. In the laboratory experiment, the ratio method was utilized, assuming that the plasma maintains local thermodynamic equilibrium. The ratio method is a widely used approach for determining plasma temperature. It operates by comparing the intensity ratio of two spectral lines corresponding to transitions within the same ionization stage of an atom or ion. The plasma temperature (T) is determined using the following equation [18]:

$$T = \frac{(E_2 - E_1)}{k \ln(\frac{I_1 \lambda_1 A_2 g_2}{I_2 \lambda_2 A_1 g_1})} \quad (1)$$

where

- T: electron temperature to be calculated (in eV).
- E_1, E_2: energy levels of the molecules or atoms (in electron volts)
- k: Boltzmann constant (approximately 1.38×10^{-23} J/K).
- I_1, I_2: intensities of radiation at wavelengths λ_1 and λ_2, respectively.
- λ_1, λ_2: wavelengths of the radiation used (in nanometers).
- A_1, A_2: statistical weights or factors related to the transitions between energy levels 1 and 2.
- g_1, g_2: statistical weights for energy levels 1 and 2, reflecting the number of ways to distribute energy among the molecules.

Electron density refers to the quantity of free electrons within a given volume. The quadratic Stark effect obtained its name because the Stark broadening is proportional to the perturbing electric field. The electron density is subsequently calculated using the broadening parameters of the required spectrum [19]. The electric field, responsible for the impact of Stark in plasmas, is produced mainly by collisions with electrons. Consequently, it can be simplified to the following equation [20]:

$$n_e = \left[\frac{\Delta\lambda}{2\omega_s}\right] N_r \quad (2)$$

Here, ω_s is the theoretical line full-width Stark broadening parameter, calculated at the same reference electron density $N_r \approx 10^{17}\,cm^{-3}$.

3. Results and Discussion

In this experiment, the spectral lines were identified using databases such as the NIST Spectral Lines Database, a reliable reference that provides accurate information about the wavelengths and intensity of spectral lines for various elements, including argon. The spectral lines of argon (Ar I) and the weak lines of ionized argon (Ar II) were identified, and the values obtained were compared with those available in the NIST database to ensure the accuracy of the results [21]. The standard and the experimental values are illustrated in Tables 1 and 2, respectively.

TABLE 1. Standard values of argon gas from NIST.

Wavelength (nm)	$g_kA_{ki} \times 10^7$	E_i (eV)	E_j (eV)
696.5431	1.92	11.548354	13.327857
706.7218	1.90	11.548354	13.302227
763.5106	12.2	11.548354	13.171778
801.4786	4.64	11.548354	13.094872
811.5311	23.2	11.548354	13.075716

TABLE 2. Observed wavelengths and their intensities of argon gas at different flow rates.

0.5 (l/min)		1 (l/min)		1.5 (l/min)		2 (l/min)		2.5 (l/min)	
λ(nm)	Intensity (a u)	λ(nm)	Intensity (a u)	λ(nm)	Intensity (a u)	λ(nm)	Intensity (a u)	λ(nm)	Intensity (a u)
696.79	450.55	696.79	2768.85	696.79	3662.04	696.79	3637.17	696.30	4378.53
707.46	426.13	706.97	2876.11	707.46	3110.58	706.97	2871.67	706.97	2111.71
763.74	3094.30	763.74	17446.00	764.22	21778.00	764.22	22819.30	763.74	26709.20
801.58	1227.90	801.58	6002.00	801.58	8369.40	801.58	8182.70	801.09	9125.70
811.28	6125.74	810.79	32101.73	811.28	43784.43	811.77	42486.30	811.28	47241.10

Figure 3 exhibits the emission spectra of argon gas (Ar I) plasma under the influence of different gas flow rates. The spectrum intensity is plotted on the vertical axis, while the wavelength is shown in nanometers on the horizontal axis. It is clear from this figure that an increase in gas flow rate increases the spectral line intensities, especially those from argon (Ar I), indicating that the gas flow directly affects the properties of plasma and intensity of emission. The main spectral lines of argon (Ar I) can be seen in the wavelength scope of about 600 to 1000 nm. The most prominent of these lines is the one at 763.51 nm. Other notable emission lines occur at 750.39, 811.53, and 772.38 nm. These lines correspond to electronic transitions within argon atoms excited in the plasma. The spectral lines appear clearly at different flow rates but with greater intensity at higher flow rates, indicating the presence of higher n_e or greater electron energy, leading to an increase in these emissions [22].

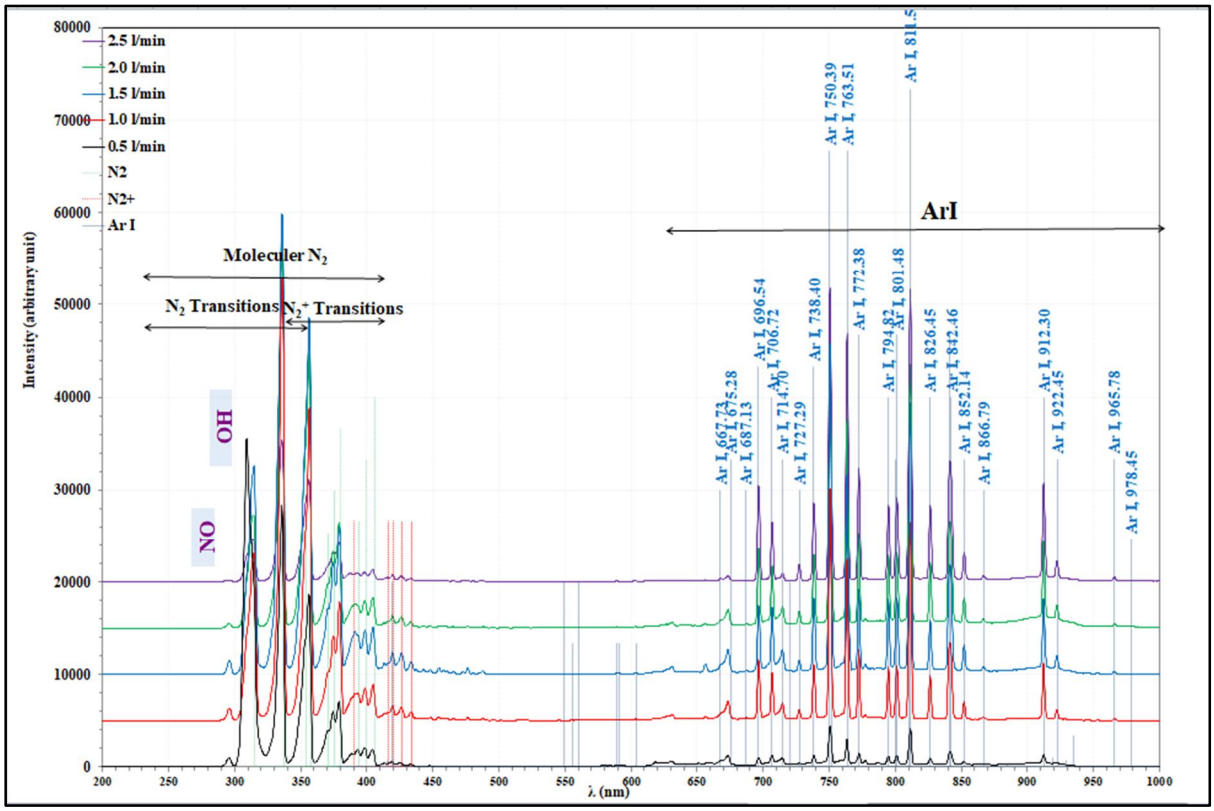

FIG. 3. Variation of intensity in terms of wavelength (nm) for diverse measurements of gas flow rate.

Molecular spectral lines of other gases, such as N_2 and N_2^+, can be observed in the wavelength region between 300 and 450 nm and are shown in Fig. 4 in more detail. These transitions express molecular interactions within the plasma, where argon, as a carrier gas, contributes to the excitation of these molecular species. Also appearing in this region are molecular lines of OH and NO molecules, which result from chemical reactions occurring within the plasma. The figure shows a significant variation in the intensity of these molecular lines depending on the gas flow rate, which illustrates the effect of different gas flow rates on the emission intensity. In the range between 308 and 315 nm, emissions of molecules such as OH and NO can be observed, which participate in chemical reactions within the plasma. Strong emissions characteristic of OH molecules appear at 308 nm. Several transitions of the molecular spectrum of nitrogen gas (N_2) have also been identified between 330 and 440 nm. These transitions are represented by the symbol Δv, which expresses the change in the quantum number of molecular vibrations. For example, in the spectral range around 357.69 nm, there are characteristic spectral lines of molecular nitrogen (N_2) with Δv = -1 and Δv = -2. This range also includes other transitions, such as Δv = 0 and Δv = -3, visible between 380 and 436 nm. In addition, molecular nitrogen ions (N_2^+) appear clearly in the region between 391 and 436 nm. Transitions in this range include ionic transitions that occur due to plasma excitation of nitrogen molecules, where an electron is lost from the molecule, resulting in the formation of ions that appear in the spectrum [23].

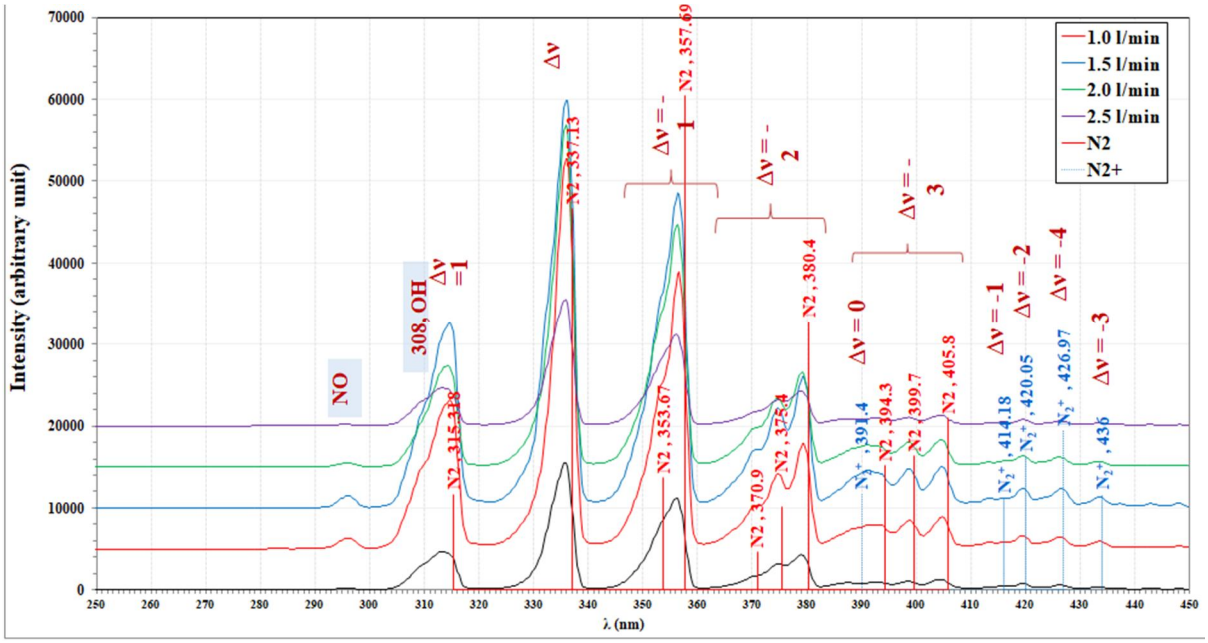

FIG. 4. Transitions of N_2.

The line at 763.51 nm was chosen because it is an isolated line that is not merged with other lines, has high intensity, and is apparent in all samples. Standard Stark coefficient values from previous studies are available for calculating n_e values. The highest peak observed in Fig. 5 demonstrates a noticeable trend: an increase in peak intensity corresponding to an increase in gas flow rate. This relationship suggests a direct correlation between the gas flow rate and the emission intensity within the plasma. As the gas flow rate rises, so does the emission intensity, indicating heightened emission activity within the plasma.

Electron temperature could be determined using Eq. (1), as illustrated in the corresponding curve in Fig. 6. Similarly, n_e can be obtained using Eq. (2).

There is less correlation in the five Boltzmann plots in Fig. 6; this is because the spectral lines chosen for these plots share the same energy level, making them particularly suitable for this study.

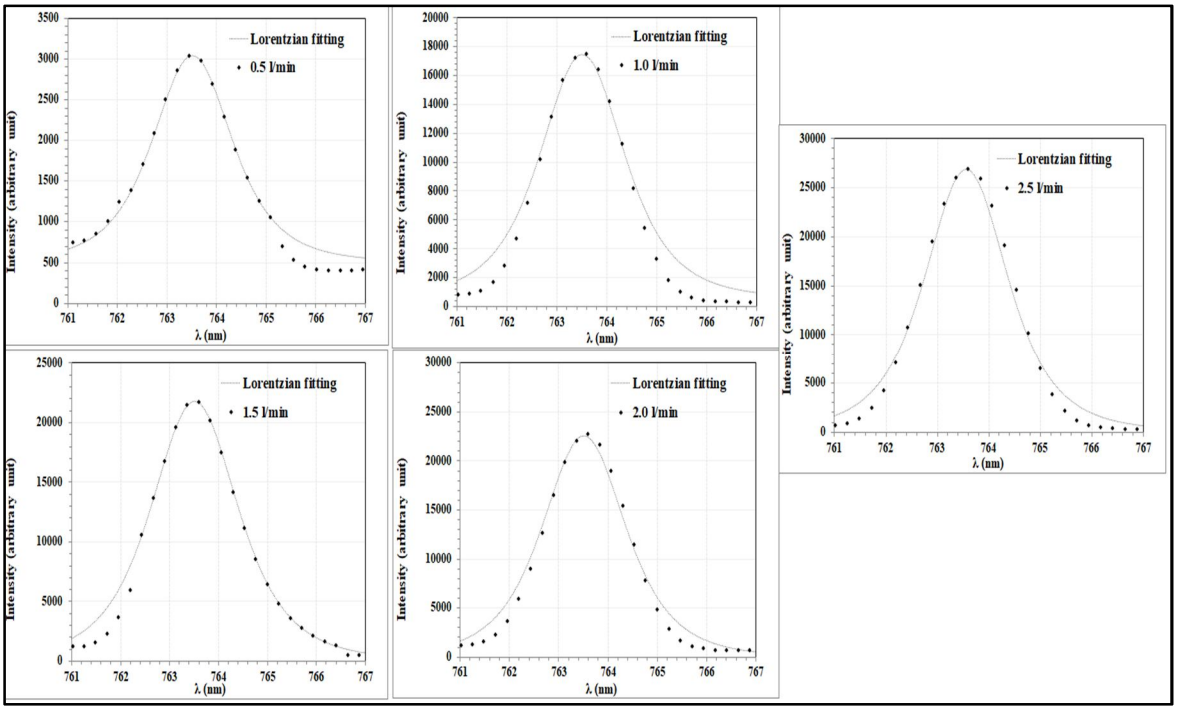

FIG. 5. Intensity variations in terms of wavelength (nm) at maximum peak for diverse gas flow rate measurements.

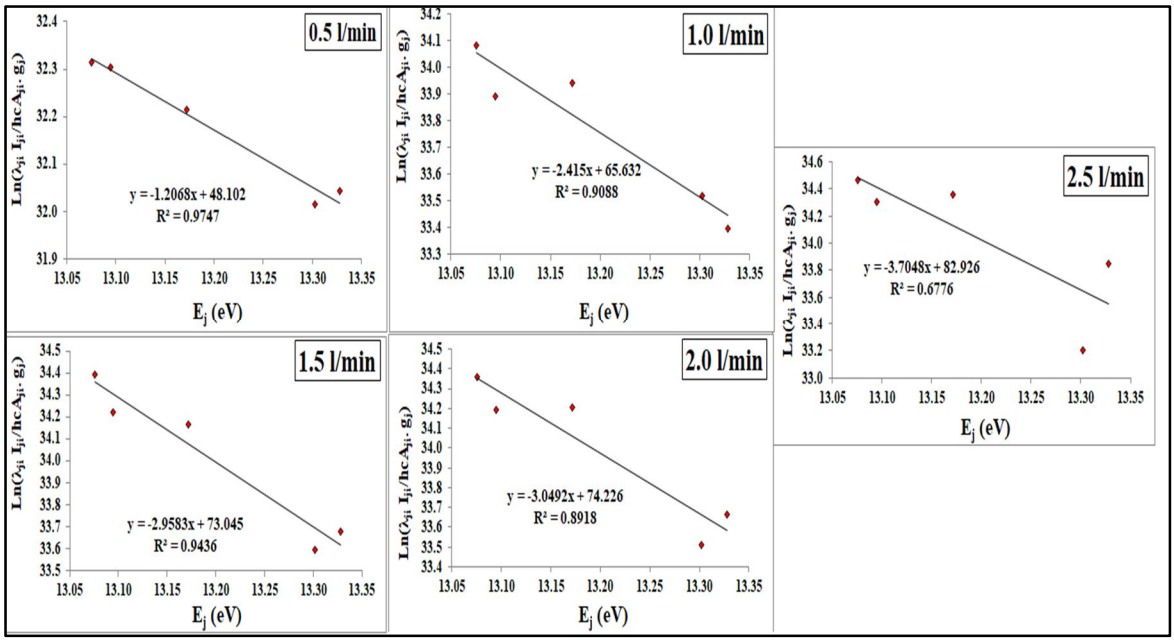

FIG. 6. Boltzmann plot for numerous gas flow rate values.

In Fig. 7, the association between n_e and T_e with respect to the gas flow rate is depicted. The figure illustrates a trend where T_e reduces as the gas flow rate ascends. Simultaneously, it demonstrates a contrasting trend where the plasma jet's electron density increases with the rise in gas flow rate. These findings align with previous observations reported by Aadim *et al.* [24, 25].

Indeed, an increased gas flow rate usually tends to increase the number of collisions between the gas atoms and plasma electrons. These collisions result in energy transfer from the electrons to the gas particles. The gas temperature ascends as this energy transfer intensifies due to increased collision frequency. Consequently, T_e decreases because a larger portion of the energy is transferred to the gas particles, thereby reducing the average energy level of the electrons within the plasma. Notably, these results align precisely with the results reported by Moon [26].

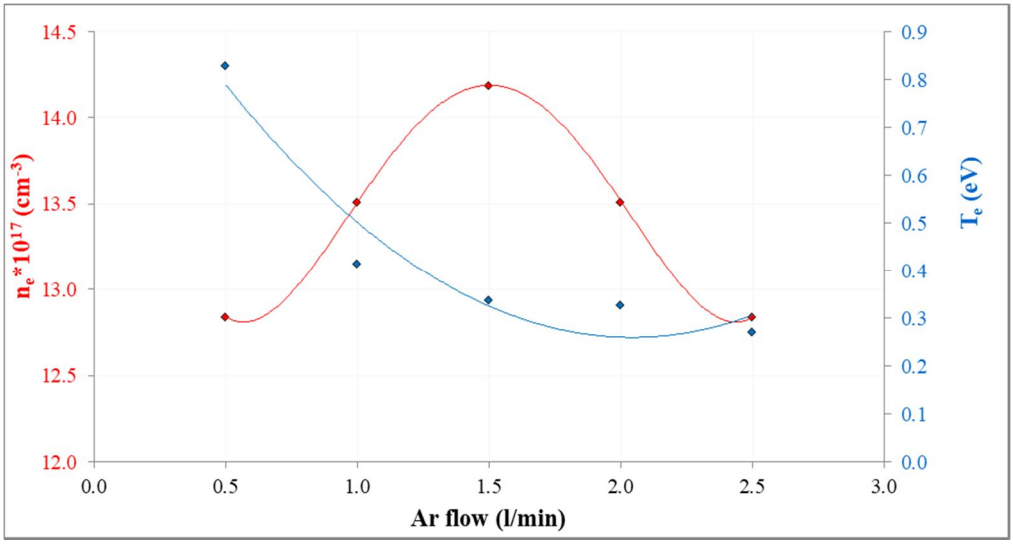

FIG. 7. Modification of T_e and n_e in terms of gas flow rate.

4. Conclusions

The presence of argon, reactive oxygen species, and reactive nitrogen in atmospheric pressure plasma was ascertained using optical emission spectroscopy. Furthermore, a correlation was observed between the gas flow rate, T_e, and n_e. Specifically, the gas flow rate exhibited a direct correlation with the electron density, while an increase in gas flow and plasma temperature demonstrated an inverse correlation.

5. Acknowledgments

This study is supported by the Plasma Physics Laboratory, Physics Department, College of Science, University of Baghdad.

References

[1] Palma, V., Cortese, M., Renda, S., Ruocco, C., Martino, M., and Meloni, E., Nanomaterials, 10 (8) (2020) 1596.

[2] Aadim, K.A., Opt. Quantum Electron., 48 (12) (2016) 545.

[3] Mazhir, S.N., Aadim, K.A., Al-Halbosiy, M.M.F., and Abdalameer, N.Kh., Indian J. Forensic Med. Toxicol., 15 (1) (2021) 2072.

[4] Abbas, I.K. and Aadim, K.A., Sci. Technol. Indones., 7 (4) (2022) 427.

[5] Ahmed, R.T., Ahmed, A.F., and Aadim, K.A., J. Opt. (India), 53 (2) (2024) 1564.

[6] Issa, M.A. and Aadim, K.A., J. Opt. (India), (2024). https://doi.org/10.1007/s12596-024-02212-2.

[7] Aadim, K.A., Photon. Sens., **7** (4) (2017) 289.

[8] Jamal, R.K., Ali, F.H., Hameed, M.M., and Aadim, K.A., Iraq. J. Sci., 61 (5) (2020) 1032.

[9] Weltmann, K.D. and Von Woedtke, T., Eur. Phys. J. Appl. Phys., 55 (1) (2011) 13807.

[10] Issa, M.A., and Aadim, K.A., J. Opt. (India), (2024). https://doi.org/10.1007/s12596-024-02034-2.

[11] Issa, M.A., and Aadim, K.A., J. Opt.(India), (2024). https://doi.org/10.1007/s12596-024-01951-6.

[12] Elahi, Z., Mahmood, S., and Zakaullah, M., Pak. J. Sci. Ind. Res. Ser. A: Phys. Sci., 66 (2) (2023) 130.

[13] Kostov, K.G., Rocha, V., Koga-Ito, C.Y., Matos, B.M., Algatti, M.A., Honda, R.Y., ... and Mota, R.P., Surf. Coat. Technol., 204 (18-19) (2010) 2954.

[14] Bates, D.R. and Bederson, B., "Advances in Atomic and Molecular Physics", (Academic Press, 1985).

[15] Evdokimov, K.E., Konischev, M.E., Pichugin, V.F., and Sun, Z., Resour.-Eff. Technol., 3 (2) (2017) 187.

[16] Rachdi, L., Sushkov, V., and Hofmann, M., Spectrochim. Acta B, 194 (2022) 106432.

[17] Amamou, H., Bois, A., Ferhat, B., Redon, R., Rossetto, B., and Matheron, P., J. Quant. Spectrosc. Radiat. Transfer, 75 (6) (2002) 747.

[18] Eggers, B., Marciniak, J., Memmert, S., Kramer, F.J., Deschner, J., and Nokhbehsaim, M., Odontology, 108 (2020) 607.

[19] Imran, H.J., Hubeatir, K.A., Aadim, K.A., and Abd, D.S., J. Phys.: Conf. Ser., 1818 (1, (2021) 012127.

[20] Jha, V.K., Mishra, L.N., and Narayan, B., Pak. J. Sci. Ind. Res. Ser. A: Phys. Sci., 66 (3) (2023) 261.

[21] Sansonetti, J.E., Martin, W.C., and Young, S.L., "Handbook of Basic Atomic Spectroscopic Data", (version 1.1. 2) (2005).

[22] Dwech, M.H., Aadim, K.A., and Hamid, L.A., AIP Conf. Proc., 2213 (2020) 020147.

[23] Kukhta, A.V. and Kazakov, S.M., Phys. Usp., 66 (2023) 173.

[24] Mohammed, R.S., Aadim, K.A., and Ahmed, K.A., AIP Conf. Proc., 2386 (2022) 080050.

[25] Ahmed, K.A., Aadim, K.A., and Mohammed, R.S., AIP Conf. Proc., 2372 (2021) 080004.

[26] Moon, S.Y., Phys. Plasmas, 9 (3) (2002) 4045.

Volume 18, Number 4, 2025. pp. 443-453

Jordan Journal of Physics

ARTICLE

Comparison of Calculated Energy Levels and Electric Quadrupole Transitions Probabilities of the Even-Even $^{144\text{-}150}$Nd Isotopes Using IBM-2, NEF and BM

Elham A. Younes[a], **Najat S. Eshaftri**[b], **Asma A. Elbndaq**[c], **Ayad Ezwam**[a], **Mohamed H. Badri**[a] and **Sadiq M. El-Kadi**[a]

[a] *Physics department, Faculty of Science, University of Tripoli, P.O.Box: 13555, Tripoli, Libya.*

[b] *General department, High Institute of Engineering Technology, Tripoli, Libya.*

[c] *General department, College of Medical Science and Technology, Tripoli, Libya.*

Doi: **https://doi.org/10.47011/18.4.3**

Received on: 31/05/2024; *Accepted on: 03/12/2024*

Abstract: The energy levels of low-lying bands were calculated using the interacting boson model (IBM-2) [1], new empirical formula (NEF) [2, 3], and Bohr-Mottelson model (BM) [4, 5], while the rest of the levels, including the negative parity bands (NPB) of even-even neodymium isotopes Nd (144-150), were calculated using only the NEF and BM. The electrical quadrupole transition probabilities $B(E2)$ of Nd nuclei were also determined. A comparison between the results and the available experimental data showed a very good agreement. To determine the property of the ground-state band, the energy ratio $r\left(\frac{I+2}{I}\right)$ as a function of the spin (I) [6, 7] was plotted.

Keywords: Neutron-rich deformed nuclei, Neodymium isotopes, Energy level structure and electrical quadrupole transition, Interacting Boson model, Bohr-Mottelson model, New empirical formula.

PACS 2010: Nuclear energy levels, 21.10.-k.

Introduction

Recently, the study of the neutron-rich deformed nuclei of the mass region A > 100 has become an interesting topic for theoretical and experimental studies. In this work, the energy-level structure and electrical quadrupole transition properties of neodymium isotopes with even neutron numbers N= 84, 86, 88, and 90 were investigated. The interacting boson model is one of the successful approaches for describing the low-lying collective properties of nuclear energy states, including the ground-state band (GSB) $I^+ = 0_1^+ + 2_1^+ + 4_1^+ + \cdots$, the gamma band $I^+ = 2_2^+ + 3_1^+ + 4_2^+ + \cdots$, and the beta band $I^+ = 0_2^+ + 2_3^+ + 4_3^+ + \cdots$ [8, 9].

For the same range of Nd isotopes, the Bohr-Mottelson model (BM) and the new empirical formula (NEF) were used to calculate the energies of the positive and the negative parity states band (NPB).

This paper aimed to calculate and compare energy levels of Nd isotopes (144, 146, 148, and 150) and their reduced electrical quadrupole transition probabilities, $B(E2)$, using the interacting boson model IBM-2, the new empirical formula (NEF), and the Bohr-Mottelson energy collective model (BM). The obtained results are compared with the available experimental data from the nuclear data sheets [10].

Corresponding Author: Elham A. Younes **Email**: el.younes@uot.edu.ly

Theory and Calculations:

A. Theory:

1. The interacting boson model (IBM-2)

The IBM was developed in 1974 by F. Iachello and A. Arima [1]. It considers pairs of valence nucleons and treat them as bosons. The number of bosons are conventionally taken to be half the number of valence particles or holes. There are several versions of the IBM. The one considered in this work is the IBM-2, which deals with even-even medium and heavy nuclei and distinguishes between proton bosons and neutron bosons. The general form of the IBM-2 Hamiltonian [11, 12] can be written as:

$$H = H_\nu + H_\pi + H_{\nu,\pi} \quad (1)$$

which consists of the neutron boson Hamiltonian (H_ν), proton boson Hamiltonian (H_π), and neutron boson-proton boson interaction Hamiltonian ($H_{\nu,\pi}$).

$$H_\rho = \varepsilon_\rho n_{d\rho} + V_{\rho\rho}, \rho = \nu, \pi \quad (2)$$

Here, ε_ρ is the average energy of boson, $n_{d\rho}$ is the number of (d)bosons and $V_{\rho\rho}$ is the interaction between identical bosons, given by:

$$V_{\rho\rho} = \tfrac{1}{2}\sum_{L=0,2,4} C_\rho^{(L)}([\,d_\rho^\dagger\, d_\rho^\dagger]^{(L)}.[d_\rho^{\sim} d_\rho^{\sim}]^{(L)}) \quad (3)$$

$$H_{\nu,\pi} = k(Q_\nu.Q_\pi) + M_{\nu,\pi} \quad (4)$$

where k is the strength of this interaction, $Q_\nu.Q_\pi$ is the quadrupole-quadrupole interaction, and $M_{\nu,\pi}$ is the Majorana interaction, defined as

$$M_{\nu,\pi} = \tfrac{1}{2}\xi_2\left(d_\upsilon^\dagger s_\pi^\dagger - d_\pi^\dagger s_\nu^\dagger\right).(d_\upsilon^{\sim} s_\pi - d_\pi^{\sim} s_\nu) + \sum_{k=1,3}\xi_k\,([d_\upsilon^\dagger\, d_\pi^\dagger]^{(k)}.[d_\pi^{\sim} d_\nu^{\sim}]^{(k)} \quad (5)$$

Here, ξ_1, ξ_2, ξ_3 are the Majorana parameters of the interaction between identical bosons ($C_\rho^{(L)}$) and the creation and annihilation operators $(d_\rho^\dagger s_\rho^\dagger)$, $(d_\rho s_\rho)$.

2. The Bohr-Mottelson (BM)

There are two forms of the BM energy expansion: the GSB and NPB levels with powers of $I(I+1)$ for deformed nuclei [4, 5].

$$E(I)_{GSB} = AI(I+1) - BI^2(I+1)^2 + CI^3(I+1)^3 \quad (6)$$

$$E(I)_{NPB} = E_0 + A'I(I+1) - B'I^2(I+1)^2 + C'I^3(I+1)^3 \quad (7)$$

where E_0 is the band head energy of the negative parity band (NPB) and the coefficients $A > A', B > B' and\ C > C'$ can be determined from a fit of the available energy levels of this band.

3. The New Empirical formula (NEF):

There are two forms of (NEF):

a- For the ground band, given by [2, 3]:

$$E(I) = \frac{A_1\, I(I+1)}{A_2\,(I+1)+I^{A_3}} \quad (8)$$

where A_1, A_2, and A_3 are the fitting parameters.

b- For negative-state band or any other band, calculated using the following formula:

$$E(I) = E'_0 + \frac{(A_1+B)I(I+1)}{A_2(I+1)+I^{A_3}} \quad (9)$$

$E'_0\ and\ B$ are parameters of the other bands and can be obtained from the value of $E(I)$ from the negative-state or from any other band.

To define the symmetry for the excited band of even-even nuclei, the following energy ratios were constructed [6, 7]:

$$r\left(\frac{I+2}{I}\right) = \frac{R(I+2/I)_{exp} - R(I+2/I)_{vib}}{R(I+2/I)_{rot} - R(I+2/I)_{vib}} \quad (10)$$

where $R(\frac{I+2}{I})_{exp}$ is the experimental energy value ratio between the ground state band energies of $(I+2)$, and I. The $R(\frac{I+2}{I})_{rot} = \frac{(I+2)(I+3)}{I(I+1)}$ are members of the rotational limit which take the limits $0.6 \le r \le 1.0$.

In the vibrational limit, the energy ratio is $R(\frac{I+2}{I})_{vib} = \frac{I+2}{I}$ in the region $0.1 \le r \le 0.35$, and $0.4 \le r \le 0.6$ for ɣ- unstable nuclei.

4. Transition probability $B(E2)$:

The electric quadropole transitions $(E2)$ are important factors within the collective nuclear structure. The $E2$ transitions in the IBM-2 are governed by the operator [13]:

$$T(E2) = e_\nu Q_\nu + e_\pi Q_\pi \quad (11)$$

$$Q_\rho = d_\rho^\dagger s_\rho + s_\rho^\dagger d_\rho + \chi_\rho [d_\rho^\dagger d_\rho^{\sim}]^{(2)} \quad (12)$$

In this expression, e_ρ is the effective quadrupole charge and χ_ρ is the quadrupole structure parameter of the neutron and proton bosons.

The electrical quadrupole transitions are also described [14] by the formula:

$$B(E2) = \frac{0.05657}{T_{1l2}^{\gamma}(ps)\, E_\gamma^5\,(MeV)}(e^2b^2) \quad (13)$$

$$T_{1/2}^{\gamma} = T_{1/2}\,(\exp)\,(1+\alpha_{tot}) \qquad (14)$$

where $T_{1/2}$ is a half-life and α_{tot} is total theoretical internal conversion coefficient given in Table 1.

TABLE 1. $T_{1/2}$ and α_{tot} values over I^+ for $^{144-150}$Nd isotopes.

I^+	^{144}Nd			^{146}Nd		
	$T_{1/2}$ psec	α_{tot}	$T^{8}_{1/2}$ psec	$T_{1/2}$ psec	α_{tot}	$T^{8}_{1/2}$ psec
2^+	2.97	0.005	2.985	20.9	0.015	21.221
4^+	7.4	0.007	7.451	3.8	0.008	3.829
6^+	20.8	0.013	21.079	--------	--------	--------
I^+	^{148}Nd			^{150}Nd		
	$T_{1/2}$ psec	α_{tot}	$T^{8}_{1/2}$ psec	$T_{1/2}$ psec	α_{tot}	$T^{8}_{1/2}$ psec
2^+	80	0.052	84.120	1480	0.857	2748.360
4^+	6.90	0.016	7.008	60.50	0.092	66.078
6^+	2.90	0.010	2.929	12.50	0.036	12.949
8^+	1.40	0.034	1.447	4.70	0.021	4.796
10^+	---------	---------	---------	2.59	0.014	2.626
12^+	---------	---------	---------	1.80	0.011	1.819

B- Calculations:

The energy eigenstates and electric quadrupole transition probabilities generated by the Neutron-Proton Boson code (NPBOS) were calculated by the best-fitting parameters listed in Table 2.

The energy levels of positive and negative bands of $^{144-150}$Nd isotopes were calculated using the BM and NEF implemented in MATLAB® 9.8 software. Table 3 shows the BM and NEF parameters of the ground-state bands of $^{144-150}$Nd isotopes, while Table 4 lists the best-fitting NEF parameters for the other states. Table 5 displays the best-fitting parameters of the other states of BM for $^{144-150}$Nd isotopes. Table 6 shows a comparison of energy levels of the IBM-2, NEF, and BM models with the experimental data for even-even $^{144-150}$Nd isotopes. The reduced transition probabilities were calculated by the NEF and BM using MATLAB® 9.8 software, and the results are shown in Table 7.

TABLE 2. IBM-2 parameters for $^{144-150}$Nd.

X_Z^A	^{144}Nd	^{146}Nd	^{148}Nd	^{150}Nd
ε_d	0.98	0.805	0.650	0.555
$\kappa_{\pi\upsilon}$	-0.215	-0.098	-0.070	-0.093
χ_π	-0.3	-1.200	-1.200	-1.200
χ_ν	-1.40	-1.100	-1.100	-1.200
ξ_2	-0.01	-0.00	0.00	0.00
CL_π	0.9	-0.600	0.0	8.0
	-0.05	0.0	0.0	0.0
	-0.125	0.0	-0.05	0.0
CL_ν	0.0	0.900	0.0	1.00
	0.0	-0.0	0.0	0.00
	0.0	-0.0	0.0	0.00

Note: All parameters are in MeV except χ_π and χ_ν.

TABLE 3. NEF & BM parameters for Ground State, even-even $^{144\text{-}150}$Nd

Isotopes	NEF Parameters			BM Parameters		
	A_1	A_2	A_3	A	B	C
^{144}Nd	0.06	-0.417	0.807	1.116×10^{-1}	2.532×10^{-3}	2.091×10^{-5}
^{146}Nd	0.116	0.327	-0.507	4.982×10^{-2}	2.143×10^{-4}	3.872×10^{-7}
^{148}Nd	0.093	0.239	0.185	4.001×10^{-2}	2.431×10^{-4}	7.350×10^{-7}
^{150}Nd	0.027	0.053	0.112	1.843×10^{-2}	4.107×10^{-5}	6.512×10^{-8}

Note: NEF & BM parameters are in MeV except A_2 and A_3.

TABLE 4: NEF parameters in MeV of other bands for even-even $^{144\text{-}146}$Nd.

Isotopes	^{144}Nd Parameters		^{146}Nd Parameters	
	E'_0	B	E'_0	B
Band 2 (Beta Band)	------	------	------	------
Band 3 $(NPB)_1$	1.0167	-0.0198	0.2309	-0.0097
Band 4 (Gama Band)	1.1991	-0.0183	0.9013	-0.0209
Band 5 $(NPB)_2$	2.0996	-0.0304	-0.1102	-0.0046
Band 6	------	------	0.2900	-0.0096
Band 7 $(NPB)_3$	------	------	-0.3666	0.0107
Band 8	------	------	-0.1702	0.0026

TABLE 4 (continued). NEF parameters in MeV of other bands for even-even $^{148\text{-}150}$Nd.

Isotopes	^{148}Nd Parameters		^{150}Nd Parameters	
	E'_0	B	E'_0	B
Band 2 (Beta Band)	0.8899	-0.0016	0.6836	0.0053
Band 3 $(NPB)_1$	0.4867	-0.0198	0.7907	-0.0088
Band 4 (Gamma Band)	1.0555	-0.0219	0.9113	0.0045

TABLE 5. BM parameters in MeV of other bands for even-even ^{144}Nd.

Isotopes	^{144}Nd Parameters			
	E_0	A'	B'	C'
Band 2 (Beta Band)	-----	------	------	-----
Band 3 $(NPB)_1$	1.43	1.75×10^{-2}	-1.79×10^{-5}	-8.73×10^{-8}
Band 4 (Gamma Band)	1.70	1.84×10^{-2}	1.49×10^{-5}	4.94×10^{-8}
Band 5 $(NPB)_2$	0.91	3.79×10^{-2}	1.31×10^{-4}	1.99×10^{-7}
Band 6	-----	------	------	------
Band 7 $(NPB)_3$	-----	------	------	------
Band 8	-----	------	------	------

TABLE 5 (cont.). BM parameters in MeV of other bands for even-even ^{146}Nd.

Isotopes	^{146}Nd Parameters			
	E_0	A'	B'	C'
Band 2 (Beta Band)	-----	------	------	------
Band 3 $(NPB)_1$	0.95	1.91×10^{-2}	-1.23×10^{-5}	-8.53×10^{-8}
Band 4 (Gamma Band)	1.35	2.11×10^{-2}	3.07×10^{-5}	3.38×10^{-8}
Band 5 $(NPB)_2$	1.67	1.27×10^{-2}	-5.97×10^{-6}	-2.02×10^{-8}
Band 6	1.58	2.32×10^{-2}	4.7×10^{-5}	4.67×10^{-8}
Band 7 $(NPB)_3$	1.87	8.67×10^{-3}	-4.56×10^{-5}	-9.88×10^{-8}
Band 8	1.41	1.21×10^{-2}	-4.79×10^{-5}	-1.47×10^{-7}

TABLE 5 (cont.). BM parameters in MeV of other bands for even-even ^{148}Nd.

Isotopes	^{148}Nd			
	Parameters			
	E_0	A'	B'	C'
Band 2 (Beta Band)	0.92	4.1×10^{-2}	3.68×10^{-4}	2.04×10^{-6}
Band 3 $(NPB)_1$	0.81	1.48×10^{-2}	-1.54×10^{-6}	-4.99×10^{-8}
Band 4 (Gamma Band)	0.69	1.19×10^{-1}	4.89×10^{-3}	6.77×10^{-5}

TABLE 5 (cont.). BM parameters in MeV of other bands for even-even ^{150}Nd.

Isotopes	^{150}Nd			
	Parameters			
	E_0	A'	B'	C'
Band 2 (Beta Band)	0.68	3.34×10^{-2}	7.13×10^{-4}	9.71×10^{-6}
Band 3 $(NPB)_1$	0.84	6.64×10^{-3}	-1.34×10^{-4}	-1.12×10^{-6}
Band 4 (Gamma Band)	0.70	8.92×10^{-2}	5.64×10^{-3}	1.41×10^{-4}

TABLE 6. Comparison of energy levels in MeV (positive & negative bands) for even-even $^{144-150}$Nd.

^{144}Nd				
Band 1 (Ground State)				
I^+	E_{exp}	NEF	BM	IBM-2
0^+	0.000	0.000	0.000	0.000
2^+	0.697	0.719	0.583	0.697
4^+	1.315	1.223	1.386	1.387
6^+	1.792	1.888	1.769	1.742
8^+	2.710	2.678	2.713	2.509
10^+	-----	3.591	9.472	-----
12^+	-----	4.628	35.183	-----
14^+	-----	5.795	105.447	-----
16^+	-----	7.098	263.868	-----
Band 3 $(NPB)_1$				
I^-	E_{exp}	NEF	BM	IBM-2
3^-	1.511	1.648	1.640	-----
5^-	2.093	2.046	1.967	-----
7^-	2.613	2.534	2.451	-----
9^-	2.903	3.103	3.088	-----
11^-	3.830	3.755	3.855	-----
13^-	4.743	4.492	4.689	-----
(15^-)	5.473	5.317	5.466	-----
(17^-)	5.967	6.236	5.976	-----
Band 4				
I^+	E_{exp}	NEF	BM	IBM-2
2^+	1.561	1.698	1.815	1.548
3^+	2.179	1.854	1.924	2.509
4^+	2.110	2.047	2.068	2.178
5^+	2.420	2.266	2.245	-----
6^+	2.218	2.508	2.456	-----
8^+	2.972	3.057	2.972	-----
(9^+)	3.234	3.362	3.278	-----
(10^+)	3.673	3.690	3.617	-----
(11^+)	4.046	4.038	3.991	-----
(12^+)	4.355	4.409	4.404	-----
(14^+)	5.379	5.218	5.375	-----

^{146}Nd				
Band 1 (Ground State)				
I^+	E_{exp}	NEF	BM	IBM-2
0^+	0.000	0.000	0.000	0.000
2^+	0.454	0.414	0.291	0.455
4^+	1.043	1.092	0.914	1.049
6^+	1.780	1.815	1.743	1.748
8^+	2.594	2.545	2.621	2.554
10^+	3.320	3.275	3.403	3.458
12^+	3.994	4.003	4.028	------
14^+	4.694	4.729	4.600	------
16^+	5.461	5.453	5.492	------
Band 3 $(NPB)_1$				
I^-	E_{exp}	NEF	BM	IBM-2
3^-	1.190	0.911	1.179	------
5^-	1.518	1.562	1.529	------
7^-	2.029	2.229	2.039	------
9^-	2.706	2.898	2.701	------
11^-	3.501	3.566	3.483	------
13^-	4.295	4.233	4.311	------
15^-	5.058	4.897	5.054	------
Band 4				
I^+	E_{exp}	NEF	BM	IBM-2
2^+	1.303	1.241	1.472	1.083
3^+	1.777	1.510	1.595	1.713
4^+	1.745	1.798	1.756	1.622
(5^+)	2.046	2.093	1.952	------
(6^+)	2.084	2.391	2.180	------
14^+	4.695	4.782	4.729	------
15^+	5.160	5.079	5.101	------
16^+	5.461	5.376	5.485	------
Band 5 $(NPB)_2$				
I^-	E_{exp}	NEF	BM	IBM-2
11^-	3.405	3.386	3.395	------
13^-	4.028	4.085	4.046	------
15^-	4.761	4.782	4.769	------
17^-	5.559	5.477	5.521	------
19^-	6.203	6.170	6.232	------
21^-	6.807	6.863	6.800	------
Band 6				
I^+	E_{exp}	NEF	BM	IBM-2
16^+	5.363	5.292	5.363	------
18^+	5.900	5.955	5.900	------
20^+	6.514	6.616	6.514	------
(22^+)	7.364	7.277	7.364	------
Band 7 $(NPB)_3$				
I^-	E_{exp}	NEF	BM	IBM-2
10^-	3.246	3.210	3.245	------
12^-	3.958	4.005	3.958	------
14^-	4.787	4.798	4.787	------
16^-	5.612	5.589	5.612	------

Band 8				
I^+	E_{exp}	NEF	BM	IBM-2
8^+	2.475	2.432	2.474	------
10^+	3.124	3.178	3.124	------
12^+	3.902	3.922	3.902	------
14^+	4.696	4.664	4.696	------
^{148}Nd				
Band 1 (Ground State)				
I^+	E_{exp}	NEF	BM	IBM-2
0^+	0.000	0.000	0.000	0.000
2^+	0.302	0.302	0.231	0.302
4^+	0.752	0.751	0.709	0.737
6^+	1.280	1.280	1.306	1.289
8^+	1.856	1.858	1.894	1.940
10^+	2.471	2.470	2.437	2.695
12^+	3.106	3.107	3.114	------
14^+	------	3.762	4.485	------
16^+	------	4.431	7.683	------
Band 2 (Beta Band)				
I^+	E_{exp}	NEF	BM	IBM-2
0^+	0.917	0.890	0.924	0.888
2^+	1.171	1.187	1.157	0.201
4^+	1.604	1.628	1.613	1.802
6^+	2.149	2.147	2.146	------
8^+	2.726	2.715	2.726	------
Band 3 $(NPB)_1$				
I^-	E_{exp}	NEF	BM	IBM-2
3^-	0.999	0.892	0.991	------
5^-	1.242	1.281	1.258	------
7^-	1.645	1.720	1.640	------
9^-	2.132	2.190	2.124	------
11^-	2.676	2.683	2.683	------
13^-	3.264	3.193	3.263	------
Band 4 (Gamma Band)				
I^+	E_{exp}	NEF	BM	IBM-2
2^+	1.249	1.287	1.241	------
3^+	1.512	1.449	1.532	------
4^+	1.683	1.631	1.661	------
(5^+)	1.688	1.828	1.699	------
6^+	2.099	2.036	2.097	------
^{150}Nd				
Band 1 (Ground State)				
I^+	E_{exp}	NEF	BM	IBM-2
0^+	0.000	0.000	0.000	0.000
2^+	0.130	0.132	0.109	0.138
4^+	0.381	0.381	0.353	0.382
6^+	0.720	0.719	0.707	0.726
8^+	1.130	1.130	1.139	1.173
10^+	1.599	1.599	1.617	1.727
12^+	2.119	2.119	2.123	------
14^+	2.682	2.681	2.663	------
16^+	3.280	3.280	3.286	------

Band 2 (Beta Band)				
I^+	E_{exp}	NEF	BM	IBM-2
0^+	0.676	0.684	0.676	0.907
2^+	0.851	0.841	0.851	0.961
4^+	1.138	1.138	1.138	1.181
6^+	1.541	1.542	1.541	------
Band 3 $(NPB)_1$				
I^-	E_{exp}	NEF	BM	IBM-2
1^-	0.853	0.824	0.853	------
3^-	0.935	0.956	0.935	------
5^-	1.129	1.157	1.129	------
(7^-)	1.433	1.412	1.433	------
Band 4 (Gamma Band)				
I^+	E_{exp}	NEF	BM	IBM-2
2^+	1.062	1.065	1.062	0.999
$3^{(+)}$	1.201	1.195	1.201	1.179
4^+	1.353	1.355	1.353	1.345

TABLE 7. Comparison of the transitional probability calculated by IBM-2, NEF, and BM to the experimental data for $^{144\text{-}150}$Nd nuclei.

	$I_i \rightarrow I_f$	$B(E_2)$ exp	$B(E_2)$ NEF	$B(E_2)$ BM	$B(E_2)$ IBM-2
		e^2b^2	e^2b^2	e^2b^2	e^2b^2
^{144}Nd	$2^+_1 \rightarrow 0^+_1$	0.1155	0.0988	0.2821	0.116
	$4^+_1 \rightarrow 2^+_1$	0.0842	0.2334	0.0227	0.152
	$6^+_1 \rightarrow 4^+_1$	0.1089	0.0206	0.3255	0.167
^{146}Nd	$2^+_1 \rightarrow 0^+_1$	0.1385	0.2182	1.2710	0.229
	$4^+_1 \rightarrow 2^+_1$	0.2077	0.1030	0.1580	0.294
	$6^+_1 \rightarrow 4^+_1$	------	------	------	0.287
^{148}Nd	$2^+_1 \rightarrow 0^+_1$	0.26904	0.26585	1.01262	0.310
	$4^+_1 \rightarrow 2^+_1$	0.43454	0.44344	0.32583	0.474
	$6^+_1 \rightarrow 4^+_1$	0.47279	0.46842	0.25449	0.518
	$8^+_1 \rightarrow 6^+_1$	0.61439	0.60509	0.55371	------
^{150}Nd	$2^+_1 \rightarrow 0^+_1$	0.55012	0.51614	1.32955	0.420
	$4^+_1 \rightarrow 2^+_1$	0.86104	0.90046	0.99758	0.618
	$6^+_1 \rightarrow 4^+_1$	0.97436	0.98263	0.78790	0.679
	$8^+_1 \rightarrow 6^+_1$	1.02550	1.01157	0.78368	--------
	$10^+_1 \rightarrow 8^+_1$	0.95025	0.94099	0.85596	--------
	$12^+_1 \rightarrow 10^+_1$	0.81637	0.82102	0.93781	--------

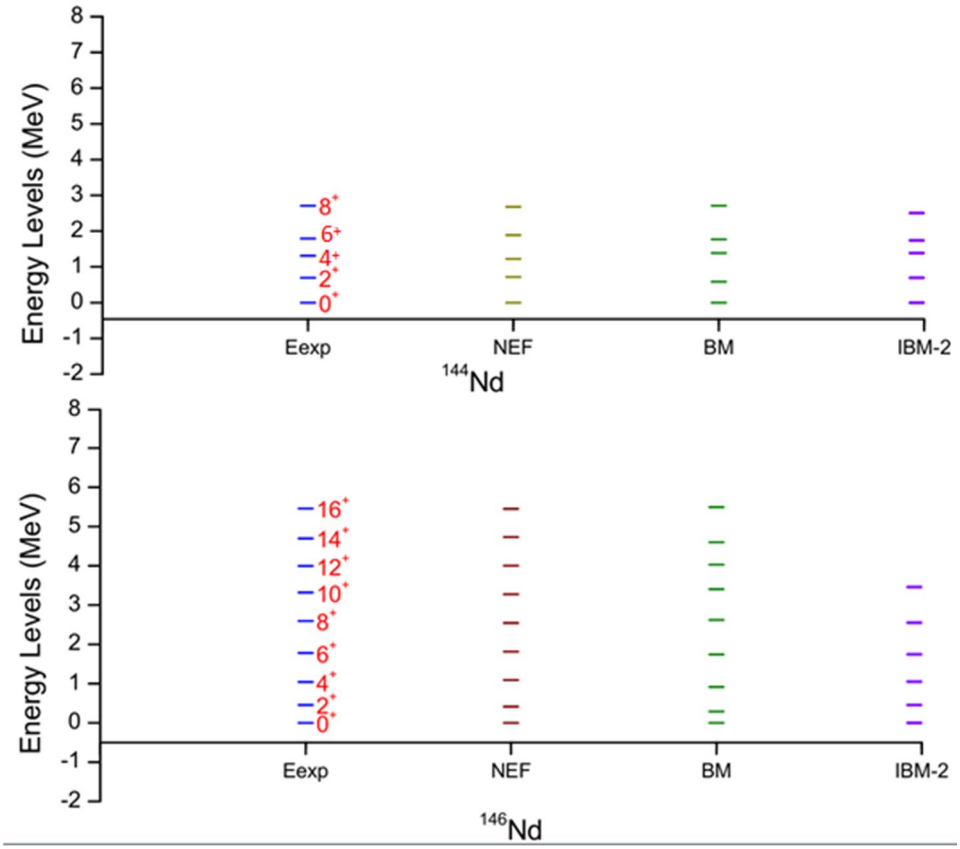

FIG. 1(a). Comparison between energy levels using NEF, BM, and IBM-2 and the experimental data [10] for even-even $^{144\text{-}146}$Nd isotopes.

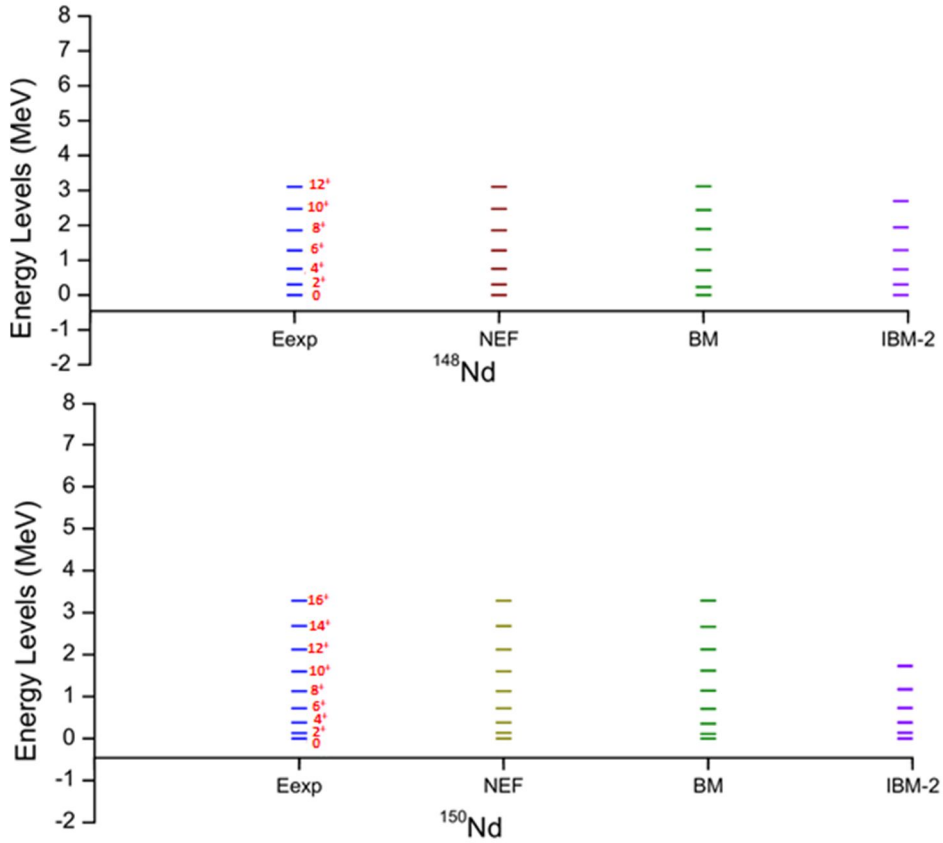

FIG. 1(b). Comparison between energy levels using NEF, BM, and IBM-2 and the experimental data [10] for even-even $^{148\text{-}150}$Nd isotopes.

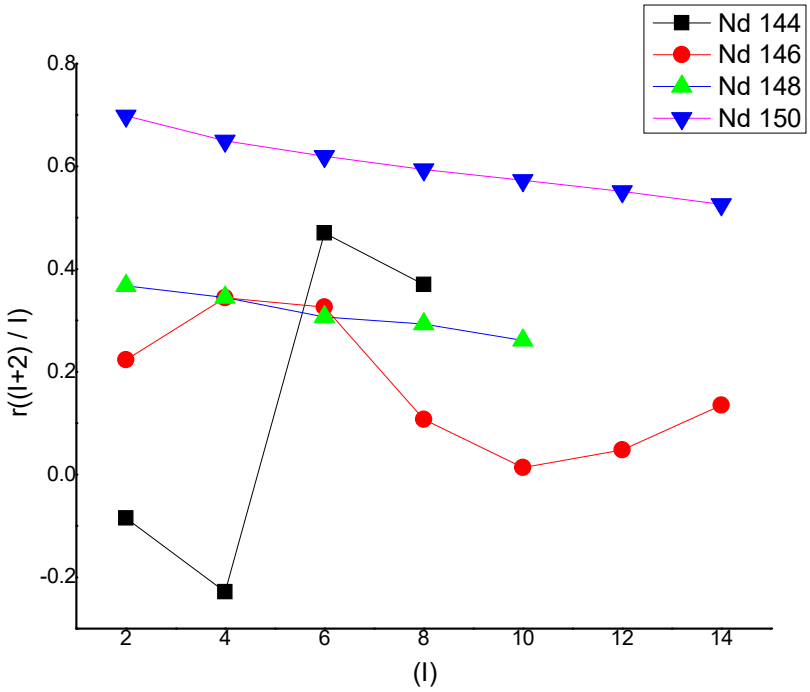

FIG. 2. The energy ratio $r\left(\frac{I+2}{I}\right)$ as function of I for even-even $^{144\text{-}150}$Nd [10].

Results and discussion

In general, the calculated energy levels of the ground-state bands for $^{144\text{ -}150}$Nd isotopes are in good agreement with the experimental data, as shown in Figs. 1(a) and 1(b). It is clear from Table 6 that calculations for the ground-state band 1 obtained using the IBM-2 are closer to the experimental data than those calculated by the BM and NEF models. The results for band 2 using the BM are noticeably better than the results obtained by the NEF and IBM-2. The results of negative bands 3 and 5 and positive band 4 using the BM are approximately exact to the experimental data.

It is obvious from the comparison of the BM and NEF calculations of other positive bands (bands 6 and 7) in Table 6 that the results of the BM and NEF are in good agreement with the experimental data.

In Fig. 2, to define the symmetry for the excited band of even-even nuclei, Nd^{144}, the energy ratio started with a small value within the vibrational limit, then rocketed sharply, reaching $r\left(\frac{8}{6}\right)$ at ɣ-unstable nuclei. The energy ratio then dropped again to the vibrational limit at higher I's. The values of the energy ratios for $^{146,\ 148}$Nd were confined in the range of 0.1-0.35 and within the vibrational limit. The calculations of Nd^{150} showed a steady decrease in energy ratio, dropping from the rotational limit into ɣ-unstable nuclei.

As shown in Table 7, the calculated transitional probability using the IBM-2 gave close results for ^{144}Nd with the experimental data, while results obtained using the NEF were in good agreement with the experimental data for ^{148}Nd and ^{150}Nd.

Conclusion

The energy levels and electric quadrupole transition probabilities of the even–even $^{144\text{-}150}$Nd isotopes were investigated using the IBM-2, NEF, and BM models. The positive-parity bands were calculated using all three models (IBM-2, NEF, and BM), while the negative-parity and other excited bands were analyzed using the NEF and BM.

The results of this work show that both the BM and NEF models reproduce the available experimental data with very good agreement. The IBM-2 model also provides satisfactory agreement with experiment, particularly for spin values below 12.

The plot of the $r\left(\frac{I+2}{I}\right)$ as a function of spin I confirms that the $^{144\text{-}148}$Nd isotopes exhibit the U(5)-O(6) property, while ^{150}Nd has the shape phase transition from SU(3)-O(6) property.

The reduced electrical quadrupole transition probabilities, $B(E2)$, were also calculated, and good agreement with experimental data was obtained for ^{148}Nd and ^{150}Nd using the NEF model.

References

[1] Iachllo, F. and Arima, A., Phys. Lett., 53B, (1974) 309.

[2] Al-Jubbori, M.A., Radhi, F.S., Ibrahim, A.A., Albakri, S.A.A., Kassim, H.H., and Sharrad, F.I., Nucl. Phys. A, 971 (2018) 35.

[3] Al-Jubbori, M.A., Kassim, H.H., Raheem, E.M., Ahmed, I.M., Khodair, Z.T., Sharrad, F.I., and Hossain, I., Ukr. J. Phys., 67 (2) (2022) 1275.

[4] Bonatsos, D., Daskaloyannis, C., Drenska, S.B., Karoussos, N., Minkov, N., Raychev, P.P., and Roussev, R.P., Phys. Rev. C, 62 (2000) 024301.

[5] Bohr, A. and Mottelson, B.R., "Nuclear Structure", Vol. II, (World Scientific, Singapore, 1998), p. 748.

[6] Bonatsos, D., Skouras, L.D., and Rikovska, J., Phys. Rev. C, 43 (1991) R952(R).

[7] Khalaf, A.M. and Ismail, A.M., Prog. Phys,. 2 (2013) 98.

[8] Iachello, F. and Arima, A., "The Interacting Boson Model", (Cambridge University Press, Cambridge, England, 1987).

[9] Hebbinghaus, G., Kutsarova, T., Cast, W., Krämer-Flecken, A., Lieder, R.M., and Urban, W., Nucl. Phys. A, 514 (1990) 225.

[10] The National Nuclear Data Center (NNDC), https://www.nndc.bnl.gov/ensdf/, 17-11 (2022).

[11] Esaftri, N.S., Bogrin, S.M., Elbndag, A.A., and El-Kadi, S.M., AL-NAWAH, 12 (18) (2020).

[12] Dejbakhsh, H., Latypov, D., Ajupova, G., and Shlomo, S., Phys. Rev. C, 46 (1992) 2326.

[13] Druce, C.H., Pittel, S., Barrett, B.R., and Duval, P.D., Ann. Phys., 176 (1) (1987) 114.

[14] Raman, S., Nestor JR, C.W., and Tikkanen, P., At. Data Nucl. Data Tables, 78 (1) (2001) 1.

Volume 18, Number 4, 2025. pp. 455-466

Jordan Journal of Physics

ARTICLE

Analysis of Generating a Microwave Frequency Comb in Laser-Assisted Scanning Tunneling Microscopy with a Semiconductor Sample

Marwan S. Mousa[a] and **Mark J. Hagmann**[b]

[a] *Department of Renewable Energy Engineering, Jadara University, Irbid 21110, Jordan.*
[b] *Department of Electrical and Computer Engineering, University of Utah, Salt Lake City, Utah, 84112, USA.*

Doi: **https://doi.org/10.47011/18.4.4**
Received on: 30/05/2024; *Accepted on: 20/10/2024*

Abstract: When a mode-locked laser is focused on the tunneling junction of a scanning tunneling microscope optical rectification generates microwave harmonics at integer multiples of the laser pulse repetition frequency. These harmonics set the present state-of-the-art for a narrow-linewidth microwave source because of the high stability of passive mode-locking in the laser. Hundreds of harmonics are measured with a signal-to-noise ratio exceeding 25 dB with a metal sample in the STM. However, the harmonics are attenuated by the spreading resistance with a resistive sample. Now the spreading resistance is quantified and analysis with equivalent circuit models is used to characterize the effects to support further measurements with semiconductors.

Keywords: Microwave frequency comb, Microwave source, Mode-locked lazer.

1. Introduction

We have previously generated a microwave frequency comb (MFC) by focusing a mode-locked laser on the tunneling junction of a scanning tunneling microscope (STM) with a metallic sample electrode. For example, the 200th harmonic at a frequency of 14.85 GHz, which is 200 times the laser pulse repetition frequency, has a power of -145 dBm, which is 25 dB above the displayed average noise level (DANL) [1]. Each harmonic has a linewidth less than 0.1 Hz, setting the present state of the art for a narrow linewidth microwave source [2]. Thus, the quality factor (Q) of the 200th harmonic exceeds 1.5x10^{11}. For comparison, the Q is typically 100 for resonant circuits with discrete components, 10^6 for metal microwave cavities, and 10^9 for superconductive microwave cavities. We attribute the extremely narrow linewidth to the high stability of the mode-locked laser, noting that if the laser pulse train were exactly periodic, the linewidth would be zero, so the Q would be infinite. With metal samples, the power at each harmonic is inversely proportional to the square of its frequency. We attribute this roll-off to shunting by the capacitance (≈ 6 pF) between the leads for the tip and sample, but within the tunneling junction, the harmonics may extend to terahertz frequencies [3].

In our first measurements of the MFC with a semiconductor, we used intrinsic (n-type) gallium nitride (GaN). As the DC bias for the STM was slowly increased, the harmonics were first seen at a value of 9 V at which the DC tunneling current was 1 μA. Then, as the bias was reduced, the harmonics continued until reaching 5 V. We measured the first five harmonics of the MFC in 1,062 scans of the spectrum analyzer over a duration of 43 minutes. However, after that, it was not possible to see the harmonics [4]. We have seen the harmonics in more recent measurements, but they do not have

Corresponding Author: Marwan S. Mousa **Email**: m.mousa@jadara.edu.jo

the stability that is found with metallic samples. The analysis in this paper was made with the objective of understanding and optimizing our measurements with semiconductors.

2. Modeling Spreading Resistance in the Semiconductor

The electrical resistance between a small contact at the surface of an object with resistivity ρ and a second contact with much greater area is called the "spreading resistance" and is independent of the location and size of the larger contact. The spreading resistance is given by ρ/4a, where "ρ" is the resistivity of the object, "a" is the radius of the contact, and the object is much larger than a [5]. We previously extended the Simmons analysis of quantum tunneling between two infinite parallel flat metal plates [6] to approximate the distribution of the tunneling current on a metallic sample in an STM by modeling the tip as a metal sphere with a flat metal plate as the sample [7]. Now, in Appendix I, we extended this method to approximate the spreading resistance in the resistive sample of an STM. Examples of these calculations are shown in Figs. 1 and 2.

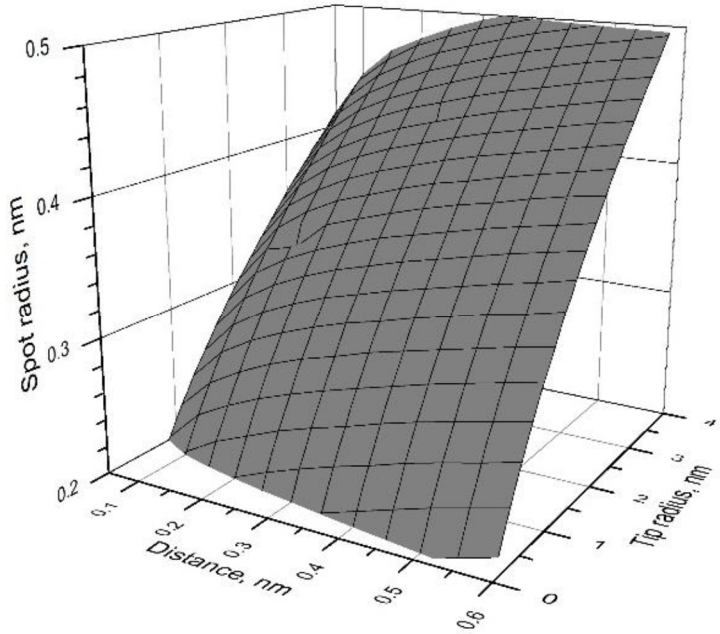

FIG. 1. Spot radius for the tunneling current.

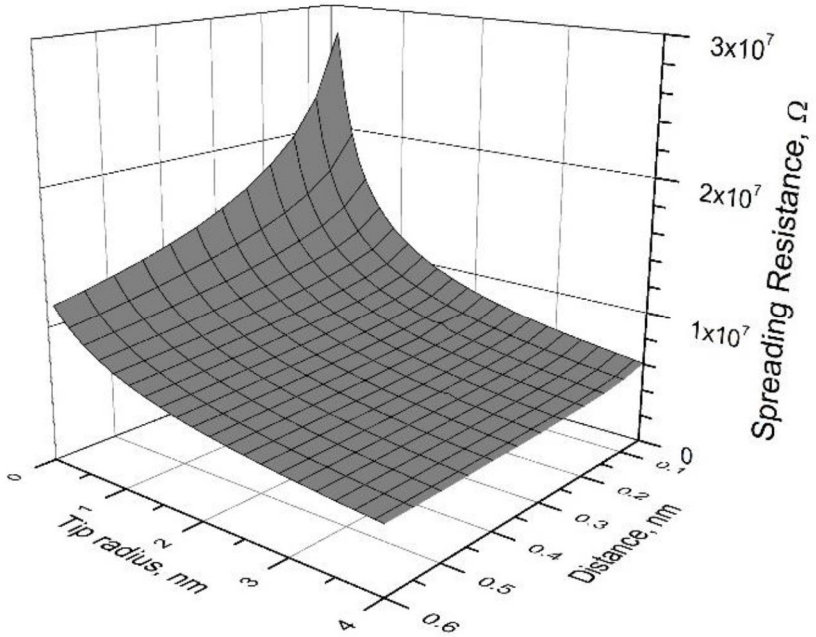

FIG. 2. Spreading resistance for the tunneling current.

Figure 1 shows the effective spot radius "a" calculated for the tunneling current at the surface of a resistive sample in an STM as a function of the tip-sample distance and the tip radius. Figure 2 shows the spreading resistance, which is proportional to the resistivity, for a sample resistivity of 1 Ω-cm. Figure 2 shows that the spreading resistance is increased by reducing the radius of the tip or the tip-sample distance. The axial extent of the contribution to the spreading resistance within the sample is comparable to the spot radius. The resolution is measured by laser-assisted scanning tunneling microscopy may be much finer than the spot size because the laser radiation is focused to a finer size by the tip, which acts as an optical antenna. By analogy, sub-nanometer resolution is already achieved in tip-enhanced Raman spectroscopy because of near-field intensification of the laser radiation by the tip [8].

3. Delimitations in the Measurement and Analysis of the MFC with a Semiconductor Sample

Figure 3 is a block diagram of the apparatus we have used to measure the MFC with a semiconductor as the sample in a commercial STM (UHV 300, from RHK Technology) at Los Alamos National Laboratory. With a metallic sample, the MFC is measured by connecting a spectrum analyzer to a Bias T inserted between the sample and the bias supply. However, with a semiconductor, each laser pulse generates a pulse of carriers that has a comparable duration (e.g., 15 fs), and simulations show that the carrier pulse undergoes severe attenuation and dispersion as it moves outward from the tip through the semiconductor [9]. Thus, the harmonics are only seen with a surface probe that is close to the tunneling junction as shown in Fig. 3. It would be simpler to measure the harmonics between the tip and the preamplifier for the STM control electronics but a Bias-T or miniature transformer inserted at that point interferes with feedback control of the tunneling current in the commercial STM to cause the tunneling current to be unstable. A rigorous analysis of the MFC with a semiconductor sample would require modeling the transport of carriers from the tunneling junction to the surface probe [9]. However, to simplify the calculations, we assume that this probe is close enough to the tip that no correction is required for attenuation and dispersion of the carriers after they have passed through the spreading resistance. In the analysis, we assume that the photon energy for the laser is less than the bandgap energy of the semiconductor to prevent surge currents caused by the formation of electron-hole pairs, which interfere with measuring the MFC [10]. We also neglect other photon processes that may occur within the semiconductor.

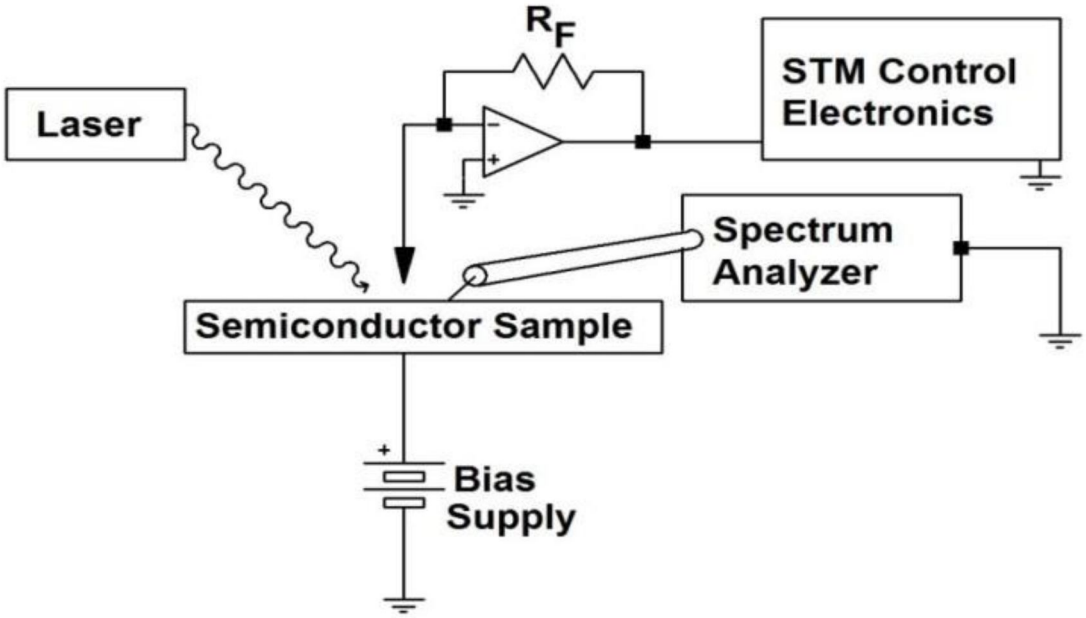

FIG. 3. Block diagram for measuring the MFC with a semiconductor in the STM.

4. Procedure for Simulations Based on the Derivations in the Appendices

4.1 Method to Determine the Operating Point with Example

First, it is necessary to determine the DC tunneling current IDC and the tip-sample distance d when the DC bias voltage VB, the effective emitting area of the tip A, and the work function φ are specified, by using procedures that are described in Appendix I. The DC equivalent circuit model for the tunneling junction of an STM with a resistive sample consists of the applied DC bias VB in series with the tunneling resistance RT and the spreading resistance of the sample RS. The tunneling resistance is defined by RT ≡ VTS/IDC, where VTS is the tip-sample voltage and IDC is the DC tunneling current. We use Eq. (1) to approximate the DC tunneling current, where the parameters α and β are given in Eqs. (2) and (3) [6]. Thus, the tunneling resistance is given by Eq. (4).

$$I_{DC} = \frac{\alpha A V_{TS}}{d} e^{-\beta d} \quad (1)$$

$$\alpha = \sqrt{2m\phi_M e}\left(\frac{e}{h}\right)^2 \quad (2)$$

$$\beta = \frac{4\pi}{h}\sqrt{2m\phi_M e} \quad (3)$$

$$R_T = \frac{d}{\alpha A} e^{\beta d} \quad (4)$$

Equation (5) from Appendix I is used to determine the spreading resistance RS, where functions F1(R) and F2(R,ρ) are defined in Eqs. (6) and (7).

$$R_S = F_2(R,\rho) \cdot e^{F_1(R).d} \quad (5)$$

$$F_1(R) = 4.773 \times 10^9 + 2.480 \times 10^8 Ln(R) \quad (6)$$

$$F_2(R,\rho) = \frac{2462\rho}{R^{0.400}} \quad (7)$$

Thus, the DC tunneling current is given by Eq. (8), which may also be written in the form of Eq. (9). We solve Eq. (9) iteratively by the method of bisection to determine the tip-sample distance d and then use Eq. (1) to determine IDC. Gaussian noise is added to simulate the measured current, which is reported to the user. However, the values of A, φ, and d are unknown to the user.

$$I_{DC} = \frac{V_B}{R_S + R_T} = \frac{V_B}{F_2(R,\rho)\cdot e^{F_1(R).d} + \frac{d}{\alpha A} e^{\beta d}} \quad (8)$$

$$F_2(R,\rho) \cdot e^{F_1(R).d} + \frac{d}{\alpha A} e^{\beta d} - \frac{V_B}{I_{DC}} = 0 \quad (9)$$

Figure 4, which was prepared by following this procedure, shows the simulated tip-sample distance d as a function of the current IDC for sample resistivities of 0, 0.001, 0.01, 0.1, 1, and 10 Ω-cm with a tungsten tip having an apex radius of 0.3 nm and a DC bias of 1 V. Note that for each value of the resistivity the curve deviates from that for zero resistivity as the current is increased because the voltage drop across the spreading resistance is greater.

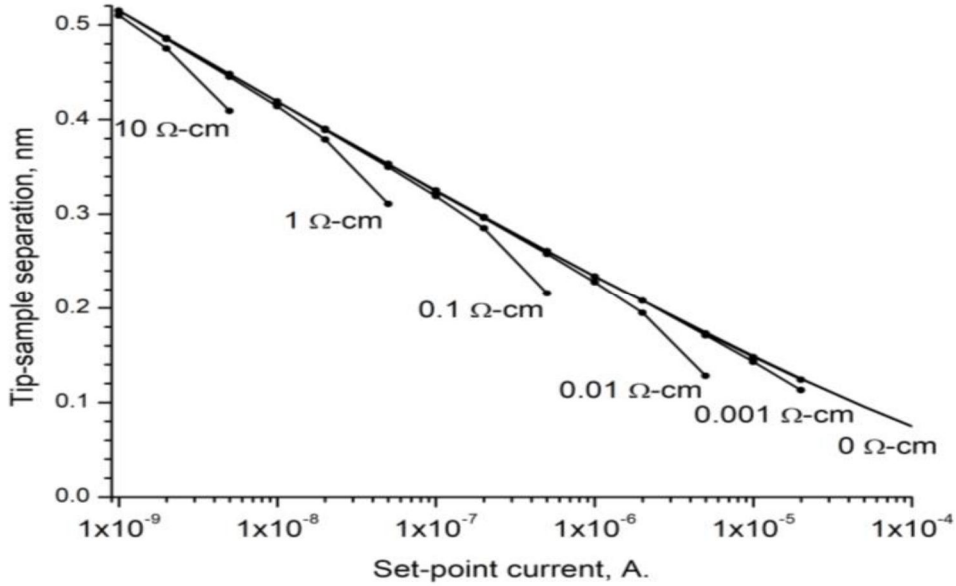

FIG. 4. Tip-sample distance vs. current for an applied bias of 1 V, and sample resistivities of 0, 0.001, 0.01, 0.1, 1, and 10 Ω-cm, from the top curve to the lower one.

4.2 Simulations of the Power at the Microwave Harmonics

In Appendix II, it is shown that the microwave power at each harmonic is given by Eq. (10), where the prefactor K depends on the nonlinear relationship of the tunneling current to the applied voltage, the power and focusing of the laser, and the harmonic number. In our simulations, we use K =1.44x10^{-34} W-mtr^2, which is based on our many measurements for the case ρ = 0 with metal samples [1].

$$P = \frac{Ke^{-2\beta d}}{d^2\left(1+\frac{R_S}{R_T}\right)^4} \tag{10}$$

5. Results of the Simulations

Figure 5 shows the simulated microwave power as a function of the applied DC bias and the DC tunneling current that were calculated using ρ = 0.1 Ω-cm in Eq. (10). Note that the microwave power is maximum and remains constant for a specific set of values for VDC and IDC.

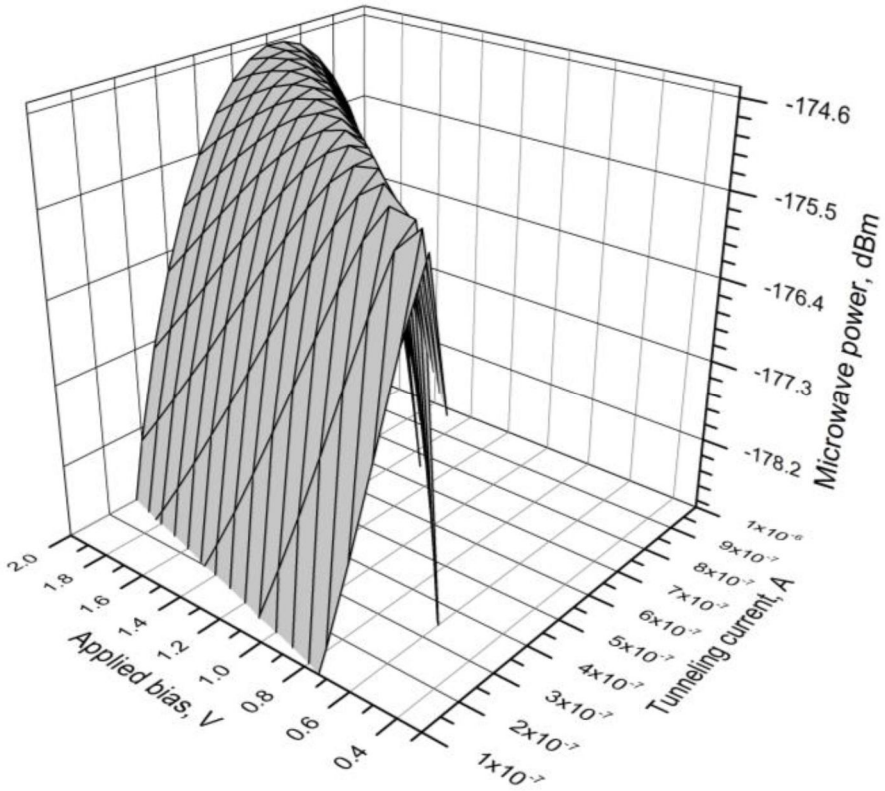

FIG. 5. Microwave power vs. applied DC bias and DC tunneling current as calculated using Eq. (10) with ρ = 0.1 Ω-cm.

Figure 6 shows the simulated microwave power as a function of the DC tunneling current ISP for ρ = 0.1 Ω-cm in Eq. (10) with DC bias values of 0.5, 1.0, 1.5, 2.0, and 2.5 V. Note that this is a cut through the "ridge" that is seen in Fig. 5 for specific values of the DC bias voltage. This figure shows that the microwave power is maximum and remains constant for a specific set of values for the bias voltage. Again, in Figs. 5 and 6, the calculations were made for a tungsten tip having an apex radius of 0.3 nm and a DC bias of 1 V. A "ridge" similar to that in Fig. 5, where the microwave power is maximum and constant, is also seen with other values of the sample resistivity. Fig. 7 shows the microwave power for each value of the sample resistivity when the applied DC bias and the DC tunneling current are chosen to obtain the maximum power for that resistivity. We have recently developed a low-noise solid-state preamplifier that increases the signal-to-noise ratio in these measurements by 14 dB with our spectrum analyzer. Thus, the displayed average noise level (DANL) may be reduced from -170 dBm (seen in Fig. 3) to as low as -184 dBm, as shown in Fig. 7. As noted earlier, the extremely narrow linewidth of the microwave harmonics makes it possible to measure attowatt level signals.

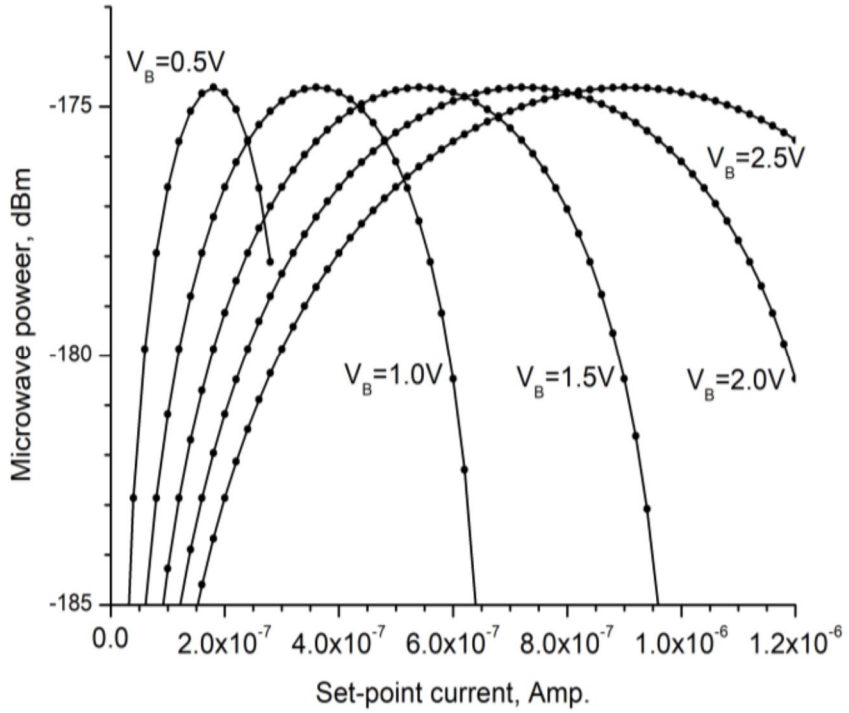

FIG. 6. Microwave power vs. DC tunneling current for specific values of the applied bias as calculated using Eq. (10) with $\rho = 0.1$ Ω-cm.

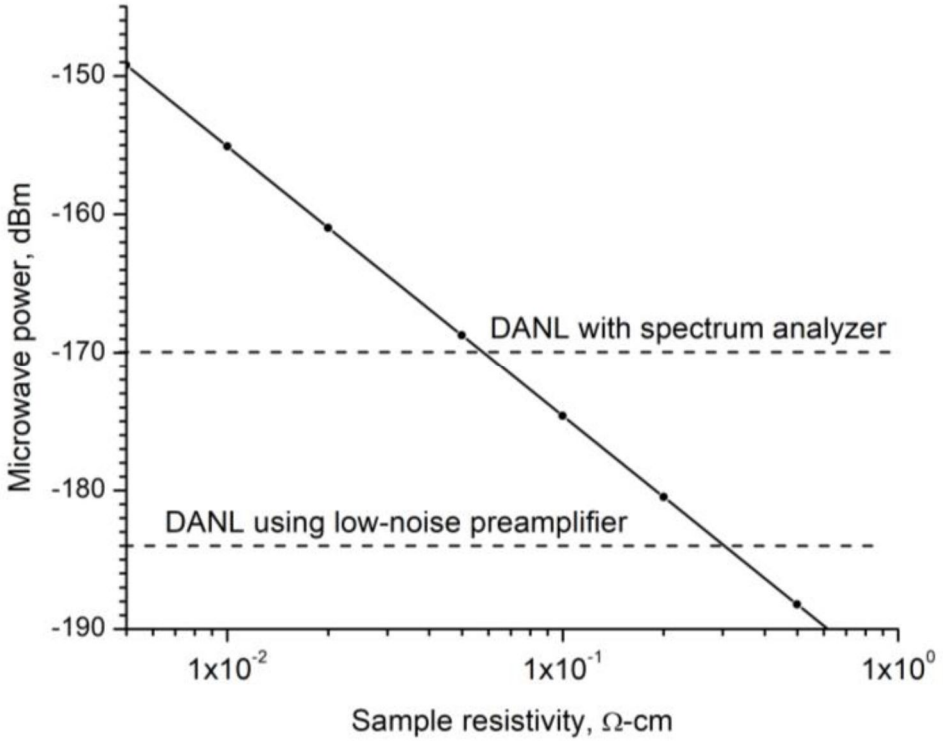

FIG. 7. Values for the microwave power, as a function of the sample resistivity, that are obtained by varying the applied DC bias and DC tunneling current to maximize the microwave power.

It may be seen in Fig. 7 that increasing the resistivity by a factor of 10 reduces the maximum possible microwave power by 19.5 dB, so that the maximum power varies approximately as the inverse square of the resistivity. For example, a 10% change in the resistivity of the sample would cause approximately a 20% change in the measured microwave power. Fig. 8 shows simulated values of the applied DC bias as a function of the DC current that give the maximum power at sample resistivities of 1.0, 0.5, 0.2, 0.1, 0.05, 0.02, 0.01, and 0.005 Ω-cm, from the top to the bottom curve. The power at each of these resistivities is

-194.1, 188.2, -180.5, -174.6, -168.7, -161.0, -155.1, and -149.2 dBm, again from the top to the bottom curve, respectively. These calculations were made for a tungsten tip having an apex radius of 0.3 nm. The reduction seen in the microwave power when increasing the resistivity is consistent with that shown in Fig. 7. A best-fit of all of the data in Fig. 8 gives the following empirical equation:

$$V_B = 2.60 \times 10^7 I_{SP} \rho^{0.975} \quad (11)$$

Figure 9 shows simulated values of the microwave power as a function of the tip-sample distance. The data correspond to three sets of simulations performed with DC currents of 10-8, 10-7, and 10-6 A, with the applied bias adjusted to maximize the power at each point. These calculations were made for a tungsten tip having an apex radius of 0.3 nm, with sample resistivities of 0.005, 0.010, 0.020, 0.050, 0.1, 0.2, 0.5, and 1 Ω-cm. Note that the three sets of data overlap in this figure.

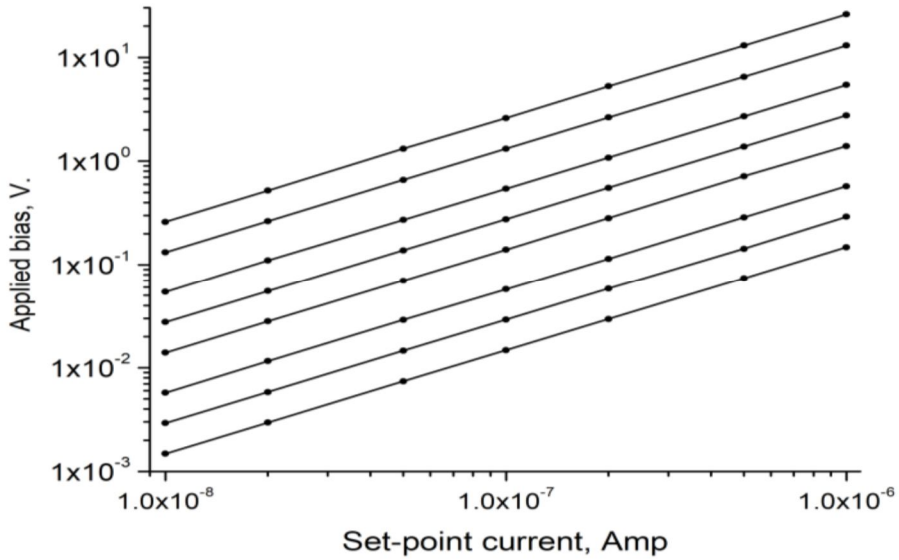

FIG. 8. Applied bias vs. current to obtain the maximum microwave power with sample resistivities of 1.0, 0.5, 0.2, 0.1, 0.05, 0.02, 0.01, and 0.005 Ω-cm. The power at each of these resistivities is -194.1, -188.2, -180.5, -174.6, -168.7, -161.0, -155.1, and -149.2 dBm from the top to the bottom of the 8 curves, respectively.

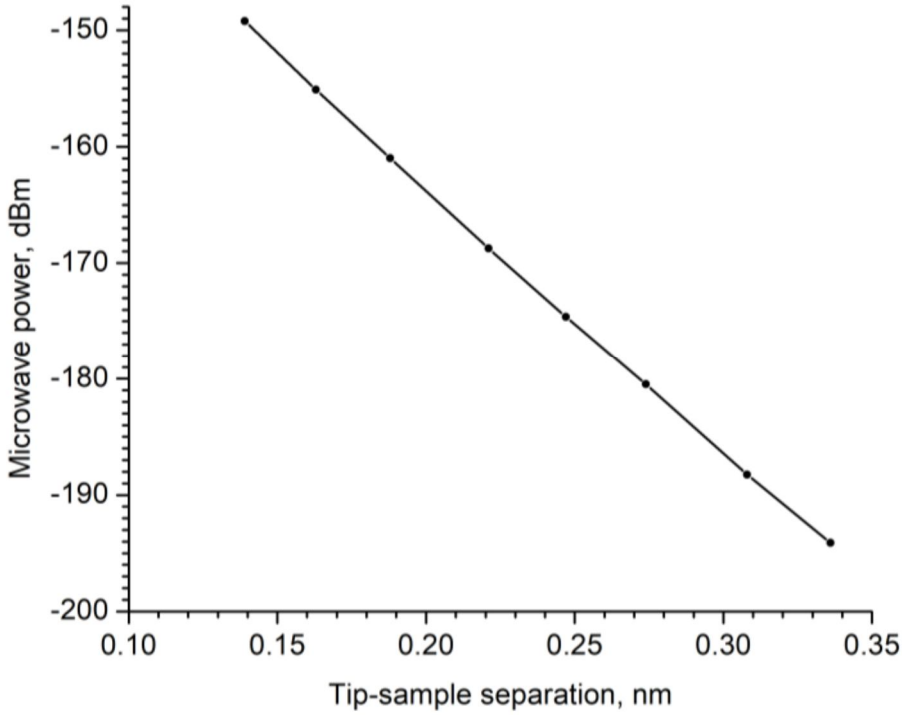

FIG. 9. Microwave power vs. tip-sample distance for three sets of simulations in which the applied bias and the current were adjusted to maximize the power at each point.

6. Possible Applications

One possible application of this technology is improved metrology for semiconductor devices. Roadmaps for the semiconductor industry request that the carrier concentration be measured with a resolution finer than 10 percent of the dimension at each lithography node. Scanning Spreading Resistance Microscopy (SSRM) is generally the method of choice for carrier profiling of semiconductor devices at and below the 20-nm lithography node in the semiconductor industry [11]. However, the diamond probes used to measure the spreading resistance in SSRM have an initial diameter of 10-15 nm that blunts to 50 nm or more during a single set of measurements [12], so this method fails to satisfy the roadmaps at the 12 and 20 nm nodes, which are now in production. We propose to develop new instrumentation for carrier profiling that is based on laser-assisted scanning tunneling microscopy, using a tunneling junction in place of the probes in SSRM, to provide sub-nm resolution while mitigating damage to the semiconductor. We would use a substitution method analogous to that already used to interpret the data in SSRM [12]. We would measure the power of the harmonics in the MFC by consecutive measurements with the test samples and standards under the same conditions of laser power, DC tunneling current, and many other parameters. We would use standards such as those already used with SSRM, which are silicon wafers with multiple sections having different known values for the carrier concentration [13]. Each sample and each standard would be cleaved and prepared with the same cleaning processes in order to compare each test sample with the standards under controlled conditions.

7. Conclusions

For each value of the DC applied bias, the DC tunneling current may be adjusted to maximize the microwave power. Also, for each value of the DC tunneling current, the DC applied bias may be adjusted to maximize the microwave power. In both cases, the maximum value for the microwave power and the value of the tip-sample distance at which it occurs are uniquely determined by the resistivity of the sample. The microwave power is generated by the nonlinear interaction of the incident laser radiation with the tunneling junction. The function of the DC tunneling current and the DC applied bias is to adjust the tip-sample distance so that the microwave power is maximized for a specific value of the sample resistivity. We are concerned about the apparent need for high DC tunneling currents when measuring the MFC with semiconductors. In our most recent measurements, scanning electron microscope (SEM) images show that the tip electrode is generally damaged at the end of each session of measurements. In our earlier measurements [4] we attribute the sudden onset of the harmonics as the DC bias was slowly increased to 9 V to the consequent reduction in the tip-sample distance, and attribute the relatively long period of time (43 minutes) in which the first 5 harmonics were measured to the gradual increase in this distance as the DC bias was slowly reduced to 5 V. The subsequent failure to detect the harmonics in that session was probably caused by a tip-crash. In tip-enhanced near-field Raman microscopy, a metal tip acts as an optical nanoantenna for near-field enhancement of the incident laser radiation at a spot of interest on the sample to obtain stronger signals and sub-nm resolution with the Raman effect [8]. By analogy, in laser-assisted scanning tunneling microscopy, the near-field enhancement of the optical radiation within the tunneling junction is strongly dependent on the tip-sample distance and the sharpness of the tip, so the resolution in imaging and the microwave power are strongly dependent on the placement of the tip and its sharpness. This shows the importance of optimizing the DC tunneling current and the applied DC bias voltage to avoid damaging the tip while obtaining the maximum microwave power and resolution.

8. Acknowledgments

This work is supported by the National Science Foundation under Grant 1648811.

Appendix I. Approximation of the Spreading Resistance

The following three equations, corresponding to Eq. 25 in Ref. [6] by Simmons, give the tunneling current density J between two parallel metal plates, where a factor of 3/2 is deleted as a typographical error [14]. From symmetry, this may be used to determine the tunneling current density between two infinitesimal objects. Here, V is the potential difference, d is the distance, m and e are the mass and charge of the electron, h

is the Planck constant, and φM is the mean of the work functions for the two infinitesimal objects.

$$J = \alpha \frac{V_{TS}}{d} e^{-\beta d} \quad \text{(A1-1)}$$

Where $\alpha = \sqrt{2m\varphi_M e}\left(\frac{e}{h}\right)^2$ (A1-2)

And $\beta = \frac{4\pi}{h}\sqrt{2m\varphi_M e}$ (A1-3)

Earlier, our group developed a method to determine the radial distribution of the tunneling current at the surface of a metal sample in an STM [7] as an extension of the analysis by Simmons. We model the hemispherical apex of the tip electrode, having radius R, to be on the z-axis with z = d in cylindrical coordinates. The surface of the sample is at z = 0, so the tunneling current in the annulus with rmin < r < rmax is given by the following expression:

$$I_{DC} = 2\pi\alpha V_{TS} \int_{r_{min}}^{r_{max}} \frac{e^{-\beta s}}{s} r dr \quad \text{(A1-4)}$$

Where $s = \sqrt{r^2 + d^2} - R$ (A1-5)

Later, we also used Eq. (A1-4) to determine the total tunneling current and its distribution at the surface of a resistive sample. In this method, we approximate the current distribution by a radial hat (chapeau) function having width "a" that is called the "spot radius", defined to contain one-half of the total current in the distribution, and setting the height to contain the total current in the distribution. This is equivalent to approximating the current distribution for a metal disk having radius a at the surface of a flat slab with resistivity ρ when the radius of the disk is much less than the thickness of the slab. Thus, we approximate the spreading resistance by using the following expression, which is appropriate for a metal disc [5]:

$$R_s = \frac{\rho}{4a} \quad \text{(A1-6)}$$

Now we have used this procedure to generate a database consisting of a matrix with 12 values for the tip radius from 0.05 to 0.60 nm in steps of 0.05 nm, and 40 values of the tip-sample distance from 0.1 to 4.0 nm in 0.1 nm steps. In order to provide a simpler method to approximate the spreading resistance, we have used Eqs. (A1-7), (A1-8), and (A1-9), determining their four numerical parameters to obtain a best fit of the database, in which the errors have a mean magnitude of 6.4 percent and a maximum of 21.7 percent for the full set. Here, the spreading resistance RS (Ω) is given as a function of the resistivity of the sample ρ in Ω-cm, with the radius of the tip electrode R, and the tip-sample distance d (both in meters).

For example, with R = 4x10-10 m, F1(R) = -5.936x108 m-1 and F2(R,ρ) = 1.414x107 Ω. Then, Eqs. (A1-7)-(A1-9) may be used to show that, for ρ = 1 Ω-cm and d = 3x10-10 m, the spreading resistance RS = 11.8 MΩ.

$$F_1(R) = 4.773 \times 10^9 + 2.480 \times 10^8 Ln(R) \quad \text{(A1-7)}$$

$$F_2(R,\rho) = \frac{2462\rho}{R^{0.400}} \quad \text{(A1-8)}$$

$$R_s = F_2(R,\rho) \cdot e^{F_1(R)\cdot d} \quad \text{(A1-9)}$$

Appendix II. Derivation of the Harmonics with a Semiconductor Sample

The following three equations, corresponding to Eq. 25 in reference [6] by Simmons, give the tunneling current density J between two parallel metal plates, where a factor of 3/2 is deleted as a typographical error [14]. From symmetry, this may be used to determine the tunneling current density between two infinitesimal objects. Here, V is the potential difference, d is the distance, m and e are the mass and charge of the electron, h is the Planck constant, and φM is the mean of the work functions for the two infinitesimal objects.

$$J = \alpha \frac{V_{TS}}{d} e^{-\beta d} \quad \text{(A2-1)}$$

Where $\alpha = \sqrt{2m\varphi_M e}\left(\frac{e}{h}\right)^2$ (A2-2)

And $\beta = \frac{4\pi}{h}\sqrt{2m\varphi_M e}$ (A2-3)

We extend the analysis by Simmons to approximate the DC tunneling current in a scanning tunneling microscope (STM), where the second and third terms within the brackets complete a power series to be consistent with measurements of the tunneling current vs. voltage in scanning tunneling spectroscopy. Here, A is the effective emitting area of the tip, and C > B2/4 because the DC tunneling current has the same sign as the bias voltage:

$$I_{DC} = \frac{\alpha A V_B}{d} e^{-\beta d}[1 + BV_B + CV_B{}^2] \quad \text{(A2-4)}$$

Equation (A2-4) is also a reasonable approximation for the DC tunneling current, even in the limit as the length of the leads to the tunneling junction is reduced to approach zero, where quasistatic approximations are

appropriate. Thus, we also use this equation at microwave and optical frequencies, following the approach that we have used previously to determine the linewidth for the harmonics of the MFC when using a metallic sample in an STM [2].

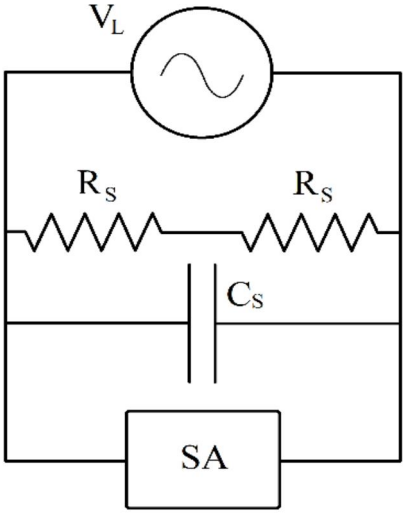

FIG. A2-1. Equivalent circuit for measuring the microwave frequency comb when the laser is focused on both the tunneling junction and the spreading resistance.

Figure A2-1 is the approximate high-frequency equivalent circuit for measuring the harmonics of the microwave frequency comb with a semiconductor sample. Then the high-frequency potential from the quasistatic electric field of the laser is imposed across the series combination of the tunneling resistance and the spreading resistance. Thus, the voltage drop across the spreading resistance reduces the voltage across the tunneling junction to attenuate the harmonics of the MFC. Then the high-frequency current through RT and RS in series is given by the following equation, where VT is the high-frequency potential across the tunneling resistance:

$$\mathrm{I(t)} = \frac{\alpha \mathrm{A}}{\mathrm{d}} \mathrm{e}^{-\beta \mathrm{d}} [\mathrm{V_T(t)} + BV_T(t)^2 + CV_T(t)^3] \quad \text{(A2-5)}$$

The tip electrode in an STM acts as an antenna in which a time-dependent feed-point voltage VL is received from the laser [6]. This potential is independent of the tip-sample distance because that distance is much less than the optical wavelength, so the optical electric field within the tunneling junction may be much greater than that in the incident field from the laser and varies inversely with the tip-sample distance. Now VL and VT are related by the following expression:

$$V_T + I(t)R_s = V_L(t) \quad \text{(A2-6)}$$

Combining Eqs. (A2-5) and (A2-6) gives the following expression in the voltage across the tunneling junction:

$$V_L(t) - V_T(t) = \frac{\alpha A R_S}{d} e^{-\beta d} [V_T(t) + BV_T(t)^2 + CV_T(t)^3] \quad \text{(A2-7)}$$

Assuming that a mode-locked laser is used with a long pulse sequence where each pulse is Gaussian with an effective width of τ, we express the time-dependent voltage across the tunneling junction by Eq. (A2-8), where the Cn are coefficients to be determined, ω0 is the optical frequency, and T is the time between consecutive laser pulses. The total voltage EL(t) is given by Eq. (A2-9).

$$V_T(t) = \sum_{-\infty}^{\infty} C_n e^{-\left(\frac{t-nT}{\tau}\right)^2} \cos[\omega_o(t-nT)] \quad \text{(A2-8)}$$

Substituting Eqs. (A2-6) and (A2-8) into Eq. (A2-7) gives the following equation where VL0 is the magnitude of VL:

$$\begin{aligned} &V_{L0} \sum_{-\infty}^{\infty} e^{-\left(\frac{t-nT}{\tau}\right)^2} \cos[\omega_o(t-nT)] - \\ &\sum_{-\infty}^{\infty} C_n e^{-\left(\frac{t-nT}{\tau}\right)^2} \cos[\omega_o(t-nT)] = \\ &\frac{\alpha A R_S}{d} e^{-\beta d} \left[\sum_{-\infty}^{\infty} C_n e^{-\left(\frac{t-nT}{\tau}\right)^2} \cos[\omega_o(t-nT)] + \right. \\ &B \left[\sum_{-\infty}^{\infty} C_n e^{-\left(\frac{t-nT}{\tau}\right)^2} \cos[\omega_o(t-nT)] \right]^2 + \\ &\left. C \left[\sum_{-\infty}^{\infty} C_n e^{-\left(\frac{t-nT}{\tau}\right)^2} \cos[\omega_o(t-nT)] \right]^3 \right] \end{aligned} \quad \text{(A2-9)}$$

Since τ << T, the double and triple products of the summations in Eq. (A2-9) are each equivalent to single summations as follows:

$$\begin{aligned} &V_{L0} \sum_{-\infty}^{\infty} e^{-\left(\frac{t-nT}{\tau}\right)^2} \cos[\omega_o(t-nT)] - \\ &\sum_{-\infty}^{\infty} C_n e^{-\left(\frac{t-nT}{\tau}\right)^2} \cos[\omega_o(t-nT)] = \\ &\frac{\alpha A R_S}{d} e^{-\beta d} \left[\sum_{-\infty}^{\infty} \mathrm{C_n e^{-\left(\frac{t-nT}{\tau}\right)^2} \cos[\omega_o(t-nT)]} + \right. \\ &\mathrm{B} \sum_{-\infty}^{\infty} \mathrm{C_n{}^2 e^{-2\left(\frac{t-nT}{\tau}\right)^2} \cos^2[\omega_o(t-nT)]} + \\ &\left. \mathrm{C} \sum_{-\infty}^{\infty} \mathrm{C_n{}^3 e^{-3\left(\frac{t-nT}{\tau}\right)^2} \cos^3[\omega_o(t-nT)]} \right] \end{aligned} \quad \text{(A2-10)}$$

Using trigonometric identities to simplify the square and cube of the cosine functions:

$$V_{L0}\sum_{-\infty}^{\infty} e^{-\left(\frac{t-nT}{\tau}\right)^2}\cos[\omega_o(t-nT)] - \sum_{-\infty}^{\infty} C_n e^{-\left(\frac{t-nT}{\tau}\right)^2}\cos[\omega_o(t-nT)] = \frac{\alpha AR_S}{d}e^{-\beta d}\left[\sum_{-\infty}^{\infty} C_n e^{-\left(\frac{t-nT}{\tau}\right)^2}\cos[\omega_o(t-nT)] + \frac{B}{2}\sum_{-\infty}^{\infty} {C_n}^2 e^{-2\left(\frac{t-nT}{\tau}\right)^2}[1+\cos[2\omega_o(t-nT)]] + \frac{C}{4}\sum_{-\infty}^{\infty} {C_n}^3 e^{-3\left(\frac{t-nT}{\tau}\right)^2}[3\cos[\omega_o(t-nT)]]+\cos[3\omega_o(t-nT)]\right] \quad \text{(A2-11)}$$

Deleting all terms at frequencies other than the optical frequency gives the following expression:

$$V_{L0}\sum_{-\infty}^{\infty} e^{-\left(\frac{t-nT}{\tau}\right)^2}\cos[\omega_o(t-nT)] - \sum_{-\infty}^{\infty} C_n e^{-\left(\frac{t-nT}{\tau}\right)^2}\cos[\omega_o(t-nT)] = \frac{\alpha AR_S}{d}e^{-\beta d}\left[\sum_{-\infty}^{\infty} C_n e^{-\left(\frac{t-nT}{\tau}\right)^2}\cos[\omega_o(t-nT)] + \frac{3C}{4}\sum_{-\infty}^{\infty} {C_n}^3 e^{-3\left(\frac{t-nT}{\tau}\right)^2}\cos[\omega_o(t-nT)]\right] \quad \text{(A2-12)}$$

Rearranging the terms in Eq. (A2-12) gives the following expression:

$$\sum_{-\infty}^{\infty}\left[V_{L0}e^{-\left(\frac{t-nT}{\tau}\right)^2} - C_n e^{-\left(\frac{t-nT}{\tau}\right)^2} - \frac{\alpha AR_S}{d}e^{-\beta d}C_n e^{-\left(\frac{t-nT}{\tau}\right)^2} - \frac{3C\alpha AR_S}{4d}e^{-\beta d}{C_n}^3 e^{-3\left(\frac{t-nT}{\tau}\right)^2}\right]\cos[\omega_o(t-nT)] = 0 \quad \text{(A2-13)}$$

But Eq. (A2-13) must be satisfied at each value of n in the summation, with the additional approximation that the coefficient C may be deleted. Thus, we have Eq. (A2-14) for the coefficients, which is used with Eq. (A2-8) to obtain Eq. (A2-15) for the potential across the tunneling junction:

$$C_n = \frac{V_{L0}}{\left(1+\frac{\alpha AR_S}{d}e^{-\beta d}\right)} \quad \text{(A2-14)}$$

$$V_T(t) = \frac{V_{L0}}{\left(1+\frac{\alpha AR_S}{d}e^{-\beta d}\right)}\sum_{-\infty}^{\infty} e^{-\left(\frac{t-nT}{\tau}\right)^2}\cos[\omega_o(t-nT)] \quad \text{(A2-15)}$$

Next, Eqs. (A2-5) and (A2-15) are combined to obtain Eq. (A2-16) for the current:

$$I(t) = \frac{\alpha A}{d}e^{-\beta d}\left[\frac{V_{L0}}{\left(1+\frac{\alpha AR_S}{d}e^{-\beta d}\right)}\sum_{-\infty}^{\infty} e^{-\left(\frac{t-nT}{\tau}\right)^2}\cos[\omega_o(t-nT)] + B\frac{{V_{L0}}^2}{\left(1+\frac{\alpha AR_S}{d}e^{-\beta d}\right)^2}\left[\sum_{-\infty}^{\infty} e^{-\left(\frac{t-nT}{\tau}\right)^2}\cos[\omega_o(t-nT)]\right]^2 + C\frac{{V_{L0}}^3}{\left(1+\frac{\alpha AR_S}{d}e^{-\beta d}\right)^3}\left[\sum_{-\infty}^{\infty} e^{-\left(\frac{t-nT}{\tau}\right)^2}\cos[\omega_o(t-nT)]\right]^3\right] \quad \text{(A2-16)}$$

Since $\tau << T$, the double and triple products of the summations in Eq. (A2-16) are each equivalent to single summations as follows:

$$I(t) = \frac{\alpha A}{d}e^{-\beta d}\left[\frac{V_{L0}}{\left(1+\frac{\alpha AR_S}{d}e^{-\beta d}\right)}\sum_{-\infty}^{\infty} e^{-\left(\frac{t-nT}{\tau}\right)^2}\cos[\omega_o(t-nT)] + B\frac{{V_{L0}}^2}{\left(1+\frac{\alpha AR_S}{d}e^{-\beta d}\right)^2}\left[\sum_{-\infty}^{\infty} e^{-2\left(\frac{t-nT}{\tau}\right)^2}\cos^2[\omega_o(t-nT)]\right] + C\frac{{V_{L0}}^3}{\left(1+\frac{\alpha AR_S}{d}e^{-\beta d}\right)^3}\left[\sum_{-\infty}^{\infty} e^{-3\left(\frac{t-nT}{\tau}\right)^2}\cos^3[\omega_o(t-nT)]\right]\right] \quad \text{(A2-17)}$$

Using trigonometric identities to simplify the square and cube of the cosine functions:

$$I(t) = \frac{\alpha A}{d}e^{-\beta d}\left[\frac{V_{L0}}{\left(1+\frac{\alpha AR_S}{d}e^{-\beta d}\right)}\sum_{-\infty}^{\infty} e^{-\left(\frac{t-nT}{\tau}\right)^2}\cos[\omega_o(t-nT)] + \frac{B}{2}\frac{{V_{L0}}^2}{\left(1+\frac{\alpha AR_S}{d}e^{-\beta d}\right)^2}\left[\sum_{-\infty}^{\infty} e^{-2\left(\frac{t-nT}{\tau}\right)^2}[1+\cos[2\omega_o(t-nT)]]\right] + \frac{C}{4}\frac{{V_{L0}}^3}{\left(1+\frac{\alpha AR_S}{d}e^{-\beta d}\right)^3}\left[\sum_{-\infty}^{\infty} e^{-3\left(\frac{t-nT}{\tau}\right)^2}[3\cos[\omega_o(t-nT)]+\cos[3\omega_o(t-nT)]]\right]\right] \quad \text{(A2-18)}$$

The objective is to determine the harmonics of the MFC in RT and RS so that all terms in Eq. (A2-18) that are at or above the optical frequency are deleted to give the following expression:

$$I(t) = \frac{1}{\left(1+\frac{\alpha AR_S}{d}e^{-\beta d}\right)^2}\frac{\alpha AB{V_{L0}}^2}{d}e^{-\beta d}\sum_{-\infty}^{\infty} e^{-2\left(\frac{t-nT}{\tau}\right)^2} \quad \text{(A2-19)}$$

Thus, we obtain Eq. (A2-20) for the power at the nth harmonic, which may be written in the form of Eq. A2-21) to show the effect of the ratio of the spreading resistance to the tunneling resistance.

$$P_n) = \frac{1}{\left(1+\frac{\alpha AR_S}{d}e^{-\beta d}\right)^4}\frac{\pi\alpha^2A^2B^2{V_{L0}}^4e^{-\beta d}}{4d^2\left[1+\left(\frac{2n\pi}{T}R_{SA}C_S\right)^2\right]}\left(\frac{\tau}{T}\right)^2 \quad \text{(A2-20)}$$

$$P_n) = \frac{1}{\left(1+\frac{R_S}{R_T}\right)^4} \frac{\pi\alpha^2 A^2 B^2 {V_{L0}}^4 e^{-\beta d}}{4d^2\left[1+\left(\frac{2n\pi}{T}R_{SA}C_S\right)^2\right]} \left(\frac{\tau}{T}\right)^2 \quad \text{(A2-21)}$$

In the main body of this documentation, we alluded to the possibility of using a substitution method to determine the spreading resistance, and thus the carrier concentration of a sample, instead of making an absolute determination of the carrier density. That is, we would determine the carrier concentration by comparing measurements of the power at one or more of the harmonics in the MFC with test samples to measurements made with a group of standards under the same conditions of laser power, DC tunneling current, and the other parameters.

In order to examine the possibility of using a substitution method, we write Eq. (A2-21) in the form of Eq. (A2-22), where G will have the same value for the test samples and the standard samples having known resistivities. Thus, if the test samples and the standards are measured at the same harmonic, the microwave power will be proportional to the prefactor γ, defined in Eq. (A2-23). Procedures for determining the resistivity from these measurements by using the prefactor are described in the body of this documentation.

$$P_n = \gamma \mathrm{F(n)G} \quad \text{(A2-22)}$$

$$\gamma = \frac{e^{-2\beta d}}{d^2\left(1+\frac{R_S}{R_T}\right)^4} \quad \text{(A2-23)}$$

$$\mathrm{F(n)} = \frac{1}{1+\left(\frac{2n\pi}{T}R_{SA}C_S\right)^2} \quad \text{(A2-24)}$$

$$G = \frac{\pi}{4}\alpha^2 A^2 B^2 {E_{L0}}^4 \left(\frac{\tau}{T}\right)^2 \quad \text{(A2-25)}$$

References:

[1] Hagmann, M.J., Taylor, A.J., and Yarotski, D.A., Appl. Phys. Lett., 101 (2012) 241102.

[2] Hagmann, M.J., Stenger, F.S., and Yarotski, D.A., J. Appl. Phys., 114 (2013) 223107.

[3] Hagmann, M.J., Coombs, D.G., and Yarotski, D.A., J. Vac. Sci. Technol. B, 35 (2017) 03D109.

[4] Rhoades, C., Rasmussen, J., Bowles, P.H., Hagmann, M.J., and Yarotski, D.A., Proc. 2016 IEEE Workshop on Microelectronics and Electron Devices, 4 pp.

[5] Gelmont, B. and Shur, M., Solid-State Electron., 36 (1993) 143.

[6] Simmons, J.G., J. Appl. Phys., 34 (1963) 1793.

[7] Hagmann, M.J. and Henage, T.E., Electron. Lett., 52 (2016) 395.

[8] Shi, X., Coca-Lopez, N., Janik, J., and Hartschuh, A., Chem. Rev., 117 (2017) 4945.

[9] Zhu, C., Andrei, P., and Hagmann, M.J., Proc. 2017 IEEE Workshop on Microelectronics and Electron Devices, 4 pp.

[10] Hagmann, M.J., Pandey, S., Nahata, A., Taylor, A.J., and Yarotski, D.A., Appl. Phys. Lett., 101 (2012) 231102.

[11] Vandervorst, W., Schultze, A., Kambham, A.K., Mody, J., Gilbert, M., and Eyben, P., Phys. Status Solidi C, 11 (2014) 121.

[12] Hantschel, T., Tsigkourakos, M., Kluge, J., Werner, T., Zha, L., Paredis, K., Eyben, P., Nuytten, T., Xu, Z., and Vandervorst, W., Microelectron. Eng., 141 (2015) 1.

[13] IMEC, Scanning Spreading Resistance Microscopy Standards SSRM-SMPL-N and SSRM-SMPL-P, available at www.brukerafmprobes.com.

[14] Matthews, N., Hagmann, M.J., and Mayer, A., J. App. Phys., 123 (2018) 13601.

Volume 18, Number 4, 2025. pp. 467-475

Jordan Journal of Physics

ARTICLE

Charge Density Distributions for Elastic and Inelastic Longitudinal Electron Scattering Form Factors of ^{28}Si and ^{32}S Nuclei

H. K. Issa and **Ghaith N. Flaiyh**

Department of Physics, College of Science, University of Baghdad. Baghdad, Iraq.

Doi: **https://doi.org/10.47011/18.4.5**

Received on: 05/06/2024; *Accepted on: 06/10/2024*

Abstract: The charge density distributions were calculated using the folding model, which was applied to study the roles of center-of-mass motion and Pauli pair association affecting the density dependence of effective two-body interactions. A formula for the two-body density applicable to light nuclei was derived in terms of the pair correlation function. For ^{28}Si and ^{32}S, the elastic electron-scattering form factors F(q) and the root-mean-square charge radii $\langle r^2\rangle^{(1/2)}$ were determined. The inelastic longitudinal electron scattering form factors associated with the isosceles transitioning T = 0 of the $(0^+ \rightarrow 2^+),(0^+ \rightarrow 2_1^+), 0^+ \rightarrow 4_1^+)$ for the ^{28}Si and ^{32}S nuclei were determined. A wave function within the model space defined by the orbits $1d_{5/2}$ $1d_{5/2}$, $2s$ $s_{1/2}$, and $1d_{3/2}$ was found to be insufficient to produce an acceptable form factor. The core-polarization impacts were assessed by incorporating the Tassie-model shape and the two-body charge density distributions into the model space, which resulted in a high degree of matching with the experimental data.

Keywords: Charge density, Elastic electron scattering, Tassie-model, Form factor and interactions.

PACS numbers: 21.30.Fe., 21.60.-n.

1. Introduction

Electron scattering is the consequence of an electromagnetic interaction. There is a multitude of theories that consider an electron as an effective instrument for the study of the structure of nuclear particles [1, 2]. The electron's fundamental attachment to the object that can be used as a targeted nucleus is well-established. It is feasible to conduct measures on the targeted nucleus without substantially altering its structure as a result of the relatively faint interaction. However, the target's shape and its relationship to nuclear particles are not known. This makes it very difficult to make distinctions between them during the examination of the results of experiments. The effect of the electron-scattering operator instantly links its cross-section to the change in the matrix components of the localized charge and current-density operator, which, in turn, is directly related to the target nucleus's structure [3].

Radhi *et al.* [4] studied the nuclear structure of ^{19}F nucleus using inelastic electron-scattering form factors, energy levels, and transition probabilities for positive and negative low-lying states. Mahmood and Flaiyh [5, 6] employed an effective two-body density operator for a point-nucleon system folded with the tensor-force correlations. The operator was used to derive an explicit form for the ground-state two-body charge density distribution (TBCDD) applicable to some light nuclei.

Sarriguren *et al.* [7] studied magnetic form factors corresponding to elastic electron scattering from odd-A nuclei using the plane-wave Born approximation.

Al-Rahmani *et al.* [8] studied short-range effects on the longitudinal Coulomb form factors C2, C3, and C4 in the ^{26}Mg nucleus. Flaiyh and

Corresponding Author: H. K. Issa **Email**: hassan.kalid@sc.uobaghdad.edu.iq

Sharrad [9] studied the effective two-body density operator for a point-nucleon system folded with the full two-body correlations (which include the tensor correlations and short-range correlations).

The folding model has proven highly effective for the phenomenology examination of nucleon-nucleus. In this approach, the scattering results are obtained using the ground-state density of the target nucleus and an effective two-body interaction [10]. In the model's initial applications, the objective density was thought to be unrelated to the effective interaction.

In this work, charge density distributions as well as elastic and inelastic form factors were investigated for the ^{28}Si and ^{32}S target nuclei. It has been previously acknowledged that electron-scattering data are inadequately described when form factors are calculated exclusively using the extensive particle-shell model space.

Thus, it has become imperative to include the consequences for the two-body effective folding model (core polarization) in the equations. This phenomenon can be attributed to the polarization of core protons by ligand protons and neutrons. The gamma-transition and the excited state of nuclei through electron-scattering have been described using the Tassie model. It is the multipole analysis of inelastic scattering. This model is limited to the standard liquid drop model when a uniform charge distribution is assumed. The Tassie model is an attempt to develop a model that is more elastic and can be modified to accommodate a non-uniform charge and mass density distribution. The density of the core-polarization transformation is contingent upon the nucleus's ground state charge density, as per this model. The ground charge density is expressed according to the two-body charge density distributions across all occupied shells, which includes the core. The Tassie model [11] provides the shape of the transition density for the excitation in question. This model, when coupled with the two-body charge density distribution and simple shell model predictions, results in a high degree of accord in both the evaluated and observed data for the longitudinal structure factors of elastic and inelastic materials during transitions J_i $T_i \rightarrow J_f$ T_f $0+ 0 \rightarrow 2_1^+ 0$ and $4_1^+ 0$ for ^{28}Si and ^{32}S nuclei.

2. Theoretical

The charge density of a nucleus composed of A particles that are shaped like points is expressed by the following operator equation [12]:

$$\rho_{ch}^{(1)}(\mathrm{r}) = \frac{1}{4\pi}\sum_{n\ell j}\eta_{n\ell j}(2j+1)\left|R_{n\ell}(\mathrm{r})\right|^2 \qquad (1)$$

where the state's livelihood percentage is represented by the parameter $\eta_{n\ell j}$, $R_{n\ell}(r)$ is the harmonic oscillator radial wave function, and (2j+1) is the occupation number of sub–orbits.

The pair-correlation function can be used to determine an equation for the density of two-body operators that are suitable for finite nuclei, based on the following relation:

$$\rho^{(2)}{}_{(\vec{r}1,\vec{r}2)} = \rho^{(1)}(\vec{r}_1)\,\rho^{(1)}(\vec{r}_2) + C(\vec{r}_1,\vec{r}_2) \qquad (2)$$

$C(\vec{r}_1,\vec{r}_2)$ is the center of mass $C_{cm}(\vec{r}_1,\vec{r}_2)$ and Pauli pair-correlation functions $C_p(\vec{r}_1,\vec{r}_2)$, respectively [13]. That is:

$$C(\vec{r}_1,\vec{r}_2) \cong C_{c.m.}(\vec{r}_1,\vec{r}_2) + C_p(\vec{r}_1,\vec{r}_2) \qquad (3)$$

where, according to Ref. [13]:

$$C_{c.m.}(\vec{r}_1,\vec{r}_2) = \frac{r_1 r_2}{2A\alpha^2}\left(\frac{1}{r_1}\frac{d\rho_1}{dr_1}\right)\left(\frac{1}{r_2}\frac{d\rho_1}{dr_1}\right) \qquad (4)$$

$$C_{p_{(\vec{r}_1,\vec{r}_2)}} \cong \frac{1}{A-1}\left[1 - \frac{c_0}{A-1}e^{\frac{K_f^2}{5}|\vec{r}_1-\vec{r}_2|^2}\right]\rho^{(1)}$$

$$C_p(\vec{r}_1,\vec{r}_2) \cong \frac{1}{A-1}\left[1-\frac{c_o}{A-1}e^{\frac{k_f^2}{5}|\vec{r}_1-\vec{r}_2|}\right] \qquad (5)$$

$$\rho^{(1)}{}_{(\vec{r}_1)}\rho^{(1)}{}_{(\vec{r}_2)}.$$

where $c_o = 3(\pi/5)^{1/2}$, α is the oscillator constant $\left(\alpha^2 = 0.99\,A^{-1/3}\right)$, and k_f is the local Fermi momentum.

By substituting Eqs. (4) and (5) into Eq. (3), and then using Eq. (3) in Eq. (2), we get:

$$\rho^{(2)}(\vec{r}1,\vec{r}2) = \rho^{(1)}(\vec{r}1)\rho^{(1)}(\vec{r}2) + \frac{r_1 r_2}{2A\alpha^2}\left(\frac{1}{r_1}\frac{d\rho_1}{dr_1}\right)\left(\frac{1}{r_2}\frac{d\rho_1}{dr_1}\right) + \rho^{(2)} \quad \frac{1}{A-1}\left[1-\frac{c_0}{A-1}e^{\frac{k_f^2}{5}|\vec{r}1-\vec{r}2|}\right]. \quad (6)$$
$$\rho^{(1)}(\vec{r}_1)\,\rho^{(1)}(\vec{r}_2)$$

The ground-state for a two-body charge density distribution, $\rho_{ch}^{(2)}(r)$, is given by the expected result for the functional two-body charge density distribution generator given in Eq. (6), which can be rewritten as

$$\rho_{ch}^{(2)}(r) = \sum_{i<j}\langle ij|\rho_{(r_i,r_j)}^{(2)}[|ij\rangle - |ji\rangle] \quad (7)$$

where $|ij\rangle$ is the two-particle wave function.

The root-mean-square charge radius for nuclei is based on the following relation:

$$\langle r^2\rangle^{1/2} = \frac{4\pi}{z}\int_0^\infty \rho_{ch}(r)\,r^4 dr \quad (8)$$

The ground-state charge density distribution can be utilized to compute the elastic electron-scattering form factors for spin-zero nuclei such as ^{28}Si and ^{32}S. All coming and scattered waves of electrons are approximated as plane waves according to the plane wave Born approximation (PWBA), where the ground-state charge density distribution is real and spherically symmetric. Consequently, the form factor is simply the Fourier transform of the ground-state charge density distribution [14, 15]:

$$F(q) = \frac{4\pi}{Z}\int_0^\infty \rho_o(\mathrm{r})\,j_0(qr)\,\mathrm{r}^2 d\mathrm{r} \quad (9)$$

where $\rho_{o\,(r)}$ $\rho_0(r)$ is the ground-state two-body charge density distribution defined in Eq. (7), and $j_0(qr) = \sin(qr)/(qr)$ $j_0(qr) = sin(qr)\ /(qr)$ is the zeroth order of the spherical Bessel function. Here, q represents the momentum transferred from the incident electron to the target nucleus. It is possible to express Eq. (9) as:

$$F(q) = \frac{4\pi}{qZ}\int_0^\infty \rho_o(\mathrm{r})\sin(qr)\,\mathrm{r}dr \quad (10)$$

The form of the factors of inelastic longitudinal electron scattering, which involves angular momentum J and momentum transfer, is expressed as [11]:

$$\left|F_J^L(q)\right|^2 = \frac{4\pi}{Z^2(2J_i+1)}\left|\left\langle f\left\|\hat{T}_J^L(q)\right\|i\right\rangle\right|^2 \left|F_{cm}(q)\right|^2\left|F_{fs}(q)\right|^2. \quad (11)$$

where $\hat{T}_J^L(q)$ $\hat{T}_J^L(q)$ is the longitudinal electron-scattering generator. Consequently, the form factors in Eq. (11) can be expressed in terms of matrix elements that are decreased in both angular momentum and isospin, as the nuclear states have clearly established isospin $T_{i/f}$ [16]. Alternatively:

$$\left|F_J^L(q)\right|^2 = \frac{4\pi}{Z^2(2J_i+1)}\left|\sum_{T=0,1}(-1)^{T_f-T_{z_f}}\begin{pmatrix} T_f & T & T_i \\ -T_{Z_f} & 0 & T_{Z_i}\end{pmatrix}\left\langle f\left\|\hat{T}_{JT}^L(q)\right\|i\right\rangle\right|^2 \left|F_{cm}(q)\right|^2\left|F_{fs}(q)\right|^2 \quad (12)$$
$$|F_{cm}(q)|^2|F_{fs}(q)|^2$$

where $T\,T$ is constrained by the subsequent selection rule:

$$\left|T_f - T_i\right| \le T \le T_f + T_i \quad (13)$$

with $T_z = (Z-N)/2$. The bracket $\begin{pmatrix} & & \\ & & \end{pmatrix}$ in Eq. (12) is the 3–*j* symbol. The decreased matrix elements in spin and isospin space of the longitudinal operator between the final and initial plurality of particle states of the structure, such as the arrangement of mixing, are expressed as a function of the one-body density matrix (OBDM) elements produced by the single-particle matrix elements of the longitudinal operator [17] as:

$$\left\langle f\left\|\hat{T}_{JT}^L\right\|i\right\rangle = \sum_{a,b} OBDM^{JT}(i,f,J,a,b)\left\langle b\left\|\hat{T}_{JT}^L\right\|a\right\rangle \quad (14)$$

Additionally, the longitudinal operator's numerous particle-reduced matrix components include two components: one for the model space and the other for the core polarization matrix element [18]. Thus:

$$\langle f\| \hat{T}_J^L(\tau_Z,q)\|i\rangle = \left\langle f\left\| \hat{T}_J^{L,ms}(\tau_Z,q)\right\| i\right\rangle + \left\langle f\left\| \hat{T}_J^{L,cor}(\tau_Z,q)\right\| i\right\rangle$$

$$\left\langle f\left\| \hat{T}_J^L(\tau_Z,q)\right\|i\right\rangle = \left\langle f\left\| \hat{T}_J^{L,ms}(\tau_Z,q)\right\| i\right\rangle + \left\langle f\left\| \hat{T}_J^{L,cor}(\tau_Z,q)\right\| i\right\rangle. \quad (15)$$

which is the model-space matrix element in Eq. (15), which can be written as

$$\left\langle f\left\| \hat{T}_J^{L,ms}(\tau_Z,q)\right\| i\right\rangle = e_i \int_0^\infty d\mathrm{r}\, \mathrm{r}^2 j_J(q\mathrm{r})\, \rho^{ms}_{J,\tau_Z}(i,f,\mathrm{r}) \quad (16)$$

The model-space transition density is $\rho_J^{ms}(i,f,r)$. This sum is calculated as the product of the OBDM and the single-particle matrix components, and it is denoted by [3]:

$$\rho^{ms}_{J,\tau_Z}(i,f,\mathrm{r}) = \sum_{jj'(ms)}^{ms} OBDM(i,f,J,j,j',\tau_z) \left\langle j\|\mathrm{Y}_J\|j'\right\rangle R_{nl}(\mathrm{r})\, R_{n'l'}(\mathrm{r}) \quad (17)$$

The core-polarization matrix element in Eq. (15) takes the following form [14, 15]:

$$\left\langle f\left\| \hat{T}_J^{L,cor}(\tau_Z,q)\right\| i\right\rangle = e_i \int_0^\infty d\mathrm{r}\, \mathrm{r}^2 j_J(q\mathrm{r})\, \rho^{core}_J(i,f,\mathrm{r}). \quad (18)$$

Here, ρ_J^{core} is the core-polarization transition density, which is contingent upon the model used for core polarization. To account for the effects of core polarization within the model space, the collective modes of the nuclei are represented by the core-polarization transition density, which complements the model-space transition density. The total transition density is calculated using:

$$\rho_{J\tau_Z}(i,f,\mathrm{r}) = \rho^{ms}_{J\tau_Z}(i,f,\mathrm{r}) + \rho^{core}_{J\tau_Z}(i,f,\mathrm{r}) \quad (19)$$

The core-polarization transition density is determined by the Tassie form, as per the collective modes of nuclei [19]:

$$\rho^{core}_{Jt_z}(i,f,\mathrm{r}) = \mathrm{N}\frac{1}{2}(1+\tau_z)\,\mathrm{r}^{J-1}\frac{d\rho_o(i,f,\mathrm{r})}{d\mathrm{r}} \quad (20)$$

which represents the base state two-body charge density distribution, as expressed in Eq. (6), and includes a proportionality constant N. The Coulomb form factor for this model is as follows [18]:

$$F_J^L(q) = \sqrt{\frac{4\pi}{2J_i+1}}\ \frac{1}{Z}\left\{\int_0^\infty \mathrm{r}^2 j_J(q\mathrm{r})\ \rho_J^{ms}(i,f,\mathrm{r})\ d\mathrm{r} + N\int_0^\infty d\mathrm{r}\,\mathrm{r}^2\, j_J(q\mathrm{r})\,\mathrm{r}^{J-1}\ \frac{d\rho_o(i,f,r)}{d\mathrm{r}}\right\} F_{cm}(q)\ F_{fs}(q) \quad (21)$$

The radial integral $\int_0^\infty d\mathrm{r}\ \mathrm{r}^{J+1} j_J(q\mathrm{r})\frac{d\rho_o(i,f,\mathrm{r})}{d\mathrm{r}}$ can be expressed as:

$$\int_0^\infty \frac{d}{d\mathrm{r}}\left\{\mathrm{r}^{J+1} j_J(q\mathrm{r})\,\rho_o(i,f,\mathrm{r})\right\}d\mathrm{r} - \int_0^\infty d\mathrm{r}\ (J+1)\mathrm{r}^J j_J(q\mathrm{r})\rho_o(i,f,\mathrm{r}) - \int_0^\infty d\mathrm{r}\ \mathrm{r}^{J+1}\frac{d}{d\mathrm{r}} j_J(q\mathrm{r})\rho_o(i,f,\mathrm{r}). \quad (22)$$

In Eq. (22), the initial term contributes zero, while the second and third terms can be joined to give:

$$-q\int_0^\infty d\mathrm{r}\,\mathrm{r}^{J+1}\rho_o(i,f,\mathrm{r})\left[\frac{d}{d(q\mathrm{r})}+\frac{J+1}{q\mathrm{r}}\right] j_J(q\mathrm{r}) \quad (23)$$

Based on the recursion link of the spherical Bessel function [19]:

$$\left[\frac{d}{d(q\mathrm{r})}+\frac{J+1}{q\mathrm{r}}\right] j_J(q\mathrm{r}) = j_{J-1}(q\mathrm{r}) \quad (24)$$

Hence,

$$\int_0^\infty d\mathrm{r}\ \mathrm{r}^{J+1} j_J(q\mathrm{r})\frac{d\rho_o(i,f,\mathrm{r})}{d\mathrm{r}} = -q\int_0^\infty d\mathrm{r}\,\mathrm{r}^{J+1}\ j_{J-1}(qr)\rho_o(i,f,\mathrm{r}) \quad (25)$$

Using Eqs. (21)-(25), the form factor may have the form:

$$F_J^L(q) = \left(\frac{4\pi}{2J_i+1}\right)^{1/2}\frac{1}{Z}\left\{\begin{array}{l}\int_0^\infty \mathrm{r}^2 j_J(q\mathrm{r})\,\rho^{ms}_{Jt_z}\,d\mathrm{r} - \\ \mathrm{N}q\int_0^\infty d\mathrm{r}\,\mathrm{r}^{J+1}\rho_o(i,f,r)\, j_{J-1}(q\mathrm{r})\end{array}\right\} F_{cm}(q)\,F_{fs}(q) \quad (26)$$

The constant of proportionality N may be identified by evaluating the form of the factor for $q=k$, resulting in the following expression:

$$N=\frac{\int_0^\infty d\mathrm{r}^2 j_J(k\mathrm{r})\rho^{ms}_{J_{T_Z}}(i,f,\mathrm{r})-F_J^L(k)Z\sqrt{\frac{2J_i+1}{4\pi}}}{k\int_0^\infty d\mathrm{r}\,\mathrm{r}^{J+1}\rho_o(i,f,\mathrm{r})j_{J-1}(k\mathrm{r})} \quad (27)$$

The transition amplitude for photon interaction at $q=k$, $B(CJ)$ as:

$$B(CJ)=\frac{[(2J+1)!!]^2\,Z^2\,e^2}{4\pi\,k^{2J}}\left|F_J^L(k)\right|^2 \quad (28)$$

The transitional amplitude $B(CJ)$ is correlated with its form factor.

$$N=\frac{\int_0^\infty dr r^2 j_J(kr)\rho^{ms}_{J_{T_z}}(i,f,r)-\sqrt{\frac{(2J_i+1)B(CJ)}{(2J+1)!!}}k^J}{k\int_0^\infty dr r^{J+1}\rho_o(i,f,r)j_{J-1}(kr)} \quad (29)$$

This is the coefficient of proportionality for open (closed) shell nuclei, which can be established by incorporating the measured reduced transitional amplitude $B(CJ)$ using Eq. (29).

3. Results and Discussion

Figures 1 and 2 illustrate the ground state charge density distributions (in fm^{-3}) in relation to r (in fm) for ^{28}Si and ^{32}S nuclei, respectively. Spreadsheet (1) contains all the parameters necessary for the calculations, including the dimension parameter of the harmonic oscillator (b). The occupancy probabilities (η_{nlj}) of the states are shown in Figs. (1) and (2), which illustrate the charge density distribution. The blue dash is the one-body charge density distribution without correction which depends on Eq. (1), the solid blue line is the two-body charge density distribution, while the black (•) "dotted symbols" are the measured data [20, 21], in units of (fm^{-3}).

Spreadsheet (1) summarizes the variables and parameters employed in the present calculations.

TABLE 1. Spreadsheet (1) of parameters used in the calculation.

^{32}S	^{28}Si	Nuclei
1.91	1.644	b
0.315	0.329	$\alpha^2\,(fm^{-2})$
1	1	$\eta_{1s_{\frac{1}{2}}}$
1	1	$\eta_{1p_{\frac{3}{2}}}$
1	1	$\eta_{1p_{\frac{1}{2}}}$
1	0.8333	$\eta_{1d_{\frac{5}{2}}}$
0.5	0.5	$\eta_{2s_{\frac{1}{2}}}$
0.25	0	$\eta_{1d_{\frac{3}{2}}}$
3.282	3.14	$\langle \mathrm{r}^2\rangle^{1/2}_{\mathrm{theo.}}$
3.239	3.085	$\langle \mathrm{r}^2\rangle^{1/2}_{\mathrm{exp.}}$ [20]

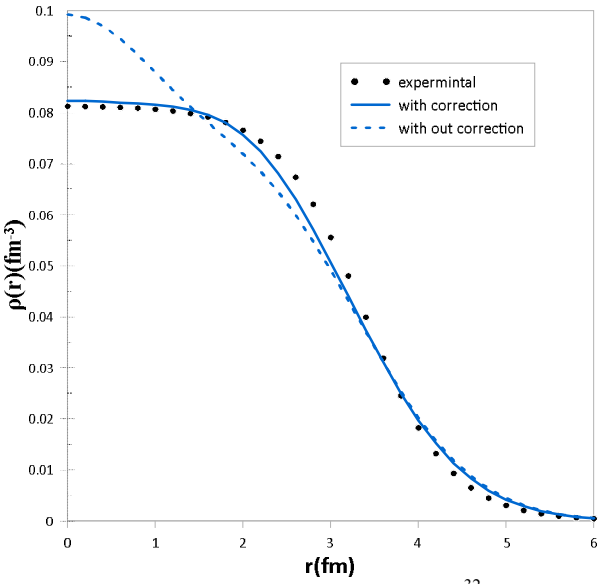

FIG. 2. Charge density distribution for the ^{32}S nucleus.

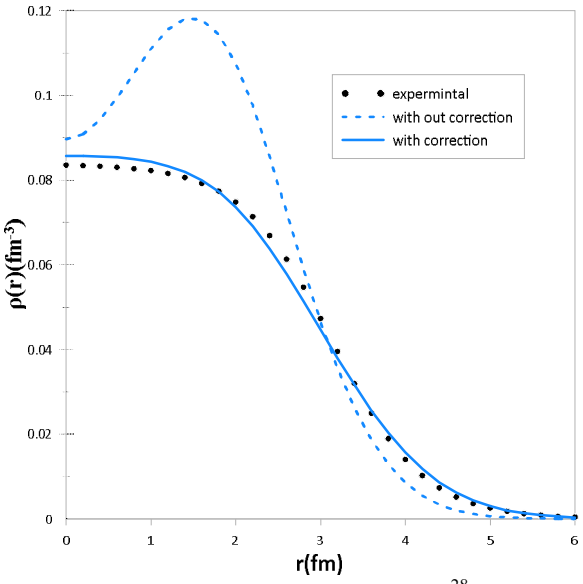

FIG. 1. Charge density distribution for the ^{28}Si nucleus.

As shown in Figs. 1 and 2, the theoretical results exhibit very good agreement with experimental data compared to the two-body charge density distribution in the region 0.5<r <2.5 due to the reduction of the hard-core effects in two-body correlations (center of mass and Pauli pair correlations). The comparison between the one-body and two-body charge density distributions demonstrates that the two-body formulation (solid line) provides a significantly better fit to the experimental data within this region.

The calculated elastic electron scattering form factors F(q) are plotted in Figs. 3 and 4, the calculated F(q)'s are limited to those of experimental data for the ^{28}Si and ^{32}S nuclei, where the blue dash is the elastic form factors without correction using Eqs. (1) and (10). The solid blue line is the two-body elastic form factors with the correction using Eqs. (7) and (10). The black (•) "dotted symbols" are the experimental data in these figures. The calculated F(q)'s are plotted as a function of q, as shown in Figs. 3 and 4. When the two-body charge density distribution is included, a second diffraction minimum appears at q = 2.4, consistent with the experimental observations. This indicates that incorporating two-body correlations yields results that closely match the measured elastic form factors.

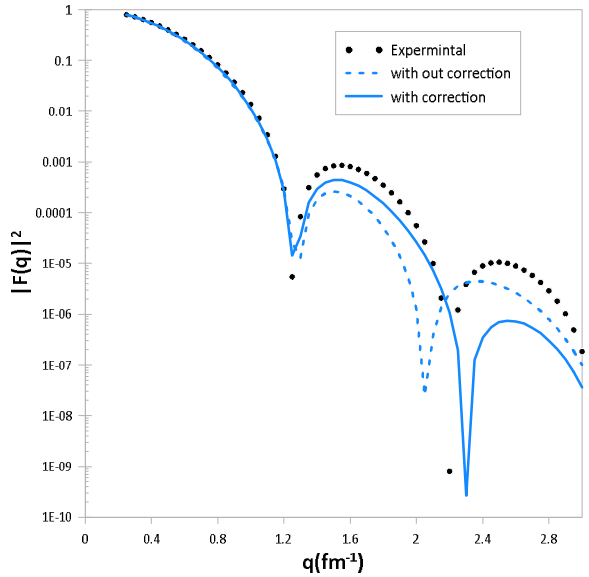

FIG. 4. The elastic form factors for the ^{32}S nucleus.

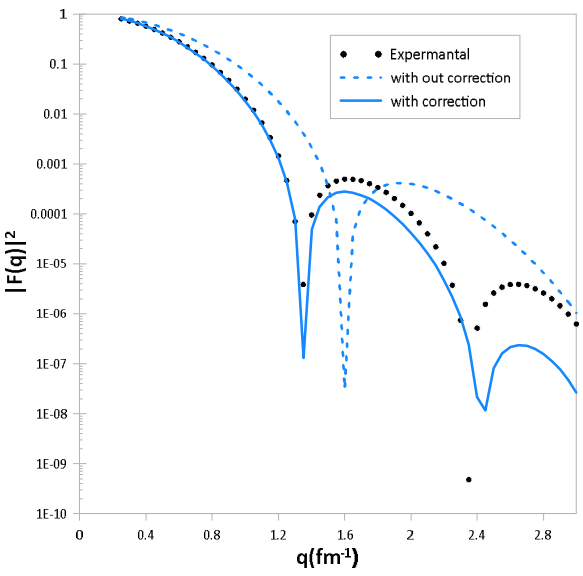

FIG. 3. The elastic form factors for the ^{28}Si nucleus.

A formula for the transition charge density given in Eq. (19) was employed to determine the inelastic longitudinal electron-scattering form factors F(q). The OXBASH code was used to calculate OBDM elements required for evaluating the form factors of open-shell nuclei. The model-space transition density was determined using Eq. (17) [22], with the interaction matrix elements taken from the USDB (Universal sd-shell B) interaction for 2s-1d shell nuclei [23]. The theoretical determination of the proportionality constant N does not involve any adjustable parameters. In this section, the computed longitudinal Coulomb C2 form factors are presented as functions of the momentum transfer q for the transitions with an observed Ex = 1.78MeV [24] and experimental value of B(C2) = 415 $e^2.fm^4$ for ^{28}Si, and observed Ex = 2.237 MeV [25] with an experimental value of B(C2) = 235 $e^2.fm^4$ for ^{32}S.

Figures 5 and 6 illustrate the calculated and experimental results. The blue dashed curves represent the model-space contributions, which include configuration mixing. The blue dash-dotted curves correspond to the core-polarization contributions, which account for two-body effects. The solid blue curves show the total calculated form factors obtained by combining the model-space and core-polarization components. The experimental data are shown as black dotted symbols (•). The results demonstrate that the experimental data cannot be reproduced using the model-space contributions alone, as these underestimate the measured values across the full momentum transfer range. However, when both the model-space effects and the core-polarization contributions are included, the calculated longitudinal C2 form factors show excellent agreement with the experimental data for all momentum transfer values q.

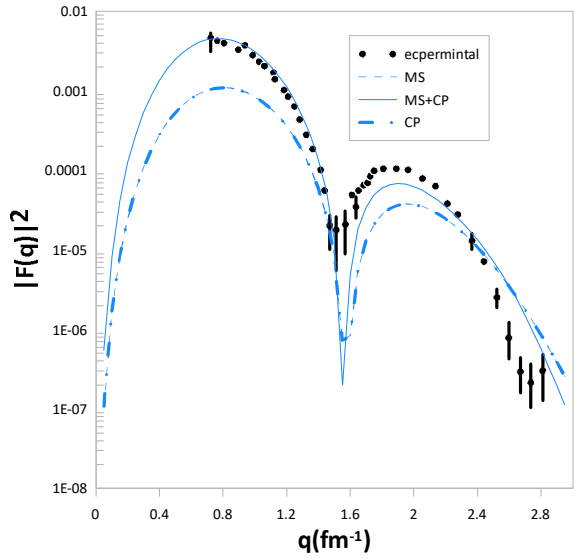

FIG. 6. The inelastic longitudinal C2 form factors for the ^{32}S nucleus.

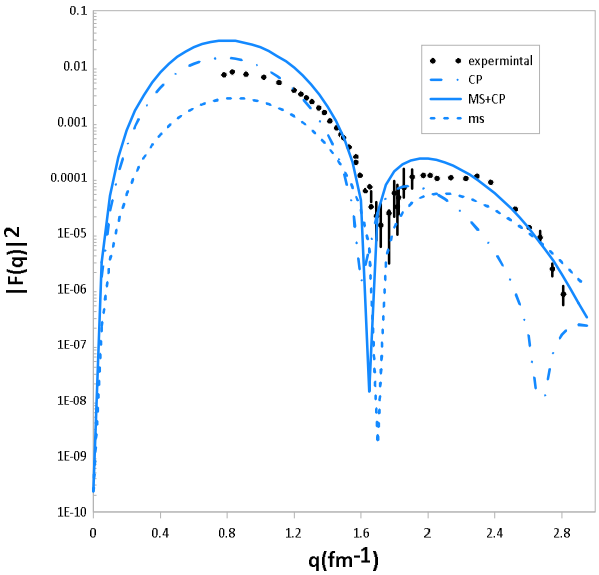

FIG. 5. The inelastic longitudinal C2 form factors for the ^{28}Si nucleus.

Figure 7 illustrates the inelastic longitudinal Coulomb C4 form factors of the ^{28}Si nucleus. The calculated longitudinal Coulomb C4 form factors are depicted in relation to the momentum transfer q for the transitions with an observed excitation energy of 4.617 MeV. The experimental B(C4) of the above nuclei is 27 500 e^2fm^4 [24]. In this figure, the blue dashed shapes symbolize the influence of the model space in ^{28}Si, adjusted for configuration mixing. The blue dash-dotted shape symbolizes the core polarization investment, which is adjusted for the effect of two bodies. The solid blue shape symbolizes the overall investment, obtained by combining the model-space and core-polarization contributions for ^{28}Si.

Figure 8 illustrates the inelastic longitudinal Coulomb C2 and C4 form factors of the ^{32}S nucleus. The calculated longitudinal C2 and C4 form factors are depicted in relation to the momentum transfer q for the transitions. For the $0^+ \rightarrow 2_2^+$ and $0^+ \rightarrow 4_1^+$ for ^{32}S with observed excitation energies of 4.282 MeV and 4.46 MeV, respectively. The experimental values of B(C2) and B(C4) of the above nuclei are 68.8, 50700 (e^2fm^4) [25]. In this figure, the blue dash shapes symbolize the influence of the C2, the blue dash-

dotted shapes symbolize C4, which includes both contributions of the model space and core polarization effect, adjusted for the effect of two bodies. The blue solid shapes symbolize the overall investigated data, calculated by combining the C2 and C4 for ^{32}S. The black (•) "dotted symbols" are the experimental data. These figures demonstrate that the model-space contribution alone cannot accurately reproduce the experimental data across the full range of momentum transfer q. However, when the effects of core polarization are incorporated, the calculated longitudinal Coulomb C4 form factors show good agreement with the experimental data throughout the entire momentum transfer range, as indicated by the solid curves.

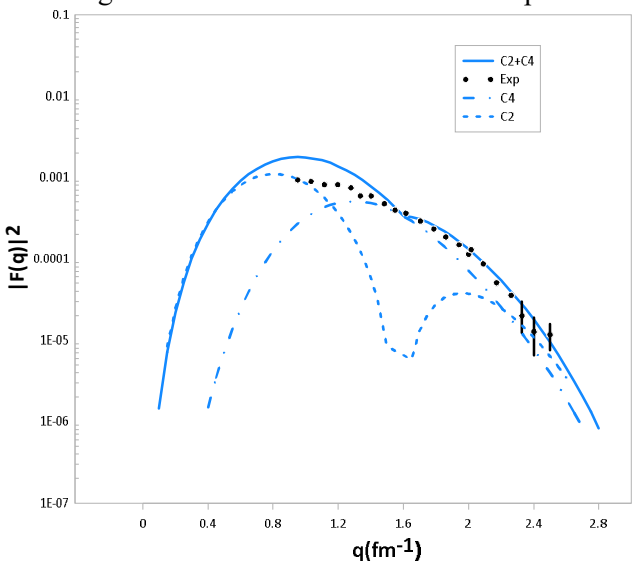

FIG. 8. Illustration of the inelastic longitudinal (C2+C4) form factors For ^{32}S nucleus.

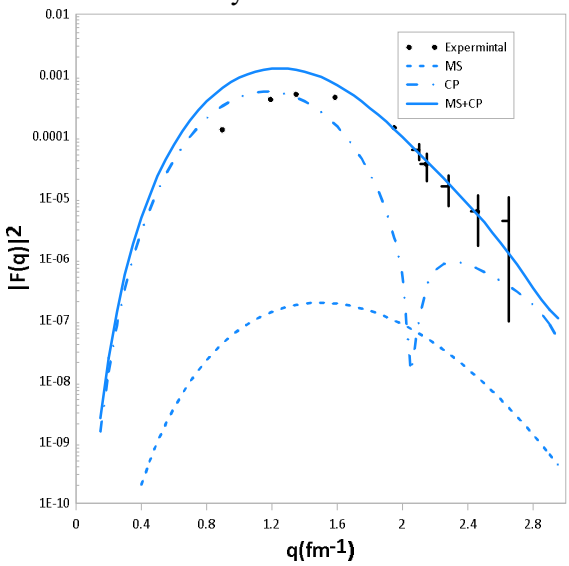

FIG. 7. Illustration of the inelastic longitudinal C4 form factors For ^{28}Si nucleus.

4. Conclusions

Based on the obtained results, we draw the following conclusions:

1. Considering the effects of the center of mass, Pauli pair correlation functions, and higher occupation probabilities is generally crucial to achieving strong agreement between the calculated charge density distributions and the experimental data for the ^{28}Si and ^{32}S nuclei.
2. The fixed characteristics and energy levels can be accurately described by the sd-shell models. However, these models are less effective in characterizing dynamical characteristics, including the rates of C2 and C4 transitions and the form factors of electron scattering.
3. The core-polarization impact improves the form factors and brings the mathematical predictions of the longitudinal form factors closer to the experimental data in the C2 and C4 transitions, which is the subject of this study.

References

[1] de Forest, T. and Walecka, J.D., Adv. Phys., 15 (1966) 1.

[2] Walecka, J.D., Nucl. Phys. A, 574 (1994) 271.

[3] Brown, B.A., Radhi, R., and Wildenthal, B.H., Phys. Rep., 101 (5) (1983) 313.

[4] Radhi, R.A., Alzubadi, A.A., and Rashed, E.M., Nucl. Phys. A, 947 (2016) 12.

[5] Mahmood, L.A. and Flaiyh, G.N., Iraqi J. Sci., 57 (2016) 1742.

[6] Mahmood, L.A. and Flaiyh, G.N., Iraqi J. Phys., 14 (2016) 129.

[7] Sarriguren, P. and Merino, D., Phys. Rev. C, 99 (2019) 034325.

[8] Al-Rahmani, A.A., Fadhil, S.N., and Hamoudi, A.K., Iraqi J. Sci., 22 (2024) 1357.

[9] Flaiyh, G.N. and Sharrad, F.I., Iran. J. Sci. Technol., Trans. A: Sci., 42 (2018) 2323.

[10] Ahmad, I., J. Phys. G: Nucl. Part. Phys., 20 (3) (1994) 507.

[11] Bergstrom, J., Kowalski, S., and Neuhausen, R., Phys. Rev. C, 25 (1982) 1156.

[12] Brown, B.A., Wildenthal, B.H., Williamson, C.F., Rad, F.N., Kowalski, S., Crannell, H., and O'Brien, J.T., Phys. Rev. C, 32 (1985) 1127.

[13] Ahmad, I. and Auger, J.P., Nucl. Phys. A, 352 (1981) 425.

[14] Benson, H.G. and Flowers, B.H., Nucl. Phys. A, 126 (1969) 305.

[15] Walecka, J.D., "Electron Scattering for Nuclear and Nucleon Structure", (Cambridge University Press, Cambridge, 2001).

[16] Donnelly, T.W. and Sick, I., Rev. Mod. Phys., 56 (1984) 461.

[17] Brussard, P.J. and Glaudemans, P.W.M., "Shell-Model applications in Nuclear Spectroscopy", (North Holland, Amesterdam, 1977).

[18] Tassie, L.J., Aust. J. Phys., 9 (1956) 407.

[19] Hassani, S., "Mathematical Physics: A Modern Introduction to Its Foundations", 2nd Ed., (Cham: Springer International Publishing, 2013), chapter 15, p.482.

[20] De Vries, H., De Jager, C.W., and De Vries, C., At. Data Nucl. Data Tables, 36 (1987) 495.

[21] Fricke, G., Bernhardt, C., Heilig, K., Schaller, L.A., Schellenberg, L., Shera, E.B., and Dejager, C.W., At. Data Nucl. Data Tables, 60 (1995) 177.

[22] Brown, B.A., Et Chegoyen, A., Godwin, N.S., Rae, W.D.M., Richter, W.A., Warburton, W.E., Winfield, J.S., Zhao, L., and Zimmerman, C.H., MSU- NSCL Rep. No. 1289, (2005).

[23] Brown, B.A. and Richter, W.A., Phys. Rev. C, 74 (2006) 34315.

[24] Li, G.C., Yearian, M.R., and Sick, I., Phys. Rev. C, 9 (1974) 1861.

[25] Wildenthal, B.H., Brown, B.A., and Sick, I., Physical Review C, 32 (1985) 2185.

Volume 18, Number 4, 2025. pp. 477-488

Jordan Journal of Physics

ARTICLE

Effect of Annealing Temperature on the Properties of Cu_2ZnSnS_4 (CZTS) Thin Films for Solar Cell Application

Akintunde A. Ajayi[a], Aderemi B. Alabi[b], Enoch D. Ogunmola[a], Ayodeji O. Salau[c,g], Samson I. Akinsola[b], Olutayo W. Abodunrin[a], Olukunle C. Olawole[e], Folasade O. Oluyemi[d], Kazeem A. Musiliyu[a] and **Funmilayo H. Abejide[f]**

[a] *Department of Mathematical and Physical Sciences, Afe Babalola University, Ado-Ekiti, Nigeria.*

[b] *Department of Physics, University of Ilorin, Ilorin, Nigeria.*

[c] *Department of Electrical and Computer Engineering, Afe Babalola University, Ado-Ekiti, Nigeria.*

[d] *Department of Science Technology, Federal Polytechnic, Ado-Ekiti, Nigeria.*

[e] *Department of Physics, Covenant University, Ota, Nigeria.*

[f] *Department of Physics, Joseph Ayo Babalola University, Arakeji, Nigeria.*

[g] *Saveetha School of Engineering, Saveetha Institute of Medical and Technical Sciences, Chennai, Tamil Nadu, India.*

Doi: **https://doi.org/10.47011/18.4.6**

Received on: 16/06/2024; *Accepted on: 04/09/2024*

Abstract: In this paper, a CZTS precursor solution was prepared using ethylene glycol, and CZTS thin films were synthesized by spraying the solution on heated substrates. The effects of annealing temperature on structural, optical, and electrical properties of the sprayed CZTS thin films were studied. XRD studies revealed a wurtzite-structured CZTS thin film at an annealing temperature of 450 °C, while images obtained from SEM showed a homogeneous and agglomerated surface at the same temperature. UV-Vis spectroscopic studies revealed increasing absorbance with an increase in wavelength and a bandgap of 1.5 eV at 450 °C. Electrical studies showed the lowest resistivity at 450 °C, and a conversion efficiency of 0.12% was obtained from a spray-fabricated CZTS absorber-based thin-film solar cell with the configuration glass/ITO/i:ZnO/n:ZnS/p:CZTS/Ag.

Keywords: CZTS, Spray pyrolysis, Annealing, Structural properties, Optical properties, Electrical properties.

1. Introduction

Thin-film solar cells have been considered as alternatives to silicon-based solar cells because relatively fewer materials are required for their fabrication [1]. In a thin-film solar cell, sunlight generates electron-hole pairs in the semiconductor material. These pairs are separated by an electric field created by a junction or doping. Electrons are collected at the bottom electrode, while holes are collected at the top. The collected carriers flow through an external circuit, generating an electric current for powering devices or storage. It should be noted that although nanocrystalline silicon thin films, which can find applications in solar cells, have been developed [25], the abundance of silicon in the Earth's crust may be threatened by its present rate of consumption [26]. Some organic-inorganic hybrid nanomaterials have been explored as alternatives to silicon [27-29], but this class of semiconductor material suffers from

Corresponding Author: Akintunde Ayodeji Ajayi **Email**: ayodejiajayijp@gmail.com

instability in the form of degradation over time due to the interactions between the organic and inorganic components or environmental factors. Moreover, their synthesis is often complex, requiring precise control over the interactions between organic and inorganic components. Copper indium gallium selenide (CIGS) and cadmium telluride (CdTe) are thin-film solar cells that have achieved commercial success. However, the indium constituent in CIGS is a rare earth element and, as a consequence, has a negative impact on the affordability of CIGS solar cells. At the same time, cadmium's carcinogenic nature raises concerns about the environmental and health effects of decommissioned CdTe solar cells [3]. Copper zinc tin sulfide (CZTS) is a suitable alternative due to the abundance of copper, zinc, tin, and sulfur in the Earth's crust. CZTS has a high absorption coefficient ($> 10^{-4}$ cm^{-1}) and a direct bandgap of 1.5 eV [4]. The theoretical conversion efficiency of the CZTS absorber-based solar cell has been calculated to be above 30%. Highly efficient CZTS absorber-based solar cells have been created through physical techniques. Nevertheless, the inclusion of vacuum equipment in this deposition process raises the market cost of the final product in the event of commercialization [5, 6].

Chemical or solution-based techniques are alternatives to physical techniques in terms of cost. The most successful CZTS solar cells to date have typically employed cadmium sulfide (CdS) as the n-type junction material or incorporated cadmium into the absorber layer [7], and a solution other than water has been used as a solvent in the case of a solution-based fabrication process. The CZTS solar cell with the present highest efficiency (12.6%) was fabricated using a solution-based technique with hydrazine employed as the solvent [8]. Hydrazine is an explosive and toxic material, and its use in commercial fabrication of CZTS solar cells will lead to extra costs due to stringent safety and handling requirements [9]. Developing a cadmium-free CZTS solar cell using both physical and chemical techniques can be challenging in terms of cost and safety. Patel and Gohel [10] investigated the effects of different solvents on the properties of CZTS thin films and found that films synthesized using ethylene glycol and propylene glycol exhibited superior characteristics. Recent studies on the influence of annealing temperature on CZTS thin films have shown that their structural, optical, morphological, and electrical properties improve with increasing annealing temperatures between 250 °C and 550 °C. Olgar *et al*. [11] synthesized CZTS thin films via magnetron sputtering and reported enhanced film properties, achieving optimal solar cell performance at 550 °C. Electrical and back-contact studies of metal/CZTS/ZnS/ZnO/FTO heterojunction devices fabricated by spray pyrolysis were conducted by Boutebakh *et al*. [36]. Their results revealed rectifying behavior in CZTS/ZnS structures for all tested back contacts, with gold (Au) exhibiting the best rectification and the highest ideality factor. These findings highlight the strong potential for developing cadmium-free CZTS-based devices capable of efficient power generation. This research addresses a significant gap in current knowledge regarding the synthesis and characterization of copper zinc tin sulfide (CZTS) thin films for solar cell applications. Despite the promising attributes of CZTS, comprehensive studies on the combined effects of solvent choice, annealing temperature, and the resulting structural, optical, morphological, and electrical properties of CZTS thin films prepared by spray pyrolysis are limited.

In our study, we utilized ethylene glycol as a solvent to synthesize CZTS thin films via spray pyrolysis and systematically examined the effects of annealing temperature on their structural, optical, morphological, and electrical properties. Our objective was to enhance understanding of how synthesis parameters influence CZTS thin-film solar cell performance, with particular emphasis on achieving improved efficiency and device characteristics for cadmium-free CZTS absorber-based solar cells.

The major contributions of this paper are summarized as follows:

i. **Methodological Advancement**: We employed ethylene glycol as a solvent for CZTS thin-film synthesis, providing a cost-effective and environmentally friendly alternative to conventional solvents. The deposition technique used is simple, scalable, and economical. Furthermore, our systematic investigation of annealing temperatures offers valuable insights into optimizing the fabrication process of CZTS thin-film solar cells.

ii. **Practical Implications**: The insights gained from our research can inform the

development of more efficient and affordable CZTS thin-film solar cells, thereby supporting the advancement of renewable energy technologies. By elucidating the relationships between synthesis parameters and material properties, this work lays the foundation for future research aimed at the commercialization of CZTS-based photovoltaic devices.

2. Materials and Methods

A precursor solution containing 0.035 M copper, 0.025 M zinc, 0.025 M tin, and 0.2 M sulfur salts was prepared for deposition on thoroughly cleaned substrates. The precursor salts used in preparing the CZTS solution are copper (II) acetate ($C_4H_6CuO_4$), zinc acetate dihydrate ($Zn(CH_3CO_2)_2.2H2O$, tin (IV) chloride pentahydrate ($SnCl_2.5H_2O$), and thiourea ($SC(NH_2)_2$), serving as the sources of copper, zinc, tin, and sulfur, respectively. A precursor of 0.015 M copper acetate was also prepared. The solvents used are deionized water and ethane-1,2-diol ($(CH_2OH)_2$), also known as ethylene glycol. All reagents were analytical grade and purchased from Sigma-Aldrich. The as-prepared precursor mixture was stirred for 1 hour using a magnetic stirrer. The concentration of thiourea was higher in order to maintain stochiometry and compensate for the loss of sulfur during pyrolysis. The CZTS precursor solution was deposited on clean glass and indium tin oxide (ITO) substrates using the spray pyrolysis technique, with the substrate surface maintained at 350 °C. The resulting CZTS thin films were annealed in a muffle furnace at temperatures of 250 °C, 350 °C, and 450 °C, and labeled samples A25, A35, and A45, respectively.

A heterojunction solar cell was fabricated using optimized CZTS and ZnS thin-film layers. A glass/ITO/iZnO/n-ZnS/p-CZTS/Ag solar cell configuration was employed in the layering process. The zinc oxide anti-reflective window layer was synthesized by spraying zinc acetate solution onto ITO-coated glass substrates in open air and annealed at 350 °C for 1 hour. This was followed by the spraying of ZnS precursor solution on the annealed ZnO anti-reflective layer and annealing of the ZnS layer at 350 °C. The p-CZTS thin-film layer was obtained by spraying the CZTS precursor onto the annealed n-ZnS layer. The p-CZTS layer was annealed at 450 °C. Silver (Ag) was used as the back contact for the cell. Colloidal silver was purchased from Sigma-Aldrich.

The structural characterization of the specimens was carried out with the aid of a Rigaku D/Max-IIIC x-ray diffractometer with a LynxEye detector using a copper target (Cuα,1.5418 Å). All x-ray diffraction (XRD) data for the samples were recorded at current and acceleration voltages of 25mA and 40 kV, respectively. Morphological and grain growth analysis of the specimen was carried out by using a Hitachi scanning electron microscope (SEM), and optical characterization was done using a CyberLab UV-vis spectrophotometer (model UV-100). Film thickness measurements were carried out using a Veeco Dektak surface profilometer. The chemical composition of the samples was studied using the energy dispersive X-ray (EDX) analysis method. Electrical characterization was carried out using the four-point probe method. The equipment employed was a Holmarc solar simulator and a Keithley source meter (Model HO-SCIVK) with indium used as the ohmic contact and with a 300 W xenon lamp. The same Keithley source meter was used to determine the current-voltage (I-V) characteristics of fabricated solar cell devices. The devices were illuminated under strong white light.

3. Results and Discussion

3.1 Structural Properties

The XRD pattern of A-25 is shown in Fig. 1, where diffraction peaks of kesterite CZTS can be observed at 2θ values of 23.00^0, 42.90^0, and 76.29^0, which can be indexed to (110), (200), and (332) reflection planes (JCPDS 26-0575). Secondary phases that can be indexed to the hexagonal plane of ZnS at $2\theta = 48.2^0$ and also ZnO at $2\theta = 67.30^0$ were observed.

The XRD pattern of A35 is shown in Fig. 2. Diffraction peaks of wurzite-phased CZTS corresponding to (100), (202), (220), and (008) reflection planes can be seen at 26.50^0, 37.35^0, 47.54^0, and 69.43^0, which are respective values of 2θ. There is no standard JCPDS card for wurzite CZTS. The crystal structure of wurtzite Cu_2ZnSnS_4 (CZTS) can be derived by substituting Zn(II) ions with Cu(I), while maintaining the Zn(II) and Sn(IV) positions in the wurtzite ZnS structure. In this structure, each sulfur ion is coordinated with two Cu(I) ions,

one Zn(II) ion, and one Sn(IV) ion, satisfying the octet rule [(8/4)+6=8]. It's important to note that in this model, the distribution of metal cations occurs randomly within the fixed framework formed by sulfur anions. Consequently, the XRD pattern of wurtzite CZTS remains largely similar to that of wurtzite ZnS [12]. Peaks corresponding to ZnS and ZnO impurities can be observed at 2θ equals 30.2^0 and 62.60^0, respectively. The XRD of A45 is shown in Fig. 3 with diffraction peaks at 2θ equals 26.97°, 37.41°, 47.50°, 69.81°, and 76.50°, which can be indexed to the (100), (202), (220), (008), and (332) reflection planes of wurzite-phased CZTS. While the solvent may have indirectly influenced the annealing process kinetics, the crystal structure phase transition from kesterite to wurzite is likely attributed to faster crystal growth facilitated by high thermal energy. These results are in agreement with Lu *et al.* [12] and Touati *et al.* [13]. The higher peak intensity observed in sample A25 may be due to the presence of a larger number of smaller crystallites in the film annealed at 250 °C. These small grains can contribute to a higher number of diffracting planes that align with the X-ray beam. As the annealing temperature increases, the additional thermal energy promotes grain growth and reorganization. Larger grains may form, leading to fewer grain boundaries and a more ordered crystalline structure. However, fewer grains align in the optimal orientation for diffraction, leading to a decrease in peak intensity. The crystallite sizes were calculated from the FWHM of the (110) orientation for sample A25 and (110) for A35 and A45. The crystallite sizes were 13.46 nm, 21.46 nm, and 45.10 nm. The results indicated that a better crystallinity is obtained at an annealing temperature of 450 °C. The crystallite sizes were calculated using Eq. (1):

$$D = \frac{0.9\lambda}{\beta\cos\theta} \quad (1)$$

where λ is the wavelength of the used X-ray beam (1.54 Å), β is the full width at half maximum, and θ is the angle of diffraction. The microstructural strain (ε) is calculated using Eq. (2), and the values obtained at different annealing temperatures are shown in Tables 1, 2, and 3.

$$\varepsilon = \frac{\beta cos\theta}{4} \quad (2)$$

Thermal expansion of CZTS thin films and substrates upon heat treatment can be correlated to strain in the films [12]. Calculation of strain for annealed CZTS thin films showed a reduction with an increase in annealing temperature. Dislocation density, which is the measure of linear crystallographic defects within the crystal structure, was calculated for annealed CZTS films using Eq. (3).

$$\delta = \frac{n}{D^2} \quad (3)$$

where D is the crystallite size and n is unity when the dislocation density is minimum. The values of the microstructural strain and dislocation density are shown in Table 1. The lowest microstructural strain can be observed in specimen A45.

TABLE 1. Details of the structural analysis of annealed CZTS thin film specimens.

Specimen	Crystallite Size (nm)	Micro strain (ε) x 10^{-3}	Dislocation density δ (lines/m^2) x 10^{15}
A25	13.46	2.77	5.52
A35	21.46	1.61	2.17
A45	45.10	0.78	0.49

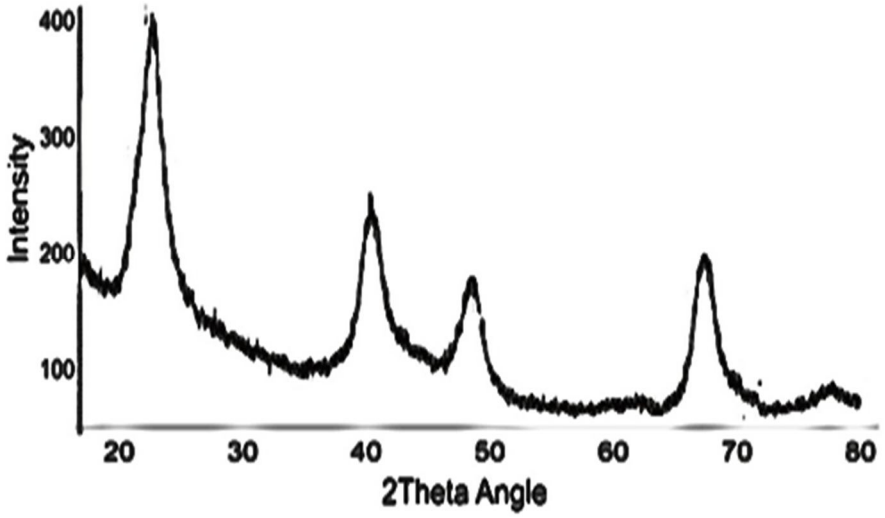

FIG. 1. X-ray diffraction pattern of CZTS thin films annealed at 250 °C (specimen A25).

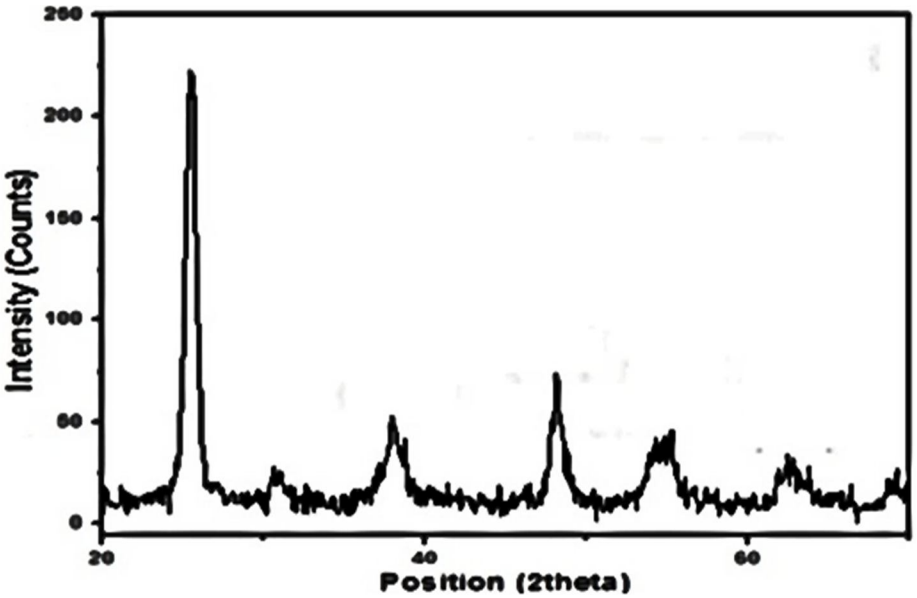

FIG. 2. X-ray diffraction pattern of CZTS thin films annealed at 350 °C (specimen A35).

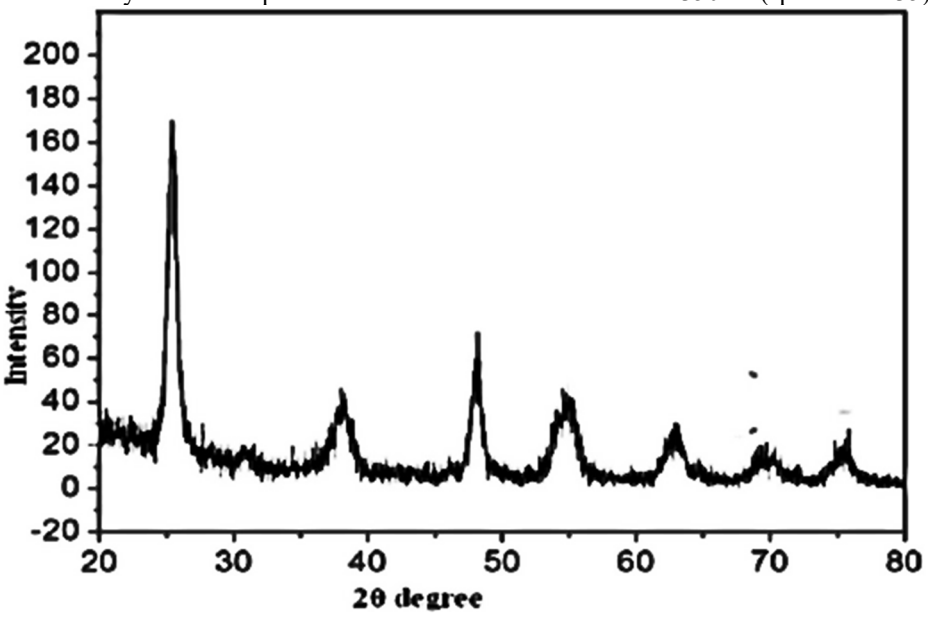

FIG. 3. X-ray diffraction pattern of CZTS thin films annealed at 450 °C (specimen A45).

3.2 Optical Properties

Figures 4 and 5 show the plots of the absorbance and transmittance versus wavelength. The highest absorbance and the lowest transmittance within the ultraviolet-visible region can be observed in A35 and A45, although the absorbance of A45 surpasses that of A35 around 550 nm wavelength. Phase change from kesterite to wurzite at 450 °C and surface roughness at that temperature may have been responsible for the increase in absorbance of A45 with increasing wavelength. The lowest absorbance and highest transmittance can be observed in A25. A good solar cell absorber material must have higher absorbance and low transmittance, and these results have demonstrated that a very efficient CZTS absorber material can be obtained at annealing temperatures of 350 °C and 450 °C. The Tauc plots are shown in Fig. 6 for A25, A35, and A45. It can be observed from the $(\alpha hf)^2$ versus hf plot that the band gap values of CZTS thin films decrease with annealing temperature. A45 has a band gap of 1.48 eV, which is almost equal to the ideal band gap of CZTS, while band gaps of 1.80 eV and 1.93 eV were obtained for A35 and A25, respectively. These results are in agreement with recent works [14, 15]. An explanation for the decrease in band gap with increasing annealing temperature in A45 is the quantum confinement effect. Quantum confinement effect is observed when crystallite size is approaching the de Broglie wavelength of an electron, and an increase in band gap has been correlated to greater quantum confinement of the grains [14].

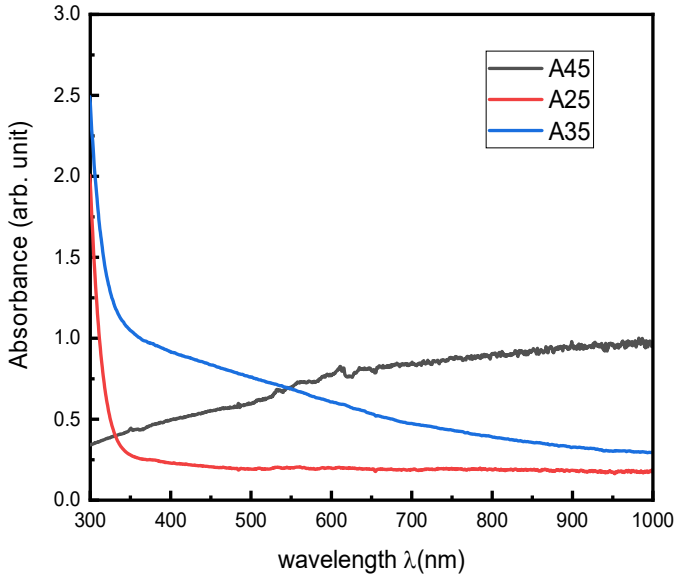

FIG. 4. Absorbance spectra of CZTS thin films with annealing temperatures.

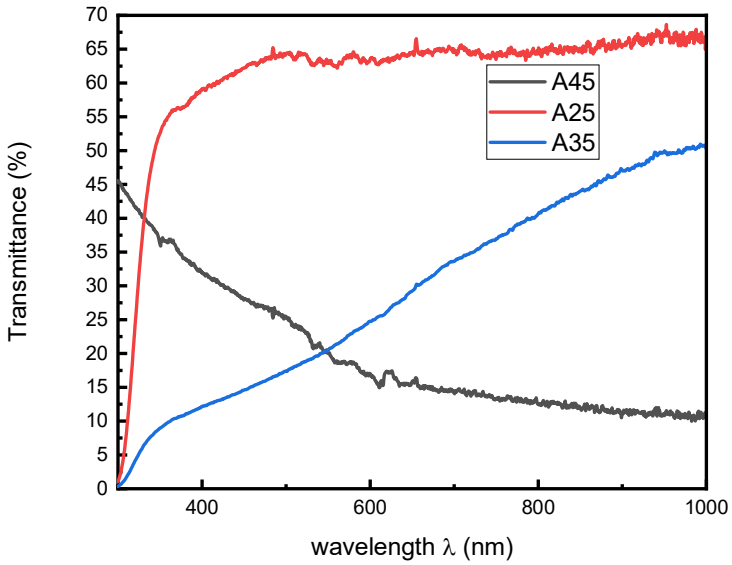

FIG. 5. Transmittance spectra of CZTS thin films with annealing temperatures.

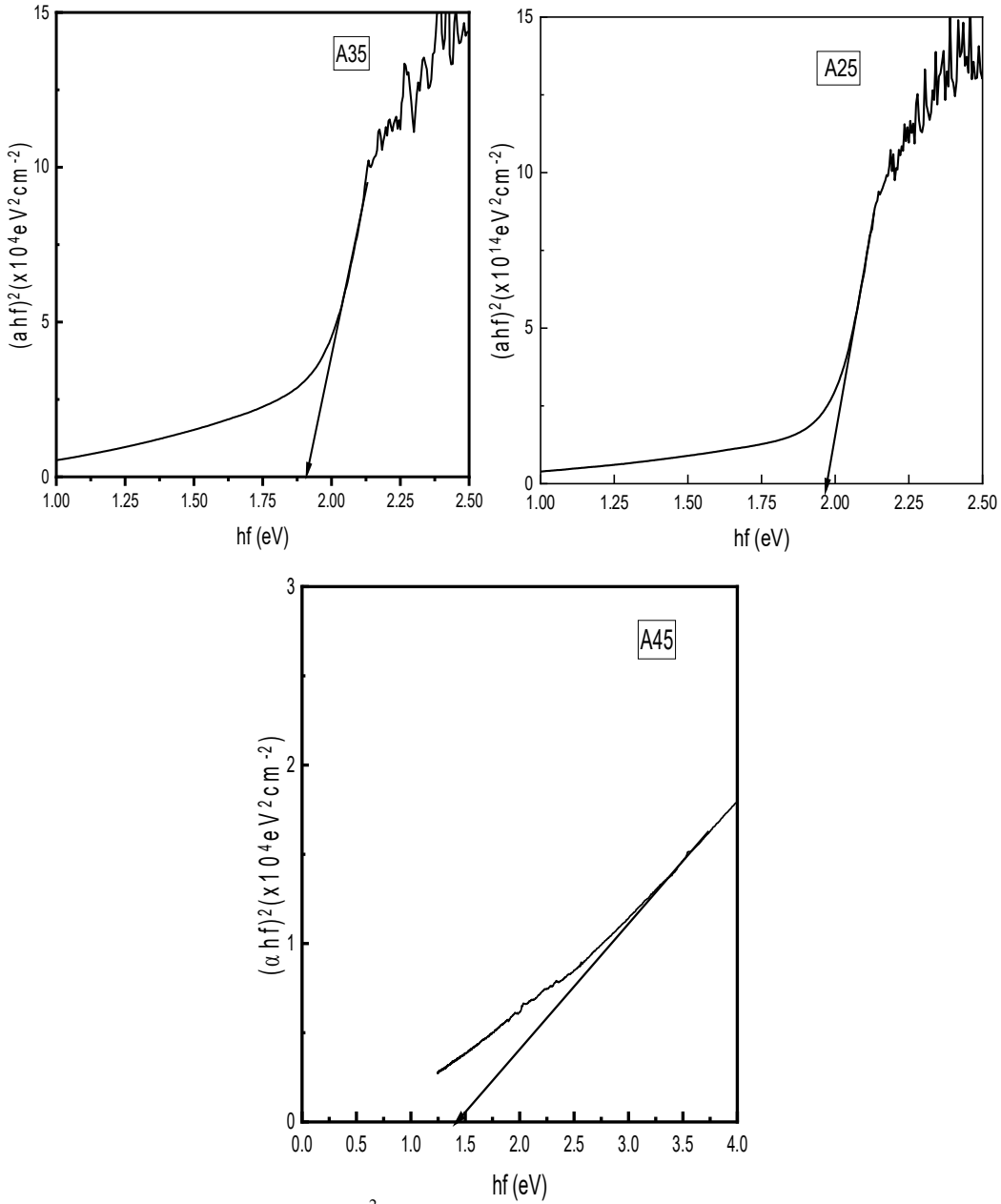

FIG. 6. Plot of $(\alpha hf)^2$ versus hf for specimens A25, A35, and A45.

3.3 Surface Morphology

The top-down SEM images of A45, A35, and A25 are shown in Figs. 7(a), 7(b), and 7(c), respectively. The increase in size of crystals in response to increasing annealing temperatures can be observed from the micrographs. These results are in agreement with previous works [16, 17]. Large voids and small crystallites with sizes below 500 nm are evident in A25. The voids observed on the surface of A25 can be attributed to the presence of an amorphous carbon layer formed beneath the thin film that did not completely evaporate during the annealing process. Upon increasing the annealing temperature to 350 °C, a reduction in voids and an increase in crystallite size were observed, although the surface morphology remained nonhomogeneous. Large crystals, which are undefined with distinct grain boundaries, can also be observed in A35, with some of the crystals having sizes greater than 2 micrometers. It has been reported that grain boundaries reduce minority carrier diffusion, which is detrimental to solar cell performance [18]. Superior surface morphology can be observed at an annealing temperature of 450 °C, with voids almost completely absent, with improved compactness and homogeneity.

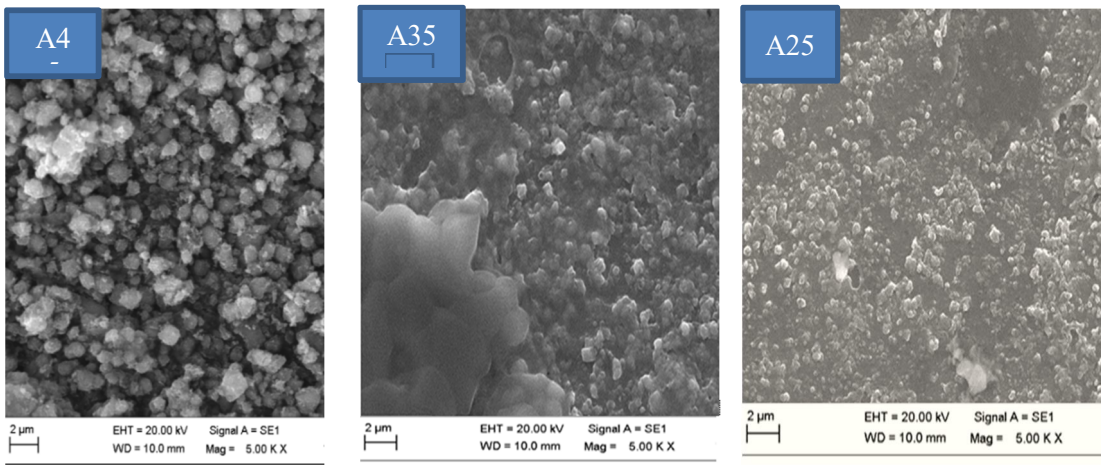

(a) (b) (c)

FIG. 7. SEM of CZTS thin film for specimens (a) A25, (b) A35, and (c) A45.

3.4 Analysis of the Composition of CZTS Thin Films Annealed at 450 °C

The EDX spectrum of A45 is shown in Fig. 8. The presence of copper, zinc, tin, and sulfur peaks in the EDX spectra confirms the composition of the CZTS compound in the A45 sample. However, it is noteworthy that all the films exhibit significant sulfur deficiency, which can be attributed to the tendency of sulfur to react with oxygen and form sulfur dioxide (SO_2), which is subsequently lost during the pyrolysis process. High percentages of carbon and oxygen seen in the spectra may not be solely as a result of oxidation of the specimen

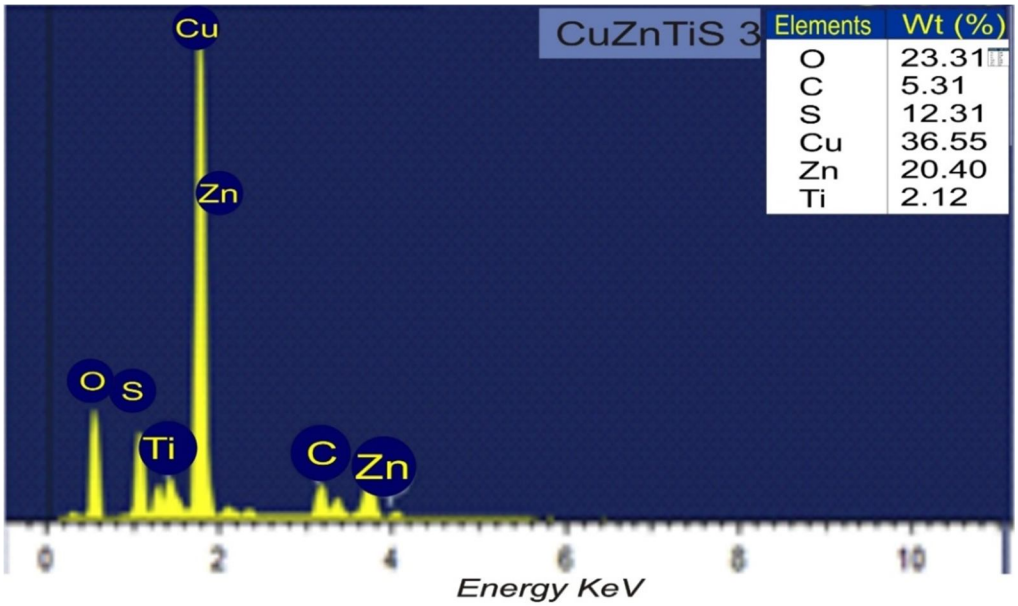

FIG. 8. EDX spectrum of A45.

3.5 Electrical Properties

The electrical properties of sprayed CZTS thin films were studied at different annealing temperatures. The resistivity of the films was obtained using Eq. (4):

$$\rho = \left(\frac{V}{I}\right)\frac{A}{L} \quad (4)$$

where V is the voltage measured across the outer probes, I is the current passing through the inner probes, A is the cross-sectional area of the CZTS thin film specimen, and L is the distance between the inner probes. The resistivity of annealed CZTS thin films is shown in Table 2. It can be observed that resistivity decreases with an increase in annealing temperature. The results show that better electrical properties can be obtained at an annealing temperature of 450 °C and are in agreement with previous works in the literature [19]. An explanation for the high resistivity of CZTS thin film annealed at 250 °C is the high microstructural strain in the films,

which can be observed in Table 1. Theoretical calculations and experimental studies have shown that strain in films is due to inhomogeneity in composition, which in turn alters the shape of the valence bands [20]. In other words, strain can be induced by secondary phases apart from the strain stemming from the film fabrication process. The result is a negative impact on hole carrier transport and electron-hole recombination at the junction. It can also be argued that high resistivity at low annealing temperatures is due to the presence of undecomposed organic residuals in the CZTS thin film. The lowest resistivity was calculated for CZTS thin film annealed at 450 °C, with the lowest micro-structural strain shown in Table 1. The electrical conductivity of CZTS films is improved at an annealing temperature of 450 °C.

TABLE 2. Electrical resistivity of CZTS thin films annealed at different temperatures.

Specimen	Sheet Resistance (Ω/sq) (x 10^7)	Resistivity (Ωcm) (x 10^{-1})	Thickness (nm)
A25	1.60	2.59	1625
A35	1.10	1.71	1620
A45	8.79	0.71	1621

3.6 Characterization of Glass/ITO/i:ZnO/n:ZnS/ p:CZTS/Ag Solar Cell

Glass/ITO/i:ZnO/n:ZnS/p:CZTS/Ag solar cells were fabricated at the optimized annealing temperature parameter that has shown the best properties for the absorber layer using the spray pyrolysis technique. The I-V characteristics of the cell, taken in the dark and under illumination, are shown in Fig. 9, where a rectifying curve with low reverse saturation current can be observed. This is evidence that the junction between CZTS and ZnS has diode characteristics, with the possibility of the production of an electron-hole pair when the heterojunction is under illumination. The results are in agreement with the work of Patel *et al.* [23] and Fathima *et al.* [24], which have exhibited comparable rectifying curves for FTO/Al:ZnO/CdS/CZTS/CuS/FTO and FTO/Ag/CdS/Ag solar cell architectures, respectively. The photocurrent output was obtained from Eq. (5).

$$\eta = \frac{P_{max}}{P_{in}} = \frac{FFV_{oc}I_{sc}}{P_{in}} \quad (5)$$

where FF is the fill factor, V_{OC} is the open circuit voltage, and I_{SC} is the short circuit current. P_{max} is the maximum power that can be delivered by the solar cell. P_{in} was calibrated to AM 1.5 to 100 mW/cm^{-2} before measurements were carried out. The photocurrent output of the cell was extremely low, with the short circuit current calculated to be 0.022 mA, and the efficiency of the cell was less than 0.1%. The low performance of the cell may be attributed to secondary phases that may have similar XRD peaks to CZTS. Since the formation of single-phase CZTS can be very challenging, ZnS and Cu_2SnS_3 (CTS) phases that have the same XRD patterns as CZTS will go undetected [21, 22]. Since ZnS was suspected to be the culprit, the CZTS absorber layer was etched with 0.1 M of HNO_3 for the removal of the ZnS phase by immersing the synthesized CZTS thin film in HNO_3 for 300 seconds. The decomposition of ZnS is represented by Eq. (6).

$$HNO_3 + ZnS \rightarrow H_2O + S + NO + Zn(NO_3)_2 \quad (6)$$

Another CZTS solar cell with the same solar architecture as the first was fabricated using the etched CZTS as an absorber layer, and the I-V characteristics of the cell, taken in the dark and under illumination, are shown in Fig. 9(a) and Fig. 9(b), respectively, while those with the HNO_3- etched CZTS layer in the dark and under illumination are shown in Fig. 10. After etching, the photocurrent increased to 0.258 mA, with a corresponding conversion efficiency of 0.13%. The wurtzite phase of the CZTS thin film annealed at 450 °C may have contributed to reduced recombination losses by providing efficient pathways for charge carriers to reach the electrodes. A summary of the I–V parameters of the fabricated solar cells is presented in Table 3. Recent literature on CZTS thin-film solar cells is summarized in Table 4. Comparison shows that the open-circuit voltage and photocurrent output of our cells are lower than those reported in literature; however, most high-performance CZTS cells involve cadmium. Moreover, some studies [30,31,37,38] incorporate germanium, which is expensive due to the high cost of achieving 99.9% purity. In contrast, our work demonstrates a simple, scalable, and environmentally friendly fabrication method using earth-abundant, low-cost, and safe materials.

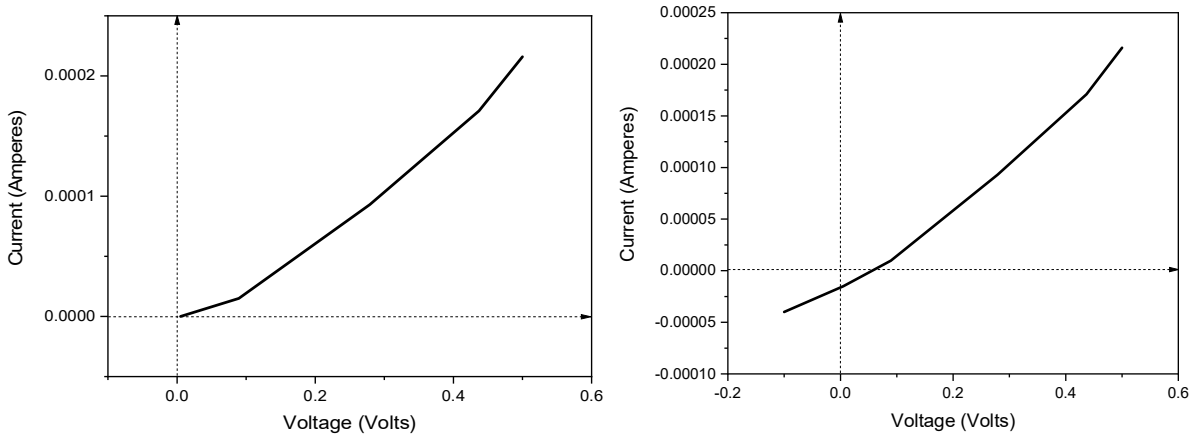

(a) (b)

FIG. 9. I-V characteristics of ITO/i:ZnO/n:ZnS/p:CZTS/Ag thin film solar cell in the dark and under illumination.

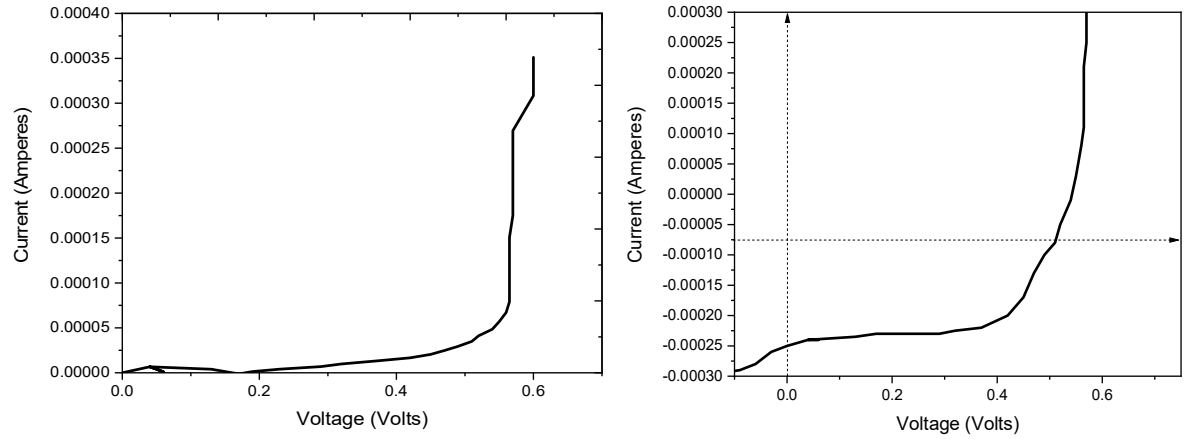

FIG. 10. I-V characteristics of ITO/i:ZnO/n:ZnS/p:CZTS/Ag thin film solar cell with HNO_3- etched CZTS layer in the dark and under illumination.

TABLE 3. Summary of the I-V characteristics of the fabricated CZTS absorber-based solar cells under illumination.

Device	Area of cell (cm^2)	V_{oc} (volts)	I_{sc} (mA)	V_{max} (volts)	I_{max} (mA)	Fill Factor	Efficiency (%)
ITO/i:ZnO/n:ZnS/p:CZTS/Ag	2.50 x 2.50	0.06	0.05	0.02	0.01	0.15	2.88×10^{-5}
ITO/i:ZnO/n:ZnS/p:CZTS/Ag (etched with HNO_3)	2.50 x 2.50	0.54	0.26	0.40	0.20	0.57	0.12

TABLE 4. Recent references on CZTS buffer layers.

CZTS Buffer Layer	Solar Cell Structure	Efficiency (%)	Deposition Method	J_{sc} (mA/cm^2)	Fill Factor	V_{oc}(mV)	Reference
Ge (alloyed with CZTS)	CZTS/Ge (followed by Sulphurization)	10.7	Sputtering	21.0	63.70	800	[30]
CdS+Salvia dye	SLG/Mo/CZTS/CdS/ ZnO/AZO	0.27	Sputtering	8.54	0.29	107.0	[31]
ZnSnO	SLG/Mo/CZTS/ZTO	9.3	Atomic Layer Deposition	21.00	65.8	736	[38]
CdS/TiO_2	SLG/Mo/CZTS/TiO_2/ AZO	3.59	Sputtering and Plasma	13.8	31.0	347	[37]

4. Conclusion

This paper presented the synthesis of CZTS thin films via the chemical spray pyrolysis technique. The effects of annealing temperature on the structural, optical, and electrical properties of the synthesized films were studied broadly. The results show the growth of the wurzite crystal structure for CZTS thin film annealed at higher temperatures. The largest grain size and lowest microstructural strain were obtained at 450 °C. SEM images showed that a more homogenous and void-free surface was obtained at 450 °C. The optical properties are widely affected by variation in annealing temperature. An increase in absorbance and a decrease in transmittance with increasing wavelength were observed at 450 °C, and a bandgap closer to the ideal bandgap of 1.5 eV was obtained. The CZTS thin film annealed at 450 °C indicated the lowest resistivity. A solar cell was fabricated with ZnS as an n-type partner, and a conversion efficiency of 0.12% was achieved.

Funding: The authors declare no funding for this research

Competing interests: The authors declare that they have no competing interests

Conflicts of interest: The authors declare that they have no conflicts of interest

Availability of data: The datasets generated during and/or analyzed during the current study are not publicly available but are available from the corresponding author on reasonable request.

Ethical Approval: Not applicable

Code availability: Not applicable

Acknowledgments: Not applicable

References

[1] Zhang, X. et al., Sci. Rep., 8 (248) (2018) 1.

[2] Zhu, R., Zhang, Z., and Li, Y., Nanotechnol. Rev., 8 (1) (2019) 452.

[3] Zappetini, A., Woodhead Publ. Ser. Electro. Opt. Mater., 2019 (2019) 273.

[4] Pal, K., Singh, P., Bhaduri, A., and Thapa, K.B., Sol. Energy Mater. Sol. Cells, 196 (2019) 138.

[5] Boersu, I. and Vasile, B.G., Materials, 15 (23) (2023) 1.

[6] Sah, M., Reddy, V.R.M, Kim, B., Patro, B., Kim, W.K., and Sharma, P., Mater., 15 (5) (2022) 6.

[7] Yan, C. et al., Nat. Energy, 3 (2018) 764.

[8] Wang. W. et al., Adv. Energy Mater., 4 (7) (2014) 1.

[9] Faremi, A.A. et al., Results Eng., 16 (2022) 100622.

[10] Patel, S.B. and Gohel, J.V., Phys. Astron. Int. J., 1 (4) (2017) 1.

[11] Olga, M.A., Sarp, A.O., Seyhan, A., and Zan, R., Renew. Energy, 179 (2021) 1865.

[12] Lu, X., Zhuang, Z., Penq, Q., and Li, Y., Chem. Commun., 47 (2011) 3141.

[13] Touati, R., Rabeh, M.B., and Kanzari, M., Energy Procedia., 44 (2014) 44.

[14] Chalapathi, U., Poornaprakash, B., and Park, S.H., Chalcogenide Lett., 15 (10) (2018) 475.

[15] Rey, G. et al., Appl. Phys. Lett., 105 (2014) 1.

[16] Izadneshan, H. and Solookinejad, G., J. Optoelectron. Nanostruct., 3 (2) (2018) 20.

[17] Singh, T., Pandya, D.K., and Singh, R., Mater. Chem. Phys., 130 (3) (2011) 1366.

[18] Raiguru, J. et al., Mater. Sci. Eng., 178 (2017) 1.

[19] Chen, L. and Park, C., Korean J. Chem. Eng., 34 (4) (2017) 1187.

[20] Patel, S.B. and Gohel, V.J., Phys. Astron. Int. J., 1 (4) (2017) 126.

[21] Syafiq, U., Ataolahhi, N., Maggio, R., and Scardi, P., Molecules, 24 (2019) 3454.

[22] Chalapathi, U., Poornaprakash, B., and Park, S., Chalcogenide Lett., 15 (10) (2018) 475.

[23] Patel, S.B. and Gohel, V.J., J. Mater. Sci. Mater. Electron, 29 (2018) 5613.

[24] Fathima, M.I., Arulamantham, A.M., and Wilson, K.S., Mater. Res. Express., 7 (2020) 1.

[25] Tripathi, R.K., Panwar, O.S., Rawal, I., Singh, B.P., and Yadav, B.C., J. Taiwan Inst. Chem. Eng., 86 (2018) 185.

[26] Franco, M.A. and Groesser, S.N., Sustainability, 13 (17) (2021) 1.

[27] Rawal, I., Tripathi, R.K., and Panwar, O.S., RSC Adv., 6 (37) (2016) 31540.

[28] Tripathi, R.K. et al., RSC Adv., 4 (97) (2014) 54388.

[29] Rawal, I., Dwivedi, N., Tripathi, R.K., Panwar, O.S., and Malik, H.K., Mater. Chem. Phys., 202 (2017) 169.

[30] Wang, A. et al., Adv. Mater., 36 (2024) 1.

[31] Najim, A.S. et al., Sci. Rep., 13 (1) (2023) 1.

[32] Orelusi, A.N., Owoeye, V.A., Dada, J.B., Salau, A.O., Boyo, H.O., and Adewinbi, S.A., J. Mater. Res., 38 (2023) 4192.

[33] Faremi, A.A., Olubambi, P.A., Salau, A.O., and Ibiyemi, A.A., Results Eng., 18 (2023) 1.

[34] Faremi, A.A., Olubosede, O., Salau, A.O., Adigbo, S.O., Olubambi, P.A., and Lawan, E., Mater. Renew. Sustain. Energy., 12 (3) (2023) 235.

[35] Salau, A.O., Olufemi, A.S., Oluleye, G., Owoeye, V.A., and Ismail, I., Mater. Today, 51 (1) (2022) 502.

[36] Boutebakh, F.Z., Zeggar, M.L., Attaf, N., and Aida, M.S., Optik, 144 (2017) 180.

[37] Tseberlidis, G., Barchiesi, E., Colombo, A., and Fabrizio, M., Eur. J. Inorg. Chem., 2023 (7) (2023) 703.

[38] Cui, X., Sun, K., Huang, J., Lee, C.-Y., Yan, C., Sun, H., Zhang, Y., Liu, F., Hossain, Md. A., Zakaria, Y., Wong, L.H., Green, M., Hoex, B., Hao, X., Chem. Mater., 30 (2018) 7860.

Volume 18, Number 4, 2025. pp. 489-496

Jordan Journal of Physics

ARTICLE

Optimization of Source Pocket Height on Source Pocket Half Hetero Dielectric Double Gate TFETs (SP-HHD-DG-TFET)

Bed P. Pandey[a], **Santosh K. Pandit**[a], **Sanju Shrestha**[a], **Kavindra K. Kavi**[b] and **Om Prakash Niraula**[a]

[a] *Central Department of Physics, Tribhuvan University, Kiritipur, Kathmandu, Nepal.*
[b] *Electronics and Communication Engineering Department, Motilal Nehru National Institute of Technology Allahabad, Prayagraj 211004, India.*

Doi: **https://doi.org/10.47011/18.4.7**
Received on: 26/06/2024; *Accepted on: 06/01/2025*

Abstract: Tunnel field effect transistor (TFET) has attracted significant attention due to its extremely low sub-threshold swing (SS) and leakage current. However, due to the ambipolar effect and relatively low ON-current, researchers are modifying the structures and selecting appropriate materials. In order to increase the ON-current, a highly dense thin layer, source pocket (SP) is used, while a hetero-dielectric gate is used to reduce ambipolar current. Hence, various characteristics, properties, and parameters of the source pocket half hetero-dielectric double gate TFET (SP-HHD-DG-TFET) are studied by varying the SP height (4, 6, and 8 nm) using the Silvaco TCAD simulator. The optimized SP height of 6 nm shows a current ratio (I_{ON}/I_{OFF}) and a sub-threshold swing (SS) to be 3.90×10^{12} and $17.59\ mV/decade$, respectively. Hence, the optimized height and the model are suggested to be useful for low-power and high-speed devices.

Keywords: Sub-threshold Swing (SS), Conductance, Source Pocket (SP), Tunneling, Off–current, On-current, Tunnel field-effect transistor (TFET).

1. Introduction

The tunnel field effect transistor (TFET) is replacing conventional MOSFET due to its small sub-threshold swing (SS), less than $60\ mV/decade$ [1], and low leakage current. Hence, it can be used for low-current and low-power circuits [2]. However, a major disadvantage is the ambipolar current effect, where the n-channel TFET behaves as an 'ON' state instead of an 'OFF' state when a high negative gate bias voltage is applied. Hence, it became difficult to use TFETs in CMOS circuit applications. To address this challenge, various techniques have been explored, such as gate engineering, drain engineering, and spacer/ energy-band engineering.

The 'OFF' state tunneling current is controlled by using an additional gate, called a tunneling gate [3], in the gate engineering technique. Alternatively, using an underlap gate-drain (UGD) in TFETs [2, 4] allows control of channel resistance near the drain channel current. However, both techniques require an additional gate or extra area near the drain. It limits the scalability of the device [5-7]. These challenges of scalability and tunneling current can be overcome by drain engineering, which involves using an undoped (UD) [5, 8, 9] or lightly doped (LD) drain, or introducing a pocket near the drain [10–13]. For instance, Dhiman *et al.* proposed a graded-doped (GD) drain TFET to mitigate the ambipolar effect [14].

On the other hand, Lu et al. [15] mentioned that due to the large and indirect bandgap of Si, Si-TFETs suffer from unacceptably low 'ON'-state currents, below the levels recommended by the International Technology Roadmap for Semiconductors (ITRS) [16,17]. The low 'ON'-current limits the switching speed of the device.

Corresponding Author: Sanju Shrestha **Email**: sanju.shrestha@cdp.tu.edu.np

To overcome this, the use of Heterojunction TFETs (HTFETs), formed by junctions between III–V semiconductors and silicon, has been suggested. For p-channel TFETs, the InAs/Si HTFET has been proposed because of its lower tunneling mass [18], which facilitates the direct tunneling process [19]. The 'ON'-state current can be improved by inserting an ultra-thin doping pocket at the junction between the heavily doped source and the intrinsic channel within the channel region [20, 21], as there will be the formation of steeper energy band bending and a reduction in the tunneling distance.

Energy-band engineering, i.e., using heterojunctions and the novel device structures of source pocket (SP), as done in the drain engineering, is used in a single device, specifically the InAs/Si heterojunction. The use of SP and junction, i.e., the hetero SP-TFET (HSP-TFET), is proposed by Lu *et al*. [15]. The authors have done comparative studies with traditional Si-TFETs and found that the proposed InAs/Si HSP-TFET significantly enhanced device performance.

Instead of using a single gate oxides of Si/Hf, horizontally stacked layers of high-k gate oxides have been shown to enhance multiple device characteristics. The decrease in the ambipolar current, along with SS values to below 5 mV/decade, is found by using SP along with a layer of high-k oxide materials in the gate [22]. Even the current switching ratio (I_{ON}/I_{OFF}) is improved by varying the concentrations of doping and the height of the SP. Wang proposes that the hetero-gate-dielectric (HGD) and SP in a DG TFET enhance I_{ON} and reduce the ambipolar current [23].

Sharma *et al.* showed that an SP of SiGe with hetero oxides gives better electrical characteristics compared to that of normal TFETs, SiO_2-gate oxide TFETs, high-k TFETs, and hetero-dielectric SP TFETs [24]. Kavindra *et al*. [25] also showed that the performance of SP hetero-dielectric double gate TFET (SP-HD-DG-TFET) is found to be better in terms of I-V characteristics, I_{ON}/I_{OFF}, and SS compared with hetero-dielectric double gate TFETs (HD-DG-TFET), high-k TFETs, and conventional DG TFETs.

Using Silvaco TCAD [26], various characteristics of the SP-half hetero-dielectric double gate TFET (SP-HHD- DG-TFET) were studied by varying the SP height. The optimized SP height significantly improves the device's properties, making it suitable for low-power, high-speed applications.

2. Device Structure, Parameters, and Simulation Details

The 2D schematic diagram of the SP-HHD-DG-TFET is shown in Fig. 1. The gate consists of SiO_2 oxide in the half region near the n-doped drain, while the other half—toward the heavily p-doped source—uses hetero high-k dielectrics, specifically HfO_2 and Al_2O_3. Since the gate structure is present on both the top and bottom sides of the channel, the device operates as a double-gate structure, which enhances channel controllability. The channel is composed of intrinsic Si, and a single, highly doped GaAs SP is introduced at the source–channel junction within the channel region. The various physical parameters used in the model are provided in Fig. 1 and summarized in Table 1. All simulations were performed using the Silvaco TCAD tool [26].

TABLE 1. Constant parameters used for simulation.

Doping Concentration (cm^{-3})	
p-type Source (n_s)	1×10^{20}
n-type Channel (n_c)	1×10^{17}
n-type Drain (n_d)	5×10^{18}
n-type SP (n_{SP})	7×10^{18}
Dielectric Constant	
SiO_2	3.9
HfO_2	25
Al_2O_3	8.5
Length of the SP (nm)	2.5
Work function of gate (eV)	4.2

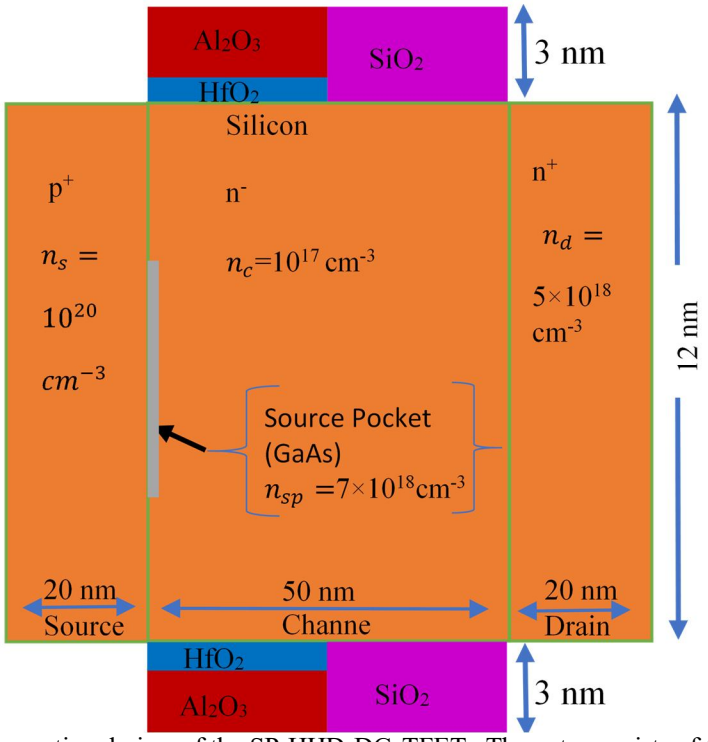

FIG. 1. Schematic cross-sectional view of the SP-HHD-DG-TFET. The gate consists of SiO_2 (3 nm in height) near the drain, and the other half with hetero-dielectrics of HfO_2- Al_2O_3 (1 and 2 nm in height, respectively) is near the source. The p-type source and the n-type drain have concentrations of 1×10^20 cm^-3 and 5×10^18 cm^-3, respectively. n-type SP of $GaAs$ and the channel of Si are with concentrations of $7 \times 10^{18} cm^{-3}$ and $1 \times 10^{17} cm^{-3}$, respectively.

3. Results and Discussion

The 2D simulated structure of SP-HHD-DG-TFET is shown in Fig. 1. The doping concentration of the heavily doped source p^+ of 20 nm in length is 10^{20}cm^{-3}. The nearly intrinsic n-type channel has a doping concentration of 10^{17}cm^{-3} and a length of 50 nm. The n −type doping concentration of SP of GaAl (length 2.5 nm), positioned between the source and the channel, is $7 \times 10^{18}\text{cm}^{-3}$. The n −type drain has a doping concentration of $5 \times 10^{18}\text{cm}^{-3}$ and a length of 20 nm. Work functions of the front gate (Fgate) and back gate (Bgate) are equal (4.2 eV). The gates are made common in the circuit connection, and the work function of the SP is 5.3 eV. All constant parameters are given in Table 1.

In order to optimize the performance of the device, the Silvaco TCAD [26] simulator is used to vary the height of the SP (4, 6, and 8 nm). The obtained simulated characteristics and properties, such as surface potential, electric field intensity, band energy, and the I-V characteristics, are given in Figs. 2, 3, 4, and 5, respectively. The calculated physical parameters of the simulation, such as V_{TH}, I_{ON}, I_{OFF}, (I_{ON}/I_{OFF}) ratio, SS, and trans-conductance (g_m), are given inTable 2.

The variation of surface potential along the channel length at $V_{GS} = V_{DS} = 1$ V is shown in Fig. 2. A sharp increase in surface potential is observed at the source–channel junction. This enhancement occurs because the gate oxide near the source consists of high-k dielectrics (HfO_2 and Al_2O_3), and the heavily doped SP further strengthens the potential. Among the examined SP heights (4 nm, 6 nm, and 8 nm), the maximum surface potential is obtained for the SP height of 6 nm, as illustrated in the inset of Fig. 2.

In contrast, near and within the drain side of the channel, the effect of SP height is insignificant, and the surface potential remains nearly constant. This indicates that the region corresponds to the depletion or space-charge region. Kavi *et al*. [25] also included the drain–channel depletion region in their modeling to achieve accurate device representation in this area.

The electric field distribution, shown in Fig. 3, exhibits a strong peak at the source–channel interface. This is attributed to the high charge

carrier density in the source region as well as in the SP. The presence of high-k hetero-dielectrics (HfO_2 and Al_2O_3) at the gate near the source further contributes to the enhanced electric field. The maximum value at the sharp peak of the electric field is due to the presence of more charge for the SP of 8 nm in height. This peak indicates an increased number of charge carriers tunneling through the junction.

Figure 4 shows the state at $V_{GS} = V_{DS} = 1$ V, i.e., at the 'ON' state. It is known that with n-type and p-type doping, the conduction band energy level decreases and the valence band level increases, respectively, i.e., the Fermi level moves towards the conduction and valence band. Under the unbiased condition, the energy band is not sharp, representing the 'OFF' state. The energy gap increases due to the reverse biasing and becomes sharp, i.e., the higher level of the conduction band energy and the lower level of the valence band energy at the source and drain sides, respectively. will come very close to each other at the channel region due to the band bending. It can be seen in the inset of Fig. 4.

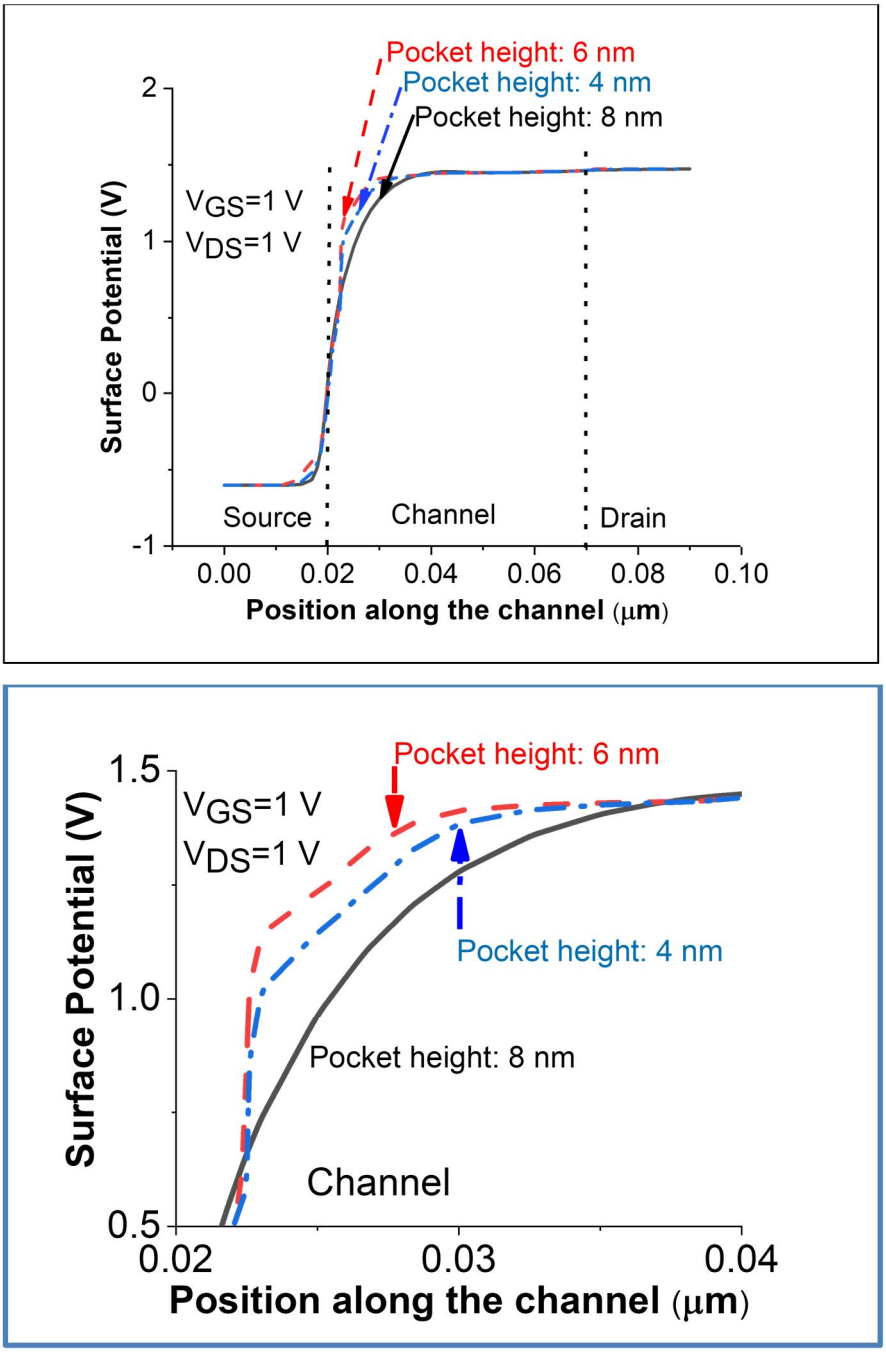

FIG. 2. Surface potential versus the position along the channel for SP heights of 4, 6, and 8 nm at $V_{GS} = V_{DS} = 1\,V$. The inset view highlights the difference in the characteristics.

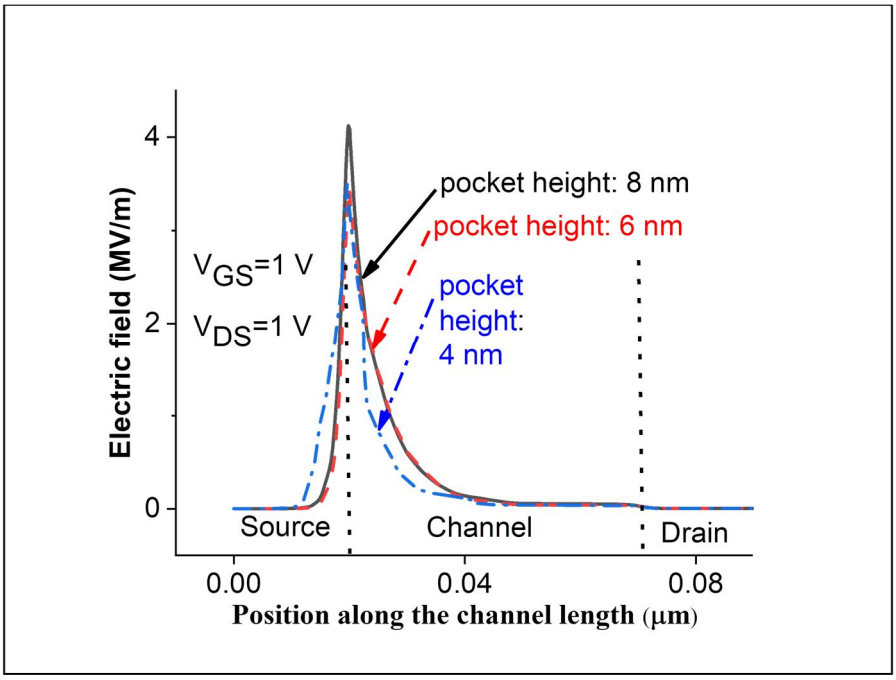

FIG. 3. Electric field versus the position along the channel length for SP heights of 4, 6, and 8 nm at $V_{GS} = V_{DS} = 1\,V$.

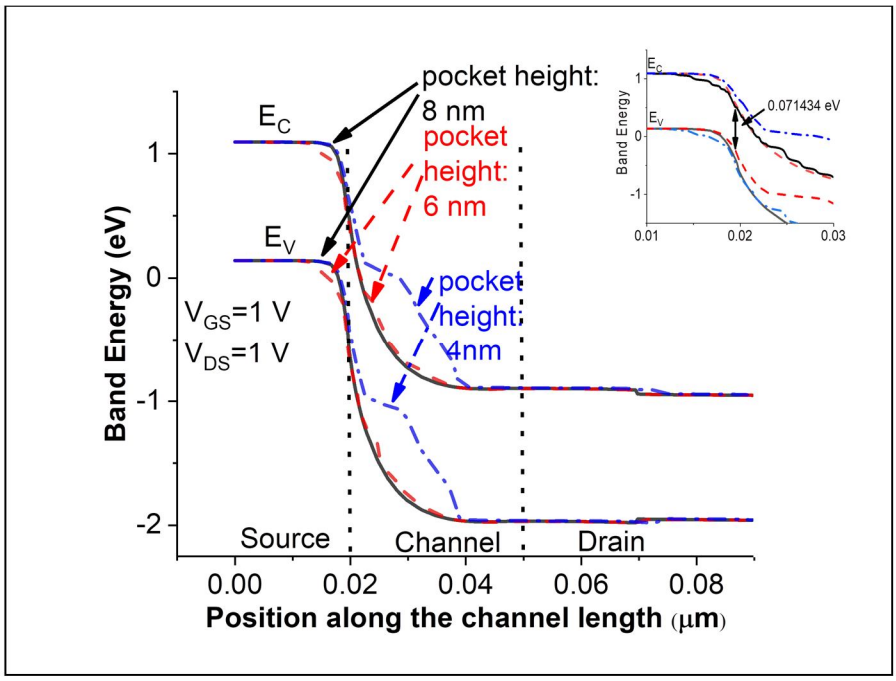

FIG. 4. Band Energy variation versus the position along the channel length for SP heights of 4, 6, and 8 nm at $V_{GS} = V_{DS} = 1\,V$.

At $V_{GS} = 0$, the width of the tunneling channel and the height of the energy band are functions of the doping concentrations. Hence, electrons do not have enough energy to move from the valence band to the conduction band. Whereas, as V_{GS} increases, both the CB and the VB energy differences increase, as is the condition of –ve biasing/reverse bias. Figure 4 shows the energy band diagram under the condition $V_{GS} = V_{DS} = 1$ V, where the energy varies along the effective channel length. With an increase in the gate voltage, more band bending takes place, i.e., the conduction band of the source and valence band of the channel/drain are increased and become sharper, causing a reduction in tunneling length, facilitating faster carrier movement in opposite directions across the source–channel junction, resulting in a higher drain current. At $V_{DS} > V_{Th}$, the electrons move from the valence band to the conduction band as

they have sufficient energy to tunnel. The inter-band tunneling is also due to the bands approaching each other, i.e., the narrowing of the effective length of the channel, corresponding to the ON-state condition. With an increase in the gate voltage, the current increases, as shown in Fig. 5. The inset view of Fig. 4 also shows the maximum narrowing of the effective channel length at $V_{GS} = V_{DS} = 1\,V$, causing such an effect. For the tunneling of the electron from the source to the drain via the channel region, the non-local band-to-band tunnel (BTBT) model is used [14, 27, 28]. Kavi *et al*. mentioned that to recombine the electron-hole pair during conduction through the channel, the Auger recombination and Shockley-Read-Hall recombination models are also used [22]. In addition, the Lombardi model is used to incorporate the effect of doping, electric field, and concentration [22]. Due to the high concentration of doping in the source and drain, compared to that of the channel, the band gap narrowing (BGN) model is incorporated [29, 30]. Collectively, these physical models are included in the simulation to accurately describe the current tunneling phenomena.

The variation of drain current versus reverse/back gate voltage for pocket heights ranging from 4 to 8 nm is given in Fig. 5 at $V_{DS} = 1\,V$. The drain current for the 8 nm pocket height is slightly higher than that for the rest of the heights, which is expected due to the availability of a larger number of carriers as the SP is heavily doped.

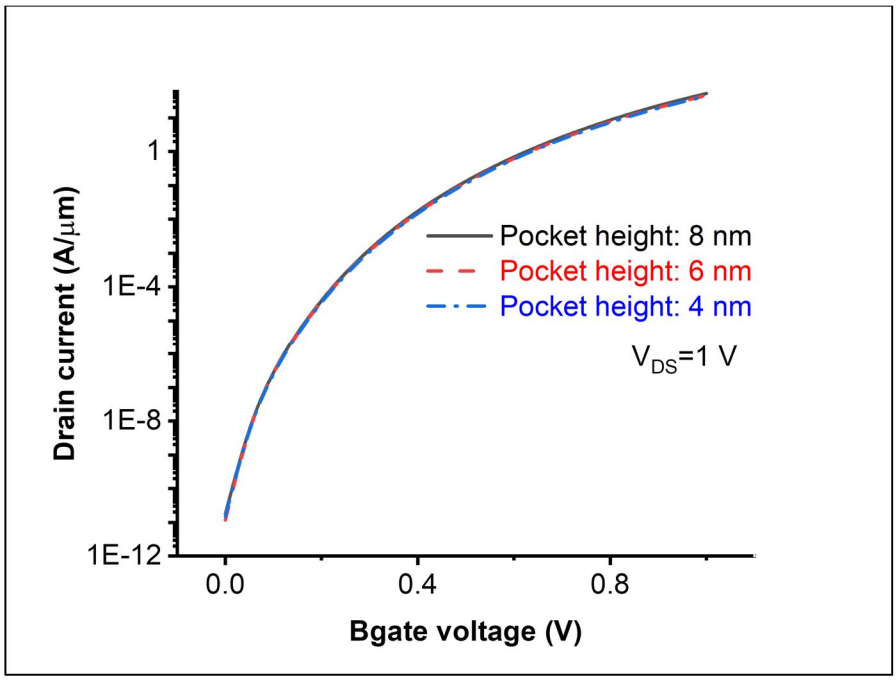

FIG. 5. Variation of drain current versus backward gate (Bgate) voltage for SP heights of 4, 6, and 8 *nm* at $V_{DS} = 1\,V$.

TABLE 2. Physical parameters obtained by simulation with the height of the SP.

S.N.	Parameters	Height of the SP (nm)		
		8	6	4
1.	V_{TH} (V)	0.3465	0.3446	0.3445
2.	I_{ON} (A/μm)	5.20×10^{-5}	4.55×10^{-5}	4.31×10^{-5}
3.	I_{OFF} (A/μm)	1.78×10^{-17}	1.17×10^{-17}	1.48×10^{-17}
4.	I_{ON}/I_{OFF}	2.93×10^{12}	3.90×10^{12}	2.91×10^{12}
5.	Sub-threshold slope	53.62	56.85	54.31
6.	SS (mV/decade)	18.35	17.59	18.41
7.	g_m (Siemen)	$3.39X10^{-4}$	2.93×10^{-4}	2.77×10^{-4}

The threshold voltage (V_{Th}) does not vary significantly with the change in pocket height. I_{ON} decreases with a decrease in the height of the SP, whereas the I_{OFF} decreases and then increases with the height of the SP. However, the current ratio is found to be maximum for the $6\,nm$ height, with a value of 3.90×10^{12}. The current ratio is close to the p-channel SP-HD-DG-TFET, reported at 4.4×10^{12} by Kavi *et al.* [25]. The SS for the $6\,nm$ SP height is $17.59\ \mathrm{mV/decade}$ and found to be the minimum when compared to that of the other heights. The trans-conductance g_m for the height is also found to be lowest, i.e., $2.93 \times 10^{-4}\,S$. So, the optimized height of the SP is expected to be appropriate for a low-power consumption application.

4. Conclusions

Due to the importance of using a SP along with the hetero-dielectrics of high-k materials in a DG-TFET, various electrical characteristics, such as surface potential, electrical energy, bandgap energy, and I-V characteristics, are studied using Silvaco TCAD simulation software.

The calculations of threshold voltage, ON and OFF currents, current ratio, SS, and transconductance are also done.

The variation of such properties and parameters due to the height of the SP on the SP-HHD-DG-TFET is studied/obtained. The SP with the height of 6 nm is found to have the highest current ratio (I_{ON}/I_{OFF}) and the lowest SS. Hence, the optimized height of 6 nm is recommended for low-power and high-frequency applications.

Acknowledgment

The authors would like to acknowledge the Research Coordination and Development Council, Tribhuvan University, Kirtipur, Nepal, for the support provided through the National Priority Area Research Project: TU-NPAR-077/078-ERG-12.

References

[1] Wang, Q., Liu, H., Wang, S., and Chen, S., IEEE Trans. Nucl. Sci., 65 (8) (2018) 2250.

[2] Nigam, K., Gupta, S., Pandey, S., Kondekar, P.N., and Sharma, D., Int. J. Electron., 105 (5) (2018) 806.

[3] Saurabh, S. and Kumar, M.J., IEEE IEEE Trans. Electron Devices, 58 (2) (2011) 404.

[4] Boucart, K. and Ionescu, A.M., IEEE Trans. Electron Devices,54 (7) (2007) 1725.

[5] Garg, S. and Saurabh, S., Superl. Micros., 113 (2018) 261.

[6] Upasana, Saxena, M., and Gupta, M., Micro Nanos., 163 (2022) 107147.

[7] Pandey, C.K., Dash, D., and Chaudhury, S., Micro Nano Lett., 14 (1) (2019) 86.

[8] Bagga, N., Chauhan, N., Gupta, D., and Dasgupta, S., IEEE Trans. Electron Devices, 66 (7) (2019) 3202.

[9] Ahmad, S.A. and Alam, N., IET IET Circuits Devices Syst., 14 (3) (2020) 288.

[10] Kumar, A. and Singh, S.S., In: 2016 Int. Conf. Commun. Signal Process. (ICCSP) IEEE (2016) 1448.

[11] Kumar, A., Superl. Micro., 100 (2016) 1073.

[12] Kumar, A., Superl. Micro., 100 (2016) 1143.

[13] Zhang, M., Guo, Y., Zhang, J., Yao, J., and Chen, J., Nano. Res. Lett., 15 (1) (2020) 1.

[14] Dhiman, P., Kavi, K.K., Ratnesh R.K., and Kumar, A., Int. Conf. Dev. Intell. Comput. Commun. Technol., (DICCT) (2023) 249.

[15] Lu, H., Lu, B., Zhang, Y., Zhang, Y., and Lv, Z., Nanomaterials, 9 (2019) 181.

[16] Noor, S.L., Safa, S., and Khan, Z.R., J. Comput. Electron., 15 (2016) 763.

[17] Semiconductor Industry Association (SIA). International Technology Roadmap for Semiconductors 2015. Available online: https://www.semiconductors.org/wp-content/uploads/2018/06/6_2015-ITRS-2.0-Beyond-CMOS.pdf (accessed on 1 February 2019).

[18] Mookerjea, S., Krishnan, R., Datta, S., and Narayanan, V., IEEE Trans. Electron Devices, 56 (2009) 2092.

[19] Das, G.D., Mishra, G.P., and Dash, S., Super. Microstr., 124 (2018) 131.

[20] Chang, H.Y., Adams, B., Chien, P.Y., Li, J., and Woo, J.C., IEEE Trans. Electron Devices, 60 (2013) 92.

[21] Mahajan, A., Dash, D.K., Banerjee, P., and Sarkar, S.K., J. Mater. Eng. Perform., 27 (2018) 2693.

[22] Kavi, K.K., Tripathi, S., Mishra, R.A., and Kumar, S., Silicon, 14 (2022) 10101.

[24] Sharma, V., Kumar, S., Talukdar, J., Mummaneni, K., and Rawat, G., Mat. Sci. Sem. Pro., 143 (2022) 106541.

[25] Kavi, K.K., Tripathi, S., Mishra, R.A., and Kumar, S., 02 August 2023, PREPRINT, Research Square, https://doi.org/10.21203/rs.3.rs-3189342/v1.

[26] ATLAS, "2D Device Simulator", (SILVACO Int. Santa Clara, CA, USA, 2019).

[27] Dhiman, P., Kavi, K.K., Ratnesh, R.K., and Kumar, A., Intern. Conf. Devc. Intel., Comp. Com. Techno. (DICCT) (2023) 1-5.

[28] Kavi, K.K., Kiroula, K., Kumar, M., Dwivedi, A., and Mishra, R.A., IEEE Stu. Conf. Eng. Sys. (SCES), (2022) 16.

[29] Gupta, A., Rai, A., Kumar, N., Sigroha, D., Kishore, A., Pathak, V., and Rahman, Z.U., Silicon, 14 (2022) 1005.

[30] Gupta, V., Awasthi, H., Kumar, N., Pandey, A.K., and Gupta, A., Silicon, 14 (2022) 2989.

Volume 18, Number 4, 2025. pp. 497-516

Jordan Journal of Physics

ARTICLE

Reuse of Waste Glass Doped with Agricultural and Mining Wastes as Radiation Shielding Materials: A Computational and Experimental Study

Zeynep AYGUN[a] and **Murat AYGUN**[b]

[a] *Vocational School of Technical Sciences, Bitlis Eren University, 13100, Bitlis, Turkey.*

[b] *Department of Physics, Faculty of Science and Arts, Bitlis Eren University, 13100, Bitlis, Turkey.*

Doi: **https://doi.org/10.47011/18.4.8**

Received on: 16/07/2024; *Accepted on: 20/01/2025*

Abstract: The objective of the study is to reuse the waste materials generated from daily household activities, as well as food and mining industries, and to determine the radiation shielding capabilities of materials produced from these wastes. In this context, four groups of waste samples were prepared using various combinations of waste glass, agricultural wastes, and mining wastes, including tea waste, eggshell waste, peanut shell waste, tincal waste, Bayburt stone waste, and green clay, mixed in different ratios. The effects of adding Ta and W to these waste-based composites on their shielding performance were also examined. The Phy-X/PSD, a widely used code, was applied to calculate the radiation protection parameters. In addition, spectroscopic results were provided based on X-ray diffraction (XRD), electron paramagnetic resonance (EPR), scanning electron microscopy (SEM), and energy dispersive spectroscopy techniques. The results of the shielding parameter analysis revealed that all prepared samples exhibited radiation shielding capability, with the second and third samples showing superior performance. The highest mass attenuation cross-section value at 0.015 MeV was observed for sample B3 (comprising waste glass, Bayburt stone waste, eggshell waste, and tungsten), measured at 34.960 cm^2g^{-1}, while the lowest value was found for sample X1 (comprising waste glass, tincal waste, and green clay), measured at 7.704 cm^2g^{-1}. A clear relationship was observed between the content of tantalum, tungsten, and eggshell waste and the radiation protection capacities of the samples. It can also be noted that the neutron shielding abilities of the samples were found to be consistent with their photon shielding properties. For sample B3, the α-W main phase at ≈40° exhibited a crystallite size of 41.51 nm, suggesting that structures with larger crystallite sizes demonstrate better shielding performance. Overall, it can be concluded that the newly developed waste-based composites show promising radiation protection characteristics. Their use as alternative materials in place of cement, aggregate, or concrete can be recommended to promote recycling and sustainable material reuse.

Keywords: Waste glass, Waste types, Phy-X/PSD, Radiation shielding capability.

PACS: 28.41.Qb, 91.62.Rt.

1. Introduction

The use of complementary cementitious materials (CCMs) to partially replace cement in concrete has recently become a widely adopted approach to mitigate the negative environmental impacts of industrial activities. Various industrial by-products have been successfully used as CCMs [1, 2]. The addition of the materials into cement can improve the durability, strength, and workability of concrete while also offering economic benefits [3]. Among these by-

Corresponding Author: Zeynep AYGUN **Email**: zeynep.yarbasi@gmail.com

products, waste glass has emerged as a candidate for use as a CCM. Waste glass has become a bigger problem as consumption increases with the increasing population all over the world. Implementing and increasing technologies for waste recycling and reuse has become a global need to focus on. Although recycling technologies are used, a high amount of waste glass is still awaiting evaluation [4]. As seen in several studies, waste glass is thought to be suitable for use as aggregate based on its characteristics and chemical composition similar to conventional CCMs [5-8]. It was reported by Kim *et al*. [5] that incorporating waste glass enhances the durability and radiation shielding performance of mortar. Binici *et al*. [6] studied the effect of eggshells on radiation shielding efficiency and concluded that their inclusion improved the protective capacity of the samples. Given its abundance and low cost, waste glass can also serve as a practical replacement for cement in concrete production [9, 10]. Taha and Nouna [10] examined the use of recycled glass in concrete as both sand and pozzolanic powder and stated that there is not much difference in compressive strength of concrete with the presence of recycled glass sand as sand replacement.

Although concrete possesses many favorable properties, it also has certain drawbacks, such as a lack of optical transparency and a reduction in mechanical strength when exposed to radiation. In this context, glass is a type of radiation shield material that can be an alternative to concrete due to its optical transparency, ease of manufacturing, non-toxicity, low cost, and physical and chemical properties. Radiation protection properties can be changed and improved by adding different materials to the glass. Soda-lime-silica (SLS) glass is a type of glass used generally in glass containers or window glass, such as bottles and jars, and is often employed as an alternative SiO_2 source. SLS glass typically appears in green or brown colors and contains elements such as Si, Na, Ca, Mg, Al, and Fe. In addition, waste materials rich in silica and calcium—such as eggshells, peanut shells, tincal waste, Bayburt stone waste, and different types of clay—can be reused to minimize environmental impact and provide economic benefits [11].

Cement production, on the other hand, is energy-intensive, costly, and associated with significant CO_2 emissions. Therefore, limestone-based materials can serve as effective fillers in concrete, among which eggshells are a viable option [12]. Other industrial waste materials, including tincal waste [13], Bayburt stone waste [14], and clay types [12], possess good refractory properties and can be recycled or repurposed as building materials. Furthermore, waste composites can be doped with heavy elements or oxides such as W, Ta, and WO_3 to enhance their radiation shielding capabilities [15, 16]. Materials containing tungsten (W) and tantalum (Ta) are characterized by a superior shielding effect due to the high atomic number and high density properties of W (Z:74, ρ:19.3) and Ta (Z:73, ρ:16.67) [16]. W and Ta are considered effective and non-toxic alternatives to lead, offering additional advantages such as high melting points, low neutron activation, and superior thermal conductivity. Moreover, Ta doping contributes to improved tensile strength at elevated temperatures [16].

Although radiation offers numerous benefits and is widely used in fields such as science, industry, agriculture, energy, medicine, and radiology, prolonged or excessive exposure can lead to serious short- and long-term health problems for individuals who work in or receive services from these sectors. Consequently, protection against the harmful effects of radiation on all forms of living organisms has become an increasingly important research focus. Recent studies have concentrated on developing shielding materials with enhanced radiation absorption capabilities. Various materials, such as glass, rock, composites, thin films, polymers, and concrete, have been investigated for this purpose, particularly those that are novel, non-toxic, cost-effective, and lightweight [4–6, 16–21]. Eid *et al*. [4] investigated the effects of adding waste glass into cement to evaluate its radiation shielding properties and found that this approach not only improves shielding performance but also supports waste reuse. Aygun *et al*. [18] reported good radiation protection performance for green and red clays reinforced with waste tire and marble dust residues. Elsafi *et al*. [19] studied the radiation shielding properties of a newly developed eco-friendly epoxy composite containing waste marble and WO3, and stated that it exhibited superior radiation protection compared to other polymers. Effective radiation-shielding materials can be developed by

optimizing parameters such as attenuation capability, environmental friendliness, and sustainability, aiming to reduce both radiation exposure and environmental pollution.

The minimization and recycling of waste materials are fundamental aspects of an effective waste management strategy. The protection of natural resources, diminishing the necessity for raw materials to manufacture new products, reducing environmental pollution, providing opportunities for new employment, and decreasing energy consumption are some of the advantages of preferring waste materials. In this context, the motivation of the study is to produce materials with strong radiation shielding performance using waste glass and other types of waste generated from daily household activities and various industries. Accordingly, the exposure and energy absorption buildup factors (EBF and EABF), linear attenuation coefficients (LAC), mass attenuation coefficients (MAC), effective atomic number (Z_eff), mean free path (MFP), half-value layer (HVL), and fast neutron removal cross-section (FNRCS), i.e. the key shielding parameters, were calculated for samples containing different proportions of waste glass (WG), green clay (GC), peanut shell waste (PSW), waste tea (WT), eggshell waste (ESW), tincal waste (TW), and Bayburt stone waste (BSW) using the Phy-X/PSD code [22]. The prepared samples were also analyzed by spectroscopic techniques, as well as their shielding abilities. X-ray diffraction (XRD) was performed to ascertain the crystalline phases or amorphous structure of the samples. Electron paramagnetic resonance (EPR) was used to investigate the magnetic features of the systems by applying a microwave frequency and an external magnetic field. Scanning electron microscopy (SEM) provided information on surface morphology, while energy-dispersive spectroscopy (EDS) was used to determine elemental composition.

The development of non-toxic and effective materials is a requirement of effective radiation protection. While meeting this requirement, it is desirable that such materials are environmentally friendly and contribute to reducing pollution. For this purpose, this study demonstrates that waste materials generated both in households and in the food and beverage industry can be repurposed as substitutes for cement, aggregate, or concrete, offering promising protective properties. By investigating newly developed waste-based materials, this work provides valuable insights into the potential reuse of waste glass and other types of waste as effective radiation shielding materials.

2. Materials and Methods

2.1. Sample Preparation

Four kinds of samples were produced and designated as the S group (S1, S2, S3), B group (B1, B2, B3), A group (A1, A2, A3), and X group (X1, X2, X3). The waste components used in the samples included waste glass (WG), green clay (GC), peanut shell waste (PSW), waste tea (WT), eggshell waste (ESW), tincal waste (TW), and Bayburt stone waste (BSW). The proportions of these components in each sample group are presented in Table 1. Initially, the waste glass and other waste materials were ground into fine powders, measured in specified quantities, and placed in porcelain crucibles. The mixtures were then melted in a furnace at 1100 °C for 2 hours, followed by heat treatment at 500 °C for 3 hours. Finally, the furnace was turned off, and the glass samples were allowed to cool naturally to room temperature. The resulting glass samples were subsequently crushed and prepared for experimental analysis. The sample preparation procedure is demonstrated in Fig. 1.

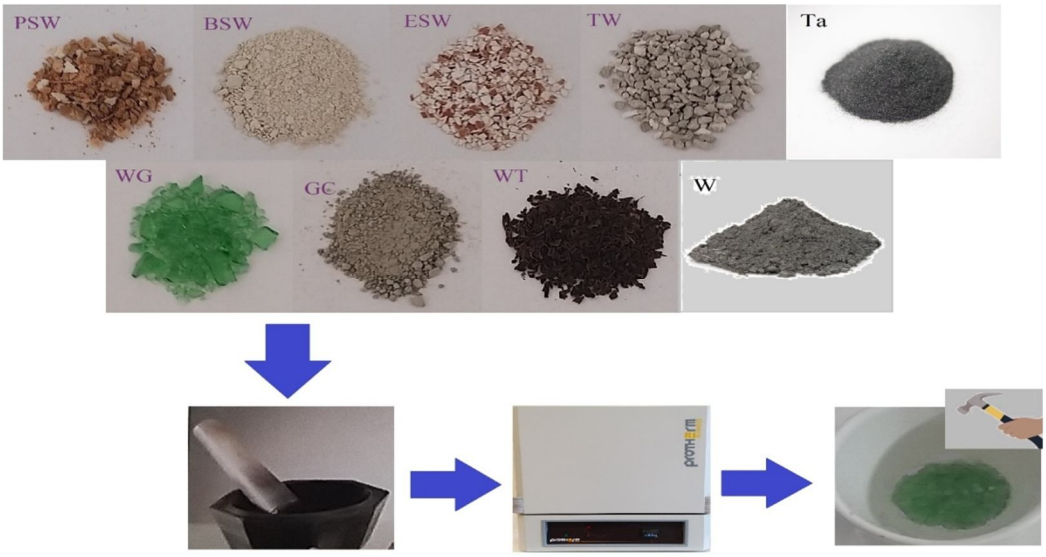

FIG. 1. Procedure of sample preparation.

TABLE 1. Compositional rate of the prepared samples.

S group	WG (%)	ESW (%)	PSW (%)	Ta (%)	W (%)
S1	80	10	10	-	-
S2	70	10	10	10	-
S3	75	10	10	-	5
B group	WG	BSW	ESW	Ta	W
B1	80	10	10	-	-
B2	70	10	10	10	-
B3	75	10	10	-	5
A group	WG	ESW	WT	Ta	W
A1	90	5	5	-	-
A2	90	4	4	2	-
A3	90	4.5	4.5	-	1
X group	WG	TW	GC	Ta	W
X1	90	5	5	-	-
X2	90	4	4	2	-
X3	90	4.5	4.5	-	1

2.2. Experimental Techniques

Room temperature EPR spectra were taken by X-band JEOL JESFA300 EPR spectrometer operating at ≈ 9.2 GHz frequency with a 100 kHz (0.0002-2mT) magnetic field modulation amplitude. A 4 mm diamagnetic tube was used for the EPR experiment. XRD patterns were taken by BRUKER D8 ADVANCE XRD. XRD results of the samples were recorded with 2.5°/min (40 kV and 40 mA) scanning speed in the range of 2Θ ≈ 10°-90° by Cu-Kα (λ = 1.54060 Å) at room temperature. SEM images were recorded by ZEISS EVO LS10. EDS was performed with a JEOL JSM-6610 spectrometer at room temperature. Powder samples illustrated in Fig. 1 were used in all experimental techniques.

2.3. Theoretical Process

The calculation of radiation shielding parameters using the Phy-X/PSD code begins by entering the material composition, which can be defined either in terms of weight fraction or mole fraction. For the determination of the attenuation parameters, material density (g/cm^3) is also necessary. The obtained results are supplied in an MS Excel file. For detailed information on the Phy-X/PSD code and the attenuation parameters, readers are referred to the work of Sakar *et al*. [22].

The rule of mixtures was used to determine the density (ρ_{mix}) of the samples [23]:

$$\rho_{mix} = \frac{\sum_{i=1}^{n} c_i A_i}{\frac{\sum_{i=1}^{n} c_i A_i}{\rho_i}} \quad (1)$$

where c_i, A_i, and ρ_i are the atomic weight of element i_{th}, atomic fraction, and density, respectively.

The MAC can be determined based on the Beer–Lambert law as:

$$I = I_0 e^{-\mu t} \quad (2)$$

$$\mu_m = \frac{\mu}{\rho} = ln(I_0/I)/\rho t = ln(I_0/I)/t_m \quad (3)$$

where t_m (g/cm^2), t (cm), μ(cm^{-1}), and μ_m(cm^2/g) are the sample mass thickness, thickness (the mass per unit area), LAC, and MAC, respectively.

The MAC for any compound can also be found by the following equation [24]:

$$\mu/\rho = \sum_i w_i \, (\mu/\rho)_i \quad (4)$$

where $(\mu/\rho)_i$ and w_i are the MAC of the ith constituent element and the weight fraction, respectively.

The HVL is the thickness of the material required to halve the amount of incident radiation, and the MFP is the distance traveled by a photon between two consecutive collisions. The MFP and HVL can be determined by the formulas [22]

$$MFP = \frac{1}{\mu} \quad (5)$$

$$HVL = \frac{In(2)}{\mu} \quad (6)$$

The atomic cross-section (ACS), the potential for interaction between atoms within a given volume of any given material, (σ_a), can be calculated as:

$$ACS = \sigma_a = \frac{N}{N_A}(\mu/\rho) \quad (7)$$

The electronic cross section (ECS), representing the probability of interaction between photons and electrons, is given by:

$$ECS = \sigma_e = \frac{\sigma_a}{Z_{eff}} \quad (8)$$

In the analysis of compounds composed of multiple elements, the atomic number of the resulting compound is designated as Z_{eff}. Z_{eff} is found with the help of Eqs. (7) and (8) as:

$$Z_{eff} = \frac{\sigma_a}{\sigma_e} \quad (9)$$

The EBF and EABF can be calculated using the formulas provided in Refs. [25, 26]. The geometric progression (G-P) fitting parameters can be obtained from Ref. [27] and used in Eq. (11). EBF and EABF can be obtained using Eq. (12) or (13) by determining K(E,x) from Eq. (14), where a, b, c, d, and X_k are the exposure G-P fitting parameters, and x is thickness in mean free path (mfp). The ratio (R) of the Compton partial mass attenuation coefficient (MAC) to the total MAC can be determined for the material at a given photon energy. R_1 and R_2 denote the $(\mu m)_{Compton}/(\mu m)_{Total}$ ratios of these two adjacent elements with atomic numbers Z_1 and Z_2. F_1 and F_2 are the corresponding G-P fitting parameters for these elements at a specific energy. X and E indicate the depth of penetration and the initial energy of the photon, respectively. The combination of K (E, X) and X represents the photon multiplication dose and defines the spectral shape [22].

$$Z_{eq} = \frac{Z_1(logR_2 - logR) + Z_2(logR - logR_1)}{logR_2 - logR_1} \quad (10)$$

$$F = \frac{F_1(logZ_2 - logZ_{eq}) + F_2(logZ_{eq} - logZ_1)}{logZ_2 - logZ_1} \quad (11)$$

$$B(E,x) = 1 + \frac{(b-1)(K^x - 1)}{(K-1)} \text{ for } K \neq 1 \quad (12)$$

$$B(E,x) = 1 + (b-1)x \text{ for K =1} \quad (13)$$

$$K(E,x) = cx^a + d\frac{\tanh\left(\frac{x}{X_k} - 2\right) - \tanh(-2)}{1 - \tanh(-2)}$$

$$\text{for } x \leq 40 \text{ mfp} \quad (14)$$

The FNRCS ($\sum R$) values of the compounds are defined by the following equation [22]:

$$\sum R = \sum_i \rho_i \left(\sum R/\rho\right)_i \quad (15)$$

where ρ_i and $\left(\sum R/\rho\right)_i$ are the mass RCS and partial density of the compound of the i^{th} constituent element, respectively.

The crystallite size is calculated by the diffraction pattern depending on the full width half height (FWHM) and the Debye-Scherrer equation [28]. Here, β is the FWHM in radians, K is the Scherrer's constant ($\cong$ 0.9), d is the average size of the crystalline, λ is the X-ray

wavelength, and θ is the Bragg angle in degrees [16]:

$$d = \frac{K\lambda}{\beta cos\theta} \quad (16)$$

3. Results and Discussion

3.1. EDS and SEM Analysis

The SEM images of the samples are given in Fig. 2. If the micrographs obtained from the surfaces of the samples are studied, smooth surfaces with some microcrystallites are seen. From the micrographs of the samples with Ta and W additions, the structures represent α-Ta, β-Ta, and α-W structures. It is obvious that Ta and W, due to their high melting points and densities, gather in some locations and thus affect the homogeneous structure of the samples.

The EDS spectra are given in Figs. 3-6, and the weight % ratios of the elements obtained from these spectra are given in Table 2. It is understood from both the mapping images and the EDS analyses that the most homogeneous structure is in the A and X samples. EDS analysis results were found to be consistent except for the B3 and X3 samples for the W amount. As a result of selecting a certain area for measurement during EDS mapping analysis, the area in question is not completely homogeneous, and W shows the feature of clumping during the melting process of the material. Since Ta and W possess considerably higher melting points than the other constituent elements, their incomplete dissolution during the casting process can lead to compositional inhomogeneities. Consequently, the EDS results for Ta and W show acceptable but slightly different values from the nominal casting ratios, likely due to limited solubility and uneven element distribution.

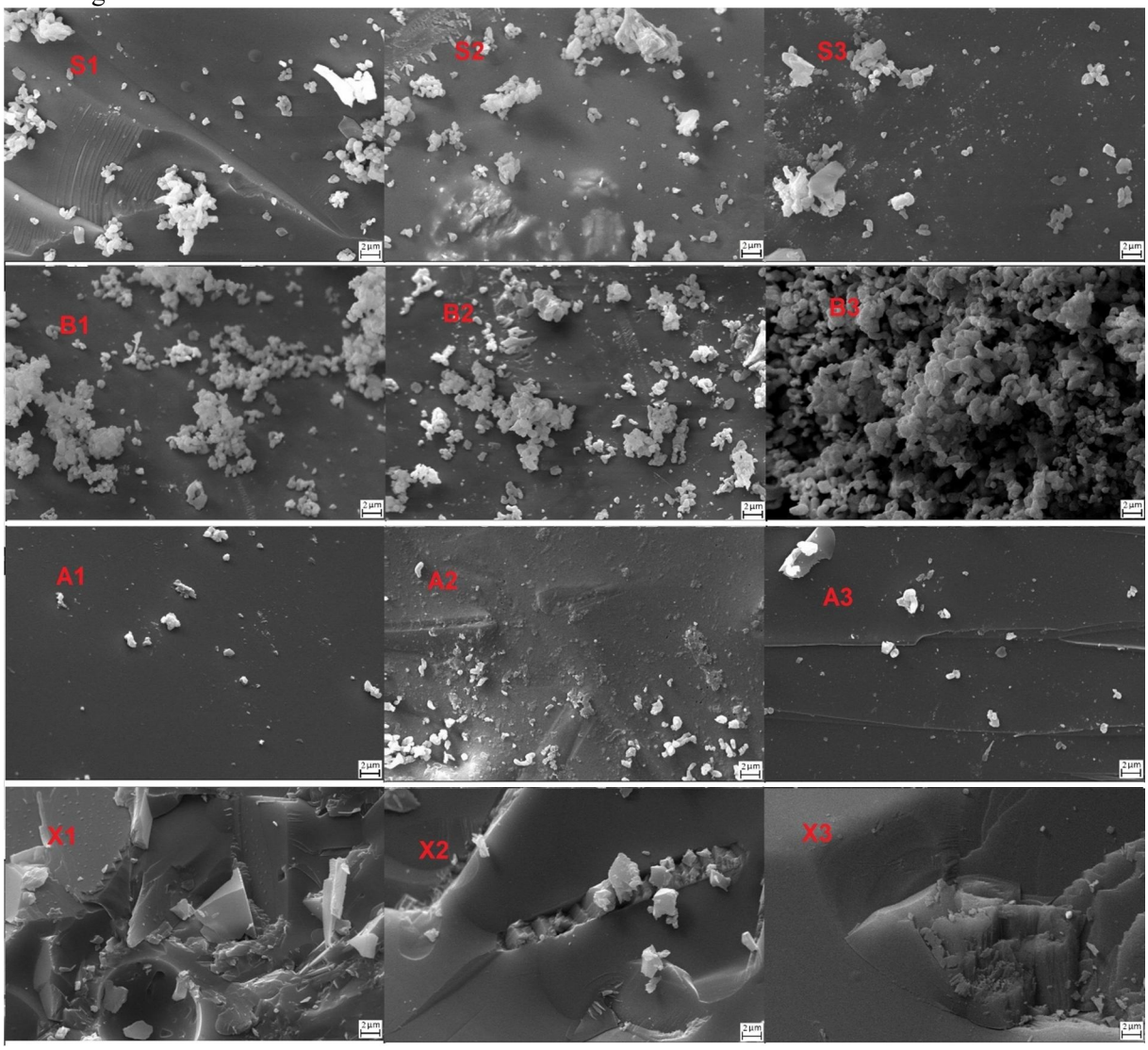

FIG. 2. SEM images of the samples.

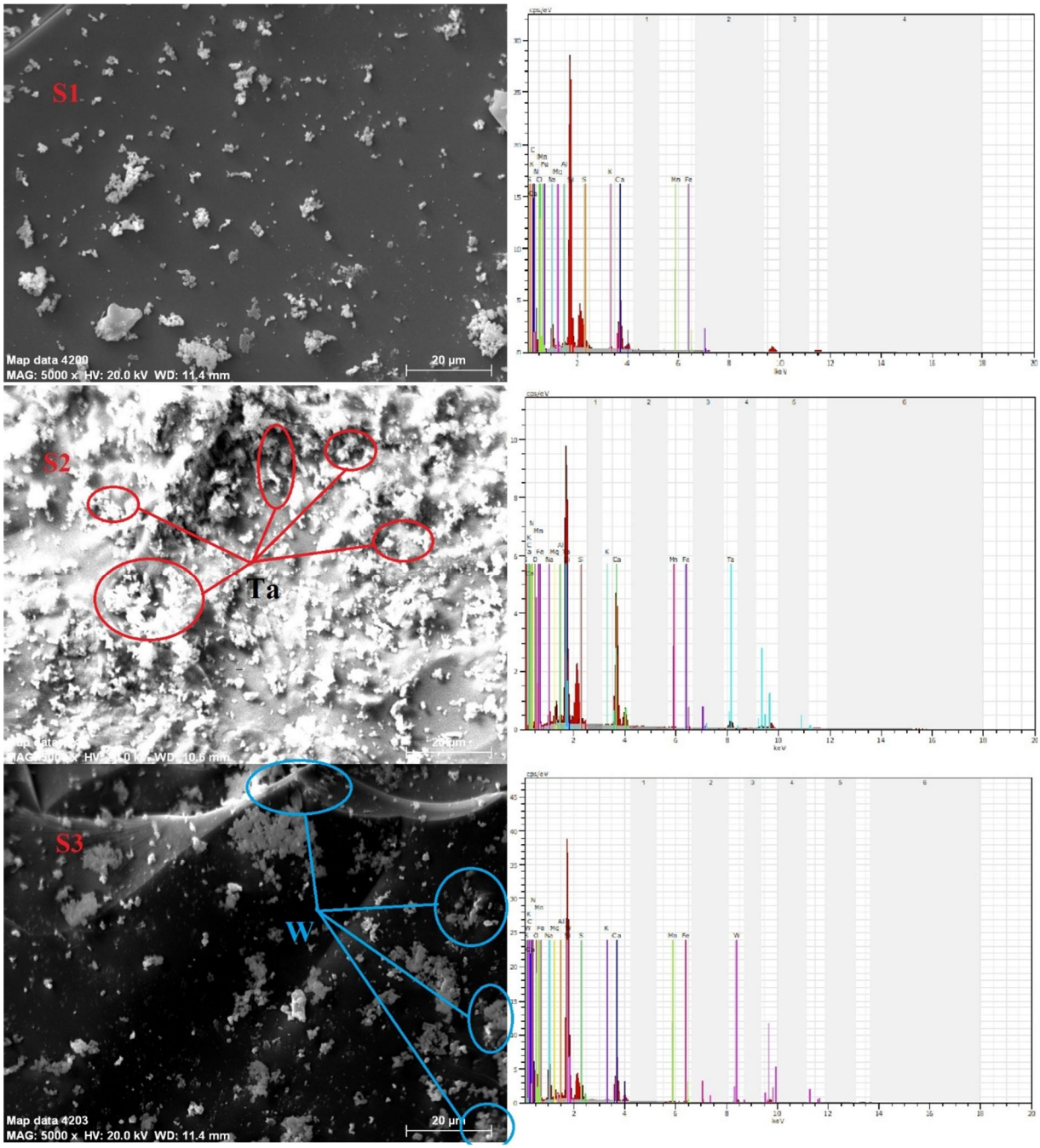

FIG. 3. The results of EDS for the S group samples.

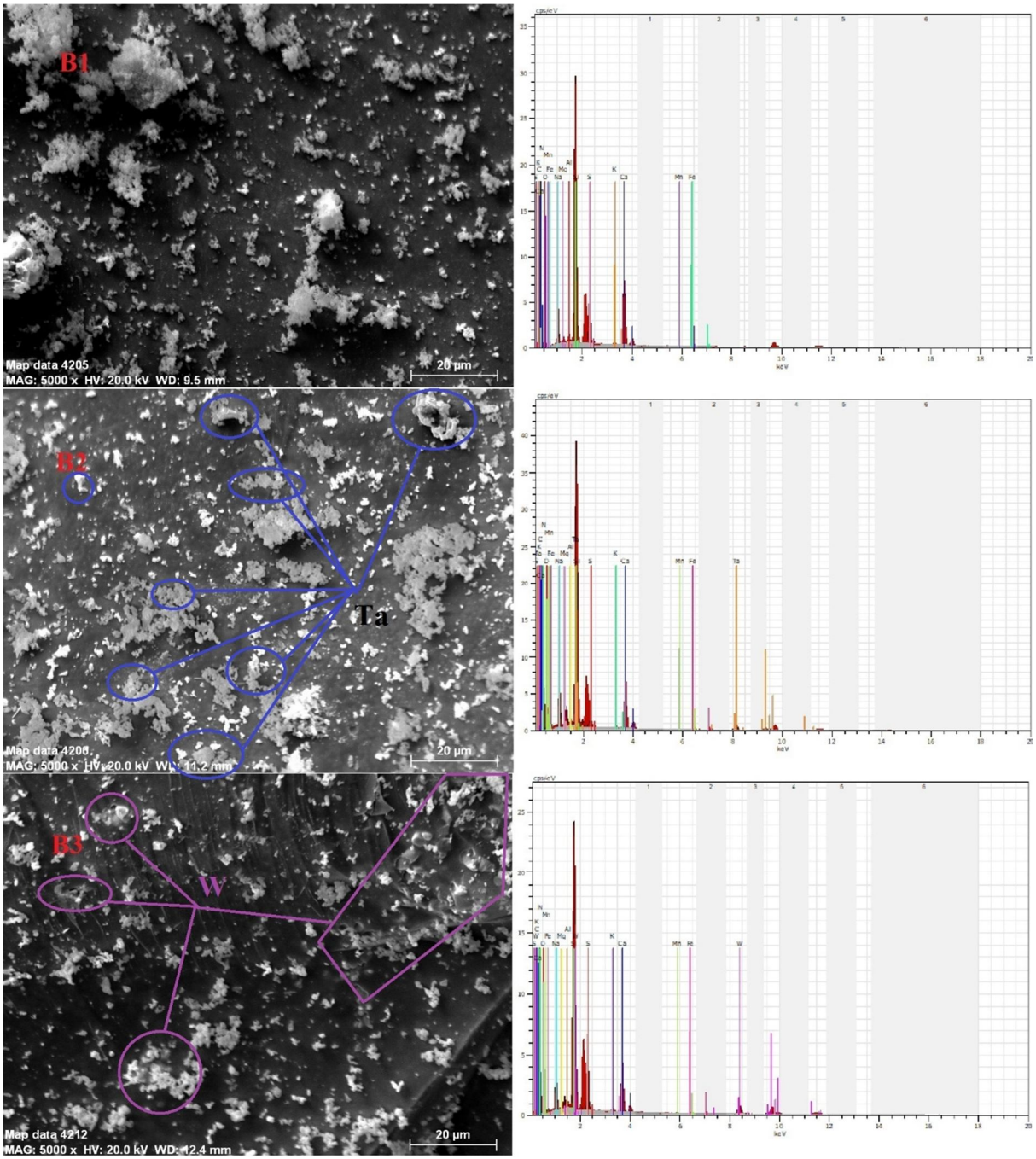

FIG. 4. The results of EDS for the B group samples.

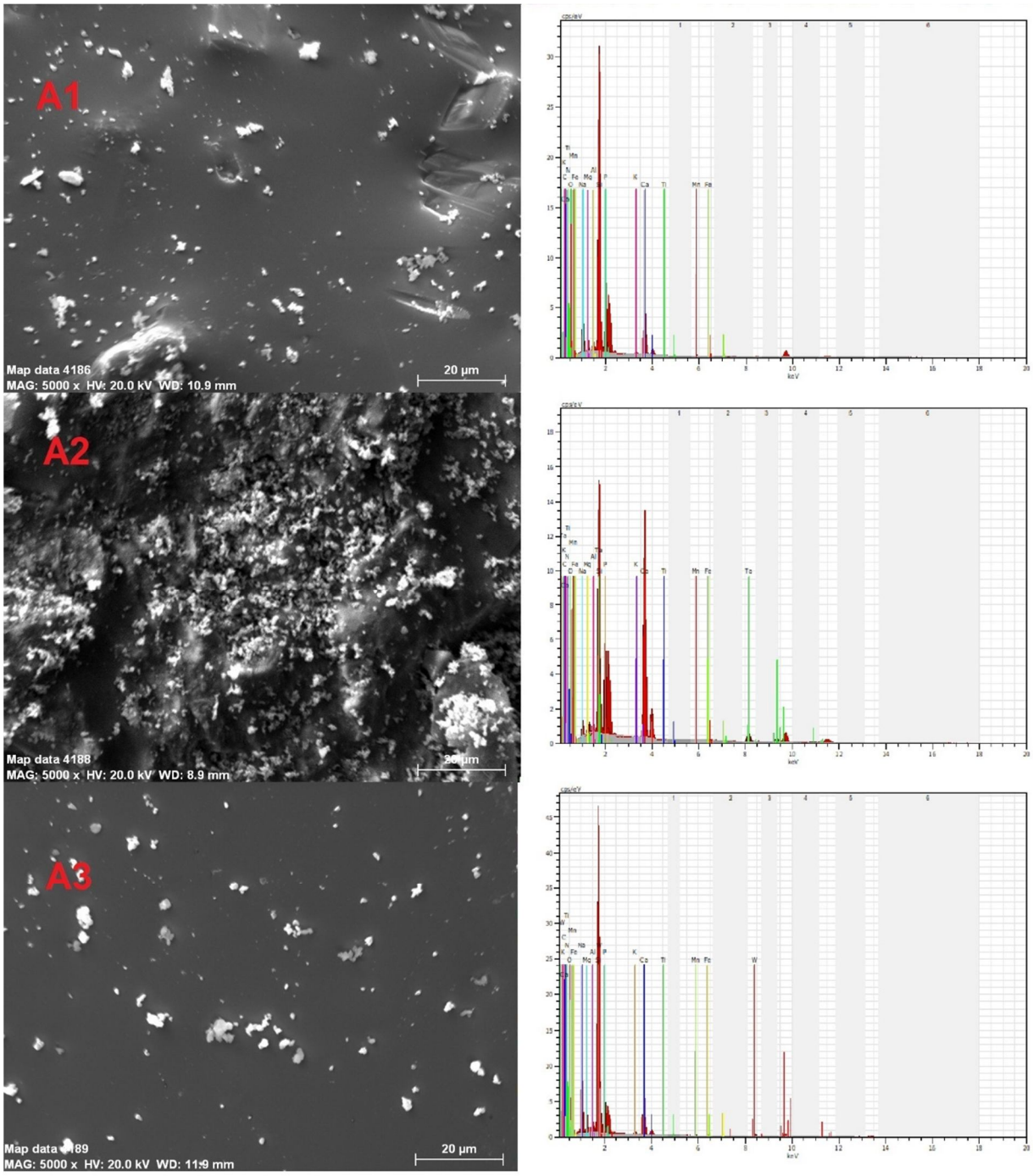

FIG. 5. The results of EDS for the A group samples.

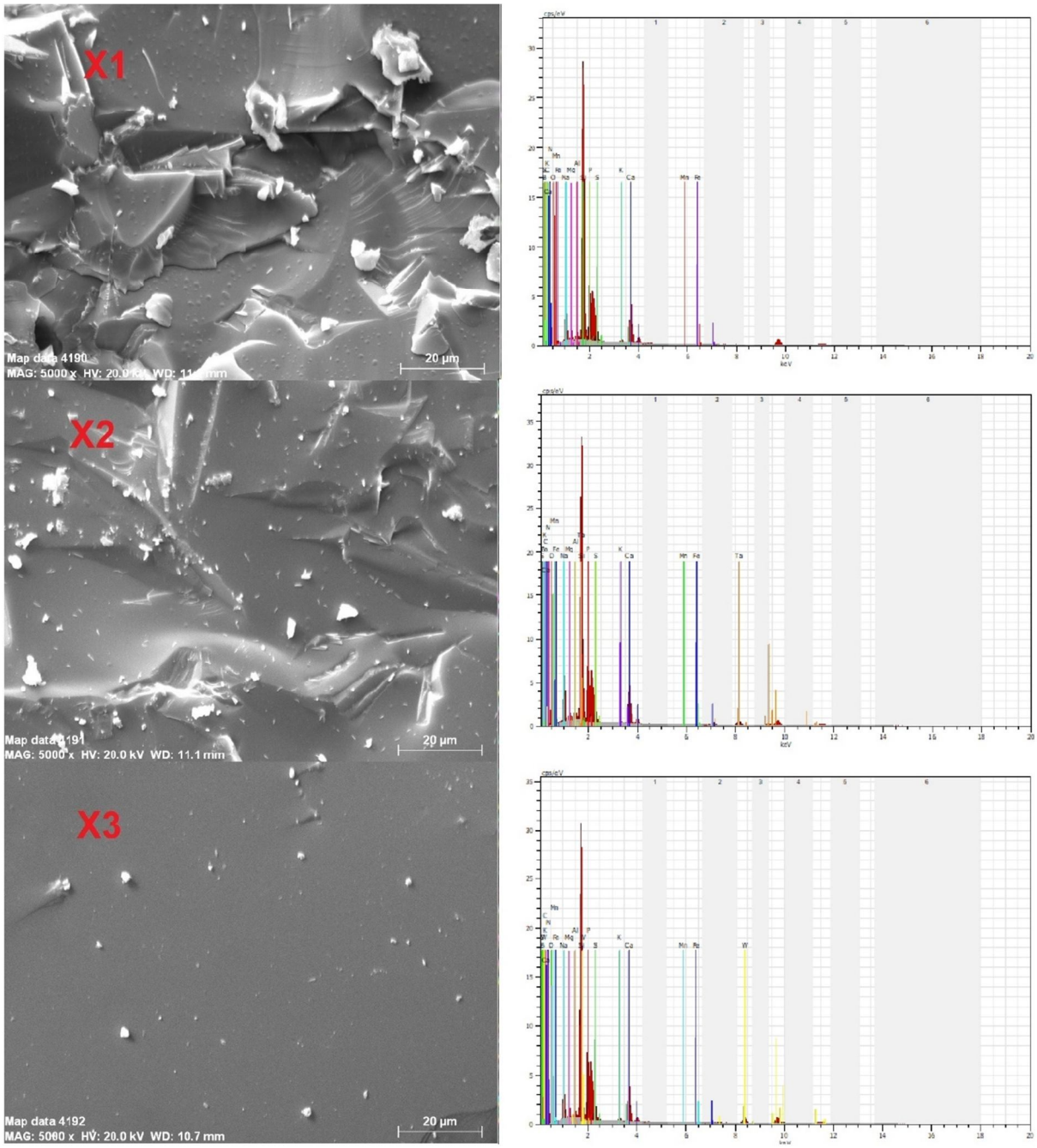

FIG. 6. The results of EDS for the X group samples.

TABLE 2. EDS results of the samples determined in the SEM images.

Samples	O	C	Ca	K	Si	Na	Fe	Ti	Mg	S	P	Al	B	N	Mn	Ta	W	Density
S1	45.10	1.21	10.86	0.33	24.37	5.53	0.37	-	0.56	5.06	-	0.71	-	5.77	0.14	-	-	1.645
S2	48.60	2.05	22.82	0.14	1.03	3.52	0.23	-	0.90	0.85	-	1.20	-	6.49	0.22	11.94	-	2.567
S3	39.27	1.12	11.02	0.39	19.26	9.78	0.29	-	1.38	2.83	-	1.23	-	3.12	0.16	-	10.14	2.566
B1	42.59	1.11	14.38	0.24	23.68	6.06	0.35	-	0.68	5.72	-	0.84	-	4.18	0.17	-	-	1.647
B2	51.68	1.84	10.45	0.28	5.00	9.55	0.21	-	1.20	0.95	-	1.36	-	4.60	0.12	12.76	-	2.695
B3	34.55	2.01	9.91	0.35	13.61	5.81	0.25	-	0.78	6.18	-	0.93	-	5.16	0.13	-	20.33	3.722
A1	44.30	1.62	8.45	0.24	23.83	6.27	0.42	0.13	1.26	-	11.6	1.32	-	0.25	0.30	-	-	1.678
A2	35.31	4.98	29.22	0.1	7.54	0.47	0.38	0.08	0.54	-	7.91	0.58	-	-	0.12	11.87	-	2.611
A3	36.86	1.01	8.02	0.43	24.54	11.63	0.25	0.06	2.27	-	5.78	1.68	-	0.01	0.10	-	7.36	2.321
X1	38.99	1.24	8.47	0.34	22.36	6.28	0.35	-	1.09	1.74	8.01	1.07	6.06	3.89	0.14	-	-	1.664
X2	27.04	0.93	9.35	0.39	21.37	6.94	0.28	-	1.21	2.05	9.98	1.18	1.59	4.12	0.14	13.42	-	2.939
X3	20.80	1.10	8.29	0.57	23.16	5.27	0.40	-	0.96	2.87	11.81	0.90	3.15	4.15	0.18	-	16.39	3.384

3.2. XRD Analysis

The room-temperature XRD patterns are displayed in Fig. 7. The observed diffraction peaks were evaluated by the literature [16, 29-34]. The X-ray analyses of the S and B groups reveal similar properties and the presence of α-Ta, β-Ta, α-W, calcite, and ferrite main phase peaks. The **S2** and **B2** samples, which were produced with Ta addition, exhibit dominant α-Ta and β-Ta. The S3 and B3 samples produced by W addition give the α-W main phase. It is observed that the A and X groups show more amorphous structure in XRD patterns. In the S and B group samples, both amorphous and crystalline features are determined.

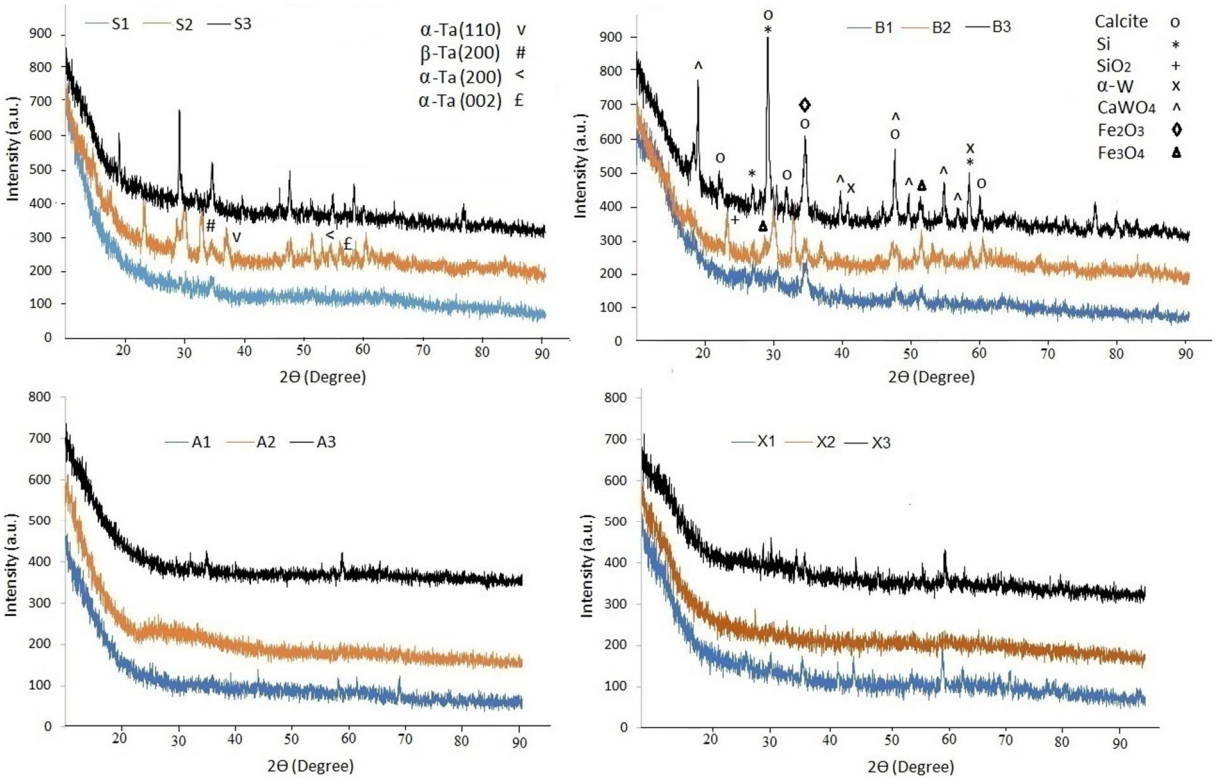

FIG. 7. XRD patterns of the samples.

The presence of the α-Ta main phase at ≈ 36°, seen in the X-ray spectra of the S2 and B2, corresponds to a crystallite size of 20.42 nm for β = 0.428. In the S3 and B3 samples, the α-W main phase at ≈ 40° has a crystallite size of 41.51 nm for β = 0.213. The crystallite size of the other main phase at ≈ 29° assigned to calcite is 27.46 nm for β = 0.318.

The relationship between crystallite size and grain size suggests that variations in crystallite size directly influence grain size. Consistently, the B3, which exhibits the largest crystal size among the samples, as determined by SEM images, also shows the largest grain size in SEM images. This correlation confirms that the calculated crystallite sizes align well with the grain size observations from SEM analysis.

3.3. EPR Study

EPR is a method used to detect paramagnetic centers in materials under the influence of an external magnetic field. The EPR resonance condition is expressed by the equation hυ = gβH, with g-value, where β is the Bohr magneton, H is the magnetic field, h is Planck's constant, and υ is the microwave frequency. This equation is used for the determination of the values. In EPR spectra, centers can originate from both crystalline and glassy regions of the material. The g-factor characterizes the paramagnetic center by indicating the effect of the local magnetic field on unpaired electrons; hence, it provides information about the orbital nature of these electrons and the type of paramagnetic center present [35]. The room-temperature EPR spectrum common to all samples is shown in Fig. 8. Fe^{+3} ions or high-spin isolated Fe^{+3} in the structure are determined with a g value of ≈ 4.21

for the samples [36]. The line was observed to be similar for all the studied samples; therefore, the spectrum of S3 is shown in Fig. 8. In general, it is expected to observe six hyperfine lines of Mn^{+2} in the EPR spectrum, but in this study, a broad EPR signal with a g-value of ≈ 1.996, which can be assigned to Mn+2 (I = 5/2) was observed. This broad signal can be the result of the random and close localization of Mn ions and their dipole-dipole or exchange interactions [37].

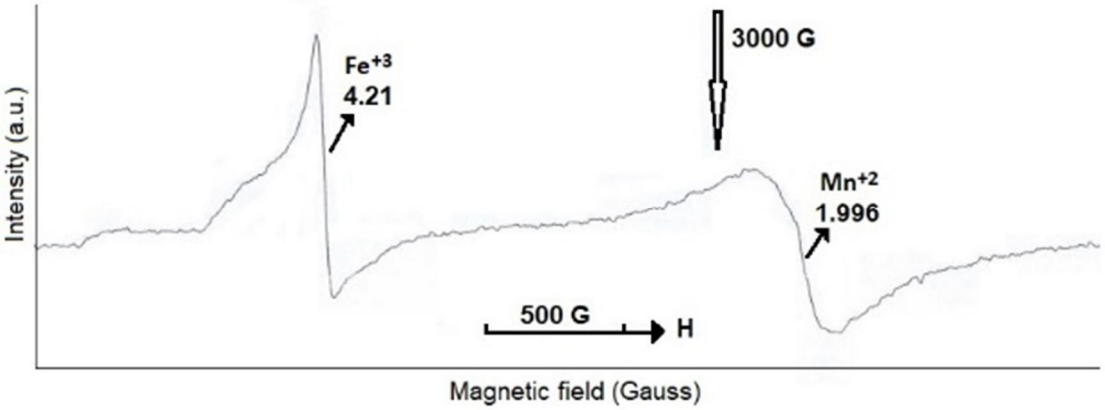

FIG. 8. EPR spectrum of the sample S3.

3.4. Radiation Protection Analysis

The Phy-X/PSD code was used to calculate radiation attenuation parameters based on the chemical compositions (w%) of the samples determined by EDS (Table 2). The variation of MAC with photon energy (1 keV–100 GeV) is shown in Fig. 9(a). The behavior in low, medium, and high energy regions corresponds to the photoelectric effect (PE), Compton scattering (CS), and pair production (PP), respectively, which influence the observed changes in MAC. To validate the results, XCom [38] calculations were also performed, showing good agreement with the Phy-X/PSD values. The MAC values at representative low, medium, and high energies calculated by both methods are listed in Table 3. The LAC values changed with photon energies (1keV-100GeV), as demonstrated in Fig. 9(b). Since LAC depends on the material density and MAC, the LAC values of all samples are observed to be similar across the energy range. Additionally, the samples' MAC results were compared with previously reported values for ordinary concrete (OC) [39] and cement [40], as shown in Fig. 9(c). At low photon energies, the MAC values (and consequently the shielding efficiencies) of the samples can be ordered as follows: B3 > X3 > A2 > X2 > S2 > B2 > S3 > A3 > Cement > B1 > A1 > S1 > X1 > OC. At high photon energies, the shielding efficiency ranking of the samples is as follows: B3 > X3 > A2 > X2 > S2 > B2 > Cement > A3 > S3 > B1 > A1 > S1 > X1 > OC. Among the samples with W addition, the B and X groups exhibit higher shielding performance, while among the samples with Ta addition, the A and X groups show better protection. Interestingly, the B and A samples without Ta or W also demonstrate higher shielding efficiency than the remaining samples. Across all energy ranges, a common observation is that all prepared samples outperform OC in radiation protection.

The variations of mean free path (MFP) and half-value layer (HVL) with photon energy are shown in Fig. 10(a)-10(b). Materials with lower HVL and MFP values are considered better shields. The B3 sample exhibits the lowest MFP and HVL values, indicating the highest shielding potential, while the X1 sample shows the highest MFP and HVL values. Based on HVL values, the order of shielding efficiency for all samples is: B3 > X3 > X2 > A2 > S2 > B2 > S3 > A3 > A1 > B1 > S1 > X1. The radiation shielding capabilities of the samples were also compared with OC and cement (Fig. 10c). It is evident that samples numbered two and three consistently have lower HVL values than OC and cement, whereas the first-numbered samples exhibit lower shielding efficiency than these conventional materials.

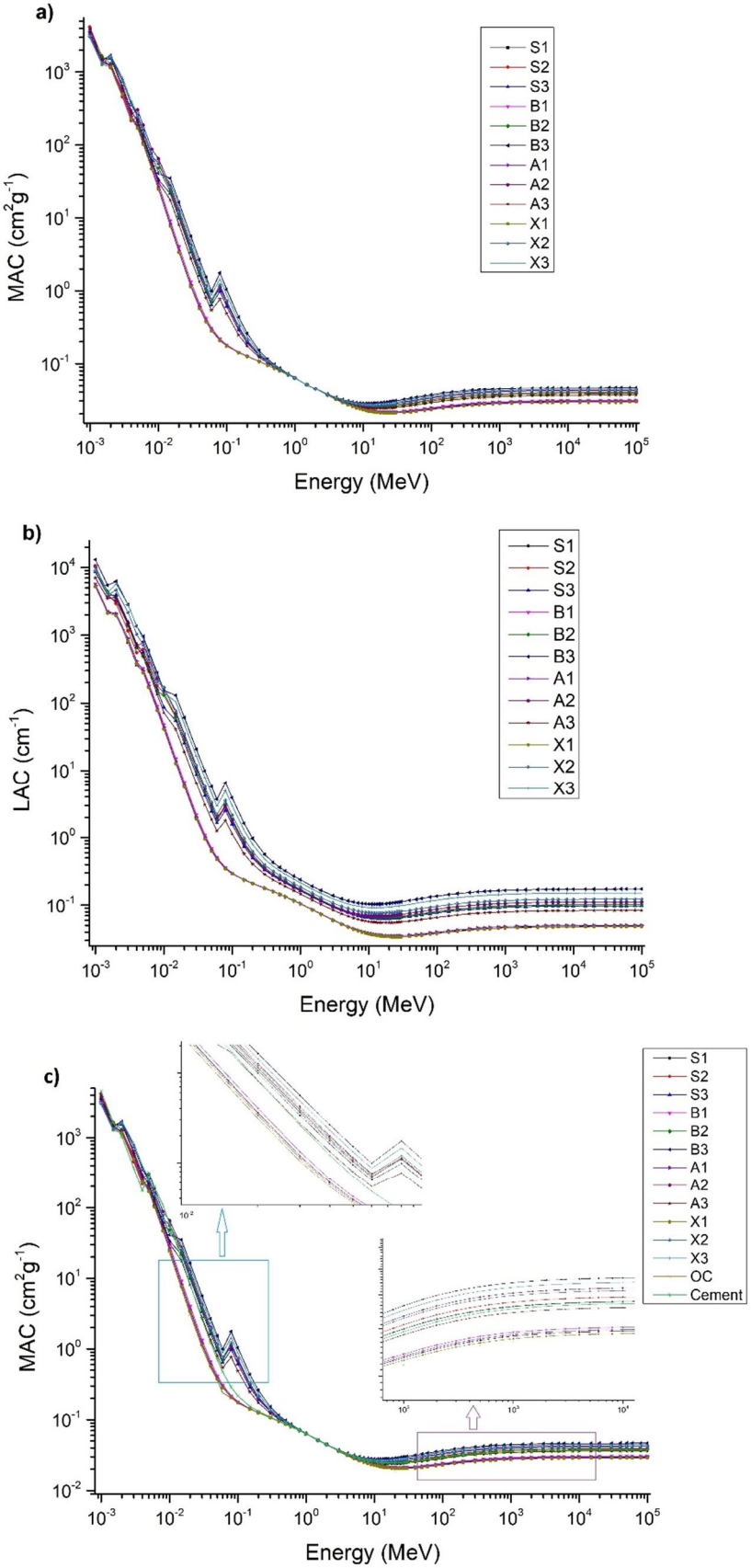

FIG. 9. The dependence of (a) MAC, (b) LAC, and (c) comparison of MAC values with OC and cement on photon energies.

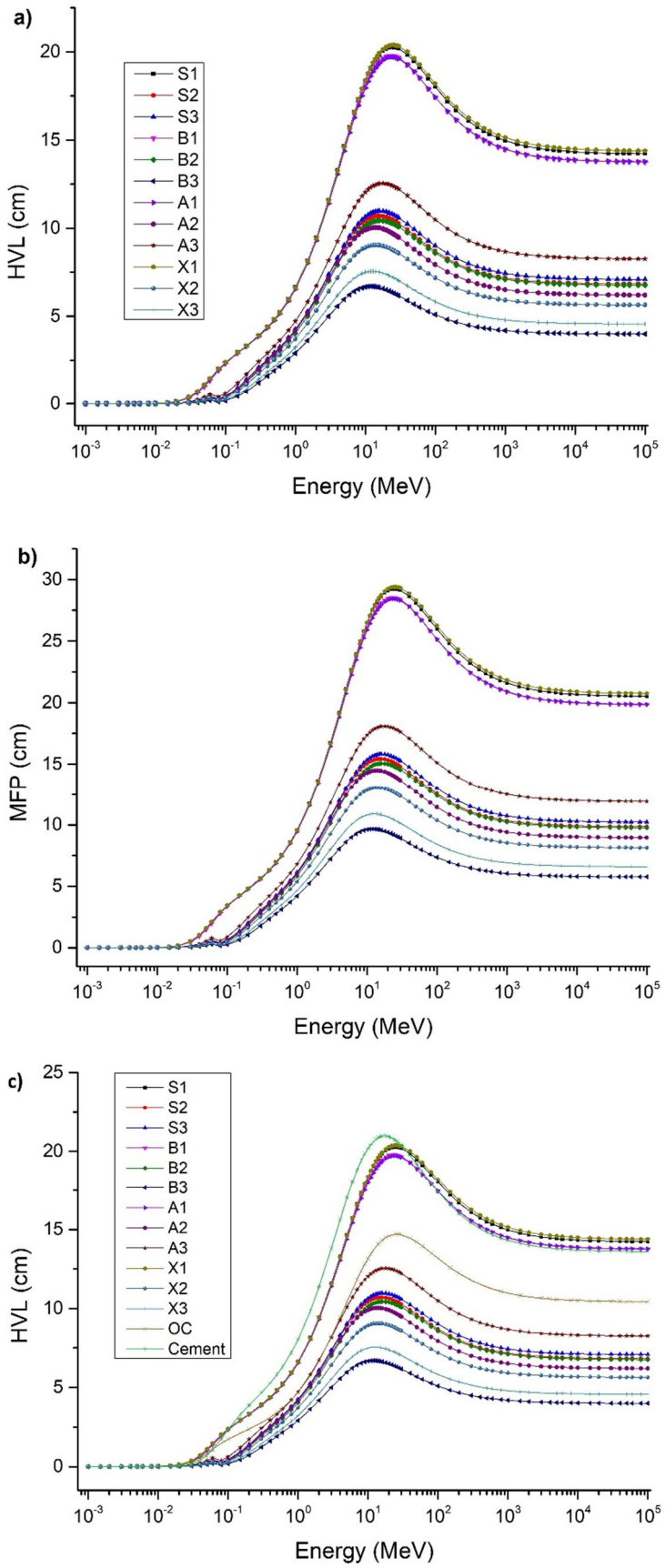

FIG. 10. The dependence of (a) HVL, (b) MFP, and (c) the comparison of HVL values with OC and cement on photon energies.

TABLE 3. MAC values of the samples obtained by Phy-X/PSD and XCom for some energies.

	1.5×10^{-3} (MeV)	1.5×10^{-2} (MeV)	1.5×10^{-1} (MeV)	1.5×10^{0} (MeV)	1.5×10^{1} (MeV)	1.5×10^{2} (MeV)	1.5×10^{3} (MeV)
S1 Phy-x/PSD	1351.6	8.164	0.143	0.052	0.021	0.025	0.029
S1 Xcom	1351.0	8.163	0.143	0.052	0.021	0.025	0.029
S2 Phy-x/PSD	1597.6	24.62	0.310	0.052	0.025	0.033	0.038
S2 Xcom	1508.0	23.41	0.300	0.052	0.025	0.032	0.038
S3 Phy-x/PSD	1523.1	21.52	0.288	0.051	0.025	0.032	0.037
S3 Xcom	1526.0	21.57	0.288	0.051	0.025	0.032	0.037
B1 Phy-x/PSD	1378.1	9.201	0.144	0.052	0.022	0.025	0.029
B1 Xcom	1378.0	9.201	0.144	0.052	0.022	0.025	0.029
B2 Phy-x/PSD	1650.0	22.78	0.318	0.051	0.025	0.032	0.037
B2 Xcom	1650.0	22.78	0.320	0.051	0.025	0.032	0.037
B3 Phy-x/PSD	1471.3	34.96	0.435	0.051	0.028	0.039	0.045
B3 Xcom	1471.0	34.96	0.435	0.051	0.028	0.039	0.045
A1 Phy-x/PSD	1333.9	8.224	0.142	0.051	0.021	0.025	0.029
A1 Xcom	1334.0	8.225	0.142	0.051	0.021	0.025	0.029
A2 Phy-x/PSD	1447.8	27.54	0.312	0.051	0.026	0.035	0.041
A2 Xcom	1448.0	27.54	0.312	0.051	0.026	0.035	0.041
A3 Phy-x/PSD	1493.7	17.69	0.248	0.051	0.024	0.030	0.035
A3 Xcom	1494.0	17.69	0.025	0.051	0.024	0.030	0.035
X1 Phy-x/PSD	1278.8	7.704	0.141	0.051	0.021	0.024	0.028
X1 Xcom	1278.0	7.702	0.141	0.051	0.021	0.024	0.028
X2 Phy-x/PSD	1335.6	25.89	0.329	0.051	0.026	0.035	0.040
X2 Xcom	1336.0	25.91	0.329	0.051	0.026	0.035	0.040
X3 Phy-x/PSD	1260.8	30.83	0.379	0.051	0.027	0.037	0.043
X3 Xcom	1261.0	30.83	0.379	0.051	0.027	0.037	0.043

The variation of Z_{eff} values versus photon energy is shown in Fig. 11. In the low-energy region, due to the PE cross-section (Z^{4-5}), the Z_{eff} values are the highest. In the mid-energy region, based on the change of CS cross-section ($E^{-3.5}$), a rapid decrease is determined. In the high-energy region, because of the variation of the PP cross-section (Z^2), the values increase slightly and then remain constant [41]. The Z_{eff} values are affected by the presence of elements with different atomic numbers within the material. Since Z_{eff} is the atomic number of the material, including more than one element, structures with large atomic number differences cause fluctuations. Samples numbered two and three, which contain Ta and W, show the highest Z_{eff} values and the most pronounced fluctuations. Consequently, B3 and X3 exhibit the highest shielding performance, while S1 and X1 show the lowest, based on Z_{eff} values.

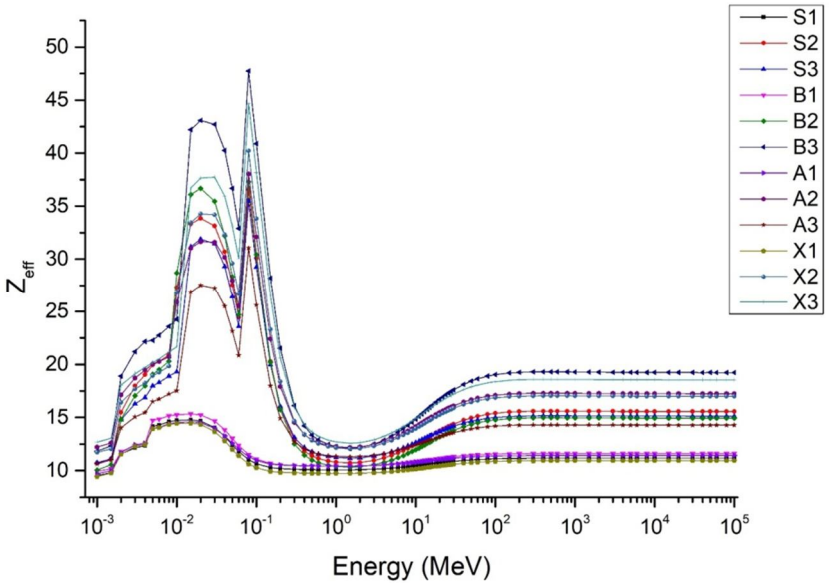

FIG. 11. The dependence of Z_{eff} on photon energies.

The EABF is the buildup factor related to the energy absorbed or deposited in the interacting material. On the other hand, EBF is another type of buildup factor in which there is an exposure to interacting material. The dependence of EBF and EABF on photon energies is illustrated in Figs. 12-13. In the low-energy region, EBF and EABF have lower values based on the PE, whereas in the mid-energy region, they have their highest values based on CS due to the scattered large number of photons. In the high-energy region, the PP effect causes strong photon absorption, and EBF and EABF decrease [41]. According to the obtained EBF and EABF values, the photons cluster relatively higher in X1 and A1 samples and lower in B3 and X3. Therefore, it is noted that the CS process is dominantly seen for X1 and A1 samples.

The samples' fast neutron shielding capabilities were also established by Phy-X/PSD, and the cross-sections are given in Fig. 14. As seen in the figure, the highest neutron attenuation is achieved for B3 and X3, the lowest attenuation is for B1, S1, and A1. It can also be concluded that FNRCS values of B3 and X3 are better than that those of the previously reported OC.

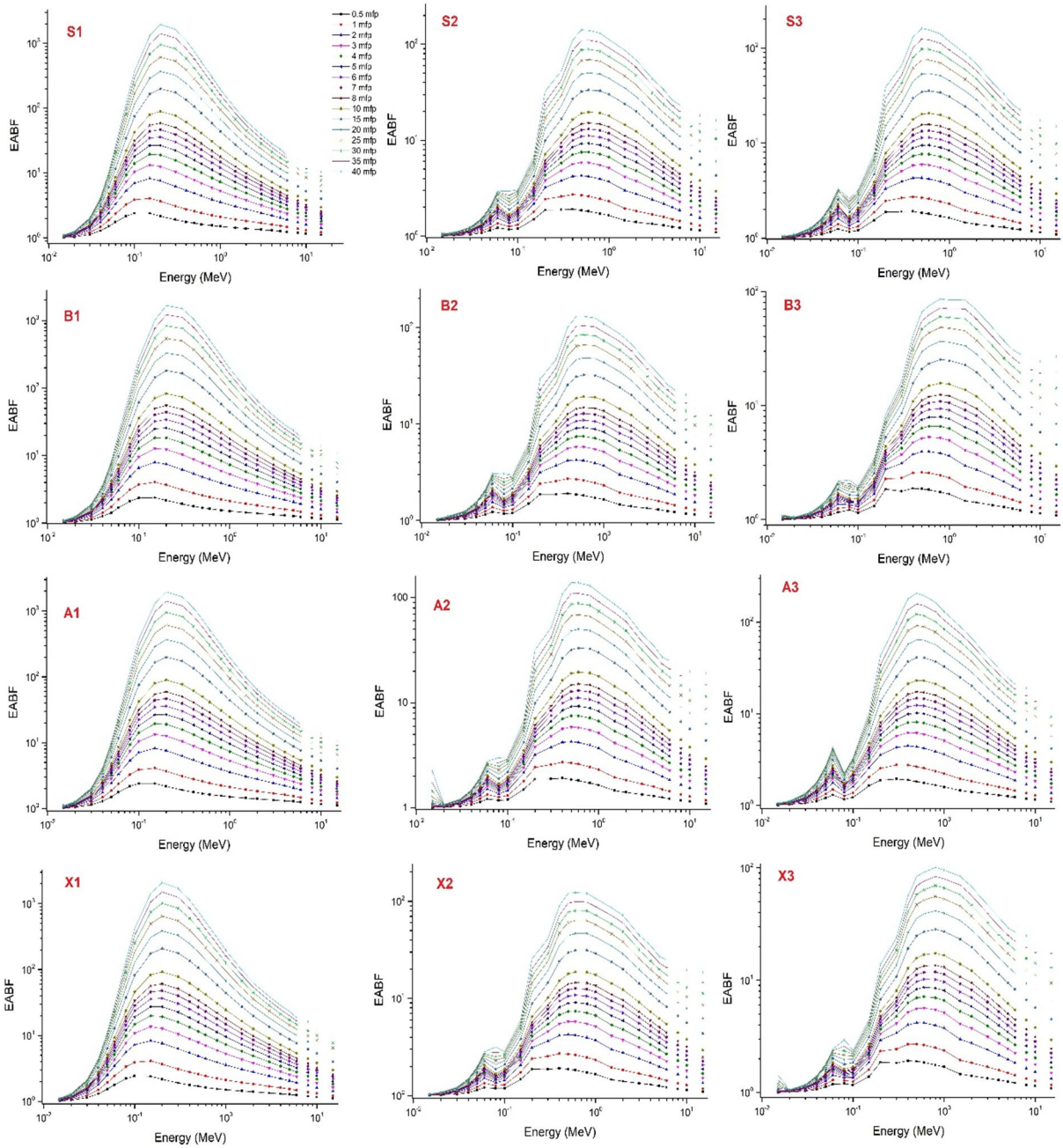

FIG. 12. The dependence of EABF values on photon energies.

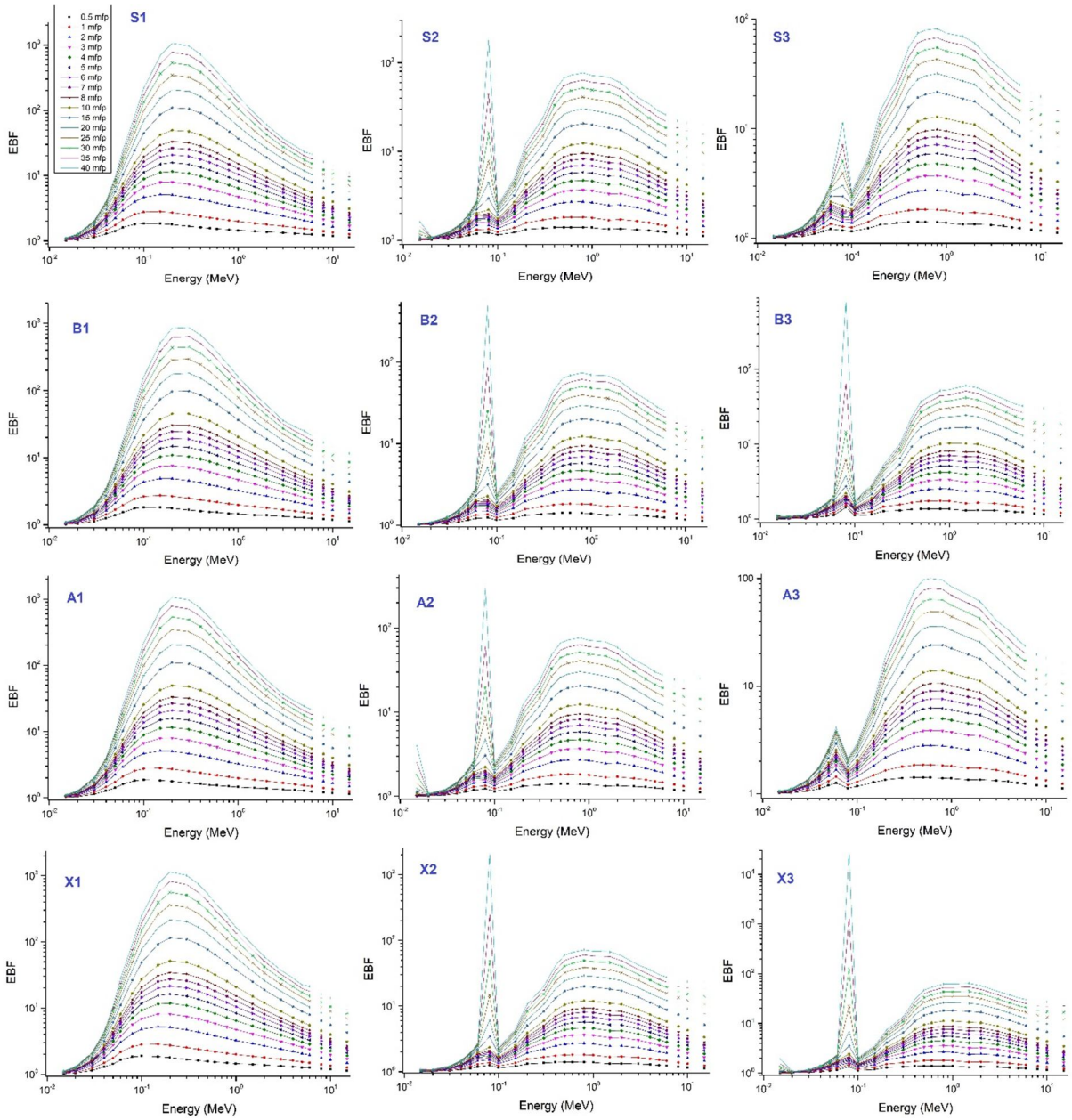

FIG. 13. The dependence of EBF values on photon energies.

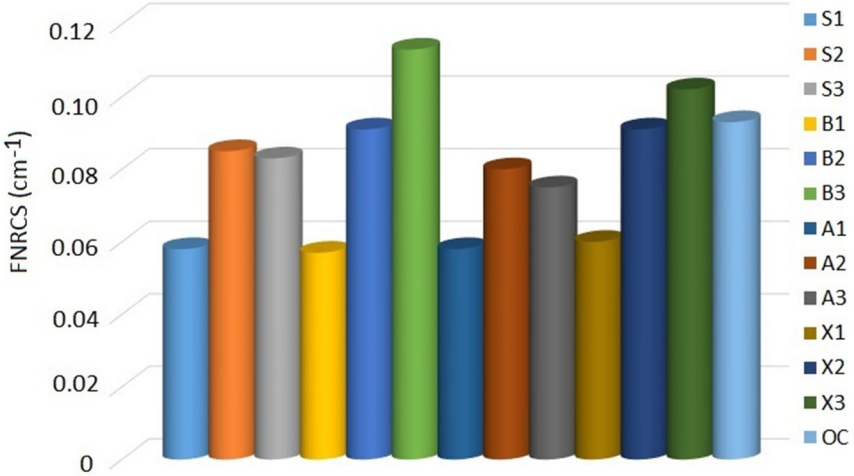

FIG. 14. The FNRCS values of the samples.

4. Conclusion

The motivation of this study was to produce alternative materials by reusing waste, aiming to achieve higher RSC. In accordance with this purpose, RSC and structural features of the waste samples were determined by Phy-X/PSD code and spectroscopic techniques. The EPR spectra revealed a signal with a g-value of 4.21, which is assigned to the ferric center. Using the Debye-Scherrer equation, crystallite sizes of the main phases were calculated based on the XRD spectra. Both EDS analysis and elemental mapping indicate that the A and X groups exhibit the most homogeneous structures. Based on the computational results of radiation shielding parameters, it is noteworthy to emphasize that the existence of heavy metal Ta and W contents with higher atomic number in the sample advances the RSCs of the material. The addition of Ta and W to the samples can also improve the mechanical features, such as tensile strength and durability of the materials. In addition, it can be said that the neutron attenuation capacity of B3 and X3 is the highest, similar to their photon attenuation capacity. Among the samples numbered one, B1 has the highest RSC, and X1 has the lowest. X2 is the most effective shield, and B2 the least among the samples numbered two. RSC of B3 is the highest, while that of A3 is the lowest within the samples numbered three. Overall, all designed waste-based samples show promise as novel radiation shielding materials. Future studies focusing on mechanical properties, such as elasticity and tensile strength through measurements of Young's modulus or Poisson's ratio, would provide additional valuable insights into the applicability of these materials.

Acknowledgement

Experimental results were obtained from the Advanced Technology Research & Application Center (ILTEK) of Selcuk University.

Competing Interests

The authors declare that they have no known competing financial interests or personal relationships that could have appeared to influence the work reported in this paper.

Ethics Approval

Not applicable

Consent to Participate

Not applicable

Consent for Publication

Not applicable

Author Contributions

All authors contributed to the study conception and design. Material preparation, data collection, and analysis were performed by Murat AYGUN and Zeynep AYGUN. The first draft of the manuscript was written by Zeynep AYGUN, and all authors commented on previous versions of the manuscript. All authors read and approved the final manuscript.

Availability of Data and Materials

Data from this study are available from the corresponding author on responsible request.

Funding

This work was supported by Bitlis Eren University Scientific Research Projects Coordination Unit (BEBAP) with a project grant number 2023.14.

References

[1] Islam, G.M.S., Rahman, M.H., and Kazi, N., Int. J. Sustain. Built. Environ., 6 (1) (2017) 37.

[2] Imbabi, M.S., Carrigan, C., and McKenna, S., Int. J. Sustain. Built. Environ., 1 (2) (2012) 194.

[3] Detwiler, R., Bhatty, J.I., and Bhattacharja, S., "Supplementary Cementing Materials for Use in Blended Cements", (Research and Development Bulletin Rd112t, Portland Cement Association, Skokie, Illinois, USA, 1996).

[4] Eid, M.S., Bondouk, I.I., Saleh, H.M., Omar, K.M., Sayyed, M.I., El-Khatib, A.M., and Elsafi, M., Nucl. Eng. Technol., 54 (4) (2022) 1456.

[5] Kim, I.S., Choi, Y.S., Choi, S.Y., and Yang, E.I., Ann. Nucl. Energy, 133 (2019) 750.

[6] Binici, H., Aksogan, O., Sevinc, A.H., and Cinpolat, E., Constr. Build. Mater., 93 (2015) 1145.

[7] Nassar, R.U.D. and Soroushian, P., Constr. Build. Mater., 29 (2012) 368.

[8] Ryou, J., Shah, S.P., and Konsta-Gdoutos, M.S., Adv. Appl. Ceram. Struct. Funct. Bioceram., 105 (6) (2006) 274.

[9] Rashad, A.M., Constr. Build. Mater., 72 (2014) 340.

[10] Taha, B. and Nounu, G., J. Mater. Civ. Eng., 21 (12) (2009) 709.

[11] Khazaalah, T.H. et al., J. Mater. Res. Technol., 19 (2022) 3355.

[12] Jasmine, J.N.Z., Ramzun, M.R., Zahirah, N.A.N., Azhar, A.R., Hana, M.A.M., Zakiah, Y.N., and Yasmin, M.R., J. Phys. Conf. Ser., 1497 (1) (2020) 012010.

[13] Mancı, A. and Sarıışık, A., Civiltech., 2019 (2019) 124.

[14] Ince, C. and Derogar, S., Emerg. Mater. Res., 7 (2) (2018) 118.

[15] Khazaalah, T.H., Mustafa, I.S., and Sayyed, M.I., Nucl. Eng. Technol., 54 (12) (2022) 4708.

[16] Aygun, M., Aygun, Z., and Ercan, E., Radiat. Phys. Chem., 212 (2023) 111147.

[17] Sayyed, M.I., Almurayshid, M., Almasoud, F.I., Alyahyawi, A.R., Yasmin, S., and Elsafi, M., Mater. (Basel), 15 (23) (2022) 8371.

[18] Aygun, Z., Aygun, M., and Yarbasi, N., J. New Results Sci., 10 (2021) 46.

[19] Elsafi, M., Almousa, N., Al-Harbi, N., Almutiri, M.N., Yasmin, S., and Sayyed, M.I., J. Mater. Res. Technol., 22 (2023) 269.

[20] Aygun, Z. and Aygun, M., Int. J. Environ. Sci. Technol., 19 (2022) 5675.

[21] Karpuz, N., J. Radiat. Res Appl. Sci., 16 (4) (2023) 100689.

[22] Sakar, E., Ozpolat, O.F., Alım, B., Sayyed, M.I., and Kurudirek, M., Radiat. Phys. Chem., 166 (2020) 108496.

[23] Xiang, C. et al., Intermetal., 104 (2019) 143.

[24] Jackson, D.F. and Hawkes, D.J., Phys. Reports, 70 (1981) 169.

[25] Harima, Y., Sakamoto, Y., Tanaka, S., and Kawai, M., Nucl. Sci. Engineer., 94 (1986) 24.

[26] Harima, Y., Radiat. Phys. Chem., 41 (1993) 631.

[27] ANSI/ANS 643. "Gamma-ray Attenuation Coefficients and Buildup Factors for Engineering Materials", (American Nucl. Soc., La Grange Park, Illinois, 1991).

[28] Scherrer, P., Röntgenstrahlen Nachr Ges Wiss Göttingen, 26 (1918) 98.

[29] Noval, V.E. and Carriazo, J.G., Mater. Res., 22 (3) (2019) e20180660.

[30] Brar, L.K., Singla, G., Kaur, N., and Pandey, O.P., J. Therm. Anal. Calorim., 119 (2015) 175.

[31] Moharana, P.L., Anwar, S., Islam, A., and Anwar, S., Perspectives in Sci., 8 (2016) 636.

[32] El-Mahllawy, M.S., Kandeel, A.M., Abdel Latif, M.L., and El Naga, A.M., Recycling, 3 (2018) 39.

[33] Aygun, Z. and Yarbasi, N., Karaelmas Sci. Engineer. J., 9 (2) (2019) 215.

[34] Polini, R., Marcucci, A., D'Ottavi, C., Nunziante, P., De Filippis, P., and Marcheselli, G., ACS Sustain. Chem. Eng., 9 (25) (2021) 8458.

[35] Filek, M., Łabanowska, M., Kurdziel, M., and Sieprawska, A., Toxins (Basel), 9 (6) (2017) 178.

[36] Aygun, Z. and Aygun, M., Spectrochim. Acta A, 166 (2016) 73.

[37] Markevich, I., Korsunska, N., Stara, T., Vorona, I., Melnichuk, O., Venger, Y., and Khomenkova, L., J. Mater. Sci. Mater. Electron., 34 (2023) 646.

[38] Berger, M.J. and Hubbell, J.H., "XCOM: Photon Cross Sections Database", (Web Version 12 National Institute of Standards and Technology Gaithersburg, MD 20899 USA, 1987).

[39] Bashter, I.I., Ann. Nucl. Energy, 24 (17) (1997) 1389.

[40] Sathiparan, N. and De Zoysa, H.T.S.M., J. Build. Eng., 19 (2018) 216.

[41] Aygun, Z. and Aygun, M., Acta Phys. Polonica A, 5 (141) (2022) 507.

Volume 18, Number 4, 2025. pp. 517-527

Jordan Journal of Physics

ARTICLE

Efros-Shklovskii Variable Range Hopping Conduction in ^{70}Ge:Ga Semiconductor at Very Low Temperature

Mohamed Errai[a,b], Mohammed Bellioua[b], Ahmed Tirbiyine[b], Abderrhman Nait Alla[c], Khalid Abbiche[a], Abdelhamid El kaaouachi[d], Lahcen Ait benali[e], El Mahdi Kamili[a], Reda El Abbadi[a] and **Mohamed Boumdyan[a]**

[a] *LAMISNE Laboratory, Polydisciplinary Faculty of Taroudant, Ibn Zohr University, 80000 Agadir, Morocco.*

[b] *LMS3E Laboratory, Faculty of Applied Sciences Ait Melloul, Ibn Zohr University, 80000 Agadir, Morocco.*

[c] *Faculty of Applied Sciences Ait Melloul, Ibn Zohr University, 80000 Agadir, Morocco.*

[d] *Physics Department, Ibn Zohr University, Faculty of Sciences, Agadir, Morocco.*

[e] *CPA-Centre Régional des Métiers de l'Enseignement et Formation CS, Casablanca, Morocco.*

Doi: **https://doi.org/10.47011/18.4.9**

Received on: 17/07/2024; *Accepted on: 06/01/2025*

Abstract: In this study, we focused on investigating the electrical transport processes within the three-dimensional ^{70}Ge:Ga system at low temperatures, ranging from 0.05 K to 0.25 K, in the absence of a magnetic field. Our analysis specifically targeted the insulating side of the metal-insulator transition (MIT). The five samples studied had Ga concentrations n ranging from 1.753 10^{17} to 1.844 10^{17} cm^{-3}. We established that the temperature T dependence of the electrical conductivity follows the Efros-Shklovskii variable range hopping (ES-VRH) mechanism between the localized states located around the Fermi level (E_F). This behavior indicates that the density of states (DOS) is canceled very close to the E_F, the formation of a soft Coulomb gap (CG) near E_F. Notably, we did not observe any transition to the Mott-VRH regime with $T^{-0.25}$, which is characterized by a nearly constant and non-zero DOS near E_F. Furthermore, we estimated some Efros and Shklovskii hopping parameters to further understand the electrical transport properties of the ^{70}Ge:Ga system.

Keywords: Variable range hopping, Electrical transport properties, Coulomb gap, Density of state, Electrical conductivity, ^{70}Ge:Ga semiconductor.

1. Introduction

Germanium, as a semiconductor material, holds significant importance in the microelectronics industry [1] due to its remarkable electrical transport properties. It finds diverse applications in various industrial sectors, including field effect transistors [2], photovoltaic cells [3], laser diodes, temperature sensors [4], photodetectors, magnetic field sensors, and fiber optic manufacturing. Additionally, germanium is widely utilized as an alloy with silicon to create high-performance integrated circuits, further extending its impact in modern electronic devices.

On the insulating side of the metal-insulator transition (MIT), the low-temperature electrical transport in insulators, amorphous, and disordered semiconductors is primarily governed by the variable range hopping (VRH) conduction mechanism [5–21]. This mechanism involves

Corresponding Author: Mohamed Errai **Email**: errai2013@gmail.com

charge carriers hopping between localized electronic states, as defined by Anderson's localization [22, 23], situated near the Fermi level (E_F). Specifically, this behavior is observed in materials where the Fermi energy lies below the mobility edge. VRH conduction establishes a relationship between electrical conductivity (σ) and temperature (T), providing insights into how the electrical conductivity varies with changes in temperature, offering valuable information about the transport properties of the materials in question.

The temperature-dependent electrical conductivity of ^{70}Ge:Ga material has been extensively studied near the MIT. Errai *et al.* [9] provided a comprehensive analysis of the transport mechanisms on both sides of the transition. For n > nc (metallic regime), the conductivity behavior is governed by weak localization and electron-electron interaction effects, while for n < nc (insulating regime), VRH conduction dominates. Their study highlighted the critical role of impurity concentration in determining the transport behavior across the MIT. Additionally, in a subsequent study focusing on the insulating side, Errai *et al.* [11] investigated the VRH conduction mechanism at very low temperatures, emphasizing the density of states (DOS) near E_F and the hopping processes between localized states. These foundational studies provide essential context for the current investigation, particularly regarding the interplay between disorder and electronic interactions in ^{70}Ge:Ga.

This study focuses on investigating the temperature-dependent electrical conductivity of ^{70}Ge:Ga material on the insulating side of the MIT in the absence of a magnetic field. By analyzing five samples with varying impurity concentrations (see Fig. 1), the research aims to elucidate the VRH conduction mechanism in this material and to characterize the DOS near E_F. The critical impurity concentration, $n_c = 1.859\times10^{17}\,cm^{-3}$, marks the transition between metallic ($n > n_c$) and insulating ($n < n_c$) regimes. This investigation seeks to deepen our understanding of the transport properties of ^{70}Ge:Ga and explore the implications of these findings for potential technological applications. It is worth noting that we have reanalyzed the experimental data for the ^{70}Ge Ga system, which was prepared and reported by Itoh *et al*. [24].

2. Theoretical Background

In the strong localization regime, electrons hop via tunneling between spatially distant but energetically close sites, and the hopping is not necessarily limited to nearest neighbors. Consequently, electronic conduction occurs through the variable range hopping (VRH) mechanism involving states close to the E_F. In this case, the temperature dependence of the hopping conductivity follows a universal form at low temperatures, expressed as:

$$\sigma = \sigma_0 \exp\left[-\left(\frac{T_0}{T}\right)^x\right] \quad (1)$$

where σ_0 represents the hopping conductivity prefactor, T denotes the Kelvin absolute temperature, and T_0 symbolizes the hopping temperature characteristic. The hopping exponent, x, depends on the dimension of the system and the specific hopping conduction mechanism. Indeed, it takes on values 1/3 and 1/4, respectively, for two-dimensional (2D) and three-dimensional (3D) materials in the case where the electrical transport is governed by the Mott variable range hopping (Mott-VRH) mechanism [25-29]. On the other hand, if x = 0.5, irrespective of the system's dimensions, the electrical conduction occurs within the Efros-Shklovskii variable range hopping (ES-VRH) regime [25-29]. In Mott 3D-VRH conduction, the hopping electrical conductivity exhibits the following behavior:

$$\mathrm{Ln}(\sigma) \propto T^{-0.25} \quad (2)$$

This dependence arises from the fundamental assumptions of Mott's theory, which states that the DOS is nearly constant around the E_F or varies very slowly. Furthermore, it assumes that long-range Coulomb interactions between charge carriers are negligible. Under these conditions, the hopping exponent takes the value x = 0.25 for 3D materials, and the temperature dependence of electrical conductivity can be expressed in a universal form known as Mott's law:

$$\sigma = \sigma_{Mott} \exp\left[-\left(\frac{T_{Mott}}{T}\right)^{0.25}\right] \quad (3)$$

where σ_{Mott} denotes a conductivity prefactor in the Mott regime and T_{Mott} represents the Mott characteristic temperature, indicating the degree of disorder, given by the relationship [37]:

$$T_{Mott} = \beta_{Mott}/k_B N(E_F)\ \xi^3 \quad (4)$$

The constant β_{Mott} is determined through numerical calculations employing the percolation method, and for 3D systems, it is evaluated as $\beta_{Mott} = 16$. In the context of Eq. (4), k_B refers to the Boltzmann constant, $N(E_F)$ represents the DOS at the E_F, and ξ signifies the localization length of the electronic wave function at zero magnetic field.

On the contrary, as per the ES-VRH model, electronic interactions gain significance between localized states, leading to a reduction in the DOS near the E_F. This interaction results in the formation of a parabolic pseudo-Coulomb gap [38, 39] at the E_F, commonly known as the soft Coulomb gap (CG). Under such conditions, the conductivity exhibits the following behavior:

$$\mathrm{Ln}(\sigma) \propto T^{-0.5} \quad (5)$$

Furthermore, it is essential to note that within the ES-VRH conduction mechanism, the DOS vanishes precisely at the E_F and exhibits a parabolic variation in the vicinity of E_F, particularly in three dimensions.

$$N(E) = \frac{3k^3}{\pi e^6}(E - E_F)^2 \quad (6)$$

The presence of the CG leads to the ES-VRH regime, where the power-law temperature dependence of electrical conductivity applies universally across all dimensions, and it is expressed as follows:

$$\sigma = \sigma_{ES} \exp[-(T_{ES}/T)^{1/2}] \quad (7)$$

In the ES regime, the conductivity prefactor is denoted as $\sigma_{ES,}$ and T_{ES} represents the characteristic ES temperature. As per the ES model, the temperature T_{ES} can be expressed using the following relation:

$$T_{ES} = \frac{\beta_{ES} e^2}{(4\pi\varepsilon\varepsilon_0)\, k_\beta\, \xi} \quad (8)$$

The expression (8), involves various parameters, where β_{ES},e, ε, ε_0, k_B, and ξ are denoted as follows: β_{ES} is a constant evaluated to be 2.8 by Shklovskii and Efros, e represents the charge of an electron, ε denotes the dielectric constant of the material (in Ge, ε is 15.4), ε_0 symbolizes the permittivity of vacuum, k_B stands for the Boltzmann constant, and ξ signifies the localization length of the wave function in zero magnetic field.

3. Results and Discussions

We conducted a thorough reanalysis of the experimental data for the ^{70}Ge:Ga system, as reported by Itoh *et al*. [24]. In Figs. 1 and 2, we present the logarithmic variations of the electrical conductivity $\ln(\sigma)$ versus $T^{-0.25}$ and $T^{-0.5}$ on the insulating side of the MIT for the five samples of the 3D system ^{70}Ge:Ga, within the temperature range of 0.02-0.25 K and at zero magnetic field.

Upon examining Figs. 1 and 2, we observe that both plots show nearly straight lines of similar quality. As a result, it becomes challenging to distinctly differentiate between the two laws, $T^{-0.25}$ (Mott VRH) and $T^{-0.5}$ (ES-VRH), solely based on these graphical representations. In order to determine an acceptable and accurate physical solution, we implemented the graphical procedure proposed by Zabrodskii and Zinoveva [40], along with the percentage deviation procedure [41-43]. These techniques facilitate the identification of the most appropriate conduction mechanism for the ^{70}Ge:Ga system in the insulating regime.

Zabrodskii and Zinoveva employed the general formula of VRH ($\sigma = \sigma_0 \exp[-(T_0/T)^x]$) to calculate the mathematical function w(T). This function exhibits a variation with temperature T, which can be expressed using the following formula:

$$w(T) = \ln\left[\frac{d\ln(\sigma)}{d\ln(T)}\right] = \ln(x) + x\ln(T_0) - x\ln(T) \quad (9)$$

Notably, Eq. (9) is equivalent to the form derived from Eq. (1). For a given point i, we can calculate the average values of w(T) and ln(T) as follows:

$$\overline{w(T_i)} = \mathrm{Ln}\left[\frac{\mathrm{Ln}(\sigma_{i+1}) - \mathrm{Ln}(\sigma_{i-1}))}{\mathrm{Ln}(T_{i+1}) - \mathrm{Ln}(T_{i-1})}\right] \quad (10)$$

with:

$$\mathrm{Ln}(T_i) = \frac{\mathrm{Ln}(T_{i+1}) + \mathrm{Ln}(T_{i-1})}{2}$$

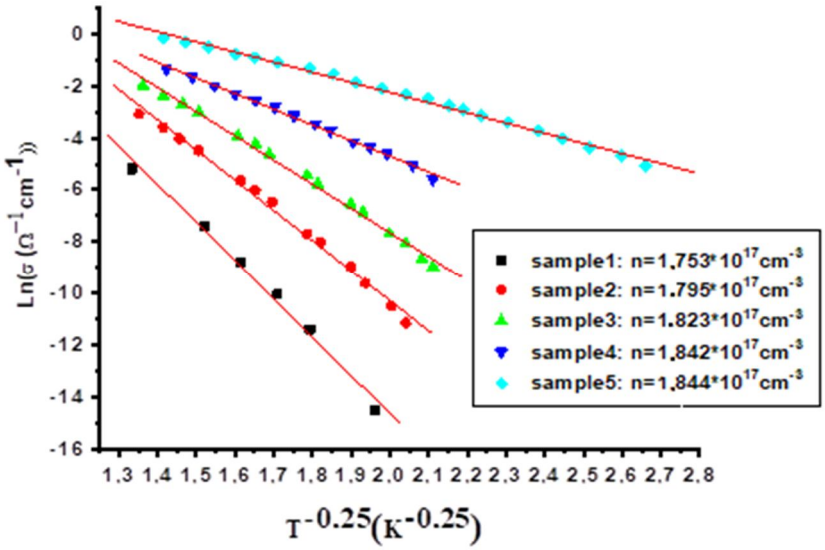

FIG. 1. Logarithmic variation of the electrical conductivity at zero field as a function of $T^{-0.25}$ for the five samples of the three-dimensional ^{70}Ge:Ga system over the full temperature range 0.05-0.25 K.

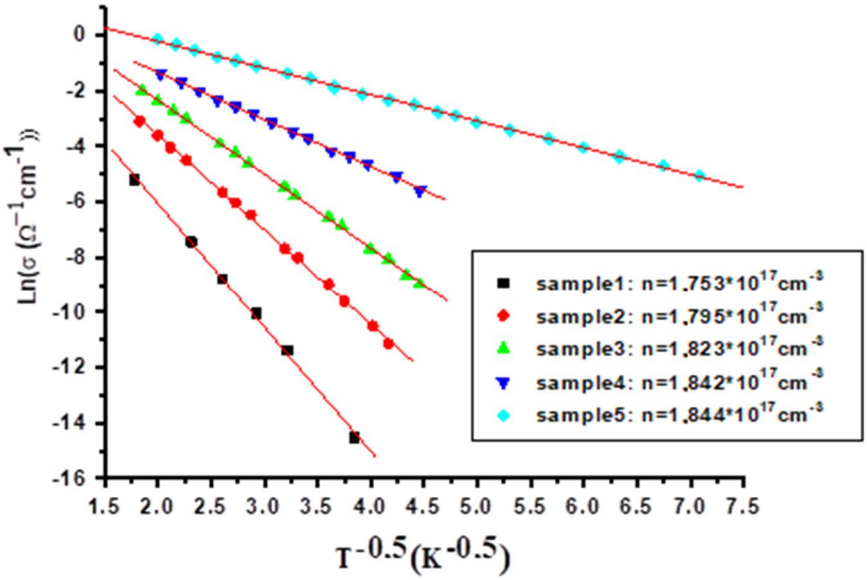

FIG. 2. Logarithmic variations of the electrical conductivity at zero field as a function of $T^{-0.5}$ for the five samples of the three-dimensional ^{70}Ge:Ga system over the full temperature range 0.05-0.25 K.

Note that the procedure of Zabrodskii and Zinoveva involves plotting the graphical representation of the function w(T) against ln(T) throughout the temperature range. This plot typically forms a straight line with a slope equal to –x, where w(T) = A-x.ln(T) and A is a constant.

If –x > 0, the sample exhibits metallic behavior and is situated on the metallic side of the MIT. On the other hand, if –x < 0, the sample is located on the insulating side of the MIT, and electrical conduction takes place through the VRH mechanism. In this scenario, two possibilities arise: x = 0.25, representing Mott-VRH conduction, and x = 0.5, indicating ES-VRH conduction.

We will now apply the procedure proposed by Zabrodskii and Zinoveva [40]. To do so, we have plotted Figures 3(a), 3(b), 4(a), 4(b), and 5, showcasing the variations of the function w(T) as a function of ln(T) for the five samples of ^{70}Ge:Ga at zero magnetic field. Upon analyzing these figures, we observe that all the plots of w(T) against ln(T) exhibit straight lines with negative slopes (–x < 0).

This clear result indicates that all five studied samples exhibit insulating behavior and are located on the insulating side of the MIT. Additionally, the values of the exponent x

closely approach 0.5, with no indication of a change in slope towards x = 0.25 across the entire temperature range of T = 0.02-0.25K (see Figs. 3, 4, and 5). This compelling finding, x = 0.5, strongly suggests that the electrical transport mechanism occurs through the ES-VRH regime at very low temperatures for these samples.

In the ES-VRH regime, the DOS is sensitive to Coulomb interactions, leading to the emergence of a parabolic Coulomb gap near the E_F at zero magnetic field. The values of the hopping exponents obtained through the Zabrodskii and Zinoveva procedure for the five insulating samples of ^{70}Ge:Ga are presented in Table 1.

In order to clearly determine the conduction type through the VRH mechanism and the values of the jump exponent for the five samples, we will employ the percentage deviation procedure. To begin, we linearize the general expression of hopping by introducing the natural logarithm. As a result, we obtain the following expression:

$$Ln(\sigma) = ln(\sigma_0) - (T_0/T)^x \quad (11)$$

Next, for each sample, we systematically vary the exponent x of the previous formula within the range of 0.1 to 1, with steps of 0.05 and 0.01 near the minimum deviation. By performing the linear regression, we can extract the corresponding values of σ_0 and T_0 for each value of x.

Finally, we calculate the percentage deviation Dev (%) [41- 43] using the following formula:

$$\mathrm{Dev}(\%) = \left[\frac{1}{n}\sum_{i=1}^{n}\left(\frac{100}{\sigma_i}\left(\sigma_{0exp}[-(T_0/T)^x] - \sigma_i\right)\right)^2\right]^{1/2} \quad (12)$$

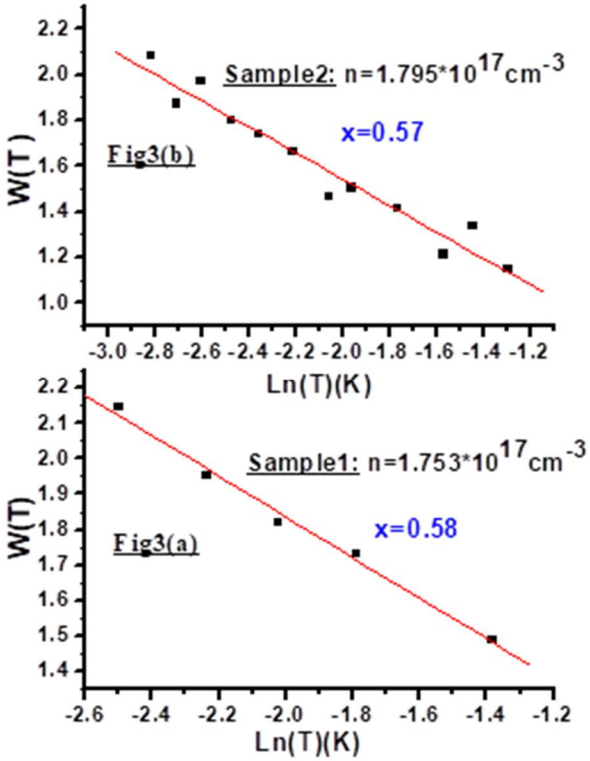

FIG. 3. Variation of the function w(T) as a function of ln(T) for samples 1 and 2 in the temperature range 0.02-0.25 K.

This process is performed for each sample and for various values of the exponent x, over the entire temperature range. It is essential to note that the minimum deviation Dev (%) corresponds to the best value of the exponent x.

The procedure involves calculating the percentage deviation Dev (%) based on the formula mentioned earlier, where n denotes the number of data points, and σ_i represents the experimental value of the electrical conductivity.

In Figs. 6(a), 6(b), 7(a), 7(b), and 8, we have presented the variations of Dev (%) plotted against the exponent x for all five insulating samples of ^{70}Ge:Ga within the temperature range T = 0.02-0.25 K.

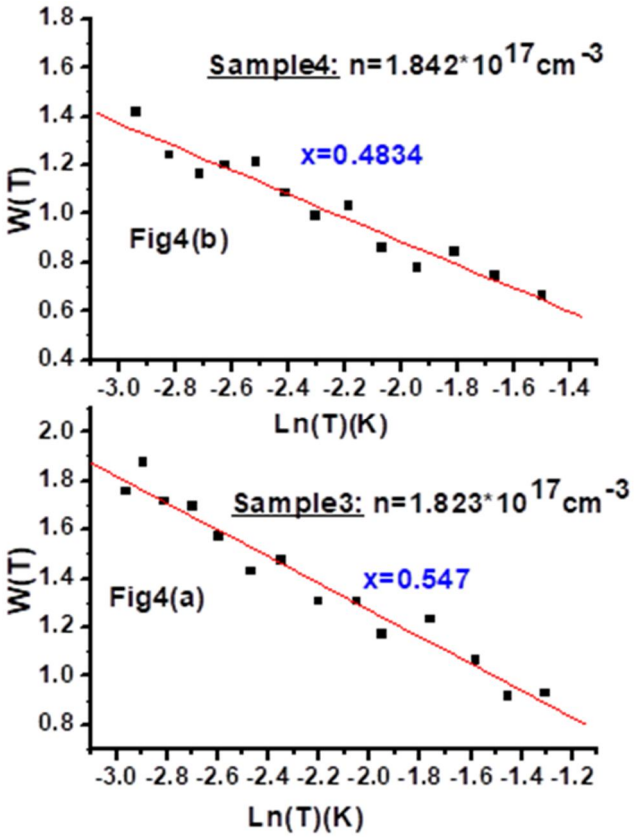

FIG. 4. Variation of the function w(T) as a function of ln(T) for samples 3 and 4 in the temperature range 0.02-0.25 K.

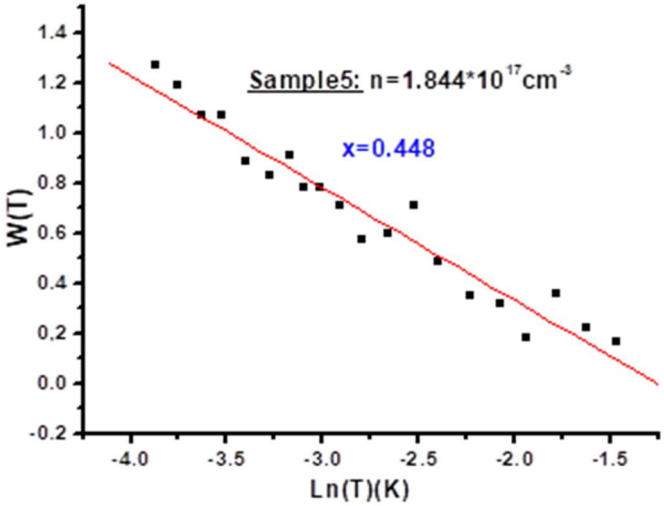

FIG. 5. Variation of the function w(T) as a function of ln(T) for sample 5 in the temperature range 0.02-0.25K.

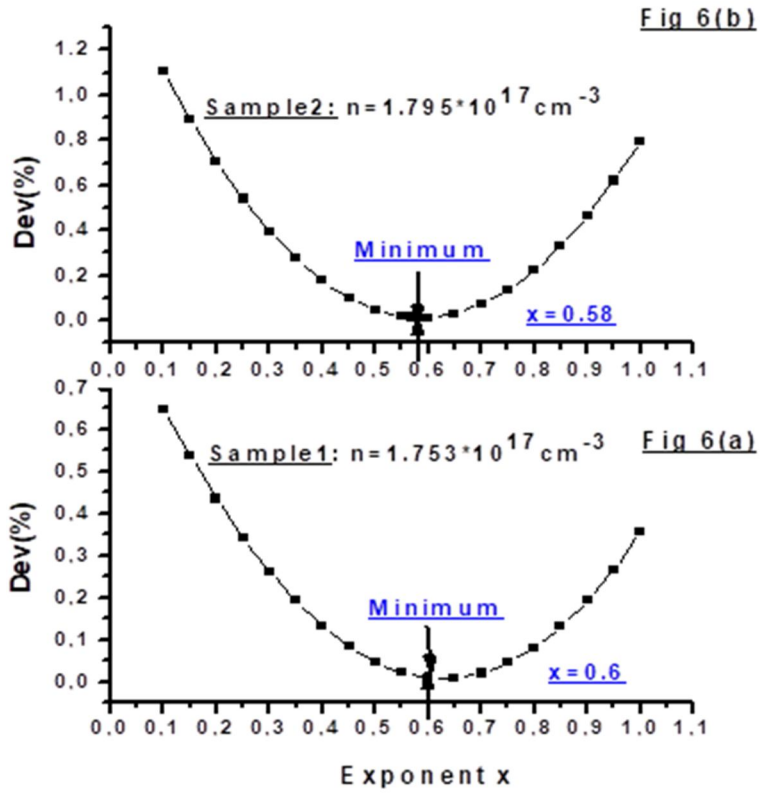

FIG. 6. Percentage deviation Dev (%) versus exponent x for insulating samples 1 and 2 in the temperature range 0.02-0.25 K.

According to these figures, the minimum values of Dev (%) are obtained for exponents x close to 0.5: x = 0.6 for sample 1, as seen in Fig. 6(a), x = 0.58 for sample 2, as seen in Fig. 6(b), x = 0.55 for sample 3, as seen in Fig. 7(a), x = 0.5 for sample 4, as seen in Fig. 7(b), and x = 0.45 for sample 5, as seen in Fig. 8. These results strongly corroborate our previous findings obtained through the procedure of Zabrodski and Zinoveva. The close agreement between the two methods provides robust evidence for the validity of the values of x determined, indicating the dominance of the ES-VRH conduction mechanism at very low temperatures for these five samples.

The latest findings from our study provide clear evidence that the dominant hopping conduction mechanism in the five ^{70}Ge:Ga samples is the ES-VRH, rather than the Mott 3D-VRH, across the entire temperature range.

This indicates that electron interactions are significant and influence the behavior of the DOS near the E_F, resulting in the creation of a parabolic pseudo-Coulomb gap at zero magnetic field. Furthermore, the values of the hopping exponent x, obtained through the numerical deviation percentage procedure [41, 43] for the five ^{70}Ge:Ga samples, are compiled in Table 1 for reference and further analysis. These results contribute to a comprehensive understanding of the electrical transport properties of the materials and emphasize the importance of considering electron-electron interactions in the insulating side of the MIT.

It is crucial to highlight that within the temperature range of 0.02-0.25 K, no transition from the ES-VRH to the Mott-VRH behavior was observed in any of the five samples. Nonetheless, this transition may take place under various circumstances. For instance, with an increase in temperature, a decrease in impurity concentration, or when the jump energies for each VRH regime become comparable.

In cases where the ES-VRH conduction mechanism is no longer dominant, the Coulomb interactions diminish, resulting in the DOS remaining nearly constant around the E_F. Notably, this transition from Efros-Shklovskii to the Mott VRH has been observed by several researchers across different localized semiconducting materials, including studies by Yamaura [44], Bedoya-Pinto [45], Zhang [46], Bennaceur [47], Errai [48], and Zhaoguo Li [49].

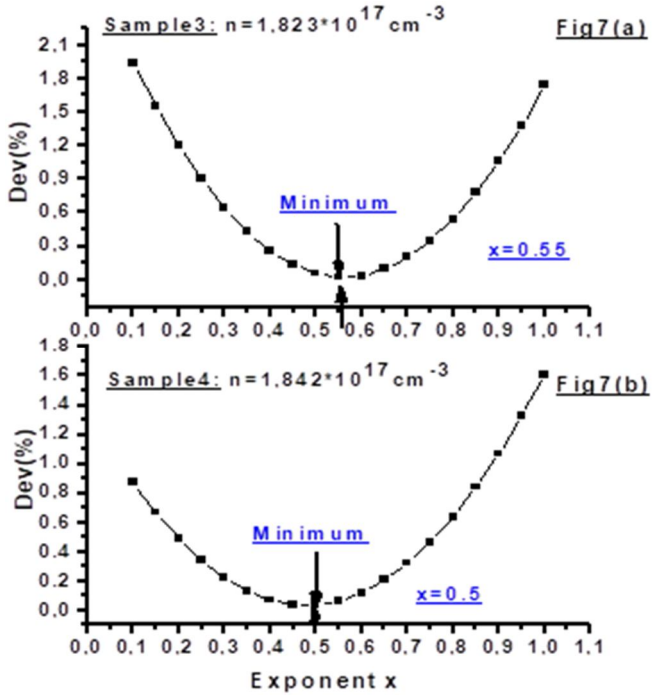

FIG. 7. Percentage deviation Dev (%) versus exponent x for insulating samples 3 and 4 in the temperature range 0.02-0.25 K

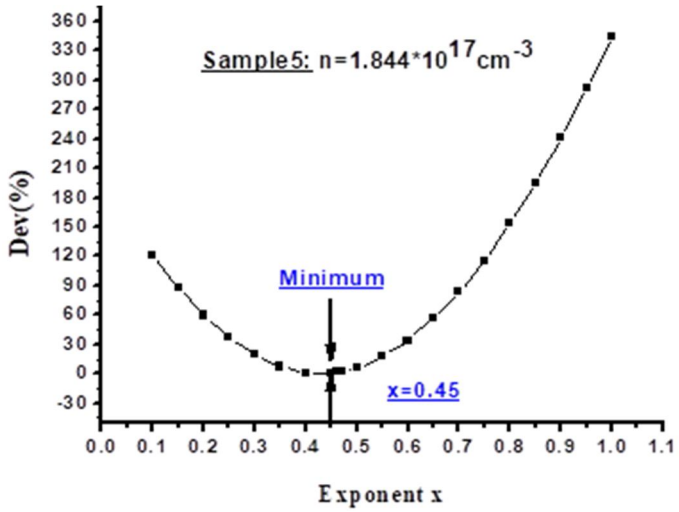

FIG. 8. Percentage deviation Dev (%) versus exponent x for insulating sample 5 in the temperature range 0.02-0.25K.

TABLE 1. Values of the *hopping* exponent x in Eqs. (9) and (12) for the five samples in the temperature range 0.05–0.25 K.

	Exponent x (Zabrodski-Zinova Method)	Exponent x (Minimum of Dev %)
Sample1	0.58	0.59
Sample2	0.57	0.58
Sample3	0.547	0.55
Sample4	0.483	0.5
Sample5	0.448	0.45

Investigating the electrical transport parameters in the ES regime is a fascinating aspect of our study. To achieve this, we utilized the data presented in Fig. 2 and applied the ES hopping formula, using the linear regression method. This enabled us to extract the two crucial parameters, T_{ES} and σ_{ES}. Furthermore, to calculate the localization length ξ, we employed Eq. (8). This calculation allowed us to evaluate the average hopping distance $R_{hop,ES}$ [28, 30] and

the average hopping energy $E_{hop,ES}$ [28, 30] using the following two equations:

$$R_{hop,ES} = \frac{1}{4} \left(\frac{T_{ES}}{T}\right)^{1/2} \xi \quad (13)$$

$$E_{hop,ES} = \frac{1}{2} K_B T \left(\frac{T_{ES}}{T}\right)^{1/2} \quad (14)$$

These determinations are vital in comprehending the electrical conduction mechanism in the ES regime and contribute to a deeper understanding of the material's transport properties.

The results obtained for all five insulating samples, covering the entire temperature range of 0.05-0.25 K, are summarized in Table 2.

It is crucial to highlight, based on the analysis of the results in Table 2, that as the impurity concentration n increases while remaining below n_c, the localization length (ξ) increases, whereas the Efros temperature (T_{ES}) decreases $\left(T_{ES} \propto \frac{1}{\xi}\right)$. In this regime, transport is governed by the ES-VRH mechanism, and Coulomb interactions between strongly localized electrons play a predominant role. When $n = n_c$, ξ becomes very large, and T_{ES} becomes very small, as the electrons become less localized. This leads to the occurrence of a metal-insulator transition (MIT), where electrical transport acquires a metallic character.

TABLE 2. The essential parameters characterizing ES VRH conduction across the five insulating samples of ^{70}Ge:Ga. These measurements were conducted within the temperature range of 0.05–0.25 K.

	n (cm-3)	σ_{ES} (Ω^{-1}cm^{-1})	T_{ES} (K)	ξ (nm)	$R_{hop,ES} \times T^{-0.5}$ (nm.K$^{-1/2}$)	$E_{hop,ES} \times T^{0.5}$ (J.K$^{1/2}$)
Sample1	1.753×10^{17}	18.8350	20.2001	146.50658	164.6169	3.1026×10^{-23}
Sample2	1.795×10^{17}	26.3510	11.7370	252.14635	215.9595	2.3649×10^{-23}
Sample3	1.823×10^{17}	20.4262	7.1387	414.5606	276.9109	1.8444×10^{-23}
Sample4	1.842×10^{17}	8.0396	2.8982	1021.1365	434.5982	1.1752×10^{-23}
Sample5	1.844×10^{17}	5.4660	0.9214	3211.7748	770.7590	0.6626×10^{-23}

4. Conclusion

In this study, we investigated the electrical transport properties of the three-dimensional ^{70}Ge:Ga system on the insulating side of the metal-insulator transition (MIT). Our analysis is done as a function of temperature and in the absence of a magnetic field. Initially, we graphically represented the function ln(σ) as a function of $T^{-0.25}$ and $T^{-0.5}$. Although both plots showed good linearity, it was challenging to differentiate between the Mott-VRH and ES-VRH conduction regimes based solely on these curves.

To resolve this issue and precisely identify the dominant hopping regime in the system, we utilized two methods: the one proposed by Zabrodskii and Zinoveva and the percentage deviation method. Remarkably, for all five samples and across the entire temperature range, the hopping exponent x was found to be very close to 0.5. This strongly suggests that the electrical conductivity follows the hopping law $\sigma = \sigma_{ES} \exp [-(T/T_{ES})^{0.5}]$, indicating that the electrical conduction occurs through the Variable Range Hopping (VRH) mechanism, specifically the Efros-Shklovskii (ES) VRH regime, without any crossover to the Mott VRH regime.

Furthermore, the behavior $\ln(\sigma) \sim T^{-0.5}$ indicates that the long-range Coulomb interactions between the localized charge carriers significantly influence the system. These interactions reduce the density of states (DOS) around the Fermi level, leading to the formation of a pseudo-parabolic Coulomb gap at the Fermi level, known as the Coulomb gap (CG). Additionally, we have determined several hopping parameters within the ES regime, further enriching our understanding of the electrical transport properties of the ^{70}Ge:Ga system on the insulating side of the MIT.

Acknowledgement

We are grateful to Professor Kohei M. Itoh, who has granted us the permission to reuse the experimental results published in the reference "M.Itoh, M.Watanabe, Y.Ootuka, and E. E.Haller, J. Phys. Soc. Jpn 73, 173 (2004)".

Conflict of Interest

The authors declare that they have no conflict of interest.

References

[1] Claeys, C. and Simoen, E., "Germanium-Based Technologies: From Materials to Devices", (Oxford: Elsevier, 2007).

[2] Hosoi, T, Suzuki, Y, and Shimura Tand Watanabe, H., Appl. Phys. Lett., 105 (2014) 3502.

[3] Matsui, T., Kondo, M., Ogata, K., Ozawa, T., and Isomura, M., Appl. Phys. Lett., 89 (2006) 142115.

[4] Mitin, V.F., Kholevchuk, V.V., and Kolodych, B.P., Cryogenics, 51 (2011) 68.

[5] Wang, D.P., Feldman, D.E., Perkins, B.R., Yin, A.J., Wang, G.H., Xu, J.M., and Zaslavsky, A., Solid State Commun., 142 (2007) 287.

[6] Bedoya-Pinto, A., Malindretos, J., Roever, M., Mai, D.D., and Rizzi, A., Phys. Rev. B, 80 (2009) 195208.

[7] Singh, V., Joung, D., Zhai, L., Das, S., Khondaker, S.I., and Seal, S., Prog. Mater. Sci., 56 (2011) 1178.

[8] Errai, M. et al., AIP Conf. Proc., 1574 (2014) 291.

[9] Errai, M., El Kaaouachi, A., and El Idrissi, H., J. Semicond., 36 (2015) 062001.

[10] Errai, M., El Kaaouachi, A., and El Idrissi, H., J. Semicond., 36 (2015) 122001.

[11] Errai, M., El Kaaouachi, A., El Idrissi, H., and Chakhmane, A., Chin. J. Phys., 55 (2017) 2283.

[12] Zeng, Y.P., Liu, Z.W., and Mikmeková, E., J. Magn. Magn. Mater., 421 (2017) 39.

[13] Yao, Y., Bo, B., and Liu, C., Curr. Appl. Phys., 18 (2018) 1492.

[14] Souri, M., Connell, J.G., Nichols, J., Terzic, J., Cao, G., and Seo, A., J. Appl. Phys., 126 (2019) 185101.

[15] Ohmura, Y., Takahashi, M., Suzuki, M., Emura, A., Sakamoto, N., Meguro, T., and Yamamoto, Y., Phys. Status. Solidi. B, 235 (2003) 111.

[16] Sharma, S.K., Sagar, P., Gupta, H., Kumar, R., and Mehra, R.M., Solid State Electron., 51 (2007) 1124.

[17] Zvyagin, I.P., Kurova, I.A., and Ormont, N.N., Phys. Status Solidi C, 1 (2004) 101.

[18] Liu, X., Riney, L., Guerra, J., Powers, W., Wang, J., Furdyna, J.K., and Assaf, B.A., J. Semicond., 43 (2022) 112502.

[19] Zhao, Y. and Wang, J., Micromachines, 13 (2022) 707.

[20] Sánchez-Trujillo, D.J., Osorio-Maldonado, L.V., and Prías-Barragán, J.J., Sci. Rep., 13 (2023) 4810.

[21] Masarrat, A. et al., J. Electron. Mater., 51 (2022) 3350.

[22] Anderson, P.W., Phys. Rev., 109 (1958) 1492.

[23] Mott, N., "Metal-insulator Transitions", (CRC Press, 2004).

[24] Itoh, K.M., Watanabe, M., Ootuka, Y., Haller, E.E., and Ohtsuki, T., J. Phys. Soc. Jpn, 73 (2004) 173.

[25] Mott, N.F. and Davis, E.A., "Electronic Processes in Non-Crystalline Materials", (Oxford University Press, 1979).

[26] Mott, N.F., "Metal-Insulator Transitions", 2nd Ed., (Taylor & Francis 2, 1990).

[27] Mott, N.F., "Conduction in Non-Crystalline Materials", (Clarendon Press, Oxford, 1993).

[28] Essaleh, L., Wasim, S.M., Marín, G., Rincón, C., Amhil, S., and Galibert, J., J. Appl. Phys., 122 (2017) 015702.

[29] Errai, M., Amrane, S., and Liang, C.T., IJTPE, 13 (2021) 170.

[30] Guo, J., Gu, H., Wei, H., Zhang, Q., Haldolaarachchige, N., Li, Y., and Guo, Z., J. Phys. Chem. C, 117 (2013) 10191.

[31] Éfros, A.L. and Shklovskii, B.I., J. Phys. C, 8 (1975) L49.

[32] Shklovskii, B.I. and Efros, A.L., "Electronic Properties of Doped Semiconductors 45", (Springer Science & Business Media, 2013).

[33] Shklovskii, B.I. and Efros, A.L., "Electronic Properties of Doped Semiconductors", (Springer Nature, 1984) 202.

[34] Shklovskii, B.I. and Efros, A.L., "Electron-electron Interactions in Disordered Systems", (1985) 409.

[35] Dlimi, S., El kaaouachi, A., Limouny, L., and Hammou, B.A., J. Semicond., 42 (2021) 052001.

[36] Zhang, L.J. et al., ACS Appl. Electron. Mater., 3 (2021) 2948.

[37] Pollak, M. and Shklovskii, B., "Hopping Transport in Solids", (Elsevier, 1991).

[38] Lee, P.A. and Ramakrishnan, T.V., Rev. Mod. Phys., 57 (1985) 287.

[39] Sandow, B., Gloos, K., Rentzsch, R., Ionov, A.N., and Schirmacher, W., Phys. Rev. Lett., 86 (2001) 1845.

[40] Zabrodskii, A. and Zinoveva, K., Sov. Phys. JETP, 59 (1984) 425.

[41] Finlayson, D.M., Mason, P.I., and Mohammad, I.F., J. Phys. C: Solid State Phys., 20 (1987) L607.

[42] Khan, A. and Hildreth, W.B., "Case Studies in Public Budgeting and Financial Management", (New York, NY: Marcel Dekker, 2003).

[43] Waller, D., "Operations Management: a Supply Chain Approach". (Cengage Learning Business Press, 2003).

[44] Yamaura, K., Young, D.P., and Cava, R.J., Phys. Rev. B, 63 (2001) 064401.

[45] Bedoya-Pinto, A., Malindretos, J., Roever, M., Mai, D.D., and Rizzi, A., Phys. Rev. B, 80 (2009) 195208.

[46] Zhang, X.Y., Chawla, J.S., Howe, B.M., and Gall, D., Phys. Rev. B, 83 (2011) 165205.

[47] Bennaceur, K., Jacques, P., Portier, F., Roche, P., and Glattli, D.C., Phys. Rev. B, 86 (2012) 085433.

[48] Errai, M., Narjis, A., Liang, C.T., Limouny, L., Dlimi, S., and Sybous, A., Chin. J. Phys., 52 (2014) 251.

[49] Li, Z., Peng, L., Zhang, J., Li, J., Zeng, Y., Luo, Y., and Wu, W., Semicond. Sci. Technol., 32 (2017) 035010.

Volume 18, Number 4, 2025. pp. 529-549

Jordan Journal of Physics

ARTICLE

On the Origin of Cosmic Microwave Background Radiation

Sergey G. Fedosin

PO box 614088, Sviazeva str. 22-79, Perm, Perm Krai, Russia.

Doi: **https://doi.org/10.47011/18.4.10**

Received on: 25/07/2024; *Accepted on: 06/10/2024*

Abstract: The alternative mechanism of the emergence of cosmic microwave background radiation (CMB), associated with the thermal radiation of primordial gas-dust clouds in the early Universe, is considered. The emergence of such clouds in the theory of infinite hierarchical nesting of matter is a natural stage in matter evolution. The mass, radius, and spatial concentration of typical primordial gas-dust clouds, the distance between neighboring clouds, and the power of CMB energy generation per unit volume and per nucleon of the early Universe were calculated. The masses and radii of these clouds correspond to the masses and radii of the observed Bok globules. The presented mechanism is consistent with the cluster model describing the appearance of angular multipoles in the CMB power spectrum. In addition to CMB radiation, cosmic infrared background (CIB) radiation and cosmic optical background (COB) radiation are also considered. According to the presented model, the sources of CIB are primordial protoplanetary clouds. As for the COB radiation, it is associated with the radiation of the first protostars. During evolution, each primordial cloud, with a mass of about 31 solar masses, first generates CMB radiation, and then CIB and COB radiations. Since protostars give rise to neutron stars, the concentration of primordial gas-dust clouds is also the concentration of observed neutron stars. In the course of the calculations, a new definition of the radiation intensity is used, which is based on the vector of the surface energy flux density and accounts for the angles of incidence of radiation on a flat receiver from all sides of the hemisphere. According to Poynting's theorem, the relationship between the intensity and energy density of black body radiation is derived from the concept of photons.

Keywords: Cosmic microwave background, Infinite hierarchical nesting of matter, Early universe, Cosmology: theory, Matter evolution.

PACS: 98.70.Vc.

1. Introduction

The cosmic microwave background radiation (CMB) in the wavelength range of 0.3-30 mm contributes most to the total energy of cosmic background radiation. The standard explanation for the origin of the CMB is based on the Big Bang concept, in which the CMB appeared in the early Universe. However, the idea of the Big Bang still has drawbacks [1]; therefore, other alternative cosmological theories continue to appear. For example, in the quasi-steady-state cosmological model, it is assumed that the CMB could be the result of processing stellar radiation by cosmic dust [2].

However, even in this case, there are difficulties associated with the fact that the CMB is too homogeneous and isotropic and exhibits an ideal blackbody spectrum. According to the dynamic Universe model [3] and the hierarchical Universe model [4], the stellar radiation in the early Universe could be sufficient for the CMB to have the observed energy density and be isotropic, so that the Big Bang is not needed. According to [5], the models based on a Universe in dynamical equilibrium without expansion predicted the 2.7 K temperature prior to and better than models based on the Big Bang. In addition, it was shown in [6] that isotopes of all the observed chemical elements can be

Corresponding Author: Sergey G. Fedosin **Email**: fedosin@hotmail.com

formed from hydrogen in stars over a timescale of approximately 100 billion years, which makes it possible to do without the Big Bang.

It is known from measurements [7] that the CMB temperature corresponds to the blackbody temperature $T = 2.7255$ K. If the CMB is in equilibrium with respect to some global blackbody of the Universe, it would have a volumetric energy density equal to $u = \frac{4\sigma T^4}{c} = 4.17\times10^{-14}$ J/m^3, where σ is the Stefan–Boltzmann constant, and c is the speed of light. This relation characterizes, for example, the state of a hollow black body, which is in thermal equilibrium with radiation in the inner cavity. The surface of such a cavity emits and absorbs radiation energy with an intensity of $I = \sigma T^4 = 3.13\times10^{-6}$ W/m^2. This means that ideal receivers, close in their properties to a blackbody, would measure within the cavity a CMB intensity on the order of I. In this case, the contribution to the intensity I will be made by photons incident on the receiver at various angles.

In measurements, the angular intensity $J = \frac{dI}{d\Omega}$ is often used, where Ω denotes the solid angle in steradians, from which the radiation arrives at the receiver. According to the Stefan–Boltzmann law, for CMB radiation—if it were in thermal equilibrium with matter as in a hollow blackbody—the following relation would be true: $J = \frac{I}{\pi} = \frac{\sigma T^4}{\pi} = 9.96\times10^{-7}$ W/(sr·m^2). This value is in accordance with the results in [8].

When plotting the radiation spectrum of a blackbody, the dependence of the spectral angular intensity $\frac{dJ}{d\nu}$ on the radiation frequency ν is usually plotted. This value reaches a maximum when a small frequency range $d\nu$ is selected near the frequency $\nu_m = 160.23$ GHz, corresponding to the maximum of the CMB radiation. In accordance with Wien's law of displacement for the frequency, $\nu_m = \frac{\alpha}{h}kT \approx 5.879\times10^{10}\cdot T$, where constant $\alpha \approx 2.821439...$, h is the Planck constant, k is the Boltzmann constant, and the radiation temperature T is measured in kelvins.

The purpose of this work is to explain the origin of background radiation in the model of a hierarchical Universe. Based on the thermal equilibrium of radiation and matter of radiation sources in the early Universe, we will find the sizes, masses, and concentration in space of these sources. As will be shown below, in the presented approach, the formula $u = \frac{4\sigma T^4}{c}$ for the energy density of background microwave radiation in the Universe can no longer be valid, nor can it be applied to the background infrared and optical radiation.

2. Definition of Intensity

The standard definition considers intensity as the amount of energy passing per unit time through a unit area oriented perpendicular to the direction of energy propagation. However, to account for different orientation angles of the receiver relative to the incident radiation, an alternative definition should be used. Within the photon framework, intensity can be regarded as the magnitude of a vector—the vector of the surface density of the radiation energy flux.

Let us assume that the radiation receiver responds only to the radiation component, which is perpendicular to the receiver plane. This can happen, for example, when the receiver is sensitive to the momenta of the photons falling on the receiver from all sides. Then, the momenta components of the set of photons, which are parallel to the receiver plane, mutually cancel each other, and the sum of the perpendicular momenta components of the photons is considered. In this case, we can assume that the energy flux surface density vector $\mathbf{I}$ is determined by the amount of incident radiation energy on the flat radiation receiver from all sides of the hemisphere per second per unit area S of the receiver, taking into account the angular dependence:

$$\mathbf{I} = \sum_i \frac{d}{dS}\left[\frac{d\left(E_i\hat{\mathbf{p}}_i\cdot\hat{\mathbf{n}}\right)}{dt}\right]\hat{\mathbf{n}} = c\sum_i \frac{d}{dS}\left[\frac{d\left(\mathbf{p}_i\cdot\hat{\mathbf{n}}\right)}{dt}\right]\hat{\mathbf{n}} =$$

$$= c\sum_i \frac{d}{dS}\left(\mathbf{F}_i\cdot\hat{\mathbf{n}}\right)\hat{\mathbf{n}} = c\sum_i \frac{dF_{in}}{dS}\hat{\mathbf{n}} = c\sum_i P_{in}\hat{\mathbf{n}} = cP_n\hat{\mathbf{n}}. \quad (1)$$

where $E_i = c\,p_i$ denotes the energy of the photon with momentum amplitude p_i; the index i specifies the photon number during summation in (1); $\hat{\mathbf{p}}_i$ is a unit vector directed along the photon momentum $\mathbf{p}_i$, such that $\mathbf{p}_i = p_i\,\hat{\mathbf{p}}_i$; $\hat{\mathbf{n}}$ is a unit normal vector directed to the receiver plane from the hemisphere; $\mathbf{F}_i = \dfrac{d\mathbf{p}_i}{dt}$ defines the force acting from the photon on the receiver; $F_{in} = \left(\mathbf{F}_i \cdot \hat{\mathbf{n}}\right)$ is the force projection on the normal; $P_{in} = \dfrac{dF_{in}}{dS}$ denotes the pressure from the photon's side, perpendicular to the receiver surface; and $P_n = \sum_i P_{in}$ is the total perpendicular pressure from all photons.

If we take into account that the electromagnetic radiation pressure is $P = \dfrac{u}{3} = \dfrac{4I}{3c}$, then according to (1), we have

$$P_n = \frac{3P}{4},\ \mathbf{I} = c\,P_n\,\hat{\mathbf{n}} = \frac{3cP}{4}\hat{\mathbf{n}}. \qquad (2)$$

In (2), the vector $\mathbf{I}$ is directed in the same way as the unit normal vector $\hat{\mathbf{n}}$ and is proportional to the speed of light and the electromagnetic pressure on the receiver.

The difference between P_n and P in (2) can be attributed to the well-known 4/3 problem, according to which the mass-energy m_P of the electromagnetic field of a charged body moving at a very low velocity, derived from the Poynting vector and proportional to the field momentum density, is 4/3 times greater than the mass-energy m_E, corresponding to the field energy density. The relation $m_E = \dfrac{3m_P}{4}$ corresponds to the equality $P_n = \dfrac{3P}{4}$, so that the radiation pressure P is related to the Poynting vector, and the pressure P_n exerted on the receiver is related to the field energy density. According to [9], the 4/3 problem occurs because the electromagnetic field energy density and the field momentum density are not the four-momentum components but rather the field stress-energy tensor components.

To check formula (1), first place the receiver on the surface of the sphere of radius r, at the center of which there is a certain source with the power of isotropic radiation W. In this situation, the radiation falls on the receiver at a right angle. In (1), the scalar product $\left(\hat{\mathbf{p}}_i \cdot \hat{\mathbf{n}}\right) = 1$ is obtained, and the energy flux density recorded in the receiver is then equal to:

$$I = \frac{W}{4\pi r^2}. \qquad (3)$$

Let us consider another situation, when one of the many existing radiation sources is the volume element dV. We can assume that $dW = \dfrac{u\,dV}{\Delta t}$ is the differential of the radiation energy, leaving the volume element dV per unit time Δt. Let us choose the hemisphere radius $R = c\Delta t$, where c is the speed of light, and place the receiver at the coordinate origin on the plane ZOX at the center of the hemisphere. This situation is shown in Fig. 1.

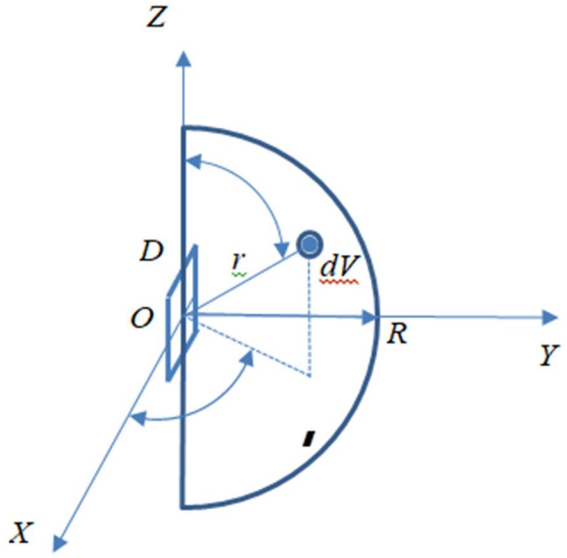

FIG. 1. The receiver D (in this case rectangular in shape) is located at the coordinate origin on the plane ZOX at the center of the hemisphere of radius R. The current radius r and the angles φ and ϕ specify the position of the radiating volume element dV in the spherical coordinate system.

Now, all the radiation energy contained in the hemisphere with a radius R falls into the receiver at time Δt. Then, in spherical

coordinates for the intensity differential of the volume element dV located inside the hemisphere at a distance r from the center, in accordance with (1) and (3), we have:

$$dI = \frac{u \sin Q \ \sin\phi \ dV}{4\pi r^2 \Delta t}, \quad (4)$$

Here, $dV = r^2 dr \sin Q dQ d\phi$ is the volume element considered as a source of isotropic radiation. The product $\sin Q \ \sin\phi$ defines the angular dependence of the radiation intensity, so that at $Q = 0$ photons move along the OZ axis and do not enter the receiver at all. At $\phi = 0$, photons move in the ZOX plane and do not enter the receiver either. If $Q = \pi/2$, and $\phi = \pi/2$, photons fall on the receiver at a right angle to its surface and make the maximum contribution to the intensity. The appearance of $\sin Q \ \sin\phi$ in (4) follows from the fact that, according to Fig. 1, $\hat{\mathbf{n}} = -(0,1,0)$, $\hat{\mathbf{p}}_i = -(\sin Q \ \cos\phi, \sin Q \ \sin\phi, \cos Q)$, and in definition (1), we have $(\hat{\mathbf{p}}_i \cdot \hat{\mathbf{n}}) = \sin Q \ \sin\phi$.

Integration over the hemisphere's volume replaces the summation in (1) and gives the following:

$$I = \frac{u}{4\pi\Delta t} \int_0^{R=c\Delta t} dr \int_0^{\pi} \sin^2 Q \ dQ \int_0^{\pi} \sin\phi \ d\phi = \frac{uc}{4}. \quad (5)$$

The calculation in (5) shows how, in the case of equilibrium blackbody radiation, we can understand the relation between the intensity I and the energy density u of radiation that enters the receiver from different directions. Hence, we can see that I is actually related to the mass-energy of the field energy density, and not to the mass-energy of the momentum density, which is found using the Poynting vector.

3. CMB Energy Production

It is known that CMB radiation originates from large distances; therefore, in one way or another, it is generated by many sources. Let us assume that, on average, each cubic meter of the early Universe was a source of the CMB and produced L joules of CMB energy per second; then, the volumetric power L of energy generation is measured in W/m^3. Next, we proceed as in [4].

Let us suppose that radiation sources uniformly fill the hemisphere, while radiation from some sources does not fall on the receiver at a right angle. This means that to determine the intensity I, we should integrate the entire hemisphere's volume and take into account the angles of incidence of radiation on the receiver, similar to (4) and the definition of intensity in (1). We will place the receiver at the origin of the coordinate system and position it in the ZOX plane to measure the CMB energy.

If some radiating volume is located at a distance r from the origin of coordinates, then the effective amount of energy dI, incident per unit time on the unit area of the receiver, will be equal to:

$$dI = \frac{L \exp\left(-\frac{Hr}{c}\right) \exp(-snr) \sin Q \ \sin\phi \ dV}{4\pi r^2}, \quad (6)$$

where H is the Hubble constant.

The first exponent $\exp\left(-\frac{Hr}{c}\right)$ in (6) describes the exponential decrease in the energy of CMB photons as they travel a distance r. As a result, the wavelength of the photons is shifted, which is known as the cosmological redshift of the spectra of distant radiation sources.

The second exponent $\exp(-snr)$ sets the degree of scattering of photons on their way to the receiver, reducing the number of arriving photons. This exponent corresponds to the Beer–Lambert law for light scattering, where s is the scattering cross section, and n is the concentration of objects scattering light.

Let us take the integral in (6) over the volume of the hemisphere of infinite radius:

$$I = \frac{L}{4\pi} \int_0^{\infty} \exp\left(-\frac{Hr}{c}\right) \exp(-snr) dr$$
$$\int_0^{\pi} \sin^2 Q \ dQ \ \int_0^{\pi} \sin\phi \ d\phi = \frac{L}{4\left(\frac{H}{c}+sn\right)}. \quad (7)$$

In (7), the relation between the measured intensity I and the volumetric power L of CMB energy generation in cosmic space is presented.

Considering that the exponent $\exp\left(-\frac{Hr}{c}\right)$ in (7) describes the exponential decrease in energy, as well as in the frequency of CMB photons as they travel a distance r, the following is obtained for the photon wavelength and redshift:

$$\lambda = \lambda_0 \exp\left(\frac{Hr}{c}\right),$$
$$z = \frac{\lambda - \lambda_0}{\lambda_0} = \frac{\lambda}{\lambda_0} - 1 = \exp\left(\frac{Hr}{c}\right) - 1,$$
$$r = \frac{c}{H}\ln(z+1). \quad (8)$$

If in (8) z is small compared to unity, then $\ln(z+1) \approx z$, which leads to the Hubble law in the form $r \approx \frac{cz}{H}$.

Due to the decrease in energy and scattering of photons in (6), some blurring of images of distant galaxies should be observed, since photons change their motion direction as a result of scattering. In fact, the observed blurring is insignificant, which can be explained by the small size of the electrogravitational vacuum particles described in [4] and [10], which are unable to significantly change the direction of the photons' momenta. We can also refer to more recent works [11-12], in which, in light of new data, the observed dependence of the duration of supernova explosions on the distance to them, the dependence of the surface brightness of galaxies on the redshift, and the relationship between redshift, relic radiation, and the blackbody spectrum were analyzed.

In addition, observations of the angular radii and surface brightness of galaxies at a given luminosity do not correspond to the expanding Universe hypothesis in the $\Lambda - CDM$ model, but are in good agreement with relation (8), which describes the relationship between distance and redshift, as well as with the static Universe model [13-14], in which the surface brightness does not depend on the redshift z. With relation (8), the supernovae type Ia data give almost the same result as the $\Lambda - CDM$ model.

4. The Sources of CMB

In the theory of infinite hierarchical nesting of matter [4], [10], [15], it is assumed that the substance of a certain level of matter arises in the course of the evolution of the substance of lower levels of matter. Therefore, stars as objects of the stellar level of matter appear after the compression of large gas clouds. The main objects of these clouds are nucleons belonging to the nucleon level of matter. In turn, the appearance of gas clouds is a consequence of the evolution of the substance of the praon level of matter, and praons can form the substance of nucleons in the same way as nucleons can form the substance of stars.

Based on this, suppose that in the early Universe, the entire volume was more or less uniformly filled with CMB sources at concentration n, the average radius of these sources was equal to a, and the effective temperature of particles on the surface of these sources was equal to the temperature T_s. In this case, we can write:

$$L = 4\pi\sigma T_s^4 a^2 n. \quad (9)$$

In (9), the CMB generation power per unit volume L is expressed through the surface area of a typical CMB source, equal to $4\pi a^2$, through the intensity σT_s^4 of radiation from this surface, and through the concentration n of CMB sources in the Universe.

Substituting L from (7) in (9) and taking into account that $I = \sigma T^4$, we find:

$$\frac{T_s^4 a^2 n}{\left(\frac{H}{c} + sn\right)} = \frac{T^4}{\pi}. \quad (10)$$

We assume that, during the time required for CMB photons to reach the Earth from distant regions of the Universe, the number of baryons and their concentration in cosmic space did not change significantly. In the first approximation, we can use the results of the $\Lambda - CDM$ model (Lambda-cold dark matter model), where the critical mass density reaches the value of $\rho_{cr} = \frac{3H^2}{8\pi G} = 9.2\times10^{-27}$ kg/m^3, if we assume that the Hubble constant H equals 70 km/(s·Mpc) or 2.268×10^{-18} s^{-1} [16].

The physical density of the visible baryonic matter in this case is $\rho_b = 0.0227\rho_{cr} = 2.1\times10^{-28}$

kg/m^3. This value is chosen in such a way that, among other things, it best fits observations of the amount of visible matter in galaxies. This approach will be sufficient for us since we will further derive various relationships, the physical meaning of which does not depend on the specific value of ρ_b.

Let us now take into account that the CMB sources, that is, the primordial gas-dust clouds, were located discretely in space with a concentration $n=\frac{\rho_b}{m}$, where m is the mass of a typical CMB source. Each source has a cross-section equal to $s=\pi a^2$. At very large distances, all sources begin to overlap, which makes it difficult to see the most distant CMB sources and weakens the intensity of the radiation that could be at the radiation receiver. This leads to the appearance of the exponent $\exp(-snr)$ in (6).

The mass of a typical source is expressed by the formula $m=\frac{4\pi a^3\rho_s}{3}=\frac{\rho_b}{n}$, where ρ_s is the mass density of the source substance. Expressing n from here and substituting into (10), while taking into account that $s=\pi a^2$, we have:

$$n=\frac{\rho_b}{m}=\frac{3\rho_b}{4\pi a^3\rho_s},\quad \frac{T_s^4}{\left(1+\frac{4Ha\rho_s}{3c\rho_b}\right)}=T^4. \qquad (11)$$

The last formula in (11) relates the radius a, mass density ρ_s of CMB sources, and the effective temperature T_s of the surface particles of these sources.

5. The Origin of Energy in CMB Sources

For the particles of numerous CMB sources to have a kinetic temperature on the order of T_s and to be able to subsequently radiate at this temperature, it is necessary that the particles of these sources somehow acquire the corresponding thermal energy as the energy of proper motion.

Let us turn to the theory of infinite hierarchical nesting of matter, according to which different matter levels are found in the Universe, and the main objects of these levels have significantly different masses and sizes. In particular, there are metagalactic, stellar, nucleon, praon, and graon levels of matter [4], [10], [15], [17-21].

All matter levels are structured by gravitational clustering. This process is accompanied by the opposite process of fragmentation when particles collide with each other and with radiation quanta. In large gas clouds, under appropriate conditions, atoms and molecules can combine under the action of gravitational forces first into molecular complexes and then into more massive dust particles, until planets, stars, and their clusters are formed. Dust particles of micron size have a fairly dense core surrounded by a layer of loose matter. The minimum time required for the formation of such particles can be estimated by the approximate formula for the radial fall of matter to the accretion center under the action of gravitation [22]:

$$t\approx\sqrt{\frac{3}{2\pi G\rho}}, \qquad (12)$$

where G is the gravitational constant, and ρ is the mass density of matter at the initial moment of fall. For example, with a density of $\rho=100$ kg/m^3 in (12), we obtain a duration of approximately 2.3 hours. The lower the initial mass density of an object is, the longer it takes for such an object to be formed. For a gas cloud with an initial density of $\rho=10^{-20}$ kg/m^3, the time t will be approximately 2.7×10^7 years. If we substitute in (12) the current density of baryonic matter, $\rho=\rho_b=2.1\times10^{-28}$ kg/m^3, the corresponding duration of metagalaxy formation will be on the order of 180 billion years.

A more accurate calculation accepted in astrophysics takes into account the time required for a gas cloud to increase its density with decreasing radius instead of taking into account the time of fall into the accretion center. Let us assume that the evolution of matter in the hierarchically structured Universe leads over time to the formation of baryonic matter with average mass density ρ_b. This process cannot be uniform everywhere, and in those places where it goes faster, the matter can compress under the action of gravitation, regardless of the

surrounding volumes of space with lower density. For the acceleration of particle motion in the gravitational field outside the gas cloud with the mass M, we have:

$$\frac{d^2r}{dt^2} = -\frac{GM}{r^2}. \quad (13)$$

Equation (13) is also suitable for describing the motion of the gas cloud's outer shell. The solution of (13) should be sought in the form $\frac{dr}{dt} = \pm\sqrt{\frac{A}{r} + B}$, $\frac{d^2r}{dt^2} = -\frac{A}{2r^2}$.

Hence, it follows that $A = 2GM$, and if $B = -\frac{2GM}{r_b}$, where r_b is the initial radius of the cloud, we obtain the relation for the velocity of the shell motion, which is associated with the law of conservation of energy:

$$\left(\frac{dr}{dt}\right)^2 = \frac{2GM}{r} - \frac{2GM}{r_b}. \quad (14)$$

For the case of cloud compression, the coordinate r decreases over time t, and therefore, we use the following equation:

$$\frac{dr}{dt} = -\sqrt{\frac{2GM}{r} - \frac{2GM}{r_b}}. \quad (15)$$

The solution of the differential equation (15), in the case of compression from radius r_b to radius r_s, is as follows:

$$t = \left[\frac{\sqrt{r_b}r}{\sqrt{2GM}}\sqrt{\frac{r_b}{r} - 1} + \sqrt{\frac{r_b^3}{2GM}}\operatorname{arctg}\sqrt{\frac{r_b}{r} - 1}\right]\Bigg|_{r_b}^{r_s} = \frac{\sqrt{r_b}r_s}{\sqrt{2GM}}\sqrt{\frac{r_b}{r_s} - 1} + \sqrt{\frac{r_b^3}{2GM}}\operatorname{arctg}\sqrt{\frac{r_b}{r_s} - 1}. \quad (16)$$

The maximum time is reached when the matter falls to the point center with the radius $r_s = 0$. Assuming that $r_b = \left(\frac{3M}{4\pi\rho_b}\right)^{1/3}$, in the case of (16), $t_{\max} = \frac{\pi}{2}\sqrt{\frac{r_b^3}{2GM}} = \sqrt{\frac{3\pi}{32G\rho_b}}$. This time depends only on the initial mass density ρ_b of the cloud and is estimated, since the solution does not consider the pressure forces in the gas cloud, which rapidly increase as the radius decreases.

Considering this approach, two scenarios are possible. In the first of them, the matter of the observable Universe with an average density ρ_b arises from praons, the smallest particles of the lowest level of matter, in a period of time determined by the physical conditions of this process. To understand how a nucleon can be formed from a set of praons, it is enough to imagine a similar process, in which a set of nucleons in a large gas cloud is compressed to the maximum extent under the action of gravitation. If the mass of the emerging star is large enough, then the result of its evolution would be a supernova and the birth of a neutron star. Praons, nucleons, and neutron stars are similar because they have the highest possible mass densities and the strongest electromagnetic fields at their levels of matter. In this case, it is assumed that at the level of nucleons the particles' matter is held together not by ordinary gravitation but by strong gravitation [10], [15].

In the second case, baryonic matter is first created; this matter is distributed in space with a certain mass density ρ_m and subsequently compressed to density ρ_b. Let ρ_b significantly exceed ρ_m. By substituting $r_b = \left(\frac{3M}{4\pi\rho_b}\right)^{1/3}$ for r_s and $r_m = \left(\frac{3M}{4\pi\rho_m}\right)^{1/3}$ for r_b in Eq. (16) and neglecting the first term, we obtain $t_{\text{m}} \approx \sqrt{\frac{3\pi}{32G\rho_m}}$. As an estimate, we will substitute here $\rho_b = 2.1\times10^{-28}$ kg/m^3 for ρ_m and will obtain the corresponding minimum compression time, if it actually took place: $t_{\min} \approx \sqrt{\frac{3\pi}{32G\rho_b}} = 145$ billion years.

For comparison, in the standard cosmological $\Lambda - CDM$ model, based on general relativity, the age of the Metagalaxy is estimated to be approximately 13.8 billion years. Moreover, to account for the spatial flatness, homogeneity, isotropy, and large-scale structure of the Universe, this model invokes the hypothesis of cosmological inflation during the early stages of

the Big Bang. The exotic character of such inflation is associated with the fact that during a period of time from 10^{-42} sec to 10^{-36} sec after the start of the Big Bang at the initial Planck matter density of approximately 10^{96} kg/m^3, the radius of the Metagalaxy should have increased by a factor of 10^{26} [23]. As can be seen from the estimates made above, if the hypothesis of cosmological inflation is not used, the minimum age of the observable Universe should be an order of magnitude greater than in the $\Lambda - CDM$ model.

We can consider a typical CMB source as a relativistic uniform system and estimate its internal thermal energy using the virial theorem [24-25]. Considering the contributions of gravitational energy and pressure field energy to the system's potential energy, according to [26], the following relation is obtained for the kinetic energy E_k:

$$E_k \approx \frac{81Gm^2}{100\sqrt{14}\,a}. \qquad (17)$$

However, the energy E_k can be approximately expressed in terms of the average temperature T_s of the source:

$$E_k \approx \frac{3mkT_s}{2m_p}, \qquad (18)$$

where the ratio of the source mass to the nucleon mass in the form $\frac{m}{m_p} = N$ specifies the total number of nucleons N as an estimate of the total number of atoms, and k is the Boltzmann constant.

Comparing expressions (17) and (18) for E_k in view of the relation $m = \frac{4\pi a^3 \rho_s}{3}$, yields the following:

$$a = \sqrt{\frac{25\sqrt{14}\,kT_s}{18\pi G m_p \rho_s}}. \qquad (19)$$

A primordial gas-dust cloud with mass m, which is the source of CMB, can be considered as a blackbody, in which matter is in thermal equilibrium with CMB radiation. The radiation energy density inside the cloud should be equal to $u_s = \frac{4\sigma T_s^4}{c}$. When a typical CMB source is formed in the form of a gas-dust cloud, the binding energy ΔE should be released, which is equal in order of magnitude to the total kinetic energy E_k of the cloud particles. A more precise estimate in [26] gives $\Delta E \approx \frac{5}{3}\left(\frac{14\sqrt{14}}{27} - 1\right) E_k \approx 1.57 E_k$. We can assume that the binding energy ΔE is radiated from the cloud by means of CMB radiation. In this case, the following equality must be satisfied:

$$u_s = \frac{4\sigma T_s^4}{c} = \frac{\Delta E}{V_s} = \frac{4.71 E_k}{4\pi a^3}, \qquad (20)$$

where $V_s = \frac{4\pi a^3}{3}$ is the cloud's volume.

Substituting E_k from (18) in (20) and considering the relation $m = \rho_s V_s$, we find:

$$\rho_s = \frac{8\sigma T_s^3 m_p}{4.71ck}. \qquad (21)$$

6. Parameters of CMB Sources

Relations (11), (19), and (21) can be considered as a system of three equations to determine unknown quantities a, T_s and ρ_s. Substituting ρ_s (21) into (19), we get:

$$a = \frac{5k}{12 T_s m_p}\sqrt{\frac{4.71\sqrt{14}\,c}{\pi G \sigma}}. \qquad (22)$$

Multiplying a (22) by ρ_s (21), we find:

$$a\rho_s = \frac{10T_s^2}{3}\sqrt{\frac{\sqrt{14}\,\sigma}{4.71\pi c G}}. \qquad (23)$$

Substituting (23) into (11) leads to a quadratic equation for T_s^2:

$$T_s^4 - T_s^2 \frac{40HT^4}{9\rho_b}\sqrt{\frac{\sqrt{14}\,\sigma}{4.71\pi c^3 G}} - T^4 = 0. \qquad (24)$$

Solving equation (24) gives the surface temperature of a typical CMB source:

$$T_s = T\sqrt{\frac{20HT^2}{9\rho_b}\sqrt{\frac{\sqrt{14}\,\sigma}{4.71\,\pi c^3 G}}+\sqrt{\frac{400\sqrt{14}\,H^2T^4\sigma}{81(4.71)\,\pi c^3 G\rho_b^2}}+1} = 3.472\text{K}. \quad (25)$$

Substituting T_s (25) into (22) and into (21), we obtain the radius a of the CMB source in the form of a gas-dust cloud and the density ρ_s of the substance of the cloud:

$$a = 2.088\times10^{16} \text{ m}. \quad \rho_s = 1.629\times10^{-18} \text{ kg/m}^3. \quad (26)$$

The radius of the cloud in (26) reaches the value $a = 0.68$ pc.

Next, taking into account (26), we find the mass of the source:

$$m = \frac{4\pi a^3\rho_s}{3} = 6.21\times10^{31} \text{ kg or } 31.2\,M_c, \quad (27)$$

where M_c is the mass of the Sun.

Parameters (26-27) of a typical CMB source correspond to a rather large gas-dust cloud, the particles of which acquire their kinetic energy due to gravitational work to compress matter. When the particles collide, the energy of motion is converted into heat and can then be radiated in the form of CMB quanta.

If we take into account that the obtained in (26-27) parameters of the sources belong to gas clouds in the early Universe, then we can expect that the first stars appeared precisely in such clouds. Later, similar clouds could give rise to the first open star clusters, which became the main elements of emerging galaxies. For comparison, the number of stars in currently observed open star clusters can be more than one hundred, the typical masses of clusters can exceed $50M_c$, the core radius can reach approximately 0.6 pc, and the radius of the corona in a typical cluster can reach 6 pc.

The concentration of CMB sources in the early Universe is found through the density of baryonic matter ρ_b and the mass m of a typical source according to the first relation in (11):

$$n = \frac{\rho_b}{m} = 3.4\times10^{-60} \text{ m}^{-3}. \quad (28)$$

If we assume that each source is located in a certain cubic volume in a cubic lattice, then the shortest distance between the nearest sources will equal $R_s = \frac{1}{\sqrt[3]{n}} \approx 6.7\times10^{19}$ m. This means that the distance between the centers of the nearest sources is $\frac{R_s}{a} \approx 3.2\times10^3$ times greater than the radius a of a typical source and is equal to the value on the order of $R_s \approx 2.16$ kpc at $a = 0.68$ pc according to (26).

The value of L, that is CMB generation power per unit volume of the Universe, is found from (9) taking into account T_s (25), a (26), and n (28), or from (7) taking into account the relations $I = \sigma T^4$, $s = \pi a^2$:

$$L = 4\pi\sigma T_s^4 a^2 n = 4\sigma T^4\left(\frac{H}{c}+\pi a^2 n\right) = 1.53\times10^{-31} \text{ W/m}^3. \quad (29)$$

The values of L may differ slightly in different directions, reflecting the variability of the Hubble parameter and the spatial matter distribution.

The average concentration of nucleons in the Universe is $n_b = \frac{\rho_b}{m_p} = 0.125$ m^{-3}. Taking this into account, from (29), the power of CMB energy generation per nucleon of the Universe is determined:

$$\frac{L}{n_b} = 1.22\times10^{-30} \text{ W/ nucleon}. \quad (30)$$

Dividing the binding energy $\Delta E \approx 1.57E_k$ of one SMB source by the number $N = \frac{m}{m_p}$ of nucleons in this source, taking into account expressions E_k (18) and T_s (25), we find the binding energy per nucleon:

$$\frac{\Delta E}{N} = \frac{4.71kT_s}{2} = 1.1\times10^{-22} \text{ J/ nucleon}. \quad (31)$$

On the other hand, an estimate of the photon's concentration in the volume of a CMB source in a state of temperature equilibrium between radiation and matter at the temperature $T_s = 3.472$ K is obtained as $n_f = \frac{\beta s_f}{k} = 8.49\times10^8$ m^{-3}, where

$s_f = \frac{16\sigma T_s^3}{3c} = \frac{4u_s}{3T_s} = 4.22\times10^{-14}$ J/(K·m^3) is the volumetric density of the CMB entropy and the coefficient $\beta = \frac{45}{4\pi^4}\int_0^\infty \frac{\xi^2 d\xi}{e^\xi - 1} \approx 0.2776...$

Dividing the photon energy density $u_s = \frac{4\sigma T_s^4}{c}$ (20) by the photon concentration n_f, we obtain the average energy per photon:

$$\frac{u_s}{n_f} = \frac{3kT_s}{4\beta} = 1.29\times10^{-22} \text{ J/photon.} \quad (32)$$

Note that the binding energy per nucleon $\frac{\Delta E}{N}$ in (31) and the energy per photon $\frac{u_s}{n_f}$ in (32) are close to each other in magnitude. After the photons leave the CMB sources, fill outer space, and reach the Earth, their average temperature decreases from the value $T_s = 3.472$ K to value $T = 2.7255$ K. In this case, the energy of a photon with a frequency of $\nu_m = 160.23$ GHz corresponding to the maximum in CMB radiation at temperature $T = 2.7255$ K is equal to $h\nu_m = 1.06\times10^{-22}$ J.

Hence, the ratio of the number of CMB photons in cosmic space to the number of matter nucleons present in this space should be on the order of unity. On average, we can assume that each nucleon of the observable Universe produces only one CMB photon.

In the course of our calculations, we assumed that all the nucleons present in the Universe with an average density of $\rho_b = 2.1\times10^{-28}$ kg/m^3 were compressed by gravitation into primordial gas-dust clouds with an average density of $\rho_s = 1.629\times10^{-18}$ kg/m^3 (26). These clouds play the role of typical CMB sources. Let $V_s = \frac{m}{\rho_s} = \frac{4\pi a^3}{3}$ denote the volume of a typical source, and let V denote the volume of the same mass of matter in the homogeneous Universe with density ρ_b and with the same mass m (27). Then, the ratio of the volumes equals $\frac{V}{V_s} = \frac{\rho_s}{\rho_b} = 7,76\times10^9$. Now, in view of E_k (18), the binding energy $\Delta E \approx 1.57E_k$ of one source, and the number of nucleons $N = \frac{m}{m_p}$ in the source, we can estimate the average CMB energy density in the Universe in the following form:

$$\bar{u} = \frac{\Delta E}{V} = \frac{1.57E_k\rho_b}{V_s\rho_s} = \frac{1.57E_k\rho_b}{m} = \frac{1.57\rho_b}{m}\frac{3kT_sN}{2} = \frac{4.71\rho_b kT_s}{2m_p} = 1.4\times10^{-23}\text{J/m}^3. \quad (33)$$

When deriving relation (20), we use the expression $u_s = \frac{\Delta E}{V_s}$. Combined with (33) and the relation $\frac{V}{V_s} = \frac{\rho_s}{\rho_b} = 7.76\times10^9$, this gives the following:

$$\frac{u_s}{\bar{u}} = \frac{V}{V_s} = \frac{\rho_s}{\rho_b} = 7.76\times10^9. \quad (34)$$

In Eq. (34), a significant difference emerges between the average CMB energy density $\bar{u}$ in (33) and the photon energy density u_s that would exist if photons were in thermal equilibrium with the matter of the CMB sources. The difference in magnitudes of u_s and $\bar{u}$ arises because the CMB generated within the volume V_s of each source was in equilibrium with matter only inside that volume. When the radiation from each source spreads into the larger cosmic volume V and mixes with radiation from nearby sources, the CMB energy density decreases from u_s to $\bar{u}$. As a result, the CMB observed on Earth is thermal radiation with an energy density $\bar{u}$ in the Universe.

In the $\Lambda - CDM$ model, the difference in quantities of u_s and $\bar{u}$ is not taken into account, and it is assumed that the energy density of the CMB is equal to $u = \frac{4\sigma T^4}{c} = 4.17\times10^{-14}$ J/m^3 in the entire space of the Universe at a temperature of $T = 2.7255$ K of CMB.

In this case, the estimate of the CMB photon concentration in the form

$n_f = \frac{\beta s_f}{k} = \frac{16\beta\sigma T^3}{3ck} = \frac{4\beta u}{3kT} = 4.1 \times 10^8$ m^{-3} applies to the entire Universe. Then, the ratio of the number of CMB photons to the number of nucleons will equal $\frac{n_f}{n_b} = \frac{n_f m_p}{\rho_b} = 3.3\times10^9$, which is close in magnitude to the ratio of the volumes $\frac{V}{V_s}$ in (34).

Hence, the following question arises: why is the number of photons so much greater than the number of nucleons? This problem, known in cosmology as the entropy problem, is usually solved via the concept of a hot Universe based on the assumption of adiabatic space expansion from the initial state of equilibrium of radiation and matter.

In contrast, in our approach, the numbers of CMB photons and nucleons are approximately the same, and there is no need for a hot Universe. Since the SMB is currently not in equilibrium with matter, the formula for energy density $u = \frac{4\sigma T^4}{c}$ cannot be applied to the entire Universe. Indeed, the primordial gas-dust clouds, which served as CMB sources in the early Universe, were distributed discretely, occupied only a small fraction of space, and therefore could not act as a global blackbody encompassing the entire Universe.

7. The Angular Harmonics of CMB

Using the Fourier transform, the observed CMB power spectrum can be expanded in terms of spherical harmonics [27-28].

The spherical harmonic $\ell = 0$ in the angular power spectrum corresponds to the average CMB temperature. The dipole anisotropy ($\ell = 1$) on the CMB temperature map has an amplitude of approximately 0.1% and is attributed to the Doppler effect caused by the motion of the Earth and Sun relative to the reference frame in which the CMB intensity is isotropic [29]. This motion alters the observed CMB wavelength depending on the angle between the Earth's velocity in cosmic space and the direction of the sky region from which the CMB originates.

The spherical harmonics $\ell \geq 2$ are related to CMB temperature fluctuations, the root-mean-square deviation of which reaches several tens of μK relative to the average temperature. The $\Lambda - CDM$ model assumes that such temperature fluctuations could be caused by fluctuations in the density of matter in the early Universe, which had the state of a very dense hot plasma of electrons and baryons.

One alternative explanation is that the angular power spectrum of the CMB can be obtained if CMB photons, upon their appearance, interact with matter, which was structured into some objects, clusters, and particles [30]. The average distance between the centers of the objects in the case of their cubic arrangement is approximately 108 m, the mass of one object is 8.8×10^{-17} kg, and the mass density of the object is 9×10^{-23} kg/m^3. Similarly, there are clusters inside the objects, the distance between the centers of which is about 12 cm. If their mass density is 9×10^{-23} kg/m^3, then the cluster mass is 1.2×10^{-25} kg. The position and amplitude of the main peak of the CMB power spectrum at $\ell \approx 360$ and of the subsequent peaks depend mainly on the mutual distances between the mentioned objects, and on their mass density and internal structure.

It is assumed that each cluster contains 40 to 100 particles, such as protons, helium nuclei, and electrons, representing an atomic–molecular complex primarily composed of hydrogen and helium. On average, each object contains approximately 10^9 clusters. The results obtained for the structure of objects, clusters, and particles were found under the condition of using a radiation wavelength equal to 1.9 mm. This wavelength corresponds to the maximum blackbody spectrum distribution at the temperature $T = 2.7255$ K and most exactly reflects the properties of CMB from the standpoint of structural analysis. Moreover, the angular power spectrum of CMB radiation is the same for all wavelengths of the CMB.

The presented parameters can be combined with the described scheme of CMB emergence in the early Universe, in which matter evolution first leads to the formation of nucleons and electrons. Then, gravitation compresses the matter into gas-dust clouds and sets the matter particles in motion. When the particles collide, the kinetic energy is converted into thermal energy and is radiated in the form of CMB photons. The mass density of objects in [30] is

less than the mass density of gas clouds, $\rho_s = 1.629\times10^{-18}$ kg/m^3, as found in (26). We can assume that the objects in [30] were located in the less dense part of the shell of gas clouds. Then, CMB photons, passing through these objects, clusters, and particles inside them, can form the currently observed angular radiation power spectrum.

The possibility that these objects, clusters, and particles could appear in primordial gas clouds follows from the value of the Jeans mass [31], which can be simplified as follows:

$$M_J \approx 26 M_c \left(\frac{T}{10}\right)^{3/2} \left(\frac{10^9}{n}\right)^{1/2}. \qquad (35)$$

The temperature T in (35) must be specified in K, and the particle concentration n must be specified in m^{-3}.

Let us substitute in (35) the cloud surface temperature $T_s = 3.472$ K (25) instead of T, and take into account $\rho_s = 1.629\times10^{-18}$ kg/m^3 (26) and the concentration of cloud particles $n_s = \frac{\rho_s}{m_p} = 9.7\times10^8$ m^{-3} instead of n. This gives $M_J = 5.4 M_c$. The Jeans mass is less than the gas cloud mass $m = 31.2 M_c$ (27), which allows fragmentation of the cloud into smaller structural components.

The nonuniform distribution of matter in cosmic space also contributes to the small-scale fluctuations in the CMB temperature. Thus, correlations between the optical radiation of galaxies and CMB fluctuations are described in [32], and for radio sources, such correlations are presented in [33]. The cold anomalies in CMB temperature are mysterious and cannot be explained from the standpoint of the $\Lambda - CDM$ model, the most famous of which is the WMAP cold spot discovered by the WMAP space observatory in the Eridanus constellation [34-35]. The cold spot is approximately $dT = 73$ μK colder than the CMB temperature, $T = 2.7255$ K.

These anomalies can be explained as follows. Since $I = \sigma T^4$ for CMB, in the first approximation, we have $dI = 4\sigma T^3 dT$. If we direct the radiation receiver exactly to the anomalous spot, then in (6), we can set $Q = \frac{\pi}{2}$, $\phi = \frac{\pi}{2}$, and we can write the following:

$$dI = 4\sigma T^3 dT = \frac{L \exp\left(-\frac{Hr}{c}\right) \exp(-snr)\ dV}{4\pi r^2}. \qquad (36)$$

According to (7) and considering the relation $I = \sigma T^4$, we find:

$$I = \sigma T^4 = \frac{L}{4\left(\frac{H}{c} + sn\right)},\ L = 4\sigma T^4 \left(\frac{H}{c} + sn\right). \qquad (37)$$

Substituting L (37) into the expression for dI (36), we find the relationship between the temperature difference dT, the distance r, and the volume dV generating CMB radiation and leading to the contribution dT to the CMB temperature T:

$$dT = \frac{T\left(\frac{H}{c} + sn\right) \exp\left(-\frac{Hr}{c}\right) \exp(-snr)\ dV}{4\pi r^2}. \qquad (38)$$

Equation (38) assumes that the volume dV contains primordial gas-dust clouds functioning as CMB sources, which, on average, have the mass density of $\rho_s = 1.629\times10^{-18}$ kg/m^3 (26) and the concentration of $n = \frac{\rho_b}{m} = 3.4\times10^{-60}$ m^{-3} (28) in the early Universe. In this case, the concentration n appears in two terms of Eq. (38). An increase in n in the term $\left(\frac{H}{c} + sn\right)$ leads to an increase of dT, while the term $\exp(-snr)$ acts in the opposite way, reducing dT. Thus, if in a certain direction in the volume dV the concentration of sources differs from the value n due to some anomaly, this will lead to a change of dT in (38).

We can see from the relation $n = \frac{\rho_b}{m}$ that if the mass m of a typical CMB source is constant, then the change in the concentration of sources n can be associated with a local change in the mass density of baryons ρ_b in the volume dV under consideration. Thus, fluctuations in the mass density ρ_b in cosmic space can influence

fluctuations in the measured CMB temperature in various directions.

According to (8), the redshift z in the model under consideration can be related to the distance r by the formula: $r = \frac{c}{H}\ln(z+1)$. As an example, let us place a certain volume dV at a distance corresponding to $z = 2$, that is, at $r = \frac{c}{H}\ln 3 = 4.7$ Gpc. Let us assume that dT equal to 20 μK, which is close to the value of the root-mean-square small-scale CMB fluctuations. Using further the relation $s = \pi a^2$, the values of $a = 2.088\times10^{16}$ m (26) and $n = 3.4\times10^{-60}$ m^{-3} (28), from (38), we find $dV = 9.35\times10^{74}$ m^3, which for a spherical volume gives the radius of this volume of the order of $R_v = 197$ Mpc. This radius is close to that of the well-known Giant Void in the constellation Canes Venatici [36]. Consequently, according to (38), the presence of such voids naturally leads to the observed CMB temperature fluctuations.

It is known that for sufficiently large spherical harmonics ℓ the relation $\theta = \frac{2\pi}{\ell}$ holds, where θ is the effective sky viewing angle [28]. The main peak in the CMB angular power spectrum occurs at $\ell \approx 360$, which corresponds to the angle $\theta \approx 1°$. Moreover, if the harmonic number $\ell < 360$ and ℓ decreases, and the angle $\theta > 1°$ and θ increases, the power in the angular spectrum decreases gradually without any particular peaks. Why do harmonics with small ℓ manifest in the spectrum in a different way than harmonics with large $\ell > 360$, which form the spectrum in the form of sinusoid damping in amplitude?

For the above example with the volume dV, let us calculate the angle θ in radians using the formula: $\theta = \frac{2R_v}{r} = 0,084$, and the angle $\theta° = \frac{180\,\theta}{\pi} = 4°,8$ in degrees. The angle θ in radians corresponds to the spherical harmonic $\ell = \frac{2\pi}{\theta} = 75$ in the CMB angular power spectrum. It turns out that supervoids with a low density of matter or, on the contrary, denser regions of space can make a significant contribution to CMB temperature fluctuations only at small ℓ. As for the appearance of spherical harmonics with large values $\ell > 360$ in the power spectrum, in the model presented above, according to [30], they are explained by the fact that CMB radiation interacts with matter, which is structured into some objects, clusters, and particles. Thus, different mechanisms lead to different forms of the CMB power spectrum for small and large spherical harmonics. In contrast, the $\Lambda - CDM$ model has difficulties explaining the low power and form of the angular spectrum for harmonics associated with large angles θ and with small ℓ [37].

8. Infrared and Optical Background Radiation

The dependence of the angular intensity J on the cosmic background radiation frequency in [9] shows that there are other angular intensity peaks near the CMB, including those of the cosmic infrared background (CIB) and the cosmic optical background (COB). The total intensity of CIB and COB radiation is almost 10 times less than the intensity of cosmic microwave background radiation (CMB).

It is believed that the main contribution to CIB and COB comes from the processing of radiation from protostars and young stars by cosmic dust. We can make this assumption more concrete. Let us apply the obtained results with respect to the CMB to estimate the parameters of space objects, which could produce CIB and COB radiation.

We can assume that the maximum J for the CIB is obtained at a radiation frequency of $\nu_{CIB} \approx 2\times10^{12}$ Hz, and for the COB, the maximum occurs at a frequency of $\nu_{COB} \approx 3\times10^{14}$ Hz. As a first approximation, let us assume that the Wien displacement law for radiation from a black body is valid for the radiation frequency. This gives the corresponding radiation temperatures $T_{CIB} = 34$ K and $T_{COB} = 5103$ K.

Substituting temperatures T_{CIB} and T_{COB} in (25) instead of temperature T makes it possible to estimate the surface temperatures of CIB and COB sources in the early Universe:

$T_{s\,CIB} = 426$ K. $T_{s\,COB} = 9.6\times10^{6}$ K. (39)

Substituting temperatures from Eq. (39) into Eqs. (21) and (22) instead of T_s, we obtain the corresponding mass densities and radii of the CIB and COB sources. We can also estimate the masses of sources by multiplying the mass density by the volume of the corresponding source:

$$\rho_{s\,CIB} = 3.01\times10^{-12} \text{ kg/m}^3. \quad a_{CIB} = 1.7\times10^{14} \text{ m.}$$
$$m_{CIB} = 6.19\times10^{31} \text{ kg.} \quad (40)$$

$$\rho_{s\,COB} = 34 \text{ kg/m}^3. \quad a_{COB} = 7.5\times10^{9} \text{ m.}$$
$$m_{COB} = 6.008\times10^{31} \text{ kg.} \quad (41)$$

According to (40), the sources of CIB radiation are gas-dust clouds with radii of the order of $a_{CIB} = 1136$ AU and with masses of $m_{CIB} = 31.1M_c$. For comparison, in the Solar System, the dwarf planet Sedna at aphelion moves away from the Sun to a distance of 937 AU. From (41) it follows that the COB radiation sources are objects with mass $m_{COB} = 30.2M_c$ and with a radius of the order of $a_{COB} = 10.8R_c$, where R_c is the radius of the Sun.

In (26) and (27), it was found that a typical CMB radiation source has a radius of 0.68 pc and a mass of the order of $31.2M_c$. The sources of radiation CIB and COB in (40)-41) also have masses of the order of $31M_c$. It turns out that during cosmological evolution, CMB microwave radiation sources first become isolated in the form of gas clouds with a radius of the order of 0.68 pc. When these clouds are subsequently compressed by gravitational forces to a radius of the order of $a_{CIB} = 1136$ AU, protoplanetary systems containing gas and dust arise, leading to the infrared background radiation CIB. The compression of clouds slows down due to the appearance of pressure in the gas, and the process of planet formation begins in the clouds. At the same time, the bulk of gas and dust in the center of each cloud continues to compress. As a result, primordial stars emerge, producing optical background radiation COB. Nuclear reactions begin in the depths of these stars, preventing the gravitational compression of matter. Thus, the CMB, CIB, and COB emissions are associated with the most long-term and equilibrium phases in the evolution of primordial gas-dust clouds.

Since the masses of CIB and COB sources approximately coincide with the mass $m = 31.2M_c$ (27) of CMB sources, the concentration of CIB and COB sources in the early Universe approximately coincides with the concentration $n = \frac{\rho_b}{m} = 3.4\times10^{-60}$ m^{-3} (28) of CMB sources. Due to their large masses, primordial stars that are the sources of COB should transform into neutron stars. Thus, the concentration n can be considered as the concentration of primordial neutron stars. The average distance between such stars can be estimated using the formula $R_s = \frac{1}{\sqrt[3]{n}} \approx 6.7\times10^{19}$ m or $R_s \approx 2.16$ kpc. On the other hand, the observable Universe has a volume of the order of 3.6×10^{80} m^3, which contains about 10^{24} stars [38]. The concentration of stars in the Universe is on the order of 3.6×10^{-56} m^{-3}. Comparing the concentration of all stars with the concentration of primordial neutron stars leads to the fact that there are about 10^4 ordinary stars per neutron star. This ratio of stars is indeed confirmed by observations.

Modern instruments allow us to measure angular power spectra not only for CMB, but also for CIB radiation [39]. Thus, the methods for analyzing the structure of radiating objects, developed in [30] for CMB, can also be applied to CIB radiation. According to [30], the mass density of the medium, which contains objects, clusters, and particles and is responsible for the appearance of CMB angular harmonics, equals 9×10^{-23} kg/m^3. This mass density does not exceed the mass density in (40-41) of the objects, which can be the sources of CIB and COB radiation. This implies the possibility that the cause of harmonics in the CMB and CIB power spectra may be the same objects, clusters, and particles located in the shells of the corresponding gas-dust clouds at different stages of compression of these clouds.

In (34), it was shown that the formula for the energy density of CMB $u_s = \frac{4\sigma T_s^4}{c} = 1.1\times10^{-13}$

J/m^3 (20), where $T_s = 3.472$ K is the temperature of CMB sources in the early Universe, cannot be applied to the entire Universe. Instead of u_s, a significantly lower average volumetric energy density of the CMB was calculated, namely $\overline{u} = 1.4 \times 10^{-23}$ J/m^3 according to (33). This occurs because the gas mass m, occupying the volume V in (34) in the initially homogeneous Universe with the mass density ρ_b, only after being compressed into a gas cloud with a volume V_s and density ρ_s. begins to radiate like a blackbody with the temperature $T_s = 3.472$ K. As CMB photons move through space, their energy decreases due to cosmological redshift. In addition, photons interact with the matter of many CMB sources and are partially scattered. As a result, the intensity of the CMB radiation decreases, and the spectrum of CMB photons becomes close to the observed spectrum of the radiation of a blackbody with temperature $T = 2.7255$ K.

For CIB and COB radiation, the situation is largely similar. As in the case of CMB radiation, CIB and COB radiation are nonequilibrium, and no global blackbody consisting of matter and enclosing the entire Universe exists for these radiation fields. Thus, in practice, we always observe discrete radiation sources which, at sufficiently large distances, merge into an almost uniform background.

9. Discussion of Results

A well-known problem of the Big Bang theory in cosmology is the complete lack of understanding of the nature of such an explosion and of the origin of matter as such. The subsequent use of the general theory of relativity in the $\Lambda - CDM$ model adds new problems, such as singularities and metric space expansion, which are incomprehensible from the perspective of physics, as well as the appearance of unidentified dark matter and mystical dark energy. The use of multiple fitting parameters in the $\Lambda - CDM$ model further undermines the credibility of the modern version of the Big Bang theory.

In [40], six fitting parameters are listed, and it is concluded that despite the accuracy of the results' fitting, it is still not enough to consider the $\Lambda - CDM$ model correct. In [13], the following conclusion was reached: "However, in cosmology, it has unfortunately been the case that even a long series of failed predictions has not generally led to the rejection of theories, but rather to their unlimited modification with ad hoc hypotheses, such as inflation, non-baryonic matter, and dark energy".

It is noted in [41] that it could be possible to improve the situation with predictions in the $\Lambda - CDM$ model if, in addition to the seven fitting parameters of the model, we would assume, for example, the existence of early or dynamical dark energy, neutrino interactions, cosmological models with additional interactions, primordial magnetic fields, modified theories of gravitation, etc.

On the other hand, cosmology in the theory of infinite hierarchical nesting of matter finds the source and cause of origin of matter and the forms of its existence in the uniform evolutionary process of transformation of the main carriers at all matter levels [15]. This means, for example, that the evolution of the matter of planets and stars at the stellar level of matter is due to the evolution and action of carriers belonging to lower matter levels. Each matter level has its own main carrier as the most stable and balanced object, such as a neutron star, nucleon, praon, graon, etc., respectively. The similarity principle assumes the existence of the same coefficients of similarity in mass, size, and speed of processes between the respective objects of the adjacent matter levels, which allows us to find the physical parameters of the main carriers of matter. As a consequence, a neutron star contains as many nucleons as each nucleon contains praons, and as each praon contains graons.

The main driving forces for matter evolution are electromagnetic and gravitational forces, which can be reduced to the action of carriers of the lowest matter levels, moving at relativistic speeds [10], [42-46]. This point of view is supported in [47] by the fact that the evolution of matter in the early Universe turns out to be little dependent on external factors and is determined mainly by internal factors.

It follows from the principle of similarity of matter levels that the analogs of a neutron star at the nucleon level of matter are nucleons, and the analogs of white dwarfs are the so-called nuons [4], which have the same mass range as

nucleons. Nuons are similar in their properties to muons, but the origins of these particles are different: nuons emerge in a manner analogous to the formation of white dwarfs in the course of the long-term evolution of matter, whereas muons appear mainly during the rapid decay of pions, which may be regarded as analogs of low-mass and therefore unstable in the decay of neutron stars. Moreover, neutral nuons play the role of dark matter, which manifests itself through gravitational effects both on the motion of stars and gas clouds inside galaxies, and on the motion of galaxies themselves during their interaction [48]. In contrast, the $\Lambda-CDM$ model encounters difficulties in explaining dark matter and in describing its evolution and origin.

The CMB generation process continues to occur today, although on a smaller scale. The properties of the coldest dark nebulae with masses up to $100M_c$ are quite close to those of primordial gas-dust clouds. Thus, practically opaque Bock globules, which are distinguished by their black color, have a temperature in the range from several degrees to 30 K and a typical mass of up to $30M_c$. From the standpoint of thermal radiation, such objects can model the properties of a blackbody quite well. Here, we provide as examples references to the spectra of the infrared sources IRS 1 and IRS 2 in [49-50] and to the spectrum of the Bok globule B335 in [51].

One review [52] described the properties of 248 small molecular clouds, most of which are Bok globules. It is assumed that in our Galaxy system, the average distance between such globules is 600 pc, and the average mass of a globule is approximately $11M_c$. This distance can be compared with the value $R_s \approx 2.16$ kpc found for the distance between the primordial gas-dust clouds of the early Universe through the concentration n of CMB sources in (28).

According to [52], for most globules the radiation temperature of gas does not exceed 4.5 K, and the kinetic temperature does not exceed 8.5 K. Since globules are heated by radiation from the surrounding star background, the dust temperature in globules turns out to be higher than the gas temperature and depends on the measured frequency band and on the size of the dust particles. On average, the dust temperature is close to 25 K. Under such conditions, the spectrum of some globules appears to be not the blackbody spectrum at one fixed temperature, but rather the sum of the spectra of individual components consisting of gas and dust.

In [53], by analyzing the absorption lines of water molecules in a large cloud of water vapor near the HFLS3 galaxy, it was found that the temperature required for this exciting radiation ranges from 16.4 to 30.2 K. Since the HFLS3 galaxy has a redshift of the order of magnitude $z = 6.34$ and is located sufficiently far away, this temperature is considered from the point of view of the $\Lambda-CDM$ model as the CMB temperature at an earlier time. Moreover, due to the space expansion since then, the CMB temperature should have decreased to the current value of $T = 2.7255$ K.

On the other hand, radiation at a temperature ranging from 16.4 to 30.2 K is quite typical for gas clouds and Bok globules under the action of radiation from surrounding stars, including those in the most distant galaxies. In the model we are considering, the CMB temperature at the moment of emission coincides with the temperature $T_s = 3.472$ K (25) of gas-dust clouds with masses on the order of $31M_c$, so distant from us that their redshift is much greater than the redshift of the observed galaxies.

How does the CMB radiation spectrum almost exactly correspond to the blackbody spectrum? Here, the following circumstances can be taken into account. First, we assume that there were no stars around the primordial gas-dust clouds of the early Universe that could noticeably heat the clouds and influence the form of the clouds' spectrum. Then, the spectrum of each cloud could be sufficiently close to the spectrum of a blackbody with the temperature $T_s = 3.472$ K.

Another circumstance is associated with the size of the visible Universe. Substituting in (8) the maximum measured value of redshift $z = 1089$ for the CMB according to [54] at $H = 70$ km/(s·Mpc), we find the radius of the visible Universe $r = 9.24\times10^{26}$ m or 30 Gpc. Light can travel this distance in $t = \frac{r}{c} = 98$ billion years. This time is less than the minimum

compression time of $t_{\min} \approx \sqrt{\frac{3\pi}{32G\rho_b}} = 145$ billion years, which was found according to (16) for the compression of all baryonic matter during the formation of the visible Universe.

It should be noted that, when measuring CMB intensity, it is necessary to exclude radiation from bright point sources, such as clusters of stars and galaxies, from the obtained data to determine the background radiation precisely. However, the redshift of the most distant observable galaxies does not exceed $z = 12$. For example, the redshift of the galaxy GN-z11 equals $z = 11.09$ according to [55]. This redshift is significantly lower than the redshift of the CMB, which reaches $z = 1089$. Thus, CMB radiation travels the main part of its way in unexplored distant regions of cosmic space.

In (6) and (7), it was taken into account that the cross-sections of CMB sources in the early Universe and the concentration of sources are such that, at very large distances, these cross-sections begin to overlap. Consequently, the Beer–Lambert law becomes valid. As a result, the CMB radiation coming to the Earth from distant sources has enough time to interact with the matter of multiple closer sources and additionally thermalize. This approach inevitably turns the CMB spectrum into an averaged spectrum that is close to the equilibrium spectrum of a blackbody.

The presented model is consistent with the results in [56], where the so-called virial gas clouds located in the halo of galaxies make it possible to explain the rotational anisotropy observed in the CMB. In [57], within the framework of the standard model of the expanding Universe, the evolution of virial clouds from the surface of the last scattering to the formation of primordial stars of population III was considered. These virial clouds, which are also in thermal equilibrium with the CMB, as in our approach, have almost the same density as the primordial gas-dust clouds in our model. Thus, the conclusions in [56-57] concerning primordial gas-dust clouds prove our calculations.

The Earth and the Sun are known to move relative to the reference frame, in which the CMB is isotropic, at a speed of approximately 370 km/s. If we take into account the motion of the Sun in our galaxy and its motion in the Local Group of Galaxies, then the speed of the Local Group of Galaxies relative to the CMB's isotropic reference frame will be about $V_g = 627$ km/s [58]. In the $\Lambda - CDM$ model, the cosmological redshift is interpreted as a result of the Universe's expansion, which has the mathematical meaning of a change in the spacetime metric, caused by an unknown factor. The physical meaning of this space expansion is an obvious subject for discussion regarding the justifiability of the use of mathematical hypotheses in the real physics of phenomena. It is assumed that at large distances from the Earth, galaxies and other objects located there are moving away from each other at tremendous speeds due to space expansion. These speeds can significantly exceed the speed V_g of motion of the Local Group of Galaxies relative to the isotropic reference frame of the CMB. So, why from the entire speed spectrum do we observe a relatively small speed V_g? Is it by chance?

From the viewpoint of the theory of infinite hierarchical nesting of matter, the answer lies in the fact that, for matter evolution and for the emergence of a new matter level with more massive objects, neither the Big Bang nor the metric expansion of spacetime nor high speeds of motion are needed. The deviation of the speed of galaxies and star clusters from the speed of the CMB's isotropic reference frame can be caused only by the gravitational action of galaxies on each other. When averaging the matter's speeds over the volume of the visible Universe, the obtained average speed must coincide with the speed of the CMB's reference frame because the CMB occurs in the early Universe and, on average, is stationary relative to the global distribution of matter.

Taking this into account, the problem of space flatness on cosmological scales becomes understandable when even at very large distances, spacetime is practically not curved. Therefore, there is no great need to calculate any curved metric, which is always needed in the general theory of relativity, even in flat Minkowski spacetime. In this case, instead of the general theory of relativity, it is more convenient to use the covariant theory of gravitation [59-60], in which the metric effects are separated from the gravitational effects. This means that

gravitation does not depend on a metric; rather, it is a real physical force, such as the electromagnetic force, which exists even in Minkowski spacetime, when there is no spacetime curvature.

Paradoxes arising from the concept of space expansion were analyzed in [61], including the violation of the law of conservation of energy for local comoving volumes, the Newtonian form of the Friedmann equations, the superluminal velocities of distant galaxies as a result of space expansion, and Hubble's law in inhomogeneous distributions of galaxies. The main reason for the appearance of such paradoxes lies in the general theory of relativity, which lacks an energy-momentum tensor of the gravitational field. This omission raises doubts about the validity of applying general relativity to cosmological models.

It was noted in [62] that the time scale in the $\Lambda - CDM$ model does not correspond to the time, which was required for the formation of large galactic clusters and voids in the early Universe. In this regard, it is assumed that this discrepancy may be due to the use of the general theory of relativity, which should be replaced with another gravitation theory, for example, modified Newtonian dynamics (MOND). The authors of [62] draw the following conclusion from their article: at the present moment, we understand neither the distribution of matter and energy in the Universe nor the law of gravitation, which governs this.

It was found in [63] that a supercluster of galaxies with a radius of about 6 Mpc rotated at an angular velocity ω equal to °2.9 degrees per 10 billion years, or $\omega = 1.6\times10^{-19}$ s^{-1}. According to [64], large galactic clusters with sizes on the order of $R_c \approx 800$ Mpc can experience general motion at velocities up to $V_c \approx 1000$ km/s. Assuming that this motion arises from rotation, for the angular velocity in the first approximation, we have $\omega_c \approx \frac{V_c}{R_c} \approx 4\times10^{-20}$ s^{-1}. The large-scale structure of the Universe has the form of a cosmic web and consists of individual filaments that contain galactic clusters. The difference ΔV in the linear velocity of rotation of different points in the filaments can reach 100 km/s at a distance ΔR between the points equal to 1 Mpc, which gives an estimate of the angular velocity of rotation $\omega_f \approx \frac{\Delta V}{\Delta R} \approx 3\times10^{-18}$ s^{-1} according to [65].

If we assume that the entire visible Universe also rotates, then its limiting rotation can be estimated by the formula for the first cosmic velocity, assuming that the matter at the edge of the Universe is in equilibrium between the gravitational force and the centripetal force:

$$\omega_U = \sqrt{\frac{GM_U}{R_U^3}} = \sqrt{\frac{4\pi G\rho_U}{3}}.$$

where M_U, R_U, and ρ_U denote the mass, radius, and mass density of the Universe, respectively. Substituting here the mass density $\rho_b = 2.1\times10^{-28}$ kg/m^3 instead of ρ_U, we find $\omega_U = 2.4\times10^{-19}$ s^{-1}, which has the same order of magnitude with respect to the rotation of large galactic structures. This rotation corresponds to a period of approximately 830 billion years.

It is obvious that any general rotation of the observable Universe contradicts the Big Bang since, due to rotation, the Universe would have a nonzero angular momentum. In the scenario of the Big Bang and subsequent inflation up to the state of the observable Universe, it turns out that, taking into account the law of conservation of angular momentum, the object that gave rise to the Universe should have had an enormous angular momentum for its small size, which seems completely improbable. At the same time, in the hierarchical model, the object, from which the early Universe was formed, could consist of a huge cloud of praons. If this cloud with the sizes of the order of the observable Universe had any general rotation, then the emerging Universe would have the same rotation after the evolution of praonic matter and its transformation into nucleons and nuons.

We believe that other, less complex cosmological problems can also find their solution within the framework of the theory of infinite hierarchical nesting of matter and a stationary Universe. For example, in [66] it is indicated that expansion of space is not required to explain the change in luminosity in the spectra of supernovae. Thus, cosmology can be constructed with a minimum of assumptions and

paradoxical conclusions that contradict the traditional logic of physics.

10. Conclusions

Cosmic microwave background radiation (CMB) and the effect of the cosmological redshift of radiation spectra are usually considered phenomena that find an acceptable explanation within the framework of the Big Bang theory. Indeed, these phenomena are difficult to interpret otherwise, which historically led to the formulation of the Big Bang concept. However, due to the significant drawbacks of this theory, which are described above, we consider this theory to be too exotic and radical and suggest another explanation for the emergence of CMB.

In our approach, the necessary source of CMB energy turns out to be gravitational energy, which, under matter clustering in primordial gas-dust clouds in the early Universe, is released in the form of the kinetic energy of motion of matter particles, according to the virial theorem. The subsequent collisions of particles convert kinetic energy into thermal energy, heating the particles, so that gas-dust clouds can radiate as blackbodies at the temperature of $T_s = 3.472$ K (25). Over the time it takes for CMB radiation to travel from distant regions of the Universe to Earth, its temperature decreases to the value of $T = 2.7255$ K.

Based on this approach, we first find formula (7) for the volumetric power L of CMB energy generation in cosmic space, and then we find the main characteristics of primordial gas-dust clouds, including their radius $a \approx 0.68$ pc (26), mass $m \approx 31 M_c$ (27), volume concentration of clouds $n \approx 3.4 \times 10^{-60}$ m^{-3} (28), and distance between neighboring clouds $R_s \approx 2.2$ kpc. For the volumetric power L of CMB energy generation, the value $L \approx 1.5 \times 10^{-31}$ W/m^3 (29) is obtained, while the generation power per nucleon of a typical gas-dust cloud, as well as per nucleon in the early Universe, is equal to $\frac{L}{n_b} \approx 1.2 \times 10^{-30}$ W/nucleon (30).

We can conclude that the CMB originated as thermal radiation from primordial gas-dust clouds. This thermal radiation could interact with a large number of particles in each cloud, which, in view of the slowly changing equilibrium state of the clouds and their opacity and weak reflection, provides the CMB radiation spectrum close to that of blackbody radiation. In addition, CMB radiation coming from very large distances passes through many separate CMB sources in the form of gas clouds on its way to Earth. This further contributes to the transformation of the CMB spectrum into a blackbody spectrum.

As indicated in Section 6 with reference to [30], the angular harmonics in the CMB power spectrum can be explained if we take into account matter clustering near the surface of primordial gas-dust clouds. This possibility is supported by the presence of both small and large dust particles observed in Bok globules, leading to significant polarization of radiation in the millimeter range [67-69] up to values on the order of 10% or more. In this regard, the degree of polarization of the CMB is also approximately 10%. Thus, the primordial gas-dust clouds responsible for generating the CMB could have evolved into structures resembling globules.

In addition to CMB, the approach under consideration can be applied to infrared background radiation (CIB) and optical background radiation (COB). The estimates made in Section 7 give reason to believe that the CIB emission could have originated in protoplanetary clouds, while the contribution to the COB emission was made by primordial stars.

Although the blackbody CMB radiation coming to the Earth from all directions has an intensity $I = \sigma T^4$, this does not mean that the ubiquitous occurrence of CMB energy density in cosmic space is equal to $u = \frac{4\sigma T^4}{c} = 4.17 \times 10^{-14}$ J/m^3, similar to blackbody radiation. As shown in (33), the average CMB energy density in the Universe should equal $\overline{u} = 1.4 \times 10^{-23}$ J/m^3. This happens because the CMB is radiation that is not in equilibrium with the global blackbody. Indeed, all CMB sources cannot form a closed surface entirely surrounding the radiation of the Universe, which is a necessary condition for the validity of the formula $u = \frac{4\sigma T^4}{c}$. The same applies to CIB radiation and COB radiation, which are also nonequilibrium.

Due to the difference between the energy density $\overline{u}$ and the energy density u_s (20) of blackbody radiation, it becomes possible to move away from the model of the hot expanding Universe. It follows from this model that the CMB energy density is equal to u everywhere, so that the ratio of the number of photons to the number of nucleons is equal to $\frac{n_f}{n_b}=\frac{n_f m_p}{\rho_b}=3.3\times10^9$, which is close in magnitude to the ratio of volumes $\frac{V}{V_s}$ in (34). In our approach, the energy density $\overline{u}$ corresponds to the condition of practically the same number of photons and nucleons, eliminating the problem of excess photons and removing the need to introduce the hot Universe model.

Statements and declarations

The authors have no relevant financial or non-financial interests to disclose.

Data availability

The data underlying this article are provided in the text and in the online supplementary material.

References

[1] Flandern, T.V., Apeiron, 9 (2) (2002) 72.

[2] Narlikar, J.V., Burbidge, G., and Vishwakarma, R.G., J. Astrophys. Astron., 28 (2007) 67.

[3] Gupta, S.N.P., J. Astrophys. Aerosp. Technol., 4 (1) (2016) 128.

[4] Fedosin, S.G., Galil. Electrodyn., 23 (1) (2012) 3.

[5] Millette, P.A., Lett. Prog. Phys., 17 (2) (2021) 216.

[6] Burbidge, G. and Hoyle, F., Astrophys. J. Lett., 509 (1998) L1.

[7] Hill, R., Masui, K.W., and Scott, D., Appl. Spectrosc., 72 (5) (2018) 663.

[8] Driver, S.P., arXiv:2102.12089.

[9] Fedosin, S.G., Int. Front. Sci. Lett., 14 (2019) 19.

[10] Fedosin, S.G., Can. J. Pure Appl. Sci., 15 (1) (2021) 5125.

[11] Ashmore, L., Vigier 11 Conference, Liege, Belgium, August (2018).

[12] Ashmore, L.A., J. High Energy Phys., Gravitation Cosm., 2 (4) (2016) 70089.

[13] Lerner, E.J., Mon. Not. R. Astron. Soc., 477 (2018) 3185.

[14] Lerner, E.J., Falomo, R., and Scarpa, R., Int. J. Mod. Phys. D, 23 (6) (2014) 1450058.

[15] Fedosin, S., "The Physical Theories and Infinite Hierarchical Nesting of Matter", Vol. 1, (LAP LAMBERT Academic Publishing, 2014), 580, ISBN 978-3-659-57301-9.

[16] Hinshaw, G.F. et al., ApJS, 208 (2) (2013) 19H.

[17] Oldershaw, R.L., Astrophys. J., 322 (1987) 34.

[18] Oldershaw, R.L., Int. J. Theor. Phys., 28 (6) (1989) 669.

[19] Oldershaw, R.L., Int. J. Theor. Phys., 28 (12) (1989) 1503.

[20] Oldershaw, R.L., Astrophys. Space Sci., 189 (1992) 163.

[21] Fedosin, S.G., Turk. J. Phys., 36 (3) (2012) 461.

[22] Shklovsky, I.S., "Stars: Their Birth, Life, Death". (San Francisco, 1978), ISBN 0-7167-0024-7.

[23] Kolb, E. and Turner, M., "The Early Universe". (Addison-Wesley, 1988), ISBN 978-0-201-11604-5.

[24] Fedosin, S.G., Contin. Mech. Thermodyn., 29 (2) (2017) 361.

[25] Fedosin, S.G., Contin. Mech. Thermodyn., 31 (3) (2019) 627.

[26] Fedosin, S.G., Middle East J. Sci., 5 (1) (2019) 46.

[27] Sievers, J.L. et al., Astrophys. J., 591 (2) (2003) 599.

[28] Hu, W. and Dodelson, S., Rev. Astron. Astrophys., 40 (2002) 1.

[29] Zyla, P.A. et al., (Particle Data Group), Prog. Theor. Exp. Phys., 2020 (8) (2020) 083C01.

[30] Červinka, L., J. Mod. Phys., 2 (11) (2011) 1331.

[31] Jeans, J.H., Philos. Trans. R. Soc. Lond., Ser. A, 199 (1902) 1.

[32] Cabré, A., Gaztañaga, E., Manera, M., Fosalba, P., and Castander, F., Mon. Not. R. Astron. Soc.: Lett., 372 (1) (2006) L23.

[33] Pietrobon, D., Balbi, A., and Marinucci, D., Phys. Rev. D, 74 (2006) 043524.

[34] Cruz, M., Martinez-Gonzalez, E., Vielva, P., and Cayon, L., Mon. Not. R. Astron. Soc., 356 (1) (2005) 29.

[35] Mackenzie, R. et al., Mon. Not. R. Astron. Soc., 470 (2) (2017) 2328.

[36] Kopylov, A.I. and Kopylova, F.G., Astron. Astrophys., 382 (2) (2002) 389.

[37] Schwarz, D.J. et al., Class. Quantum Grav., 33 (18) (2016) 184001.

[38] Marov, M.Y., "The Structure of the Universe", In: "The Fundamentals of Modern Astrophysics", (2015), pp. 279-294, ISBN 978-1-4614-8729-6.

[39] Maniyar, A.S., Lagache, G., Béthermin, M., and Ilić, S., A&A, 621 (2019) A32.

[40] Debono, I. and Smoot, G.F., Universe, 2 (4) (2016) 23.

[41] Di Valentino, E. et al., Class. Quantum Grav., 38 (15) (2021) 153001.

[42] Fedosin, S.G., Phys. Sci. Int. J., 8 (4) (2015) 1.

[43] Fedosin, S.G., WSEAS Trans. Appl. Theor. Mech., 10 (3) (2015) 31.

[44] Fedosin, S.G., J. Fundam. Appl. Sci., 8 (3) (2016) 971.

[45] Fedosin, S.G., J. Fundam. Appl. Sci., 9 (1) (2017) 411.

[46] Fedosin, S.G., Jordan J. Phys., 17 (1) (2024) 87.

[47] Suzuki, T.L. et al., Publ. Astron. Soc. Jpn., 71 (4) (2019) 69.

[48] Clowe, D. et al., Astrophys. J., 648 (2) (2006) L109.

[49] Beichman, C.A. et al., Astrophys. J. Lett., 278 (1984) 145.

[50] Beichman, C.A. et al., Astrophys. J., 307 (1986) 337.

[51] Keene, J. et al., Astrophys. J. Lett., 274 (1983) 143.

[52] Clemens, D.P., Yun, J.L., and Heyer, M.H., Astrophys. J. Suppl., 75 (1991) 877.

[53] Riechers, D. et al., Nature, 602 (2022) 58.

[54] Lineweaver, C. and Davis, T.M., Sci. Am., 292 (3) (2005) 36.

[55] Oesch, P.A. et al., Astrophys. J., 819 (2) (2016) 129.

[56] Qadir, A., Tahir, N., and Sakhi, M., Phys. Rev. D, 100 (4) (2019) 043028.

[57] Tahir, N. et al., Eur. Phys. J. C., 81 (2021) 827.

[58] Kogut, A. et al., Astrophys. J., 419 (1993) 1.

[59] Fedosin, S.G., Can. J. Phys., 93 (11) (2015) 1335.

[60] Fedosin, S.G., Int. Lett. Chem. Phys. Astron., 78 (2018) 39.

[61] Baryshev, Y., AIP Conf. Proc., 822 (2006) 23.

[62] Asencio, E., Banik, I., and Kroupa, P., Mon. Not. R. Astron. Soc., 500 (4) (2021) 5249.

[63] Lee, J.H. et al., Astrophys. J., 884 (2) (2019) 104.

[64] Salehi, A., Yarahmadi, M., and Fathi, S., Mon. Not. R. Astron. Soc., 504 (1) (2021) 1304.

[65] Wang, P. et al., Nat. Astron., 5 (2021) 839.

[66] Crawford, D.F., Open Astron., 26 (1) (2017) 111.

[67] Ward-Thompson, D., Kirk, J.M., Crutcher, R.M., Greaves, J.S., Holland, W.S., and Andre, P., Astrophys. J., 537 (2000) L135.

[68] Matthews, B.C. and Wilson, C.D., Astrophys. J., 574 (2002) 822.

[69] Zielinski, N., Wolf, S., and Brunngräber, R., A&A, 645 (2021) A125.

Volume 18, Number 4, 2025. pp. 551-560

Jordan Journal of Physics

ARTICLE

Results of Observations for Three Confirmed Exoplanets Using UV/IR Cut Filter

Mohammad F. Talafha[a], **Abdelrazek M. K. Shaltout**[b], **Ali G. A. Abdelkawy**[b] and **. M. Beheary**[b]

[a] *Sharjah Academy of Astronomy, Space Sciences and Technology SAASST, University of Sharjah, UAE.*

[b] *Department of Astronomy and Meteorology, Faculty of Science, Al-Azhar University, Cairo, Egypt.*

Doi: **https://doi.org/10.47011/18.4.11**

Received on: 08/10/2024; *Accepted on: 10/12/2024*

Abstract: We present the exoplanet transit phenomena detected by the Sharjah Astronomical Observatory (SAO-M47) located in Sharjah, United Arab Emirates. In this work, we observed the transits of three hot Jupiter exoplanets, TrES-1b, WASP-104b, and HAT-P-54b, using a UV-IR cut filter with a bandwidth range from 420 to 685 nm. The obtained results were compared with data from a previously published paper and other observations conducted with several filters to identify differences in the analysis of these three hot Jupiter exoplanets. In general, the study focused on how changes in a planet's size are influenced by the particles in its atmosphere. Obtained by using a wide-band UV-IR cut filter and multiwavelength observations, this work's results are comparable to the previous work, specifically regarding the relationship between fine and large particles and the detected scattering effect by blocking the host star light. Several other parameters, such as orbit inclination (i) and transit duration T_{dir}, are also presented with the obtained results, namely, 1.205 ± 0.019 R_{JUP}, 1.028 +0.046 / -0.049 R_{JUP}, and 1.079+0.040/-0.042R_{JUP} for TrES1b, HAT-P-54b, and WASP-104b, respectively. The rest of the parameters are included in the tables.

Keywords: Exoplanet, HAT-P-54b, WASP-104b, TrES-1b, Sharjah Astronomical Observatory (SAO), Photometry transit.

Introduction

Transit photometry is considered the most functional method for detecting distant planets that transit between a star and the Earth. Conducted with this method, regular observations of giant exoplanets are necessary to improve their parameters and ephemerides, thereby assisting in explaining their peculiarities. When a planet crosses (or transits) in front of its parent star's disk, the observed brightness of the star is noticed to drop by a small amount. The depth of transit depends on the relative sizes of the star and the planet [1]. This method of detection is called transit photometry. The transit method enables us to measure the radius of a planet, its inclination, impact parameter, and transit time. The transit of exoplanets allows us to test planetary structure and evolution theories [2].

Observational astronomy becomes science only when we can start to answer questions quantitatively: How far away is that object? How much energy does it emit? How hot is it? The most fundamental information we can measure about celestial objects past our solar system is the amount of energy, in the form of electromagnetic radiation, that we receive from that object. This quantity we will call the flux. The science of measuring the flux we receive from celestial objects is called photometry [3].

Corresponding Author: Mohammad F. Talafha **Email**: mtalafha@sharjah.ac.ae

In the search for extrasolar planets, many methods such as direct imaging, radial velocity, and gravitational lensing have been employed, but the transit method, also known as transit photometry, has proven to be mankind's most effective tool, as it has been responsible for the discovery of exoplanets. Of the 4108 confirmed planets as of the end of January 2020, 3160 were detected using this technique (NASA Exoplanet Archive) (https://exoplanetarchive.ipac.caltech.edu).

In 1992, the first exoplanets around the pulsar PSR B1257+12 were discovered by the detection of the anomalies in the pulsation period [4]. Since then, many amateur astronomers have attempted to measure the signature light-curve dips of known transiting exoplanets in the early 21st century, such as HD209458b [1] and TrES-1b [1, 5], and have reached more than 5700 exoplanets by the year 2024.

There are many techniques used in transit photometry observations to extract more information about the planets, such as defocusing and multiwavelength observations. Here, we used a wide-band filter covering the near-ultraviolet to far-red range (420 – 685 nm) to examine the light curve shape compared with the previous results obtained by using narrow-band or specific filters. The light dispersion depends on the particle size under Mia and Rayleigh scattering methods. From this relationship, we can infer which particle sizes are dominant in the atmosphere.

Target Selection and Observation

We present here the selection and observation of three target exoplanets, chosen according to several specific criteria. The first criterion was to select exoplanets with a transit depth greater than 0.01 mag, as listed in the Exoplanet Transit Database (ETD) (http://var2.astro.cz/ETD). Currently, the Exoplanet Transit Database [6], run by the Czech Astronomical Society since 2009, is the largest repository of such data, containing over 10,000 transit light curves for more than 350 exoplanetary systems [6, 7]. The second condition required that each observation cover the entire transit event, beginning at least 30 minutes before and after the predicted transit interval. The third one was that the target exoplanet be positioned at a high altitude in the sky, corresponding to minimal airmass. Finally, the fourth condition required that the host star's magnitude not exceed 14 mag, which defines the detection limit for the SAO. Based on these conditions, three targets were selected: TrES-1b, WASP-104b, and HAT-P-54b. **TrES-1b** is an exoplanet discovered by the Trans-Atlantic Exoplanet Survey [5]. It is located approximately 512 light-years from the Sun and orbits its host star at a semi-major axis of 0.0393 ± 0.0011 AU [8]. The initially published transit depth was 0.0208 mag [6], and the host star has an apparent V magnitude of 11.79 and is classified as a K0V-type star. TrES-1b lies in the constellation Lyra [5] and has a radius of 1.08 R_{JUP}, a mass of 0.729 M_{JUP}, an orbital period of 3.03 days, and an orbital inclination of 88.2 degrees [9].

HAT-P-54b was discovered and confirmed in 2015 and is among the lowest-mass stars known to host a Hot Jupiter exoplanet, located at a distance of 443 ± 11 light-years [10, 11]. Its transit depth is 0.0265 mag [6], and it orbits a K-dwarf star with an apparent magnitude of V = 13.5. The planet has a radius of 0.944 ± 0.028 R_{JUP}, a mass of 0.760 ± 0.032 M_{JUP}, an orbital period of 3.7998 days, and an orbital inclination that reaches up to 88.04 degrees.

Finally, **WASP-104b** located at a distance of 466 ± 33 light-years, consists of a single star–planet system. Its transit depth is 0.0158 mag [6], and the host star has a V magnitude of 11.1, classified as a G8 main-sequence star [12]. WASP-104b has a radius of 1.1 R_{JUP} [12], a mass of 1.3 M_{JUP}, and an orbital inclination of 83.63 degrees [6]. It is a hot Jupiter that orbits its host star in a circular path with a period of 1.75 days. All the information is displayed in Table 1.

TABLE 1. Reference parameters of the target exoplanets and their host stars.

Targets	TrES-1b	HAT-P-54b	WSAP-104b
R_{JUP}	1.08	0.944±0.028	1.1
M_{JUP}	0.729	0.760±0.032	1.3
Inclination(degree)	88.2	87.04	83.63
Orbital period (Day	3.03	3.7998	1.76
Depth of transit (mag)	0.0208	0.0265	0.0158
Host star (mag)	11.79	13.505	11.1
Host star (Distance Ly)	512	433±11	466±33
Classification of host star	K0V	K	G8

Increasing capabilities of instruments and skills allow amateur astronomers to engage in the exoplanet discovery race and follow-up observations using the transit method, along with university and professional astronomers, in searching for new transiting exoplanets. As an increasing number of submeter-aperture telescopes become employed in these searches, it is important to quantify the detection levels that can be attained with such equipment and to identify analytically methods that can be used to detect and characterize transit light curves [5]. Sharjah Astronomical Observatory (SAO-M47) [25] contains a 0.431m robotic telescope, which makes the observatory unique in the Middle East region, where there are no other professional observatories equipped with similar specialized instruments. Moreover, the robotic telescope is fully automated and protected by a four-meter-diameter dome equipped with a weather station. The telescope is a PlaneWave CDK17 Schmidt-Cassegrain reflector attached to a 4k x 4k SBIG 16803 CCD camera with a filter wheel containing JOHNSON/BESSEL U, B, V, R, and I filters. SAO was built in SAASST for educational purposes, serving undergraduate students throughout the UAE. The University of Sharjah has opened opportunities for students pursuing an M.Sc. degree in Astronomy and Space Sciences, and it plays a vital role in supporting graduate students who are enrolled in this program to conduct their research.

Table 2 presents the log of photometric observations, including the target name, dates of observation, exposure time, number of frames, and photometric precision (SNR). The same observational procedures and analysis methods were applied to all three targets (TrES-1b, HAT-P-54b, and WASP-104b), except for the exposure time. For the analysis described here, only complete transit light curves were used, acquired under conditions determined by the observatory location and the high altitude of the targets in the sky, approximately 50 degrees above the horizon.

Observation planning was based on the Exoplanet Transit Database (ETD) [6], which provided the exact time and date of each transit, as well as the azimuth, altitude of the targets, and other necessary information for following the transit. A UV–IR cut filter (4200–6850 Å) was used for all observations.

Data acquisition and analysis were carried out in two steps. First, MaximDL software was used for telescope guiding, image capture, and reduction. In the second step, the data were analyzed to generate light curves and exoplanet parameters using ManuWin and AstroImageJ software.

TABLE 2. Log of target observations.

Parameters	TrES-1b	HAT-P-54b	WASP-104b
Date of observation	16th June 2018	8th Dec.2018	6th Feb. 2019
Number of Frames	73	29	59
Exposure Time	120sec	300sec	120sec
Filter	UV-IR cut	UV-IR cut	UV-IR cut
Binning	1x1	1x1	1x1
Airmass (min – max)	1.06 – 1.18	1.03 – 1.2	1.05 – 1.15
SNR	~1000	~500	~1000

Observing TrES-1b:

Within the American Association of Variable Star Observers (AAVSO) and transit search networks, many astronomers - expert and amateur - report exoplanet transit light curves and share their results with one another [5]. These data are also published in the Transit Exoplanet Database (TED), as was done for our observations.

TrES-1b was discovered by the Trans-Atlantic Exoplanet Survey (TrES) and is located at coordinates R.A. 19h 04m 09.8s, Dec. +36° 37′ 57″ (J2000) [13].

Our observations of TrES-1b began on 16 June 2018 at 20:20:28 UT (JD 2458286.3475462962) and continued until the last image at 23:26:43 UT (JD 2458286.4910300928). The mid-transit time (TC) occurred at 21:55:22 UT (HJD 2458286.41612 ± 0.00057). An exposure time of 120 s was used to increase the signal-to-noise ratio. Observations started 25 minutes before ingress and ended 15 minutes after egress. A total of 73 images were obtained during the observation period, as shown in Fig. 1.

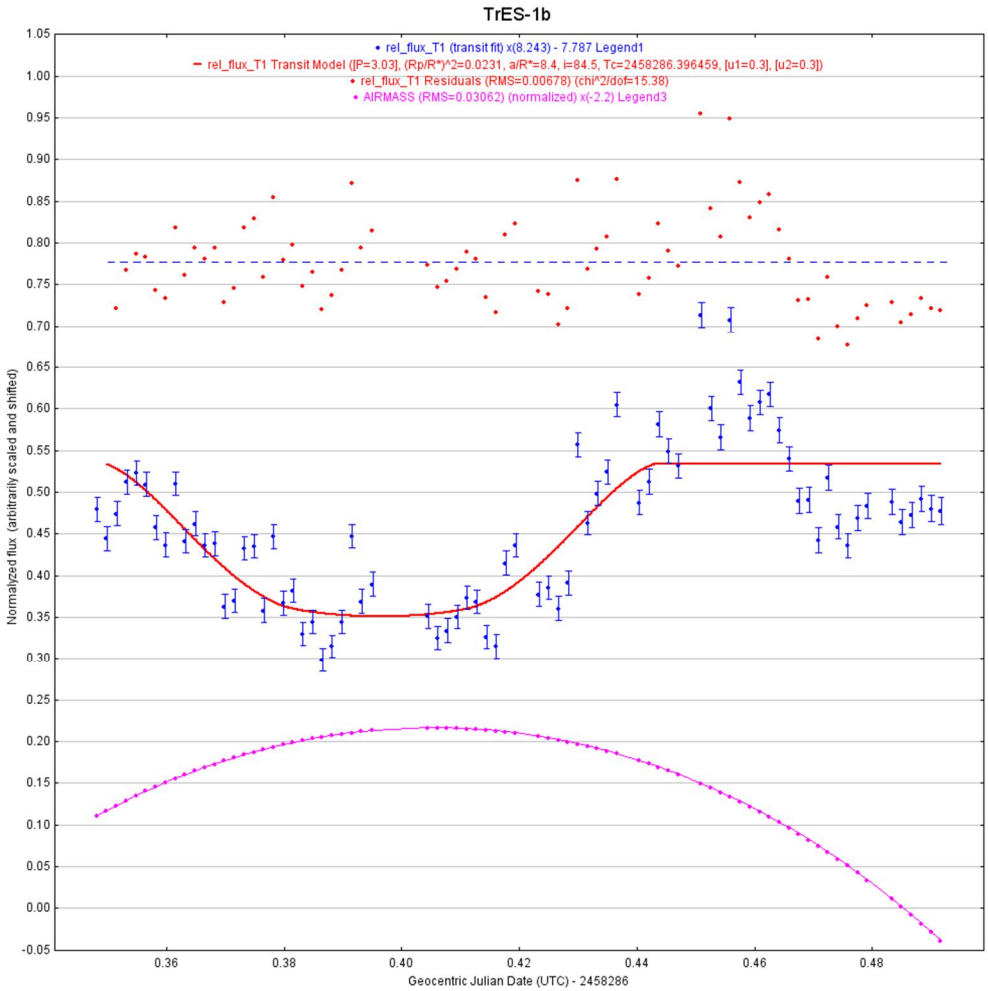

FIG. 1. Top: Residuals of the fitted data. Middle: The best solution for the transit of TrES-1b. Bottom: Air mass during the observation.

Observing HAT-P-54b:

Following the breakdown of two of its orientation wheels, the Kepler space telescope was repurposed in a mission called K2 [10]. In this mission, the Kepler space telescope was utilized to observe 10 fields along the ecliptic plane over a span of two years. For various reasons, the number of stars that can be seen in each field is significantly lower than in the first Kepler mission. Due to this, early perceptions of K2 fields by ground-based telescopes to pre-select targets are very beneficial [10]. The exoplanet HAT-P-54b is in the primary field that can be seen by the K2 mission, known as Feld 0. This planet, found by the HATNet study, is the first transiting planet identified in this field [10]. Initial photometric observations of the star HAT-P-54 were carried out by the fully automated HATNet system [10]. It was found that the radius of HAT-P-54b is smaller than 92% of the known transiting planets with masses greater than that of Saturn [11]. The host star has V = 13.505 ± 0.060, a mass of 0.645 ± 0.020 M_{sun} and a radius of 0.617±0.01 R_{sun}, making HAT-P-54 one of the lowest-mass stars known to host a hot Jupiter [10]. HAT-P-54 was observed by Sharjah Observatory on 8 December 2018. The first image was taken at 20:31:16 UT (JD 2458486.3475462962), with the ingress of the transit occurring at 21:06:00 UT at an altitude of 82° (E), giving an ingress duration of 35 minutes. The last image was taken at 23:22:06 UT (2458486.4910300928 JD), resulting in an egress duration of 25 minutes at an altitude of 75° (W). The mid-transit time was observed at 22:12:44 UT (Tc = 2458461.42204 ± 0.00134 HJD) [6], as shown in Fig. 2.

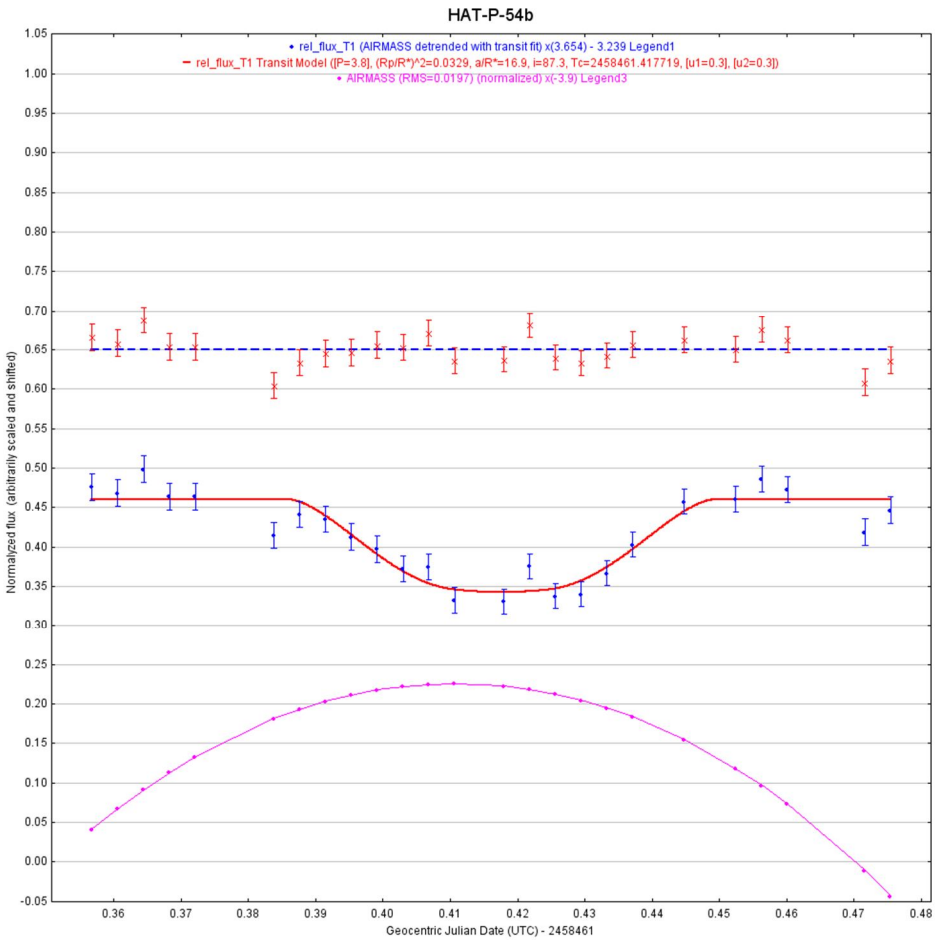

FIG. 2. Top: Residuals of the fitted data. Middle: The best solution for the transit of HAT-P-54b. Bottom: Air mass during the observation.

Observing WASP-104b:

Information regarding planets transiting stars that are brighter than those observed by Kepler is required to expand our knowledge of the range of properties exhibited by the nearby planets, as well as to advance our understanding of planetary formation and evolution [14]. WASP-104b is a transiting hot Jupiter in a 1.76-day circular orbit around a V = 11.1 G8 main-sequence star. The planet has a mass of 1.3 M_{JUP} and a radius of 1.1 R_{JUP} [12].

Sharjah Astronomical Observatory was successful in observing the full transit of WASP-104b on 6 February 2019. Observations started at 19:31:13 (2458521.3133449075JD) with the first touch of the transit beginning at 20:21 (63 SE), meaning that it took 50 minutes for ingress. The last image was at 22:37:01 (2458521.4423726853 JD). The egress of the transit was at 22:06 UT (72 S), making it ~30 minutes after egress of the transit. The mid of the transit was at 21:14 (Tc = 2458521.37323 ± 0.00101JHD) [6] at an altitude of 71 S. A long exposure time (120 sec) was used for raising the SNR, with the best value of SNR achieved in image 14 (SNR ~1010 and 1/SNR ~ 0.001). The light curve appears with 59 images during the observation period, as shown in Fig. 3.

Analysis and software:

For analyzing and creating the light curve, two different software packages were used. First, the Muniwin package was employed to produce the light curve based on the observed magnitude dip. The optimal aperture photometry was selected for processing, with careful choice of comparison stars. The results were saved as a .txt file and submitted to the TRESCA transit model on the Exoplanet Transit Database (ETD) website [6] (http://var2.astro.cz/ETD/observers.php) to calculate exoplanet parameters and plot the light curves. The air mass curve and the fitted transit observations in the TRESCA model were used to derive the parameters for our observational light curves, which are presented in Table 3.

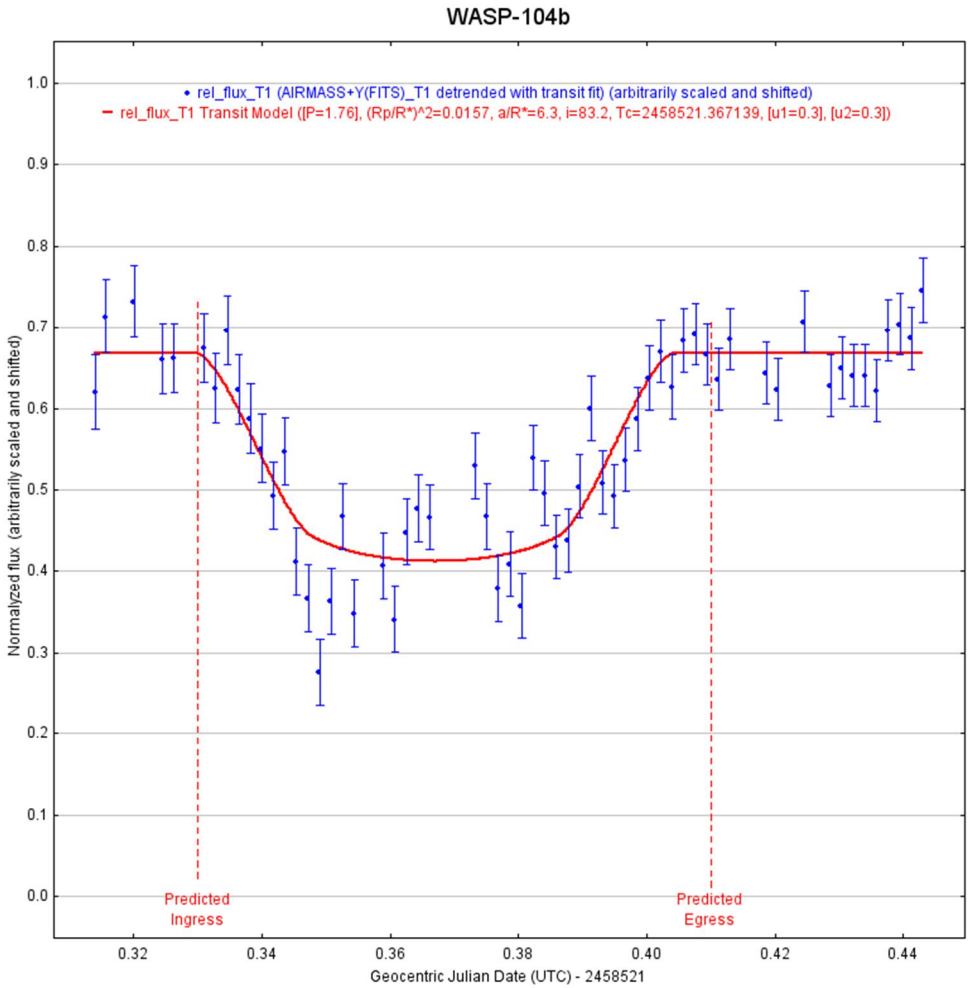

FIG. 3. Top: Residuals of the fitted data. Middle: The best solution for the transit WASP-104b. Bottom: Air mass during the observation.

TABLE 3. Parameters and observational solutions generated by the Exoplanet Transit Database (TRESCA) model.

Targets & Parameters	TrES-1b	HAT-P-54b	WASP-104b
Orbit inclination(i)	87.65◦	86.53◦	88.67°
Transit depth (mag)	0.0249± 0.0008	0.0321± 0.003	0.0144± 0.0011
Transit duration (min)	144.8± 2	95.9± 6	99.2± 4
R of planet (R_{JUP})	1.205	1.028	1.079
Fit data	2	3	3

The second software used for calculations was AstroImageJ, which allows fitting and plotting of the data [15]. In this software, some parameters, such as the host star radius and the planet period, are fixed. Figure 1 shows the light curve of the exoplanet's full transit, with the fitted data overlaid, alongside the air mass curve to illustrate the observing conditions. The red in the legend lists the transit solution numbers for this transit. The same applies to Figs. 2 and 3.

Discussion:

Observing the primary transit of an exoplanet at multiple wavelengths allows researchers to investigate the composition and structure of its atmosphere. The measured Rp/R∗ depends on the opacity of the planetary atmosphere and thus allows for useful insights into the atmosphere's spectral features and composition. If the opacity in the near-UV band is dominated by Rayleigh scattering of molecular hydrogen, it may be possible to place strong upper limits on the planet's 10-bar radius [16]. The apparent size of the planet is determined from the flux dip

relative to the out-of-transit flux, as shown in Figure 4. The star magnitude varies when different filters are used. In our observations, using a wide wavelength filter, such as a UV-IR cut filter (420 – 865 nm), Fig. 5, the magnitude should decrease or the flux increase. On the other hand, the exoplanet does not play a part in the change in magnitude related to the flux; rather, it will show more wavelength blocking depending on the atmosphere's particle size. Axiomatically, it is independent of the different magnitudes of the host star before and during the transit. The wavelength-dependent transit depth indicates the atmosphere composition of an exoplanet [17]. Differences, such as asymmetric transit shapes, longer durations, or significantly deeper transit depths (>∼1%) compared to the optical filter [16], provide direct evidence of the significant effects of using wide-band filters, particularly in the blue and near-UV wavelengths.

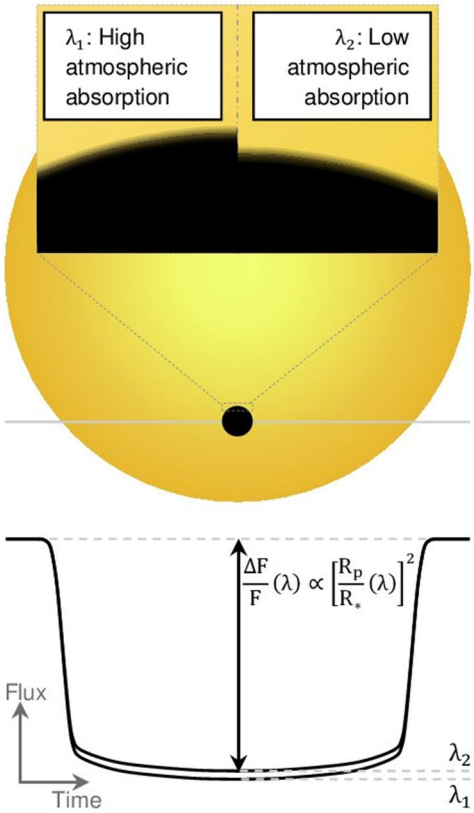

FIG. 4. Transit-depth variations, ΔF/ F (λ), caused by the wavelength-dependent opacity of a transiting planet's atmosphere. The stellar disk and planet are unresolved; the observed flux variation corresponds to a point source [24].

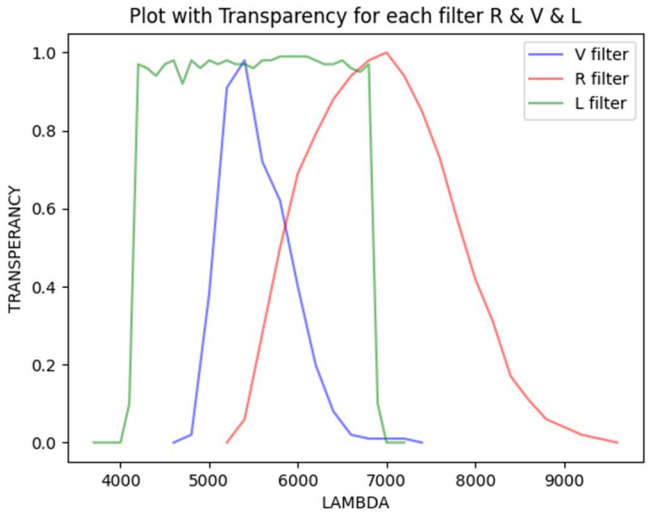

FIG. 5. Filter transparencies: R-Red, V-Visual, and L- Luminous.

This band allows us to determine the correlation between fine and large particles in the exoplanet's atmosphere by comparing the planet's size using the R and L filters. The observed visible size from a single observation is provided in Table 4. Based on this, we can estimate the distribution, amount, and concentration of particles spread around the planet. These particles are necessarily small and light because Rayleigh scattering is more effective than Mie scattering, as shown in Fig. 6. These results demonstrate the significant effects of using a wide-band filter, especially in the blue and near-UV wavelengths. This band allows us to assess the correlation between fine and large particles in the exoplanet's atmosphere by the ratio of the planet's size measured with the R and L filters, with the net visible size from a single observation summarized in Table 4.

TABLE 4. Comparison of (R p / R s) results from multiwavelength observations with those from this work.

HAT-P-54b			TrES-1b			WASP-104b		
Filter	Transit depth	References	Transit depth	Filter	Reference	Transit depth	Filter	Reference
V	0.15616	[19]	0.1382	V	[20]	0.124	V	[21]
I	0.16898	[19]	0.13686	z	[22]	0.129	R	[21]
R	0.17516	[19]	0.08	Ks	[23]	0.12140	I, z	[14]
L	0.18133	This Work	0.15218	L	This Work	0.12512	L	This Work
Expected literature value	0.1572	[10]	0.130	R	[8]	0.121	R	[12]

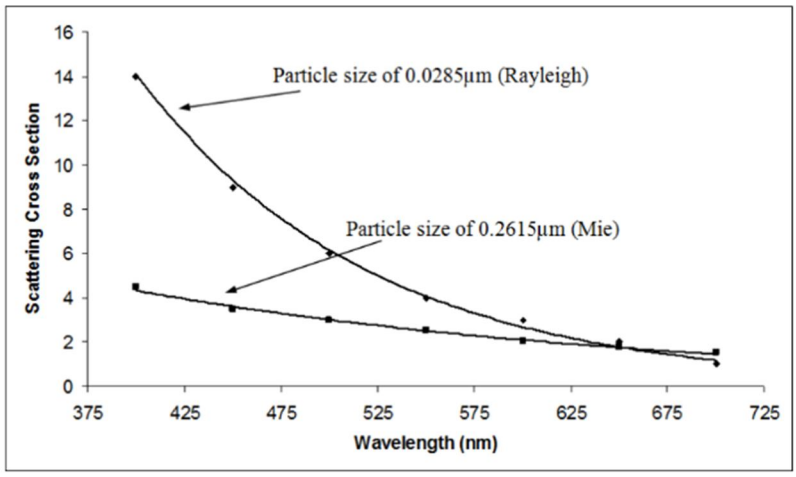

FIG. 6. Effects of Rayleigh and Mie scattering cross sections as a function of wavelength for different particle sizes [26].

These types of observations are indispensable for further investigations of exoplanet atmospheres and for comparisons with planets in the Solar System, such as recent studies combining CHEOPS and TESS data to examine differences in transit depths. The authors summarize several factors that affect transit depth; by default, variations in measured exoplanet size arise from differences in the sensitivity of the TESS and CHEOPS instruments, as well as the effects of limb darkening at shorter wavelengths, to which CHEOPS is more sensitive than TESS [18]. We know that stellar magnitudes vary when observed through different filters. Using a wide-band filter, such as a UV–IR cut filter (420–865 nm), the observed magnitude should be equal to or lower than that obtained with a narrow-band filter, and the measured flux should be the same or higher. The exoplanet itself does not directly affect this change in magnitude; rather, the observed flux variation reflects wavelength-dependent blocking by particles in the planet's atmosphere. This effect is independent of the host star's magnitude before or during the transit. Based on these observations, we can estimate the distribution, quantity, and concentration of particles surrounding the planet. These particles are necessarily small and light, as Rayleigh scattering is more effective than Mie scattering, as shown in Fig. 6. Near-UV transits may also exhibit asymmetries in their light

curves, including differences in ingress/egress timing, asymmetric transit shapes, longer durations, or significantly deeper transit depths (>1%) compared to observations in the optical [16].

TrES-1b:

- The orbit inclination is lower by 0.5°
- The planet radius obtained from the transit solution is large by around 10%.
- The larger radius of the planet leads to the conclusion that it is of a lower density.

HAT-P-54b:

- The orbit inclination is lower by 0.5°
- The planet radius obtained from the transit solution is larger by around 9%.
- The larger radius of the planet leads to the conclusion that it is of a lower density.

WASP-104b:

- The orbit inclination is higher by 0.5°.
- The planet radius obtained from the transit solution is almost similar to the previously published values.

Conclusion

In this paper, we investigated the capability of the Sharjah Optical Observatory in observing and detecting the transit of exoplanets. Despite the light-polluted location, we were able to observe and detect the transit. Our results show a clear match with the results from the previous observations and confirm the Jupiter-type exoplanets. Even under the difficult observation conditions, such as light pollution, low-latitude sites, and non-clear atmosphere, exoplanets can still be observed and confirmed. We demonstrate that exoplanet transits can be observed from suboptimal sites using relatively small telescopes. Our observatory is fully capable of observing exoplanets, even though it is located within a city with a high level of light pollution. Notably, the Sharjah Optical Observatory is the first observatory in the Gulf region to successfully observe exoplanets. Moving forward, we aim to expand our efforts to observe more exoplanets through transit photometry and to incorporate spectroscopy, providing training opportunities for students and establishing a community of exoplanet observers in the region.

Acknowledgements

We would like to extend our sincere gratitude to Spencer Mung, an IAESTE intern at the Sharjah Academy for Astronomy, Space Sciences, and Technology, for his invaluable efforts in editing, and to Ms. Nora Alamiri, Eng.Trifa al-Kaabi, Eng. Ibrahim Al-Sabt, Ms. Asmaa Alhameed, and Mr. Ahmad Al-Hariri for their assistance in review and editing. This research is based on data from the ETD database and makes use of the SIMBAD database via the Astrophysics Data Abstract Service. The authors are also grateful to the anonymous referee for their valuable notes and recommendations.

References

[1] Barkaoui, K. et al., J. Phys.: Conf. Ser., 869 (2017) 012073.

[2] Shporer, A. et al., ApJ, 690 (2009) 1393.

[3] Romanishin, W., "An Introduction to Astronomical Photometry Using CCDs", (Rochester, NY, 2002).

[4] Rabus, M. et al., Astron. Astrophys., 508 (2) (2009) 1011.

[5] Bissinger, R., Soc. Astron. Sci. Ann. Symp., 24 (2005) 81.

[6] Poddaný, S. et al., New Astron., 15 (3) (2010) 297.

[7] Kokori, A., ApJS, 258 (2) (2022) 40.

[8] Alonso, R. et al., ApJ, 613 (2) (2004) L153.

[9] Laughlin, G. et al., ApJ, 621 (2) (2005) 1072.

[10] Bakos, G.A. et al., AJ, 194 (4) (2015) 149.

[11] Kjurkchieva, D.E. et al., Serb. Astron. J., 198 (2019) 55.

[12] Močnik, T. et al., AJ, 156 (2) (2018) 44.

[13] Price, A. et al., J. Am. Assoc. Var. Star Obs., 34 (2005) 1.

[14] Smith, A.M. et al., Astron. Astrophys., 570 (2014) A64.

[15] Collins, K.A. et al., AJ, 153 (77) (2017) 1.

[16] Turner, J.D. et al., Mon. Not. R. Astron. Soc., 459 (1) (2016) 789.

[17] Yang, F. et al., Astrophys. Space Sci., 366 (2021) 83.

[18] Gaidos, E. et al., Mon. Not. R. Astron. Soc., 468 (3) (2017) 3418.

[19] Saha, S. et al., AJ, 162 (1) (2021) 18.

[20] Narita, N. et al., Publ. Astron. Soc. Jpn., 59 (4) (2007) 763.

[21] Valyavin, G.G. et al., Astrophys. Bull., 73 (2018) 225.

[22] Winn, J.N. et al., ApJ, 657 (2007) 1098.

[23] Adams, E.R. et al., AJ, 146 (1) (2013) 9.

[24] De Wit, J. and Seager, S., Science, 342 (6165) (2013) 1473.

[25] Talafha, M.F., Shaltout, A.M., Abdelkawy, A.G., and Beheary, M.M., New Astronomy, 119 (2025) 102379.

[26] Bin Omar, A.F. and Bin MatJafri, M.Z., Sensors, 9 (10) (2009) 8311.

الجداول: تعطى الجداول أرقاما متسلسلة يشار إليها في النص. ويجب طباعة كل جدول على صفحة منفصلة مع عنوان فوق الجدول. أما الحواشي التفسيرية، التي يشار إليها بحرف فوقي، فتكتب أسفل الجدول.

الرسوم التوضيحية: يتم ترقيم الأشكال والرسومات والرسومات البيانية (المخططات) والصور، بصورة متسلسلة كما وردت في النص.

تقبل الرسوم التوضيحية المستخرجة من الحاسوب والصور الرقمية ذات النوعية الجيدة بالأبيض والأسود، على ان تكون أصيلة وليست نسخة عنها، وكل منها على ورقة منفصلة ومعرفة برقمها بالمقابل. ويجب تزويد المجلة بالرسومات بحجمها الأصلي بحيث لا تحتاج إلى معالجة لاحقة، وألا تقل الحروف عن الحجم 8 من نوع Times New Roman، وألا تقل سماكة الخطوط عن 0.5 وبكثافة متجانسة. ويجب إزالة جميع الألوان من الرسومات ما عدا تلك التي ستنشر ملونة. وفي حالة إرسال الرسومات بصورة رقمية، يجب أن تتوافق مع متطلبات الحد الأدنى من التمايز (1200 dpi Resolution) لرسومات الأبيض والأسود الخطية، و 600 dpi للرسومات باللون الرمادي، و300 dpi للرسومات الملونة. ويجب تخزين جميع ملفات الرسومات على شكل (jpg)، وأن ترسل الرسوم التوضيحية بالحجم الفعلي الذي سيظهر في المجلة. وسواء أرسل المخطوط بالبريد أو عن طريق الشبكة (Online)، يجب أرسال نسخة ورقية أصلية ذات نوعية جيدة للرسومات التوضيحية.

مواد إضافية: تشجع المجلة الباحثين على إرفاق جميع المواد الإضافية التي يمكن أن تسهل عملية التحكيم. وتشمل المواد الإضافية أي اشتقاقات رياضية مفصلة لا تظهر في المخطوط.

المخطوط المنقح (المعدّل) والأقراص المدمجة: بعد قبول البحث للنشر وإجراء جميع التعديلات المطلوبة، فعلى الباحثين تقديم نسخة أصلية ونسخة أخرى مطابقة للأصلية مطبوعة بأسطر مزدوجة، وكذلك تقديم نسخة إلكترونية تحتوي على المخطوط كاملا مكتوبا على Microsoft Word for Windows 2000 أو ما هو استجد منه. ويجب إرفاق الأشكال الأصلية مع المخطوط النهائي المعدل حتى لو تم تقديم الأشكال إلكترونيا. وتخزن جميع ملفات الرسومات على شكل (jpg)، وتقدم جميع الرسومات التوضيحية بالحجم الحقيقي الذي ستظهر به في المجلة. ويجب إرفاق قائمة ببرامج الحاسوب التي استعملت في كتابة النص، وأسماء الملفات على قرص مدمج، حيث يعلَم القرص بالاسم الأخير للباحث، وبالرقم المرجعي للمخطوط للمراسلة، وعنوان المقالة، والتاريخ. ويحفظ في مغلف واقٍ.

حقوق الطبع

يُشَكِّل تقديم مخطوط البحث للمجلة اعترافاً صريحاً من الباحثين بأنّ مخطوط البحث لم يُنْشَر ولم يُقَدَّم للنشر لدى أي جِهَة أخرى كانت وبأي صيغة ورقية أو إلكترونية أو غيرها. ويُشترط على الباحثين ملء أنموذج يَنُصُّ على نقْل حقوق الطبع لتُصبح ملكاً لجامعة اليرموك قبل الموافقة على نشر المخطوط. ويقوم رئيس التحرير بتزويد الباحثين بإنموذج نقل حقوق الطبع مع النسخة المُرْسَلَة للتنقيح. كما ويُمنع إعادة إنتاج أيِّ جزء من الأعمال المنشورة في المجلّة من دون إذن خَطِّيٍّ مُسْبَق من رئيس التحرير.

إخلاء المسؤولية

إن ما ورد في هذه المجلة يعبر عن آراء المؤلفين، ولا يعكس بالضرورة آراء هيئة التحرير أو الجامعة أو سياسة اللجنة العليا للبحث العلمي أو وزارة التعليم العالي والبحث العلمي. ولا يتحمل ناشر المجلة أي تبعات مادية أو معنوية أو مسؤوليات عن استعمال المعلومات المنشورة في المجلة أو سوء استعمالها.

الفهرسة: المجلة مفهرسة في:

Scopus	**Emerging Sources Citation Index (ESCI)** Journal Impact Factor 2022 0.7
ULRICHSWEB GLOBAL SERIALS DIRECTORY	

معلومات عامة

المجلة الأردنية للفيزياء هي مجلة بحوث علميّة عالمية متخصصة مُحكمة تصدر بدعم من صندوق دعم البحث العلمي والابتكار، وزارة التعليم العالي والبحث العلمي، عمان، الأردن. وتقوم بنشر المجلة عمادة البحث العلمي والدراسات العليا في جامعة اليرموك، إربد، الأردن. وتنشر البحوث العلمية الأصيلة، إضافة إلى المراسلات القصيرة Short Communications، والملاحظات الفنية Technical Notes، والمقالات الخاصّة Feature Articles، ومقالات المراجعة Review Articles، في مجالات الفيزياء النظرية والتجريبية، باللغتين العربية والإنجليزية.

تقديم مخطوط البحث

تقدم المخطوطات إلكترونيًا عن طريق موقع المجلة: https://jjp.yu.edu.jo

ويجري تحكيمُ البحوثِ الأصيلة والمراسلات القصيرة والملاحظات الفنية من جانب مُحكِّمين اثنين في الأقل من ذوي الاختصاص والخبرة. وتُشَجِّع المجلة الباحثين على اقتراح أسماء المحكمين. أما نشر المقالات الخاصّة في المجالات الفيزيائية النَشِطَة، فيتم بدعوة من هيئة التحرير، ويُشار إليها كذلك عند النشر. ويُطْلَب من كاتب المقال الخاص تقديم تقرير واضح يتّسم بالدقة والإيجاز عن مجال البحث تمهيداً للمقال. وتنشر المجلةُ أيضاً مقالات المراجعة في الحقول الفيزيائية النشطة سريعة التغيُّر، وتُشَجّع كاتبي مقالات المراجعة أو مُستَكتبيها على إرسال مقترحٍ من صفحتين إلى رئيس التحرير. ويُرْفَق مع البحث المكتوب باللغة العربية ملخص (Abstract) وكلمات دالة (Keywords) باللغة الإنجليزية.

ترتيب مخطوط البحث

يجب أن تتم طباعة مخطوط البحث ببنط 12 نوعه Times New Roman، وبسطر مزدوج، على وجه واحد من ورق A4 (21.6 × 27.9 سم) مع حواشي 3.71 سم ، باستخدام معالج كلمات ميكروسوفت وورد 2000 أو ما استُجِدَ منه. ويجري تنظيم أجزاء المخطوط وفق الترتيب التالي: صفحة العنوان، الملخص، رموز التصنيف (PACS)، المقدّمة، طرق البحث، النتائج، المناقشة، الخلاصة، الشكر والعرفان، المراجع، الجداول، قائمة بدليل الأشكال والصور والإيضاحات، ثَمَّ الأشكال والصور والإيضاحات. وتُكْتَب العناوين الرئيسة بخطٍ **غامق**، بينما تُكْتَب العناوين الفرعية بخطٍ *مائل*.

صفحة العنوان: وتشمل عنوان المقالة، أسماء الباحثين الكاملة وعناوين العمل كاملة. ويكتب الباحث المسؤول عن المراسلات اسمه مشارا إليه بنجمة، والبريد الإلكتروني الخاص به. ويجب أن يكون عنوان المقالة موجزا وواضحا ومعبرا عن فحوى (محتوى) المخطوط، وذلك لأهمية هذا العنوان لأغراض استرجاع المعلومات.

الملخص: المطلوب كتابة فقرة واحدة لا تزيد على مائتي كلمة، موضحة هدف البحث، والمنهج المتبع فيه والنتائج وأهم ما توصل إليه الباحثون.

الكلمات الدالة: يجب أن يلي الملخص قائمة من 4-6 كلمات دالة تعبر عن المحتوى الدقيق للمخطوط لأغراض الفهرسة.

PACS: يجب إرفاق الرموز التصنيفية، وهي متوافرة في الموقع http://www.aip.org/pacs/pacs06/pacs06-toc.html.

المقدمة: يجب أن توضّح الهدف من الدراسة وعلاقتها بالأعمال السابقة في المجال، لا أن تكون مراجعة مكثفة لما نشر (لا تزيد المقدمة عن صفحة ونصف الصفحة مطبوعة).

طرائق البحث (التجريبية / النظرية): يجب أن تكون هذه الطرائق موضحة بتفصيل كاف لإتاحة إعادة إجرائها بكفاءة، ولكن باختصار مناسب، حتى لا تكون تكرارا للطرائق المنشورة سابقا.

النتائج: يستحسن عرض النتائج على صورة جداول وأشكال حيثما أمكن، مع شرح قليل في النص ومن دون مناقشة تفصيلية.

المناقشة: يجب أن تكون موجزة وتركز على تفسير النتائج.

الاستنتاج: يجب أن يكون وصفا موجزا لأهم ما توصلت إليه الدراسة ولا يزيد عن صفحة مطبوعة واحدة.

الشكر والعرفان: الشكر والإشارة إلى مصدر المنح والدعم المالي يكتبان في فقرة واحدة تسبق المراجع مباشرة.

المراجع: يجب طباعة المراجع بأسطر مزدوجة ومرقمة حسب تسلسلها في النص. وتكتب المراجع في النص بين قوسين مربعين. ويتم اعتماد اختصارات الدوريات حسب نظام Wordlist of Scientific Reviewers.

Subscription Form

Jordan Journal of PHYSICS

An International Peer-Reviewed Research Journal issued by the Support of the Scientific Research and Innovation Support Fund

Published by the Deanship of Research & Graduate Studies, Yarmouk University, Irbid, Jordan

Name: ..... الأسم:

Specialty:..... التخصص:

Address: ..... العنوان:

P.O. Box:..... صندوق البريد:

City & Postal Code: ..... المدينة/الرمز البريدي:

Country: ..... الدولة:

Phone: ..... رقم الهاتف:

Fax No:..... رقم الفاكس:

E-mail:..... البريد الإلكتروني:

No. of Subscription: ..... عدد الإشتراكات:

Method of Payment:..... طريقة الدفع:

Amount Enclosed:..... المبلغ المرفق:

Signature: ..... التوقيع:

Cheques should be paid to Deanship of Research and Graduate Studies - Yarmouk University.

I would like to subscribe to the Journal
For

- One Year
- Two Years
- Three Years

One Year Subscription Rates

	Inside Jordan	Outside Jordan
Individuals	JD 8	€ 40
Students	JD 4	€ 20
Institutions	JD 12	€ 60

Correspondence

Subscriptions and Sales:

Prof. Muhammad S. Bawa'aneh
Deanship of Research and Graduate Studies
Yarmouk University
Irbid – Jordan
Telephone: 00 962 2 711111 Ext. 2074
Fax No.: 00 962 2 7211121

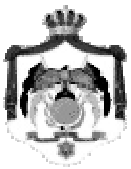

المملكة الأردنية الهاشمية

جامعة اليرموك

المجلة الأردنية

للفيزياء

مجلة بحوث علمية عالمية متخصصة محكّمة

تصدر بدعم من صندوق دعم البحث العلمي والابتكار

المجلد (18)، العدد (4)، تشرين الأول 2025م / جمادى الأول 1447هـ

المجلة الأردنية

للفيزياء

مجلة بحوث علمية عالمية محكّمة

المجلد (18)، العدد (4)، تشرين الأول 2025م / جمادى الأول 1447هـ

المجلة الأردنية للفيزياء: مجلة علمية عالمية متخصصة محكّمة تصدر بدعم من صندوق دعم البحث العلمي والإبتكار، عمان، الأردن، وتصدر عن عمادة البحث العلمي والدراسات العليا، جامعة اليرموك، إربد، الأردن.

ترسل البحوث إلى العنوان التالي:

الأستاذ الدكتور محمد سالم بواعنة

رئيس تحرير المجلة الأردنية للفيزياء

عمادة البحث العلمي والدراسات العليا، جامعة اليرموك

إربد ، الأردن

هاتف 7211111 2 962 00 **فرعي** 2074

E-mail: *jjp@yu.edu.jo* **Website**: *http:// jjp.yu.edu.jo*